NASA Technical Memorandum 4069
Volume 2

Microgravity Science and Applications Flight Programs, January–March 1987, Selected Papers

NASA Office of Space Science and Applications
Washington, D.C.

National Aeronautics
and Space Administration

Scientific and Technical
Information Division

1988

CONTENTS

VOLUME II

GLASSES AND CERAMICS

FLUORIDE GLASS: CRYSTALLIZATION, SURFACE TENSION AND BUBBLES IN LOW GRAVITY

R. H. Doremus
Materials Engineering Department
Rensselaer Polytechnic Institute
Troy, New York 12181

ABSTRACT

Fluoride glass was levitated acoustically in the ACES apparatus on STS-11, and the recovered sample had a different microstructure from samples cooled in a container. Further experiments on levitated samples of fluoride glass are proposed. These include nucleation, crystallization, and melting observations, measurement of surface tension of molten glass, and observation of bubbles in the glass. Ground experiments are required on sample preparation, outgassing, and surface reactions. The results should help in the development and evaluation of containerless processing, especially of glass, in the development of a contaminent-free method of measuring surface tensions of melts, in extending knowledge of gas and bubble behavior in fluoride glasses, and in increasing insight into the processing and properties of fluoride glasses.

BACKGROUND

Fluoride Glass

A variety of fluoride glasses based on zirconium, hafnium or thorium fluoride are being intensively investigated because they are transparent in the infrared to 8 μm and beyond.[1-4] Optical components such as lenses, prisms, and fibers for use in the infrared can be made of these glasses. An especially attractive application envisions fiber optic wave guides for long distance communication. Fibers of vitreous silica are already being used for this purpose. The length of each link in a communication chain is limited by optical scattering and absorption; silica has a minimum combined absorption at about one μm. The fluoride glasses have in theory a much deeper minimum than silica at longer wavelengths because their absorption edge is further into the infrared. Much progress has been made in forming fibers for these purposes and reducing their absorption and scattering losses.

Optical fibers are being investigated as sensors for a wide variety of environmental factors, including temperature, pressure, displacement, acoustic field, electromagnetic waves, and even composition.[8] Availability of glasses with wider ranges of transparency in the infrared should provide new and improved sensors.

These fluoride glasses satisfy the requirements of high value and low volume materials for space processing. If different compositions with a larger range of infrared transparency could be made because of the reduced contamination and wall nucleation during containerless processing, many more valuable glasses would be available.

These fluoride glasses are made by melting the constituent fluorides together with ammonium bifluoride ($NH_4F \cdot HF$) in a vitreous carbon crucible in an atmosphere of 3% chlorine in dry nitrogen. A composition extensively studied, and the one used for the shuttle experiment, is 62 mole% ZrF_4, 33% BaF_2 and 5% LaF_3, designated as ZBL glass. A maximum temperature of about 900°C was required to ensure complete melting. The molten glass was cast into brass or steel molds, annealed near the glass transition temperature of about 320°C, and cooled slowly to room temperature. Spheres of glass were cast for flight experiments; they contained a bubble of entrapped air.

The crystallization and melting of ZBL and many other fluoride glasses were studied with differential scanning calorimetry (DSC), X-ray diffraction, and the scanning electron microscope.[5-7] Surface crystallization leads to crystals about 10 μm in size and a peculiar wrinkling of the surface.[6] In ZBL glass the crystalline phases that form are $BaZrF_6$ and BaZ_2F_{10}; each of these phases has two polymorphs.[5] In ZBL glass fine crystals grow spherically in the glass volume when it is heated in the DSC_5; when the glass melt is cooled slowly, large columnar crystals are nucleated on the container walls and grow into the melt, as shown in Fig. 14, App. I.

These columnar crystals were not found in a crystallized sample from the shuttle flight, shown in App. I. This sample was levitated in the furnace in the field of view up to about 450°C, when it was lost from view for the rest of the flight. It is possible that the sample stuck to a portion of the wire holding cage, because one piece of the sample had a dark rim or line depression on it, perhaps from contact with the cage. Thus crystallization on cooling from the molten condition probably took place more uniformly and on a smaller scale than if the sample crystallized from a crucible. More experiments are needed to test these possibilities. The post-flight analysis of the sample is described in a report attached as an appendix.

It seems likely that the columnar crystals of Fig.14 are caused by nucleation on the wall of the platinum crucible, and heat flow from the melt to the cooler wall. The absence of a container for a levitated sample precludes this mechanism of crystallization, and should lead to a more uniform fine crystallization thoughout the sample volume. This kind of uniform nucleation should require a greater undercooling, and so should occur only at slower cooling rates as compared to the crystallization nucleated on the crucible wall. More experiments on levitated samples are needed to test these possibilities.

The solubilities, diffusion coefficients, and reactivities of gases in fluoride glasses are poorly known. Gases in these glasses can influence processing, including fining (removal of bubbles), formation of defects, crystallization rates, and chemical reactivity. Vaporization rates and vaporized species have been little studied. Further knowledge of gaseous behavior in fluoride glasses is essential to control processing, fining, crystallization, and defect formation.

Containerless Processing

The possibility of making and studying liquid and solid materials without a container has exciting potential for increased learning about these materials. For glasses the advantages of purity and reduction of nucleation by the container could lead to new compositions and methods of forming.

Various ways of holding levitated samples in position are being explored. Acoustic levitation is particularly attractive because it can be used for any kind of sample and position controlled by the geometry of the system and the power fed to the acoustic drivers. A three-axis acoustic levitator (ACES) has been designed and built at the Jet Propulsion Laboratory (JPL), and was used to levitate a one cm. sphere of fluoride glass in shuttle flight STS-11. A single-axis acoustic levitator is being developed under the supervision of Marshall Space Flight Center. Air jet levitators are also being built and tested, and electrostatic levitation is possible for a dielectric sample. It will require much further testing to determine which systems are optimum for levitating different materials of interest at different conditions of temperature and atmosphere.

Surface Tension

The surface tension of high-temperature melts is usually measured by a sessile or pendant drop experiment.[9,10] However, the surface tension of a liquid can be strongly influenced by contamination with impurities, and these methods require that the drop rest on a substrate or be held by a tube or rod. If the melt is reactive, there is also a possibility of contamination from these foreign materials. Thus it would be highly desirable to find a method of measuring surface tension of a levitated melt at high temperatures. The vibration of a drop depends on its surface tension, so the vibration of a levitated drop, excited by an acoustic field, can be used to measure its surface tension. This method is being developed at JPL by Drs. Taylor Wang and Daniel Elleman and their colleagues, and has been successful for drops at room temperature.

Bubble Motion and Shrinkage

One of the most difficult steps in preparing glass, especially for optical purposes, is to remove bubbles in the viscous melt. In commercial practice bubbles are removed both by expanding and rising to the glass surface and by shrinking.[11-13] However, in low gravity bubbles will not "rise", and their motion and growth or shrinkage are important factors in making a bubble-free glass.

Diffusion of gas into the glass appears to control bubble shrinkage in most glasses.[11,12,14] Complete mathematical solutions to the problem of diffusion-controlled shrinkage of a bubble are difficult, so a variety of approximation methods have been used.[11-15] Weinberg and his collaborators have explored a variety of conditions and solutions of bubble growth and shrinkage equations (see refs. 15 and 16 and references therein). From these equations it is possible to calculate diffusion coefficients and solubilities of gases in melt from the rate of shrinkage of a gas bubble in the melt. Thus measurements of bubble shrinkage rates can give valuable information on processing of glass and on the properties of gases in the glass. A levitated drop has the advantage that the bubble is likely to be stationary, giving relatively simple mathematical boundary conditions Effects of convection are reduced in low gravity; these effects could be important in the relatively fluid melts of the fluoride glasses.

PROPOSED FLIGHT EXPERIMENTS

Crystallization and melting experiments on a levitated sphere of ZBL glass are proposed. The glass will be heated at a constant rate of from five to twenty degres per minute from the glass transition temperature of about 300°C up to a temperature (about 600°C) when the glass is completely molten. The nucleation and growth of crystalline phases and their melting will be observed during the heating. After the sample is held for several (up to 30) minutes at 600°C for the surface tension experiment, it will be cooled in the furnace at a rate similar to the heating rate. Again the nucleation and growth of crystalline phases will be observed. When the sample is completely crystallized (below about 450°C) it will be captured by a restraining cage, so it will hold together for post-flight analysis.

Surface tension of the glass melt will be measured from the vibrating molten sample, excited by the acoustic field. This experiment is being developed by Dr. Dan Elleman and his colleagues at JPL. They have measured surface tensions of levitated liquid drops at room temperature by this method. The details of this method are discussed in a memorandum by Dr. Elleman; a copy is included as an appendix to this proposal. If the viscosity is low enough, the frequency w_n of an oscialIting drop in the nth mode is given by:

$$w_n^2 = n(n-1)(n+2)\sigma/\rho R^3 \quad (1)$$

where σ is the surface tension, ρ is the density, and R the radius of the drop. The viscosity of the fluoride glass at 620°C is apparently low enough for this equatiodn to be valid.

Changes in the size and position of an air bubble in the sample will be observed throughout the heating and cooling cycle. The rate of growth or shrinkage of the bubble will give some information on the solubility anbd diffusion of gases in the glass; a complete interpretation of such results would require extensive ground-based experiments to determine these quantities for comparison with zero gravity results. Such experiments are not part of this proposal. Bubble motion should indicate flow in the glass, if any, and forces such as gravitational, thermal, and surface tension. Again a complete analysis would probably require extensive ground experiments.

Post-flight analysis of the sample will include chemical analysis, microscopic analysis in the SEM, and X-ray diffraction. The results from the experiment on STS-11 showed (from EDS analysis on the SEM) that the sample had the same zirconium-to-barium ratio as the starting glass, and that the crystalline phases were mostly $BaZrF_6$ and $BaZr_2F_{10}$, which are the same phases found when the fluoride glass crystallizes on heating, and upon cooling from the melt, on the ground. However, the proportions of the various α and β polymorphs of these phases of the levitated sample were different from those found in a crystallized glass cooled slowly from the melt. The microstructures of the space and ground samples were also quite different, as shown in the report included as Appendix I. Additional work is proposed to give more information on differences between samples cooled in the levitated condition and in a crucible.

EQUIPMENT

The experiments on fluoride glass in flight STS-11 were carried out in the ACES equipment built at JPL. Most aspects of this equipment functioned well, for example, the computorized controls and the furnace. However, there were two factors that need improvement if the proposed experiments are to be carried out successfully in this equipment. These are the viewing capability and the sample stability. The engineering group at JPL is working on improving these factors and ground tests are planned to see if the improvements are adequate. Additional discussion of the equipment and its functioning is given in Appendix I.

As part of the cooperation with JPL for the STS-11 experiment, a small Science Working Team was established to help in developing the ACES equipment and the experiment. Engineering and scientific personnel from JPL met with two outside members (Prof. S. Subramanian, Clarkson, and Dr. Ray Downs, KMS Fusion) and Prof. R. H. Doremus as Chairman. This group was very important in the success of the experiment, because it provided close, critical cooperation between the Principal Investigator for the experiments (Prof. Doremus) and the engineers and scientists at JPL. The two outside members gave critical, objective help throughout. A continuation of a similar group for any future experiments is proposed.

GROUND-BASED EXPERIMENTS

Preparation of spherical samples of fluoride glasses for the flight experiments will be continued. An especially important problem is outgassing of samples as they are heated. (See report in Appendix I.) During the flight experiment the viewing became rapidly more cloudy as the sample was held at 600°C. Apparently the alumina window was etched by a corrosive gas, which was probably hydrofluoric acid from the sample. The fluoride glasses are melted in an excess of ammonium bifluoride ($NH_4F \cdot HF$) to convert any oxide impurities to fluorides, and it is quite possible that some HF is retained in the glass after it is quenched.

Fluoride glasses will be melted with purified starting materials without ammonium bifluoride, and samples will be tested for gaseous products up to 650°C. Outgassing will be followed with weight change in a sensitive microbalance (Cahn), and gases emitted will be analyzed by mass spectrometry. The reactivity of the glass with inconel alloy, the material of construction of the ACES furnace, will also be studied.

The vaporization of zirconium fluoride, perhaps after reaction with water vapor, is another possible source of HF:

$$ZrF_4 + 2H_2O_{(g)} = ZrO_2 + 4HF_{(g)} \qquad (2)$$

At room temperature, the standard free energy change for this reaction is about +52 kj/mole, so it is unfavorable; however, at 625°C it is about -106 kj/mole. Thus at the melt temperatures reaction 2 is quite favorable, and any small amount of water in the sample or system will react with the glass to form HF gas.

When the fluoride glass is heated in humid air to about 600°C, where it is molten, a white film forms on the surface, probably composed of zirconium oxide from reaction 2; in dry nitrogen the film is absent. More experiments on the reaction of water and other gases such as chlorine, used in the melting of the glasses, are proposed to determine surface condition and reaction products. A surface unreactive to water can form on the fluoride glass,[17] and its nature will be investigated.

There have been several investigations of the reaction of liquid water with the fluoride glass[18-20]; our work will continue with support from the National Science Foundation.

SIGNIFICANCE OF THE WORK

The main goal of this work is to develop the capabilities of containerless processing, especially of glasses. The experiments on nucleation, crystallization and melting will help to show whether or not there are advantages in containerless processing for making new glass compositions, and to gain more insight into the role of containers, gravity, and convection in these processes. The measurement of surface tension of levitated samples should be valuable for reactive melts and those highly sensitive to contamination. Growth, shrinkage, and motion of bubbles in the glass melt in low gravity should show the importance of convection and forces low compared to gravity on these processes. The experiments should also give considerable additional information in these areas for fluoride glasses, which show great promise for applications as otpical components, especially fiber-optic wave guides.

REFERENCES

1. M. Poulain, M. Chanthanasinh and J. Lucas, Mater. Res. Bull. 12, 151 (1977).

2. C. T. Moynihan, M. G. Drexhage, B. Bendow, M. Saleh-Boulos, K. P. Quinlan, K.-H. Chung, and E. Gbogi, ibid 16, 25 (1981).

3. M. Drexhage et al. and S. Takahashi et al. in "Physics of Fiber Optics", B. Bendow and S. S. Mitra, eds., Am. Ceramic Soc., Columbus, Ohio, 1981, pp. 57-73, 74-83.

4. C. M. Baldwin, R. M. Almeida and J. D. Mackenzie, J. Noncryst. Solids 43, 309 (1981).

5. N. P. Bansal, R. H. Doremus, A. J. Bruce and C. T. Moynihan, J. Amer. Cer. Soc. 66, 233 (1983); Mat. Res. Bull. 19, 577 (1984); to be published.

6. N. P. Bansal and R. H. Doremus, J. Amer. Cer. Soc. 66, C-132 (1983).

7. M. C. Weinberg, G. F. Neilson and G. L. Smith, J. Noncryst. Solids 56, 45 (1983); Mat. Res. Bull., (1984).

8. "Seminar on Optical Fiber Sensors", Amer. Cer. Soc. Bull. 63, 496 (1984).

9. J. K. Davis and F. E. Bartell, Anal. Chem. 20, 1182 (1948).

10. A. W. Adamson, "Physical Chemistry of Surfaces", John Wiley, New York (1976), p. 28ff.

11. C. H. Greene and R. F. Gaffney, J. Amer. Chem. Soc. 42, 271 (1959).

12. R. H. Doremus, ibid 43, 655 (1960).

13. M. Cable, Glass Tech. 2, 60 (1961).

14. R. B. Brown and R. H. Doremus, J. Am. Cer. Soc. 59, 510 (1976).

15. M. C. Weinberg, P. J. K. Onorato and D. R. Uhlmann, ibid, 63, 175, 435 (1980); 64, 676 (1981).

16. R. S. Subramaniam and M. C. Weinberg, AIChEJ 27, 739 (1981).

17. C. Burman, W. A. Lanford, R. H. Doremus, and D. Murphy, Appl. Phys. Lett. 44, 845 (1984).

18. C. J. Simmons, H. Sitter, J. H. Simmons and D. C. Tran, Mat. Res. Bull. 17, 1203 (1982).

19. S. Mitachi, Phys. Chem. Glasses 24, 146 (1983).

20. R. H. Doremus, N. P. Bansal, T. Bradner and D. Murphy, J. Matls. Sci. Lett. 3, 484 (1984).

N89-20307

CONTAINERLESS PROCESSING OF GLASS FORMING MELTS IN SPACE

by

D. E. Day and C. S. Ray
Graduate Center for Materials Research and
Department of Ceramic Engineering
University of Missouri-Rolla
Rolla, Missouri 65401

For presentation to:

Technical Review Committee
Microgravity Science Review
Marshall Space Flight Center

11 February 1987

ABSTRACT

The near weightlessness of a material in the reduced gravity environment of space offers the unique opportunity of melting and cooling glass forming compositions without a container. This reduces (or eliminates) the heterogeneous nucleation/crystallization which usually occurs at the walls of the container, thereby, extending the range of glass forming compositions. New glasses with interesting properties and glasses of ultra-high chemical purity can be made by containerless processing.

Based primarily on this idea, containerless glass forming experiments, which used a single axis acoustic levitator/furnace (SAAL), have been conducted on SPAR rocket flights, VI and VIII, and on Space Shuttle missions, STS-7 and STS-61A. The experiments on the Space Shuttle were designed to include other studies related to melt homogenization and mixing, development of techniques for preparing uncontaminated pre-flight samples, and simple shaping experiments. Knowledge about these factors is useful for planning and standardizing future containerless processing experiments in space.

Motion pictures of solid and liquid samples from the most recent experiment (STS-61A) showed that fluid melts can be successfully levitated and positioned with an acoustic field at temperatures up to 1550°C for several minutes. A ternary calcia-gallia-silica glass containerlessly melted in micro-g, provided evidence for a 2 to 3 fold increase in the tendency for glass formation in space. This is preliminary verification that heterogeneous nucleation is reduced in containerless melts. Melt homogenization for this calcia-gallia-silica melt was reasonably fast in space even with the lack of gravity-driven convection. Hot-pressing appears to be a feasible way of preparing precursor samples for use in containerless experiments in micro-g. Comparison of these results with those of earlier containerless experiments, from SPAR VI and STS-7, shows a progressive advancement in the science and technology of materials processing in space.

The objectives of future flight experiments on glass forming systems, which take advantage of the gravity-free environment of space, such as diffusion in the absence of gravity-driven convection, shaping of simple shapes using acoustic forces, preparation of glass composites from immiscible liquids, etc., are also briefly discussed.

1. INTRODUCTION

A serious factor that prevents many compositions from forming glass on earth is heterogeneous nucleation/crystallization which normally occurs at the melt-container interface. The impurities dissolved from the container material can also act as potential nucleation sites for heterogeneous crystallization as well as contaminating the melt. The net volume fraction, V_c/V, crystallized in a melt in time, t, is expressed as [1,2]

$$V_c/V = \pi/3 \; I(T)u^3(T)t^4 \qquad (1)$$

where I and u are the nucleation and crystal growth rates, respectively, and both are functions of temperature, T. I in Eq. (1) generally includes both the homogeneous and heterogeneous nucleation rates. A foreign surface (or substrate) in contact with a melt provides heterogeneous nucleation sites which lower the thermodynamic barrier for nucleation. Thus, heterogeneous nucleation is more favorable than homogeneous nucleation. Regardless of the nucleation mechanism, crystallization of a melt can be avoided when it is cooled at a sufficiently high rate so that a glass is obtained, i.e., $V_c/V < 10^{-6}$. Depending on the characteristics of a particular system, there exists a minimum cooling rate for which the level of crystallization is just detectable ($V_c/V \approx 10^{-6}$). This rate is known as the critical cooling rate for glass formation, R_c.

I and u reach a maximum at some temperature where the increasing thermodynamic force for crystallization on cooling is counteracted by the increasing viscosity of the melt. The combined temperature dependence of I and u results in a nose-shaped curve on a temperature-time plot, see Fig. 1, which is known as temperature-time-transformation (or TTT) diagram [3].

The slope for the cooling curve which originates at the liquidus temperature and just touches the nose of the TTT diagram is considered to be R_c. The melt transforms to a crystalline or glassy solid when it is cooled at a rate $R < R_c$ (cooling curve intersects the TTT diagram) or $R > R_c$, respectively.

The near weightlessness of a material, solid or liquid, in the micro-g environment of space makes a container unnecessary. The absence of a container eliminates the possibility of a melt being contaminated by impurities from the container. Heterogeneous nucleation/crystallization can be suppressed, therefore, for containerless melts. The crystallization of such a melt will be determined primarily by the inner curve for homogeneous nucleation in Fig. 1. If homogeneous nucleation only occurs in space, then a melt can be cooled to glass at a cooling rate which is less than R_c on earth where heterogeneous nucleation is present because of the container. The suppression of heterogeneous nucleation in a containerless melt effectively lowers the nucleation rate, I, in Eq. (1) which decreases the volume fraction crystallized, V_c/V, or increases the glass formation tendency. This possibility for enhanced glass formation tendency for containerless melts in space can be utilized to prepare glasses from compositions which may have interesting optical, electrical, or physical properties and whose crystallization during cooling cannot be avoided on earth. Furthermore, the elimination of impurities from the container makes it possible to prepare chemically ultrapure glasses which could be used for special applications such as lasers, optical waveguide fibers, etc. Preparing ultrapure glasses on earth can be a difficult to impossible task, especially if high melting temperatures are required and the melts are highly fluid and chemically reactive.

Based primarily on this idea, containerless glass melting experiments, which used a single axis acoustic levitator/furnace (SAAL), have been conducted in micro-g by R. A. Happe [4,5] of Rockwell International in SPAR rocket flights VI and VIII, and by ourselves on Space Shuttle missions, STS-7 [6] (June 1983) and STS-61A [7,8] (October 1985). The SAAL, which consists of a 4" x 4" x 4.5" furnace with four silicon carbide heating elements, a sound source, and a reflector for levitating and positioning a sample in the high temperature portion of the furnace, a mechanism for inserting and retrieving the sample from the furnace, and a motion picture camera for recording the sample while being processed in the SAAL, is described in detail elsewhere [9,10]. The SAAL used in rocket flights had the capability of processing only one sample, while that used in the Space Shuttle could process eight samples consecutively. Other subjects such as melt homogenization and mixing, developing techniques for preparing uncontaminated preflight (precursor) samples, and simple shaping experiments, were also investigated in the Space Shuttle experiments. The results from these experiments have provided valuable knowledge for the behavior of containerless melts at high temperatures and have been useful for planning and standardizing future containerless experiments in space.

The SPAR experiments have been included in this report since the final analysis of the SPAR VI sample was our responsibility [9]. Also, the same SAAL design was used for all the containerless experiments, so a brief review of the SPAR experiments provides a better chronological description of the operational performance of the SAAL for processing multicomponent, glass forming melts in space. However, the present paper primarily deals with the results of the most recent experiment conducted on the Space Shuttle STS-61A which used the MEA/A-2 (Materials Experiment Assembly) flight hardware. The earlier experiments will be referred to and discussed only when a comparison of the results is needed.

Finally, the objectives of future flight experiments on glass forming systems, which take advantage of the reduced gravity environment of space, such as diffusion in the absence of gravity-driven convection, shaping of simple shapes using acoustic forces, and the study of immiscible liquids, are briefly discussed.

2. EXPERIMENTAL

Eight spherical samples, ≈6 ± 1 mm in diameter, were used in the MEA/A-2 experiment, STS-61A. Each sample had one or more of the following objectives: 1) to obtain quantitative evidence for the suppression of heterogeneous nucleation/crystallization (or enhanced glass formation) in containerless melts in micro-g, 2) to study melt homogenization in the absence of gravity-driven convection, 3) to perform comparative property analysis of glasses melted on earth and in micro-g, 4) to develop procedures for preparing precursor samples that yield bubble free, high purity, chemically homogeneous melts in micro-g, 5) to determine the feasibility of shaping glass shells in micro-g for use as laser fusion targets, and 6) to assess the operational performance of the SAAL for processing multicomponent, glass forming melts in micro-g. The composition, purpose, and the temperature/time planned for the containerless processing of each sample are given elsewhere [7,8].

Each sample was held in an individual sample injector/retrieval system, which was fitted in a carousel assembly in the SAAL. The sample processing procedure was fully automated. During operation, the sample injector moved inside the furnace through a gate and released the sample for stable positioning at the potential energy minimum of the sound field confined between the sound source and reflector of the SAAL. After melting, the sample was cooled by temporarily turning off the power to the furnace and opening a gate on one side of the furnace wall. At the completion of processing, the sample was retrieved, the carousel assembly rotated, and the second sample automatically moved to the position of the sample injection gate.

The critical cooling rate for glass formation, R_c, was used as the quantitative parameter for the suppression of heterogeneous nucleation/crystallization. As discussed earlier, if heterogeneous nucleation caused by a container is absent in containerless melts, then it should be possible to quench such melts to glass using cooling rates which are less than R_c measured on earth where heterogeneous nucleation is present. Thus, the ratio R_c (earth) to R_s (space) for melts quenched to glass in micro-g should exceed unity and the numerical value of this ratio can be used as a quantitative measure of the degree to which glass formation is enhanced, or, conversely heterogeneous nucleation/crystallization is suppressed in containerless melts. Samples whose R_c on earth is several times higher than the cooling rate of the SAAL furnace used in micro-g (≈5°C/s) was used to provide evidence for enhanced glass formation in micro-g.

Melt homogenization in the absence of gravity-driven convection in micro-g was to be investigated by observing the level of homogeneity achieved in precursor samples made with known chemical inhomogeneities. Hot-pressed samples containing relatively large SiO_2 particles (100 - 300 µm) and a sample which contained a colored spot on its external surface were used for this purpose. In addition, a sodium-borate sample containing gas bubbles at known locations was used to provide information for the behavior of gas bubbles in liquid melts and supplemental data for melt homogenization in micro-g.

Glass shells of uniform sphericity and wall thickness, and several millimeters in diameter have important uses in laser fusion technology as inertial confinement fusion (ICF) targets. They are essentially impossible to fabricate on earth, however, due to gravity induced distortion. As there is no buoyant force in micro-g, a bubble initially present inside a glass should not necessarily escape when the glass is remelted in space. On the other hand, surface tension forces should reshape the sample into a spherical shell, perhaps of uniform wall thickness, when it is levitated and melted without a container. A soda-lime-silica glass shell containing an air bubble ≈3.75 mm in diameter was used for this purpose. Lastly, several physical, optical, thermal, and mechanical properties for glasses made in micro-g were compared with the same properties measured for glasses of identical composition made on earth.

An important practical objective of this experiment was to determine the suitability of hot-pressed, precursor samples for use in containerless melting. Hot-pressed precursor samples have the advantage of being easily prepared without contamination from a container. A sample larger than that needed can be hot-pressed, with only the uncontaminated core being used for the experiment in space. It is important to know the maximum size of the chemical inhomogeneities that can be tolerated in a hot-pressed precursor which will yield a chemically homogeneous, multicomponent melt in a reasonable time when melted in micro-g.

3. RESULTS AND DISCUSSION

The film and flight data for this experiment indicate that the first three samples were processed in a containerless manner according to the planned time-temperature schedule. None of the remaining five samples were inserted into the furnace, levitated, or melted. Of the three samples processed, sample 2 which was a hot-pressed $35.7CaO-39.3Ga_2O_3-25SiO_2$, mol%, composition had more than one scientific objective on MEA/A-2, i.e., 1) to verify enhanced glass formation in micro-g, 2) to evaluate melt homogenization and mixing in the absence of gravity-driven convection, and 3) to assess precursor preparation technique. The planned and observed temperature-time profile for the containerless melting of sample 2 is given in Fig. 2. The first sample was a non-melting alumina and was used for an engineering checkout of the SAAL.

A. Flight Events for Sample 2

When sample 2 was recovered from the MEA/A-2 flight hardware, it was stuck to one side of the platinum wire cage, see Fig. 3, which surrounded the sample primarily for the purpose of preventing it from being lost if, for any reason, it should escape from the acoustic energy well. The motion picture film for sample 2 clearly showed that the sample struck and adhered to the cage when the cooling gate of the SAAL opened for cooling. The instability of sample 2 and its movement out of the acoustic well coincided with the opening of the cooling gate. Several factors may have caused sample 2 to escape from the acoustic well. Opening the cooling gate could have produced a temperature gradient, which in turn may have produced pressure gradients inside the furnace which were sufficient to displace the sample from the acoustic energy well.

B. Enhanced Glass Formation for Sample 2

When examined with a scanning electron microscope (SEM), that part of sample 2 touching the cage wires was seen to be crystalline. The crystallized region extended about 1 mm along the surface of the sample from both sides of the wire and slightly less than 1 mm (0.8 to 0.9 mm) into the interior of the sample. The central part of sample 2 which did not touch the wires was glassy. A few scattered crystals confined only to the external surface of the glassy region was also observed. The sample is estimated to contain 70 to 80% glass, the remainder being crystalline. It is believed that sample 2 would have been totally glassy if it had not touched the cage which produced heterogeneous nucleation/crystallization. The average cooling rate between 1450 and 1000°C, as calculated from two thermocouples within about 1 cm of the sample on MEA/A-2, was ≈ 4.2°C/s. This is lower than the critical cooling rate, R_c, measured on earth (11.3 ± 2°C/s) for a sample of identical composition by a factor of 2.7. This indicates that containerless melting in space has improved the glass formation tendency of this calcia-gallia-silica composition by a factor of between 2 and 3. Based on the measured R_c value and nose temperature (≈1215°C), a TTT diagram for this composition having a sample size identical to sample 2 (diameter ≈6.5 mm) has been estimated and is shown in Fig. 4. Superimposed on the TTT diagram is the actual cooling curve of flight sample 2, which is seen to pass through the crystallized region inside the TTT diagram. This indicates that a sample cooled on earth at a rate equal to that used in the flight experiment would be totally crystalline. The fact that sample 2 returned as a glass clearly demonstrates that containerless melting increased the glass formation tendency of this calcia-gallia-silica composition. Although the data are limited, the most likely explanation for these results is the reduction in heterogeneous nucleation in the containerless melted sample.

C. Melt Homogenization for Sample 2

As mentioned earlier, the sample 2 precursor was made by hot-pressing crystalline powders. This sample contained random heterogeneities in the form of 100 - 300 μm silica particles dispersed in the fine-grained calcia-gallia matrix, see Fig. 5. No remnants of these silica particles or regions rich in silica were detectable by SEM on either the external surface or in the bulk of sample 2 after melting in space. The relative composition at different locations on the external surface and in the interior (fracture surface) of sample 2 was determined by energy dispersive x-ray analysis (EDAX) and is shown graphically in Fig. 6. The compositions determined at different, randomly chosen locations in the bulk are close to the actual composition and the scatter in composition is significantly less than that for the external surface. This shows that the bulk of sample 2 is more homogeneous than the external surface which is also consistent with the fact that the external surface was partially crystallized. The complete dissolution of the large silica particles to form a reasonably homogeneous glass in a melting time of ≈4 min at an average temperature of 1475°C suggests that the chemical homogenization process is reasonably fast in space for this low viscosity melt, even in the absence of gravity-driven convection. Hot-pressing appears to be a feasible way of preparing high purity, precursor samples for use in flight experiments which will yield a chemically pure, homogeneous glass in micro-g within a reasonable time.

D. Comparison of Properties for the Glasses Melted in Space (Sample 2) and on Earth

Due to its small size and partial devitrification, only a few properties could be measured for flight sample 2. The refractive index, dispersion, and Abbe number for this glass, as measured by the Becke line technique, are compared in Table I with those of a glass of identical composition melted on earth. While there are slight differences in the properties of the two glasses, the differences are not considered to have practical significance. The crystallization of the space and earth-melted glasses were also studied by differential thermal analysis (DTA) at a heating rate of 10°C/min. A comparison of the DTA curves in Fig. 7 shows that the crystallization for the space and earth melted glasses is essentially identical. The appearance of a large exothermic peak with a small shoulder on the low temperature side in the DTA curve shows that two compounds crystallize from this glass. They have been

Table I. Refractive index, dispersion, and Abbe number for the 35.7CaO-39.3Ga_2O_3-25SiO_2, mol%, glass melted in space and on earth.

	Space Sample 2 (MEA/A-2)	Earth sample
Refractive Index ($\pm$0.001)	1.729	1.712
Dispersion	0.028	0.018
Abbe Number ($\pm$3.5)	26.1	40.5

identified by powder x-ray diffraction (XRD) as β-Ga_2O_3 and ($2CaO \cdot Ga_2O_3 \cdot SiO_2$). The same two compounds were also observed when the crystallized region of the space melted sample was examined by SEM and EDAX, see Fig. 8, and by Debye Scherrer XRD. The larger peak at ≈887°C in Fig. 7 corresponds to the crystallization of ($2CaO \cdot Ga_2O_3 \cdot SiO_2$) as determined by examining the crystallization of a glass whose composition is ($2CaO \cdot Ga_2O_3 \cdot SiO_2$). The smaller peak (≈855°C) in Fig. 7 is attributed to the crystallization of β-Ga_2O_3.

The infrared transmission of the space and earth melted calcia-gallia-silica glass are compared in Fig. 9. There is no significant difference in the IR transmission of these two glasses.

E. <u>Analysis of Sample 3</u>

Sample 3, which was a soda-lime-silica glass shell containing a large air bubble, was used to assess the feasibility of removing the irregularities from its inner surface and reshaping it into a spherical shell of uniform wall thickness by remelting it in micro-g. Radiographic analysis of the post flight sample confirmed that it was no longer a shell, but an ellipsoidal piece of solid glass whose largest and smallest diameter differed by ≈0.521 mm (diameter, max = 5.334, min = 4.813 mm). The reason why the bubble escaped and how the sample deformed to an ellipsoidal shape is not clear at this point, and is still being investigated. One possible explanation for the escape of the bubble is the existence of a temperature gradient, which could establish a surface tension gradient in the sample. Marangoni flow could have caused the bubble to move to the region of lower surface tension (hot spot) and escape from the sample.

The possibility that sample 3 could have been distorted by rapid spinning when it was molten has been examined. Calculations show that a rotational speed of ≈1220 rpm would be required to produce the shape and dimensions identical to flight sample 3 [11]. There is no definite evidence showing whether sample 3 was spinning while molten, but this speed is considered unrealistically high. Another possibility is that the sample was deformed by acoustic forces since recent calculations indicate [12] that these forces increase during cooling and may not be negligible as has been assumed previously.

F. Operational Performance of SAAL

The operation of the SAAL in space for high temperature liquid samples was generally satisfactory. All the principal features of the SAAL such as sample insertion and levitation, temperature control of the furnace, etc., operated as intended for the first three samples. An excellent photographic record of the sample processing sequences in micro-g, which gives a good optical view of the samples and their movements at elevated temperature, was obtained. The reason why the furnace did not operate beyond the third sample is not precisely known, but it appears that a lack of liquid coolant for the flight hardware created an overtemperature condition which caused the premature shutdown of the furnace. However, the performance of the SAAL in the MEA/A-2, STS-61A experiment is considered to be significantly improved compared to that for the MEA/A-1, STS-7 experiment [6].

This is the first time that liquid samples have been successfully levitated in space at high temperatures (1250 to 1500°C) for periods of 4 to 12 min. This time period is reasonably long compared to that for the earlier SPAR VI, SPAR VIII, and STS-7 containerless experiments. The glass forming melt was levitated only for 27 s in SPAR VI [4,9] and for 83 s in SPAR VIII [5] before it touched and stuck to the platinum wire cage. The only sample which showed evidence of being partially melted in MEA/A-1 [5] had a composition identical to sample 2 in MEA/A-2, but it is difficult to say how long it was levitated in the SAAL as no photographic evidence was obtained. This sample was also found stuck to the cage wires when removed from the MEA/A-1 flight hardware and was totally crystalline.

The sample injection mechanism worked perfectly for MEA/A-2 and the sample was more stable compared to the earlier experiments. In SPAR VI and VIII, the sample moved about and touched the cage several times just after being released inside the platinum cage in the SAAL furnace. The samples then remained stationary for a brief period (27 s in SPAR VI and 83 s in SPAR VIII) whereupon they again started moving and stuck to the cage long before the cooling gate was opened for cooling. This indicates that the displacement of these samples out of the acoustic well was caused not by any external force but by an instability in the acoustic field itself. No such instability of the acoustic field was observed for any of the three samples processed in MEA/A-2, except that sample 2 escaped from the acoustic well when the cooling gate was opened.

4. RATIONALE FOR FUTURE EXPERIMENTS IN MICROGRAVITY

In future containerless experiments on glass forming systems, it is planned to study other phenomena requiring a gravity-free environment. For example, mass transport by diffusion is nearly always masked by that due to gravity-driven convection on earth. In low gravity, diffusion-controlled transport can be studied independently and more accurate information about the atomistic or microscopic nature of a material can be obtained.

It is difficult and often impossible to independently study homogeneous and heterogeneous nucleation in fluid melts on earth. This can be accomplished in micro-g for containerless melts and basic information about the nucleation mechanism can be obtained.

In fluid liquids, such as alkaline earth borates and metals, it is difficult to study the mechanism and kinetics of phase separation (immiscible liquids) on earth, because the two liquids have different densities and separate too rapidly for measurements. In space, where density-driven motion is greatly suppressed, phase separation in liquids can be studied without interference from gravity-driven convection. Studies in space should provide valuable scientific information for these interesting systems and offer the potential of yielding composite materials with interesting microstructures and properties. The measurement of surface properties (surface tension, emissivity, vaporization) of a solid or liquid material is another important area of investigation. To obtain uncontaminated surfaces on earth is a difficult to impossible task, but containerless processing in micro-g offers the opportunity to investigate an uncontaminated and unsupported surface. Many properties such as strength, surface flow, surface nucleation and crystallization, ion-exchange reaction, surface-surface interaction, and rate of gas evolution or vaporization, can be studied to gain a better understanding of the physical, chemical, and structural characteristics of surfaces.

Forces which are weak compared to gravity-driven convection, but may become significantly large in the absence of convection, can also be studied in micro-g. The effect of these forces on the processing of a material can be investigated. For example, surface tension which is expected to be important in micro-g can be used to homogenize a melt by Marangoni flow. Forces arising from electric, magnetic, or acoustic fields can be used to control the shape of a melt in micro-g, thereby, avoiding the mechanical stress or distortion normally introduced in the material as a result of treatments like cutting, grinding, or polishing.

5. CONCLUSIONS

The following conclusions summarized below are based on all flight experiments conducted to date, but especially on the results of the MEA/A-2 flight experiment.

A. Enhanced Glass Formation

Two glass forming compositions (calcia-gallia-silica and soda-lime-silica) were successfully melted and cooled to glass while levitated in space. The calcia-gallia-silica composition requires a cooling rate ≈11 to 12°C/s to form glass on earth for the sample size used in the space experiment. This cooling rate is 2 to 3 times higher than the cooling rate (≈4°C/s) for the MEA/A-2 experiment which yielded a glass for this composition. Clearly, the glass formation tendency for this calcia-gallia-silica composition is increased by 2 to 3 times when melted in space without a container.

B. Melt Homogenization and Precursor Preparation Technique

A usable and homogeneous glass was obtained for the calcia-gallia-silica composition for the melting time and temperature used in the flight experiment. Initially, this sample was made by hot-pressing crystalline powders and contained random heterogeneities of pure silica particles. Chemical homogenization of this low viscosity melt was reasonably fast even in the absence of gravity-driven convection. Hot-pressing appears to be a feasible way to prepare chemically pure samples for materials processing in space.

C. Comparison of Properties

The comparison of selected properties for the space and earth-melted calcia-gallia-silica glasses shows that the refractive index, dispersion, and Abbe number are slightly different, but there is no detectable difference in their infrared transmission or crystallization behavior. For this particular glass composition, melting in space produced no important difference in properties.

D. Shaping

Since the bubble escaped from the soda-lime-silica glass shell when it was remelted in space, the feasibility of shaping a glass shell in micro-g has not been fully demonstrated. The reshaping of glass shells in space is still considered feasible once the reason responsible for bubble motion is identified.

E. Operational Assessment of SAAL

The operation of the single axis acoustic levitator/furnace in space for high temperature liquid samples was generally satisfactory for the MEA/A-2 experiment. For the first time, liquid samples have been successfully levitated in space at high temperatures (1250 to 1500°C) for periods of 4 to 12 minutes. All the principal features of the SAAL such as sample insertion and levitation, temperature control of the furnace, etc. operated as intended for the first three samples. An excellent photographic record of the sample processing sequences in micro-g, which gives a good optical view of the samples and their movements at elevated temperature, was also obtained.

6. FUTURE WORK

Based on the operational performance of the SAAL and the results obtained from the glass melting experiments, it is believed that a valuable advancement in the science and technology of materials processing in space has been achieved. Nevertheless, the basic scientific objectives regarding enhanced glass formation, melt homogenization and mixing, bubble behavior, and reshaping simple shapes in space have not been completely fulfilled. The results of the MEA/A-2 experiment which demonstrate the enhancement of glass formation in space are encouraging and need to be verified for other potentially useful compositions.

ACKNOWLEDGEMENT

Thanks are due to Dr. N. J. Kreidl, consultant on this research, for many helpful discussions and suggestions, to Mr. F. Gac of Los Alamos National Laboratory for supplying the soda-lime-silica glass shell, to Dr. C. Rey of Intersonics, Inc. for many practical suggestions, and to Dr. R. S. Subramanian of Clarkson University for providing the sodium-borate sample.

REFERENCES

1. D. R. Uhlmann, "A Kinetic Treatment of Glass Formation", J. Non-Cryst. Solids, 7, 337-348 (1972).

2. H. Yinnon and D. Uhlmann, "A Kinetic Treatment of Glass Formation. V. Surface and Bulk Heterogeneous Nucleation", J. Non-Cryst. Solids, 44, 37-55 (1981).

3. W. D. Kingery, H. K. Bowen, and D. R. Uhlmann, Introduction to Ceramics, 2nd Edition, Wiley, NY, 1976, pp. 347.

4. R. A. Happe, SPAR VI Experiment Report: Containerless Processing of Glass Experiment 74-42, NASA TM-82433: Space Processing Applications Rocket, Project SPAR VI Final Report, October 1981, Chapt. III.

5. R. A. Happe and K. S. Kim, NASA TM-82578, Space Processing Applications Rocket, Project SPAR VIII Final Report, June 1984, Chapt. IV.

6. D. E. Day and C. S. Ray, Final Report for MEA/A-1 Experiment 81F01, NASA Contract NAS 8-34758, April 1984.

7. D. E. Day and C. S. Ray, Final Report for MEA/A-2 Experiment 81F01, NASA Contract NAS 8-34758, November 1986.

8. C. S. Ray and D. E. Day, "Glass Formation in Microgravity", Proceedings of the Materials Research Society (MRS) Symposia on Materials Processing in the Reduced Gravity Environment of Space, Eds. R. H. Doremus and P. C. Nordine, Vol. 87, 1986.

9. C. S. Ray and D. E. Day, "Description of the Containerless Melting of Glass in Low Gravity", National SAMPE Technical Conference Series, 15, 135 (1983).

10. R. R. Whymark, C. Rey, and J. Yearnd, "Acoustic Levitation Materials Processing System", 17th Aerospace Science Meeting, New Orleans, LA, January 1979, pp. 15-17.

11. F. Gac, Los Alamos National Laboratory, Los Alamos, NM, Private Communication.

12. C. Rey, Intersonics, Inc., Northbrook, IL, Private Communication.

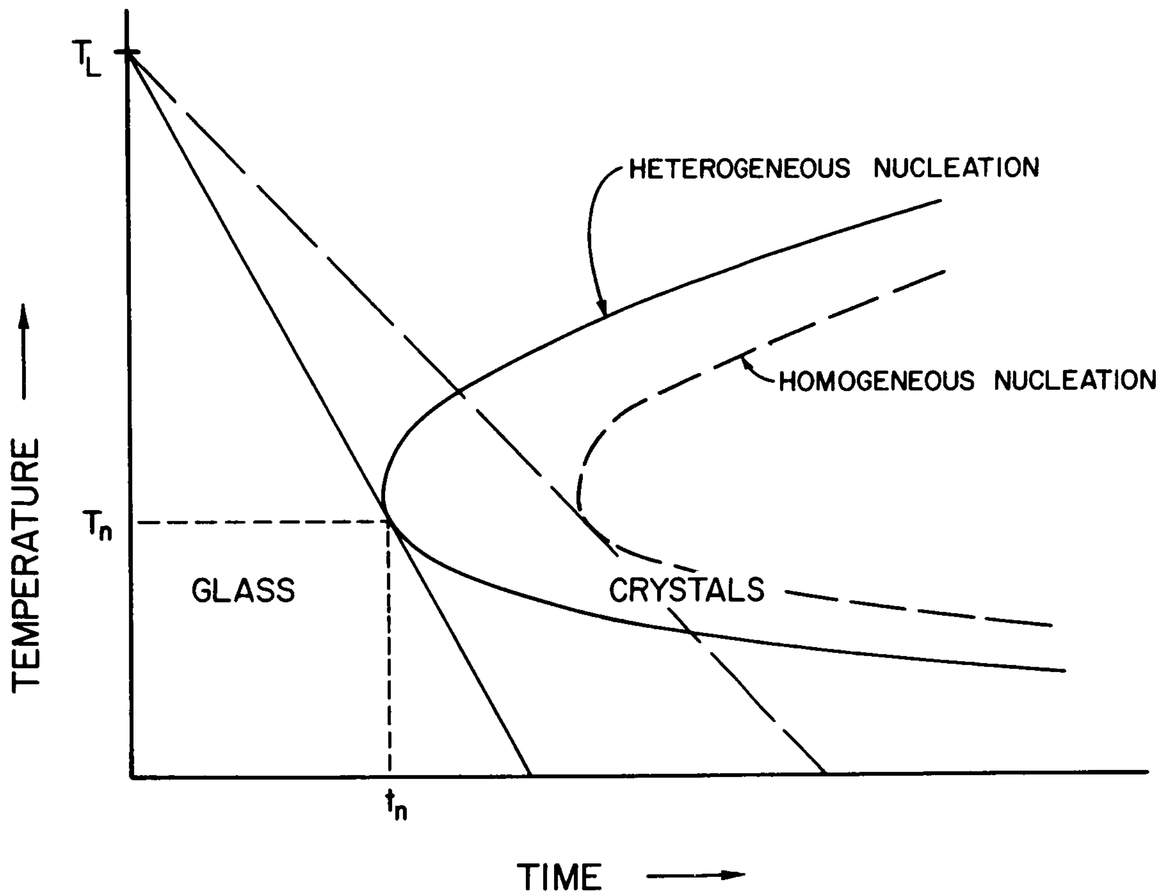

Figure 1. Typical time-temperature-transformation (TTT) diagram for a glass forming material.

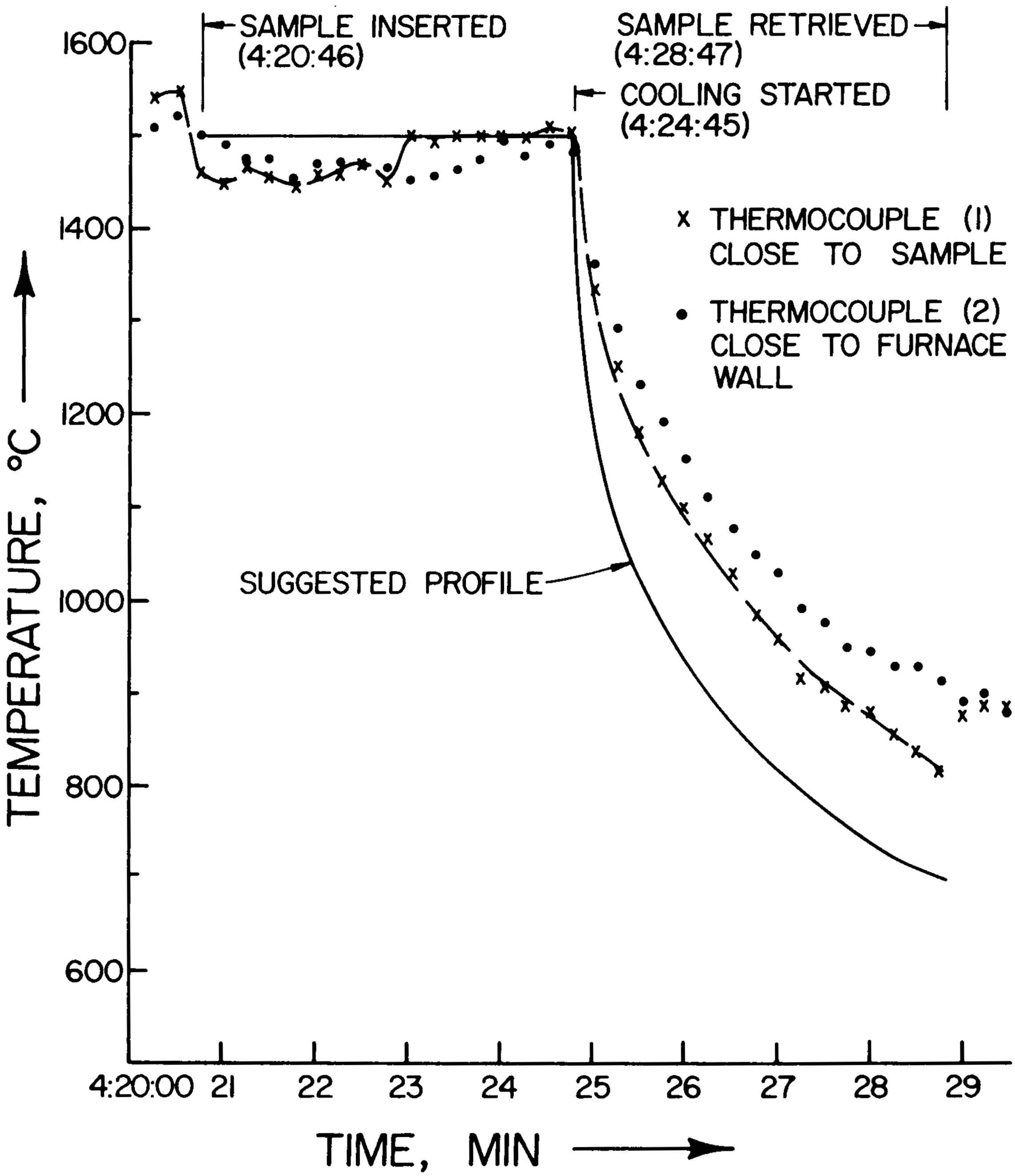

Figure 2. The planned and observed time-temperature profile for 35.7CaO-39.3Ga_2O_3-25SiO_2, mol%, hot-pressed sample (#2) when processed in the single axis acoustic levitator, MEA/A-2.

ORIGINAL PAGE IS
OF POOR QUALITY

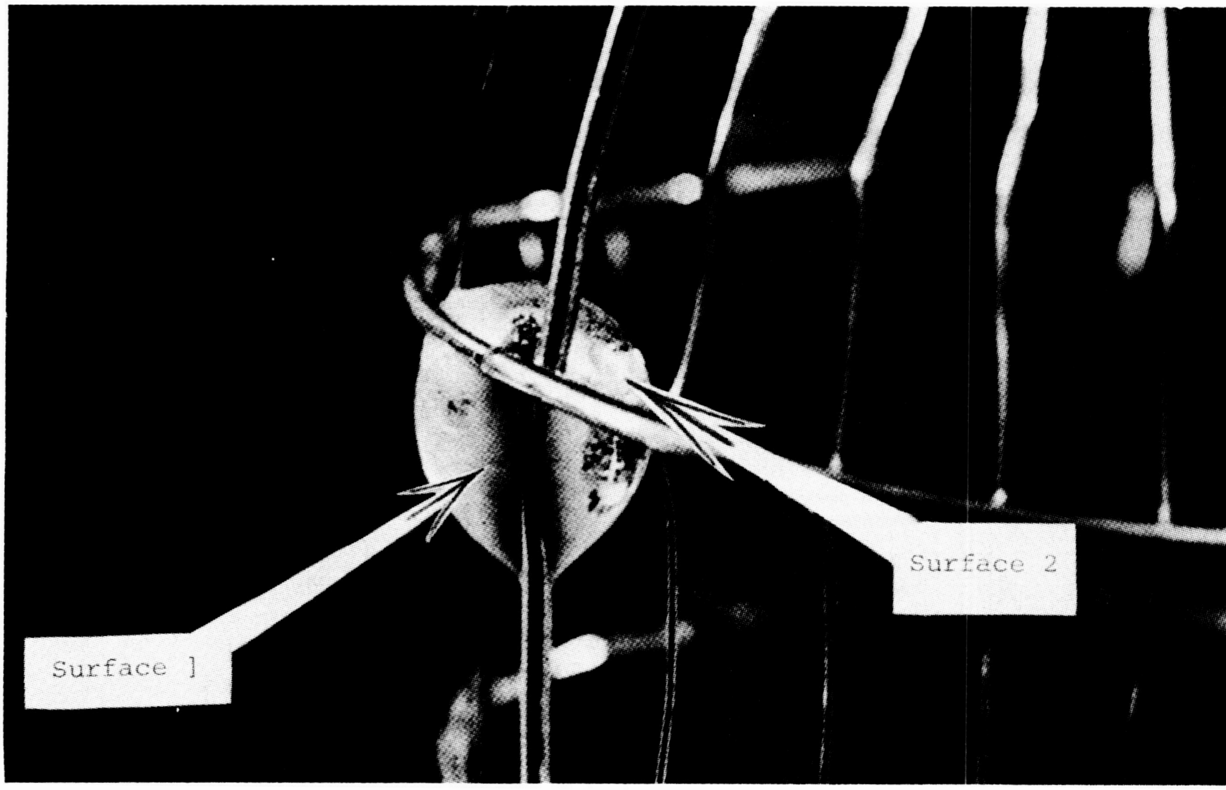

Figure 3. Flight sample 2 ($35.7CaO-39.3Ga_2O_3-25SiO_2$, mol%, hot-pressed) stuck to platinum wire cage while levitated and melted in space (MEA/A-2).

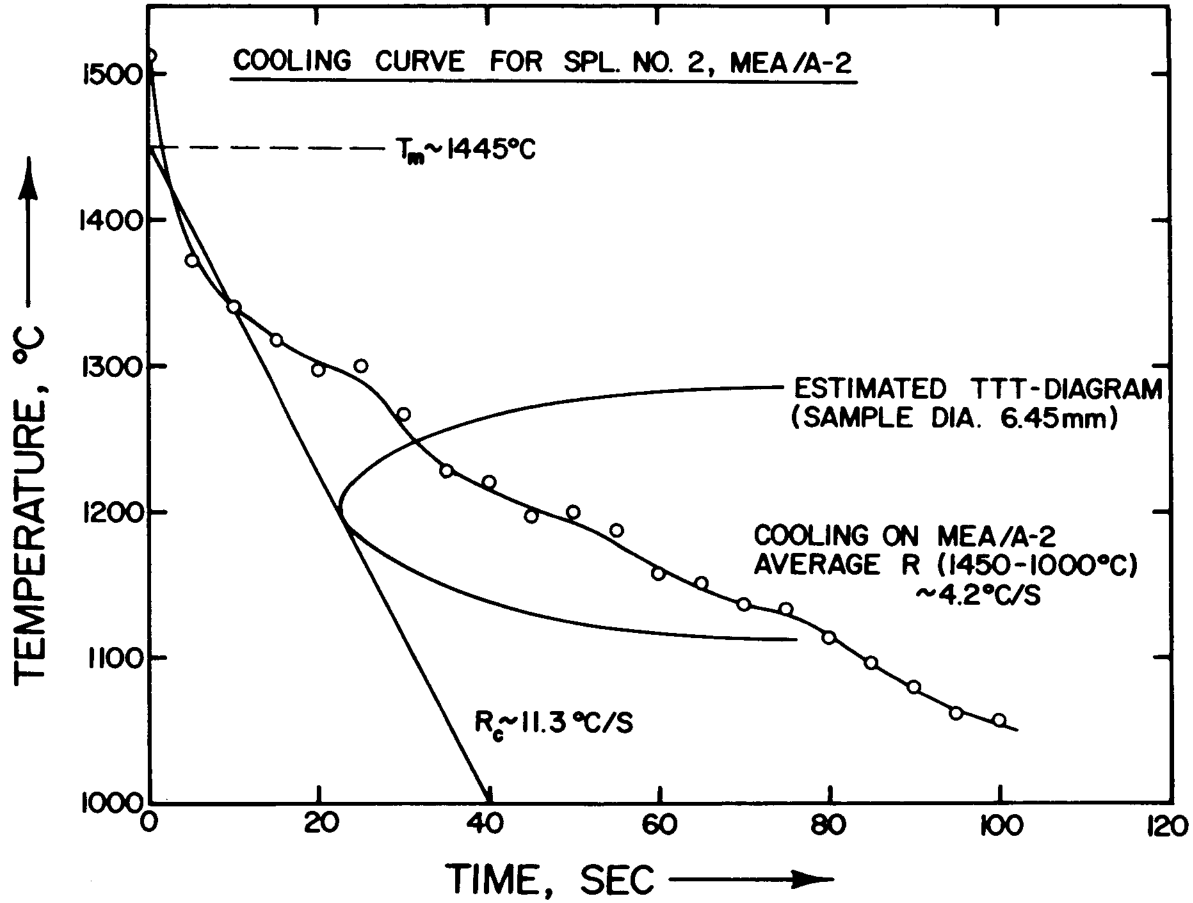

Figure 4. The estimated TTT diagram for the 35.7CaO-39.3Ga_2O_3-25SiO_2, mol%, composition for sample diameter ≈6.5 mm and the cooling rate measured for sample 2 in MEA/A-2.

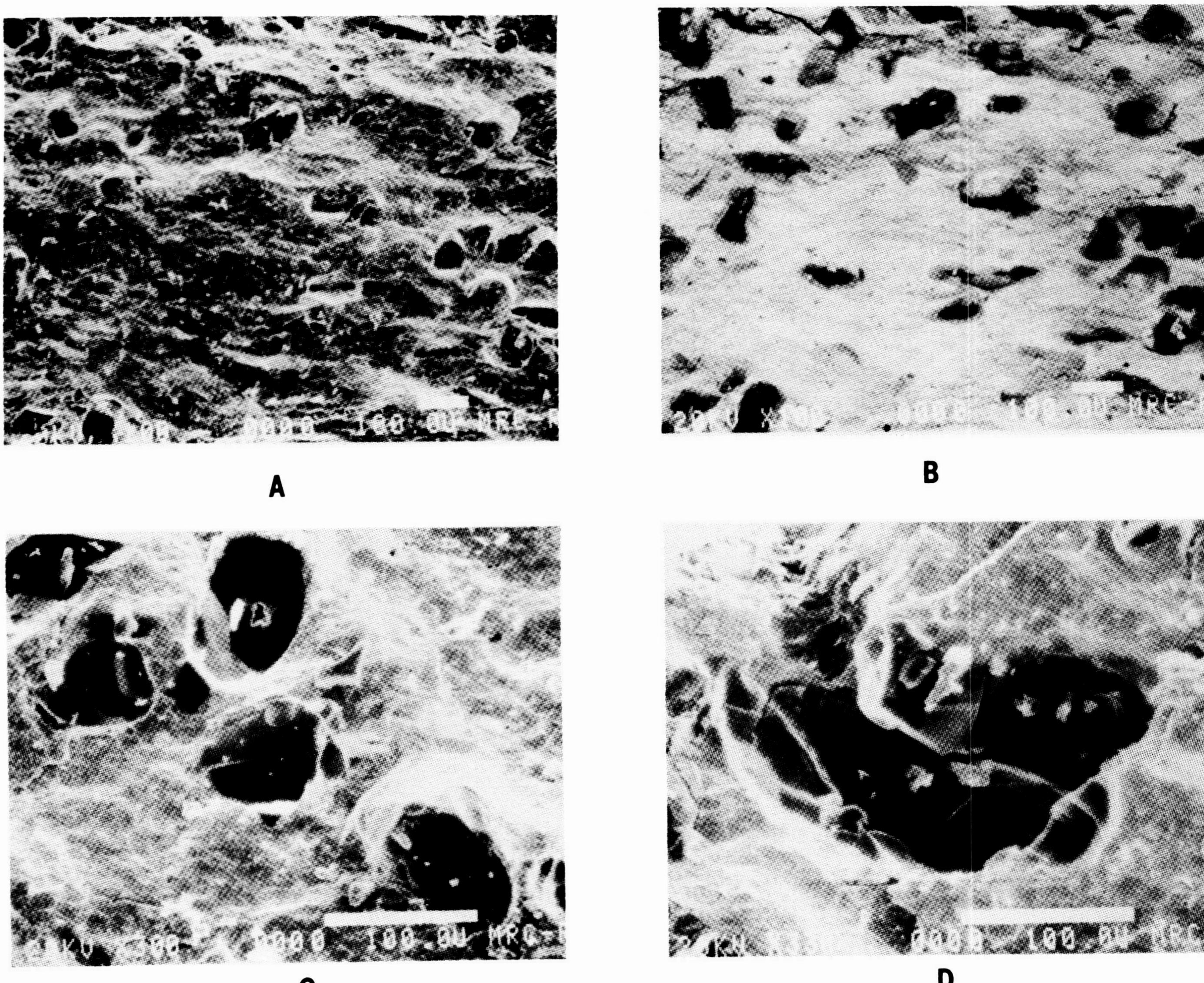

Figure 5. Appearance of the interior of the hot-pressed $35.7CaO-39.3Ga_2O_3-25SiO_2$, mol%, precursor as seen by SEM. Dark regions are silica particles. B is the back scattered photograph of the sample shown in A. C shows silica particles ≈100 micrometer size while larger silica particles ≈300 micrometer in size are shown in D.

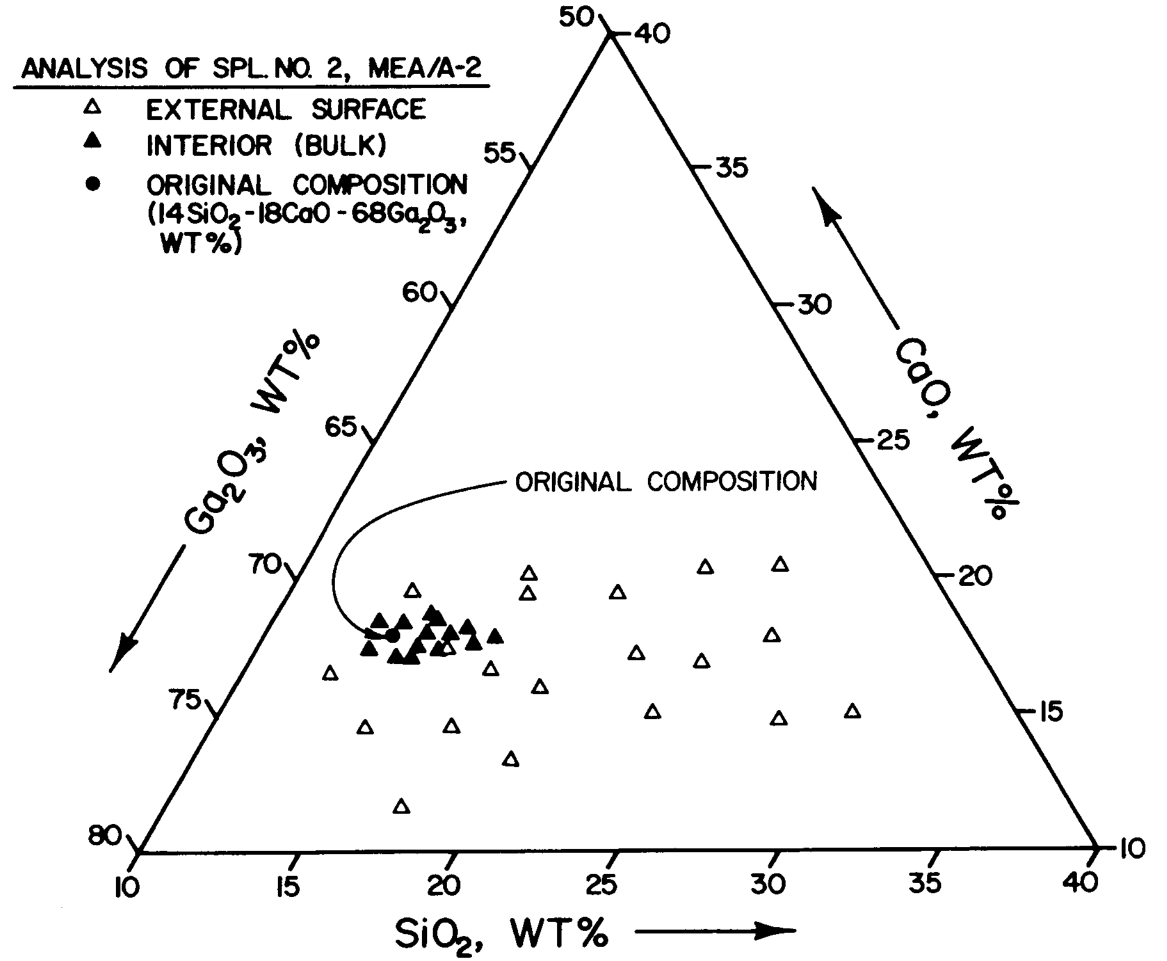

Figure 6. Composition of the external surface and the interior of flight sample 2 ($35.7CaO-39.3Ga_2O_3-25SiO_2$, mol%, hot-pressed) as determined by EDAX.

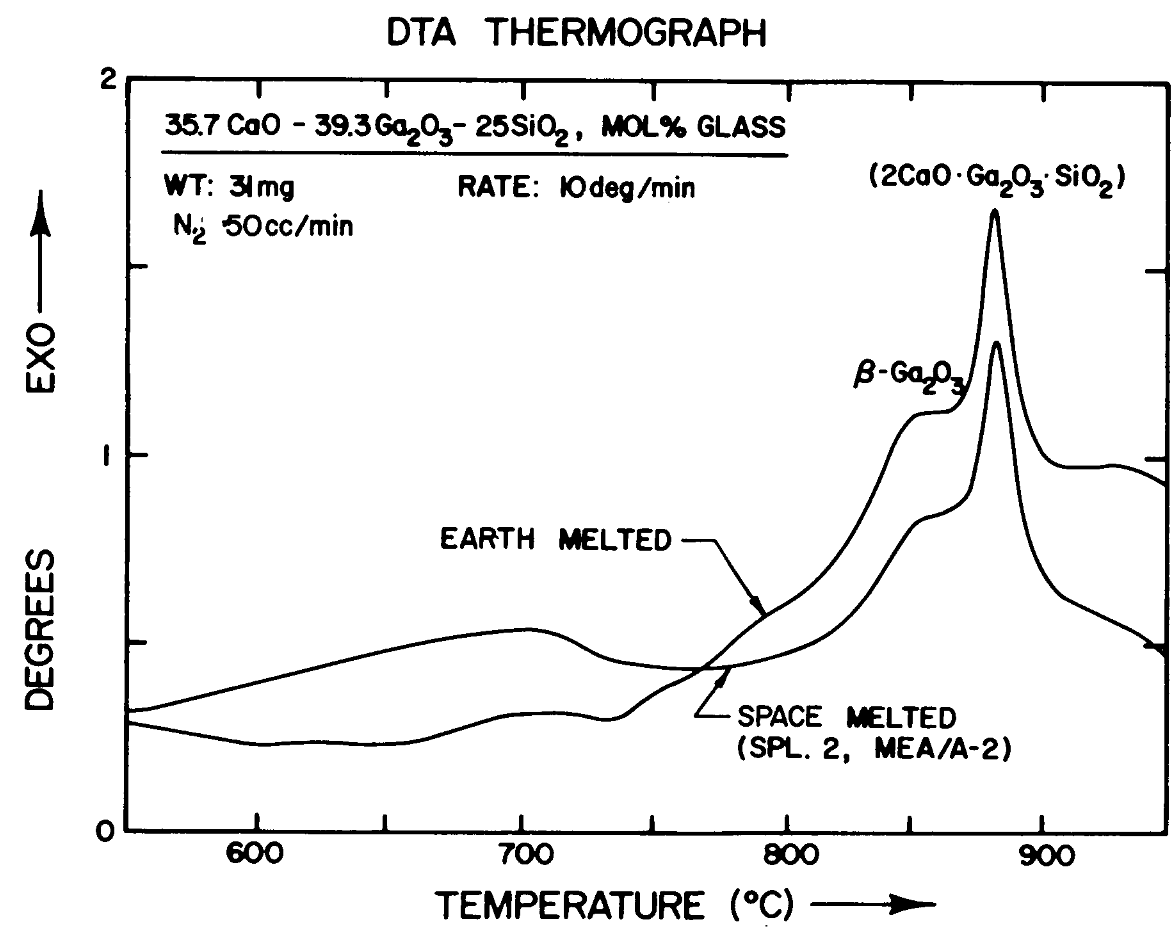

Figure 7. DTA thermogram for the 35.7CaO-39.3Ga_2O_3-25SiO_2, mol%, glasses melted in space (MEA/A-2) and on earth.

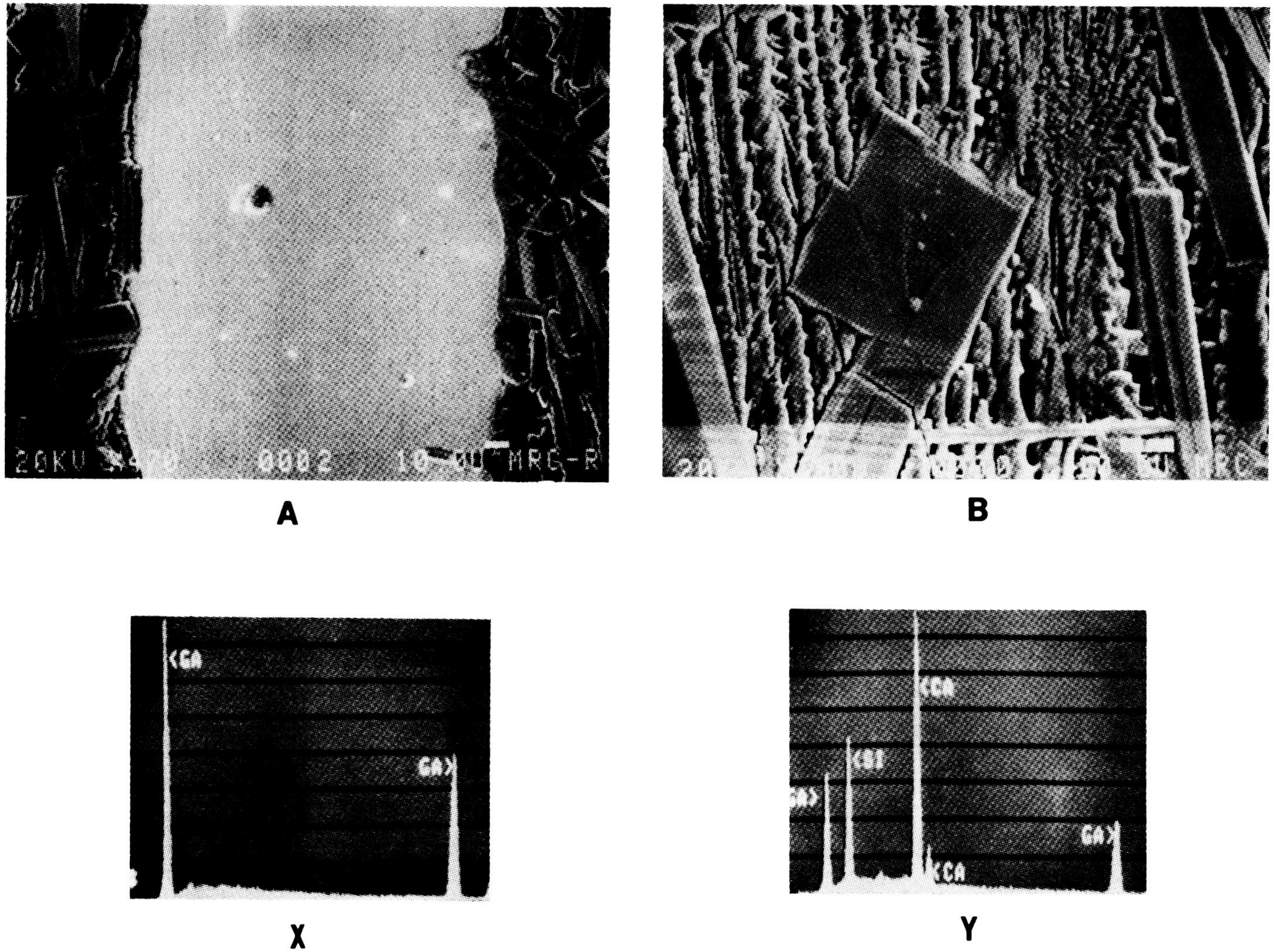

Figure 8. External surface of flight sample 2 ($35.7CaO-39.3Ga_2O_3-25SiO_2$, mol%, hot-pressed) in the vicinity of the vertical platinum wire imbedded in the sample (shown as surface 1 in Fig. 3). The wide light band in A is the platinum wire imbedded in the sample. Crystals are visible on both sides of the platinum wire. Two crystalline phases, as shown in B, were observed. The plane flat crystals contain Ga only (see X). The rough needle shaped crystals contain Ca, Ga, and Si (see Y).

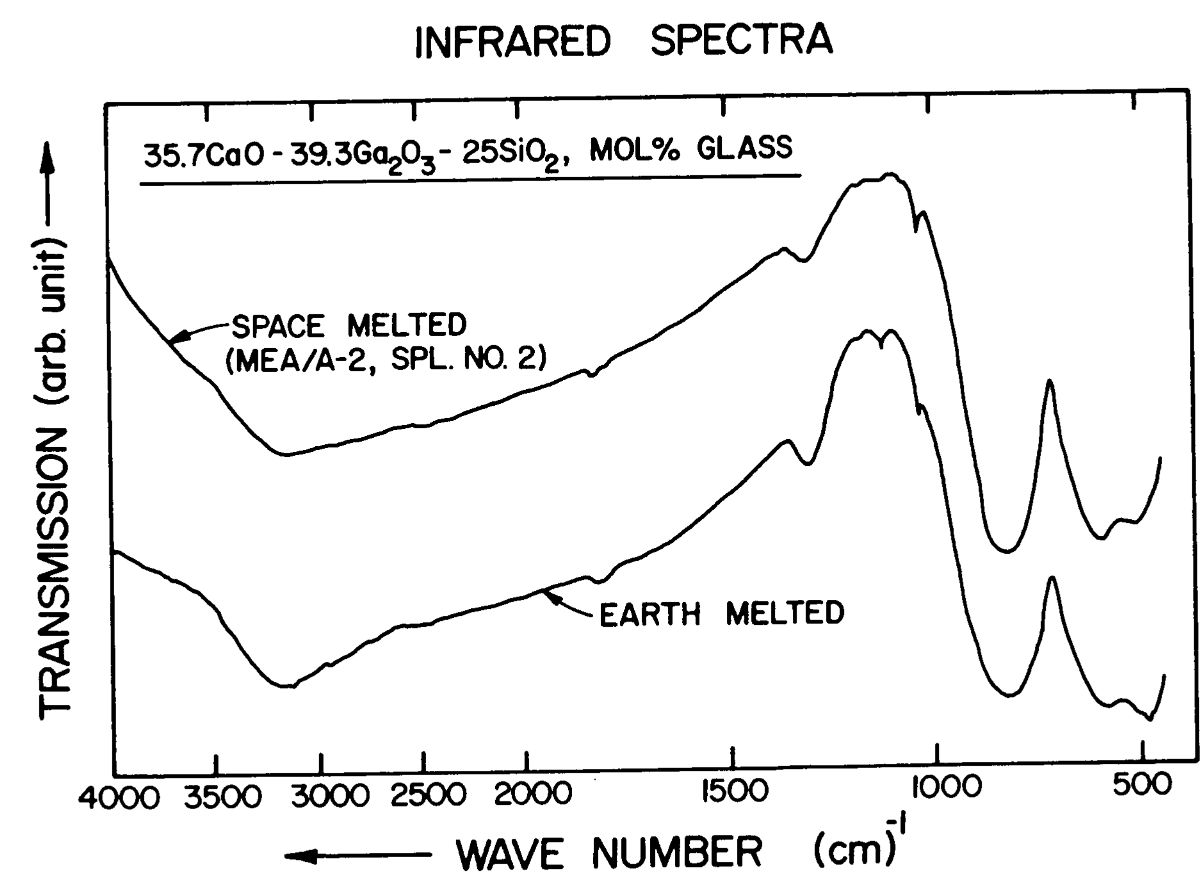

Figure 9. IR transmission for the $35.7CaO-39.3Ga_2O_3-25SiO_2$, mol%, glasses melted in space (MEA/A-2) and on earth.

N89-20308

Acoustic Containerless Experiment System
A Non-Contact Surface Tension Measurement

D. D. Elleman, Principal Investigator
T. G. Wang, Co-Investigator
M. Barmatz, Project Scientist

Jet Propulsion Laboratory
California Institute of Technology

ABSTRACT

The Acoustic Containerless Experiment System (ACES) was flown on STS 41-B in February 1984 and was scheduled to be reflown in 1986. The primary experiment that was to be conducted with the ACES module was the containerless melting and processing of a fluoride glass sample. A second experiment that was to be conducted was the verification of a non-contact surface tension measurement technique using the molten glass sample.

The ACES module consisted of a three-axis acoustic positioning module that was inside an electric furnace capable of heating the system above the melting temperature of the sample. The acoustic module is able to hold the sample with acoustic forces in the center of the chamber and, in addition, has the capability of applying a modulating force on the sample along one axis of the chamber so that the molten sample or liquid drop could be driven into one of its normal oscillation modes. The acoustic module could also be adjusted so that it could place a torque on the molten drop and cause the drop to rotate.

In the ACES, a modulating frequency was applied to the drop and swept through a range of frequencies that would include the $n = 2$ mode. A maximum amplitude of the drop oscillation would indicate when resonance was reached and from that data the surface tension could be calculated.

For large viscosity samples, a second technique for measuring surface tension was developed. A rotating liquid sample will distort into an oblate spheroid with axial symmetry along the axis of rotation. The magnitude of distortion or flattening of the sample depends on the rotation rate, the drop size, the density, and the surface tension of the molten sample. Thus again, if all the parameters except the surface tension are known, it can be calculated from the degree of distortion.

The results of the ACES experiment and some of the problems encountered during the actual flight of the experiment will be discussed in the presentation.

INTRODUCTION

A large variety of material science experiments proposed for space flight require an accurate measurement of the physical properties of the molten material during the processing phase. Among those physical properties of interest are the surface tension and the viscosity of the liquid phase of the material. Surface tension is of particular interest in undercooling experiments and in experiments where knowledge of surface contamination is important. In addition, many of the material science experiments are of the containerless processing type, either because of the corrosive nature of the material, or the desire to eliminate contamination of the sample. The containerless nature of the experiment requires that any physical properties measurement on the sample be performed in a contactless manner.

The Acoustic Containerless Experiments System (ACES) was flown on STS 41-B in February 1984 and was scheduled to be reflown in 1986. The primary experiment that was to be conducted was the containerless melting and processing of a heavy metal fluoride glass sample with R. Doremus being the Principal Investigator. This particular flight of the ACES module with the glass sample offered a unique opportunity to test several non-contact surface tension measurement techniques that had been developed at JPL. They could be tested and verified without requiring any modifications to the ACES module.

ACES MODULE

The ACES module consists of a three-axis acoustic positioner (See Figure 1). High-intensity sound waves are generated by the three acoustic drivers located on three orthogonal walls of the acoustic chamber (See Figure 2). These sound waves generate a steady-state force which is used to position the sample in the center of the chamber when the system is acoustically tuned to its fundamental mode.[1,2,3] An acoustic torque on the sample can be generated with variable magnitude and direction by adjusting the relative acoustic phase between the X and Y drivers.[4] Normal-mode oscillation of the molten sample can be induced by an adjustable low-frequency modulation of the acoustic force on the Z axis of the chamber.[5] The position oscillation and rotation of the sample can be recorded for subsequent analysis by a video recording system that has a view along the Z axis (See Figure 1). The entire acoustic chamber is in a furnace system that is capable of heating the chamber up to a temperature of approximately 600°C. Pre-flight ground-based measurements of the temperature profile of the chamber and sample are shown in Figure 3.

MEASUREMENT TECHNIQUE

Two separate and distinct methods of measuring surface tension of the sample were to be tested in the ACES flight. The drop oscillation technique and the drop rotation technique are now described.

In the drop oscillation technique, the sample is held in the center of the chamber while the sample is in the molten state and the Z axis acoustic modulation force is swept through a frequency range that will drive the molten sample into one of the lower normal-mode drop oscillations (See Figure 4 for modes n = 2, 3, and 4 shapes). The normal-mode oscillation frequencies for the inviscid case is given by

$$w_n^2 = n(n-1)(n+2)\frac{\sigma}{\rho R^3} \tag{1}$$

where w_n is the drop oscillation frequency for mode n, σ is the surface tension, ρ is the density and R is the sample radius.[6,7]

For the viscous case, the drop oscillation frequency for mode $n=2$ is given approximately by

$$w^2 = \left[\frac{8\sigma}{\rho R^3} - \frac{25 v^2}{R^4} \right] \tag{2}$$

where v is the viscosity of the sample.[8,9]

As the modulation frequency is slowly swept through the drop-mode $n=2$ frequency range given by equation (2), the amplitude of the drop oscillation increases and reaches a maximum when the conditions of equation (2) are satisfied. It decreases again as one passes on through the frequency range. Thus a measurement of w can be obtained by observing at what frequency the maximum amplitude occurs. It is then possible to calculate the surface tension from the relationship

$$\sigma = \frac{\rho R^3}{8} \left(w^2 + \frac{25 v^2}{R^4} \right) \tag{3}$$

where w is the maximum amplitude oscillation frequency for $n=2$. For the metal fluoride samples employed in the experiment, 62 mole % ZrF_4, 33% BaF_2, and 5% LaF_3, the ground-based data was ρ = 4.34 gm/cm^3, R = 0.5 cm, v = 0.1 stokes, and σ = 179 dyne/cm^2. The viscosity correction term represents only a few tenths of a percent correction and will be neglected. If these physical parameters for the sample are put into equation (1), one obtains an anticipated normal mode frequency of 51.04 rad/sec or 8.18 HZ.

The primary error in the measurement, as demonstrated by ground-based work, is in the determination of the maximum amplitude normal-mode frequency, particularly as the viscosity increases above 1.0 poise. The resonance peak becomes quite broad as one sweeps through the frequency range and the peak can no longer be accurately measured. In fact, a 3% error in the measurement of the frequency represents a 6% error in the surface tension σ. Laboratory measurements and data from the DDM spacelab experiment show that for low viscosity fluids such as water, accuracies of 2% in surface tension are not unreasonable; however, for large viscosity samples, much larger errors are possible. In fact, as the oscillation becomes critically damped, this technique cannot be used for surface tension measurements. For most metalic material samples, and certain glass samples, this is not a particular problem, but for high-viscosity glass samples, the technique cannot be employed.

A measurement of the viscosity of the sample can be made using the oscillation technique by either measuring the width of the resonance peak as one sweeps through resonance, or more easily by measuring the free decay of the oscillating sample and noting the decay of the amplitude which is given by $A_n = A_o e^{-\beta_n t}$ where A_n is the amplitude of the n^{th} mode, A_o is the amplitude at time t = 0, or the start of the decay, and β_n is given by

$$\beta_n = \frac{(n-1)(2n+1)v}{R^2} \tag{4}$$

where R is the radius of the sample and v is the viscosity.

The second method of measuring surface tension employs the ability to rotate the molten sample until the spherical sample is flattened into an oblate spheroid.[10-13] This method works particularly well with higher-viscosity samples, in fact, just those samples in which the drop oscillation technique does not work.[14]

Figure 5 shows a cross sectional view of the equilibrium shape of the axial symetrical drop under rotation. The degree of distortion depends on the rotation rate Ω given in units of $8\sigma / \rho R^3$.

Thus it is seen that the degree of distortion from spherical shape depends on the surface tension σ, the density ρ, and the radius R of the molten drop. Laboratory measurements with small drops held in an electrostatic levitator have shown that accuracies of within several percent can be obtained if rotation rates measured to within a percent can be made.[15] It should be noted that the calculated axial shapes assume the fluid in the sample is in solid-body rotation. This is easily obtained for high-viscosity samples at low rotational accelerations.

ACES FLIGHT RESULTS

Unfortunately, no useful data was obtained on the surface tension measurement experiment during the flight of STS 41-B of the ACES module because of a number of instrument malfunctions. During the heat-up period of the furnace system, the fluoride glass sample evolved HF gas, which subsequently damaged the window through which the video image of the sample was to be viewed and recorded. The window was fogged to such an extent that no useful images of the sample were obtained while the sample was in the molten state. Without imaging data, no analysis of the surface tension measurement experiment was possible.

Other problems with the instrument also developed during the flight that had serious effects on conducting the surface tension measurement. An instability developed in the feedback system that resulted in the continuous large scale motion of the sample within the chamber that eventually led to the sample striking one wall of the chamber and subsequently sticking to the wall. Thus, even if the window had not fogged over, we could not have successfully conducted the experiment. Post-flight analysis of the instrument problems by engineers and acoustic scientists uncovered where the problems with the instrument occurred and a redesign of the instrument has corrected these deficiencies. Right now. the ACES module is in storage; however, there are no plans at the present time to refly the instrument. It is felt that it is important to demonstrate the feasibility of measuring the surface tension in a non-contact manner, using the techniques described in this paper, in light of the importance of these parameters in many of the proposed material science experiments. To date, we have shown that these techniques can be used in the laboratory for millimeter-sized samples in a restricted viscosity range, but without a flight opportunity, we cannot demonstrate applicability of these techniques for a wide range of the parameters in a flight environment.

REFERENCES

1. Wang, T. G., Saffren, M. M., and Elleman, D. D., "Acoustical Levitation for Space Processing," Astron. and Aeron. 12, 7 (1974).

2. Wang, T. G., Saffren, M. M., and Elleman, D. D., "Acoustical Chamber for Weightless Positioning," Proc. AIAA ISS (1974).

3. Barmatz, M. B., "Overview of Containerless Processing Technologies," Proc., Symp. of Mat'ls. Processing in the Reduced Gravity Environ. of Space, Boston (November 1981) (Elsevier, New York, 1982), p. 25.

4. Busse, F. H., and Wang, T. G., "Torque Generated by Orthogonal Acoustic Waves," J. Acoust. Soc. Am., 69, 1634-1639 (1981).

5. Wang, T. G., Saffren, M. M., and Elleman, D. D., "Drop Dynamics in Space," Proc. Int'l. Colloquia on Drops and Bubbles (1975).

6. Foote, G. B., "A Theoretical Investigation of the Dynamics of Liquid Drops," (Ph. D. thesis), Univ. of Arizona (1971).

7. Miller, C. A., and Scriven, L. E., "The Oscillations of a Fluid Droplet Immersed in Another Fluid," J. Fluid Mech., 32, Part 3, 417-435 (1968).

8. Valentine, R. S., Sather, N. F., and Heideger, W. J., "The Motion of Drops in Viscous Media," Chem. Eng. Sci., 20, 719-729 (1965).

9. Davis, T. V., and Hagdon, D. A., "An Investigation of Droplet Oscillations During Mass Transfer," Proc. Roy. Soc., A243, 492 (1957).

10. Chandrasekhar, S., Ellipsoidal Figures of Equilibrium, Yale University Press, New Haven (1969) (see references).

11. Rayleigh, Lord, "Equilibrium of Revolving Liquid Under Capillary Forces," Phil. Mag., 28, 161 (1914).

12. Appell, P., Traite de Mecanique Rationelle, Vol. 4, Pt. 1, Chap. IX, Gauthier-Villars, Paris (1932).

13. Chandrasekhar, S., "The Stability of a Rotating Liquid Drop," Proc. Roy. Soc. (London), 286, 1 (1965).

14. Wang, T. G., Trinh, E. H., Croonquist, A. P., and Elleman, D. D., "Shapes of Rotating Free Drops: Spacelab Experimental Results," Phys. Rev. Lett., 56 (5), (1986).

15. Rhim, W. K., Chung, S. K., Trinh, E. H., Hyson, M. T., and Elleman, D. D., "Large Charged Drop Levitation Against Gravity," IEEE-IAS (1986) (Accepted).

FIGURES

ACES FURNACE CANISTER

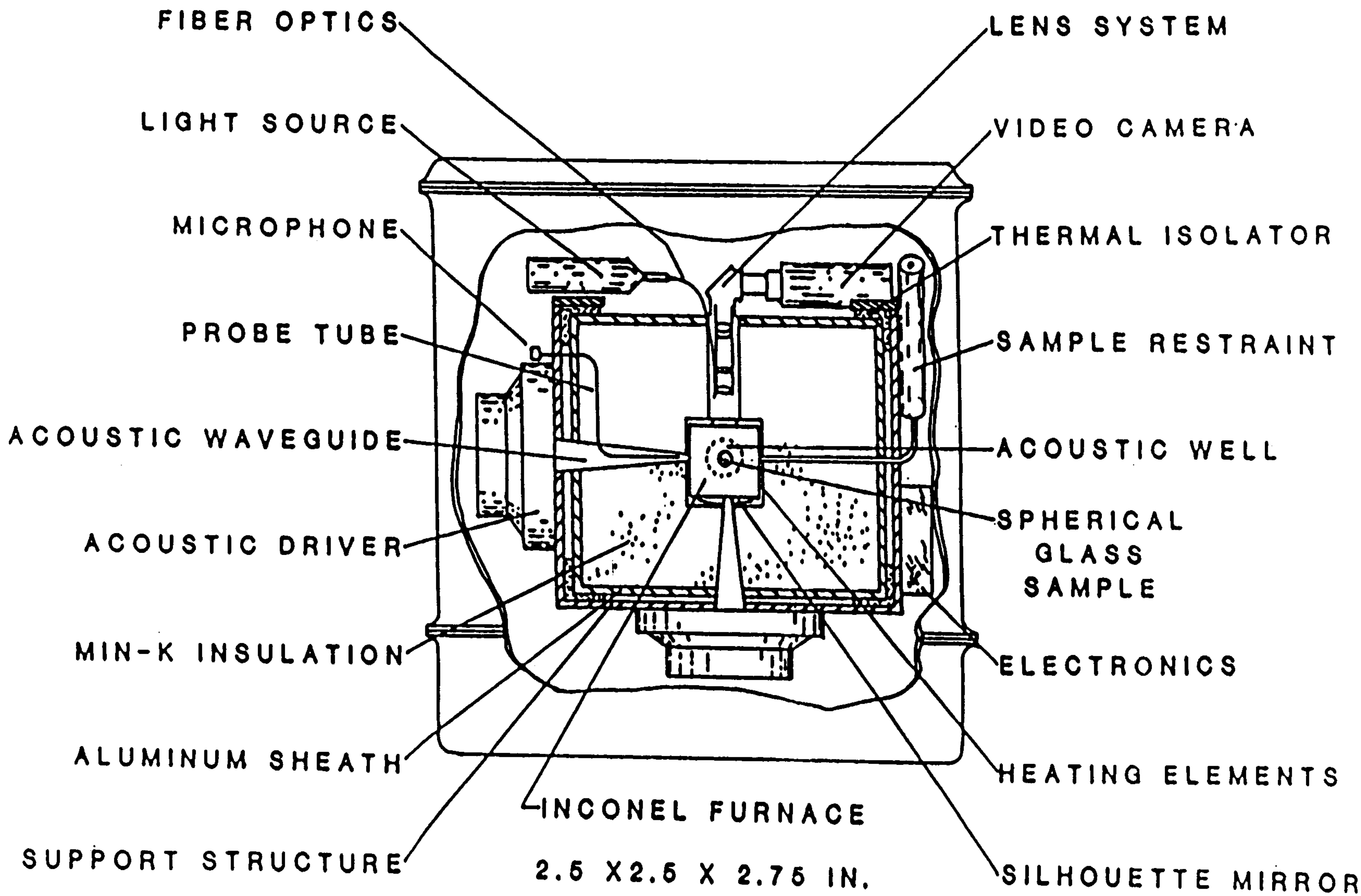

FIGURE 1

TRIPLE AXIS ACOUSTIC LEVITATION

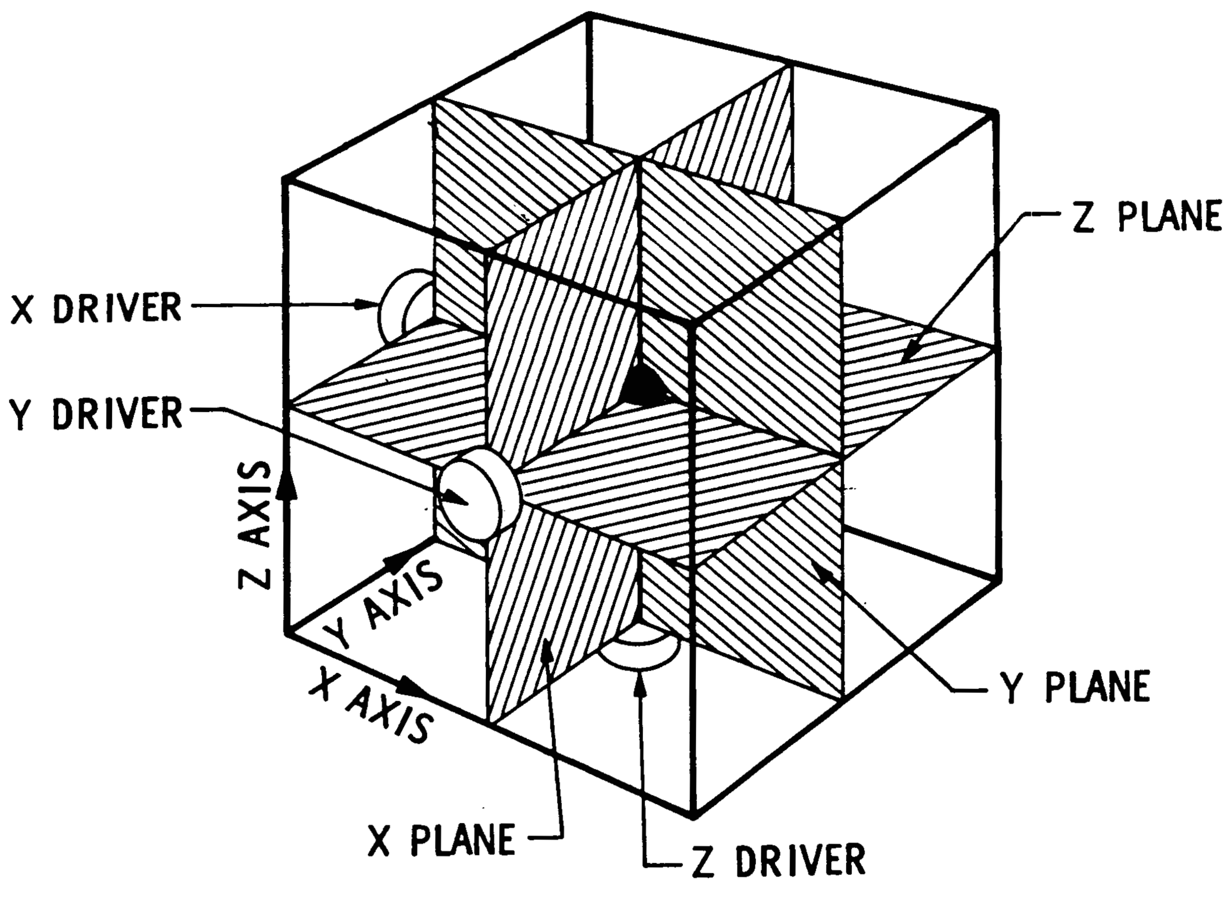

FIGURE 2

SAMPLE DYNAMIC TEMPERATURE RESPONSE (FLIGHT DATA)

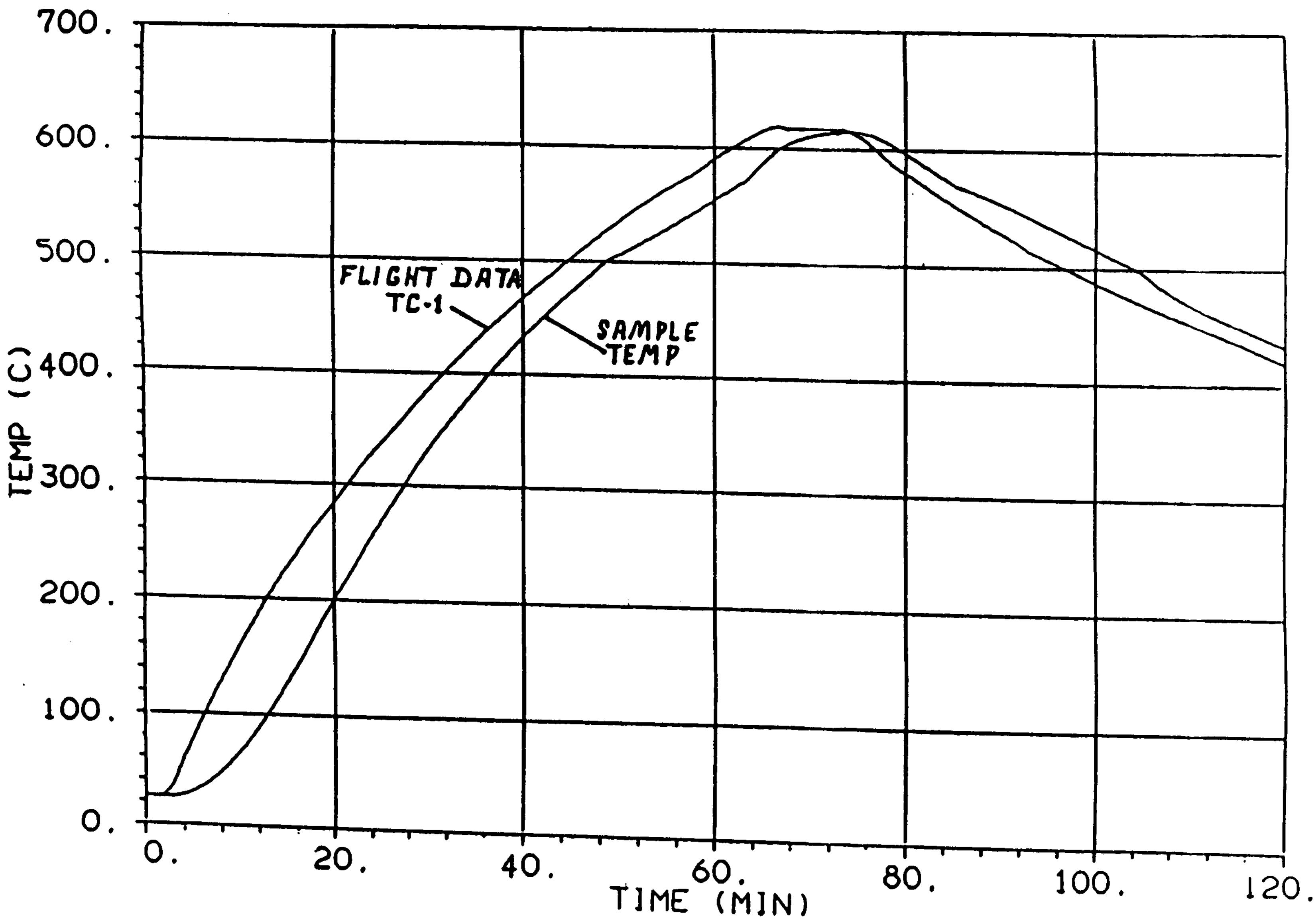

FIGURE 3

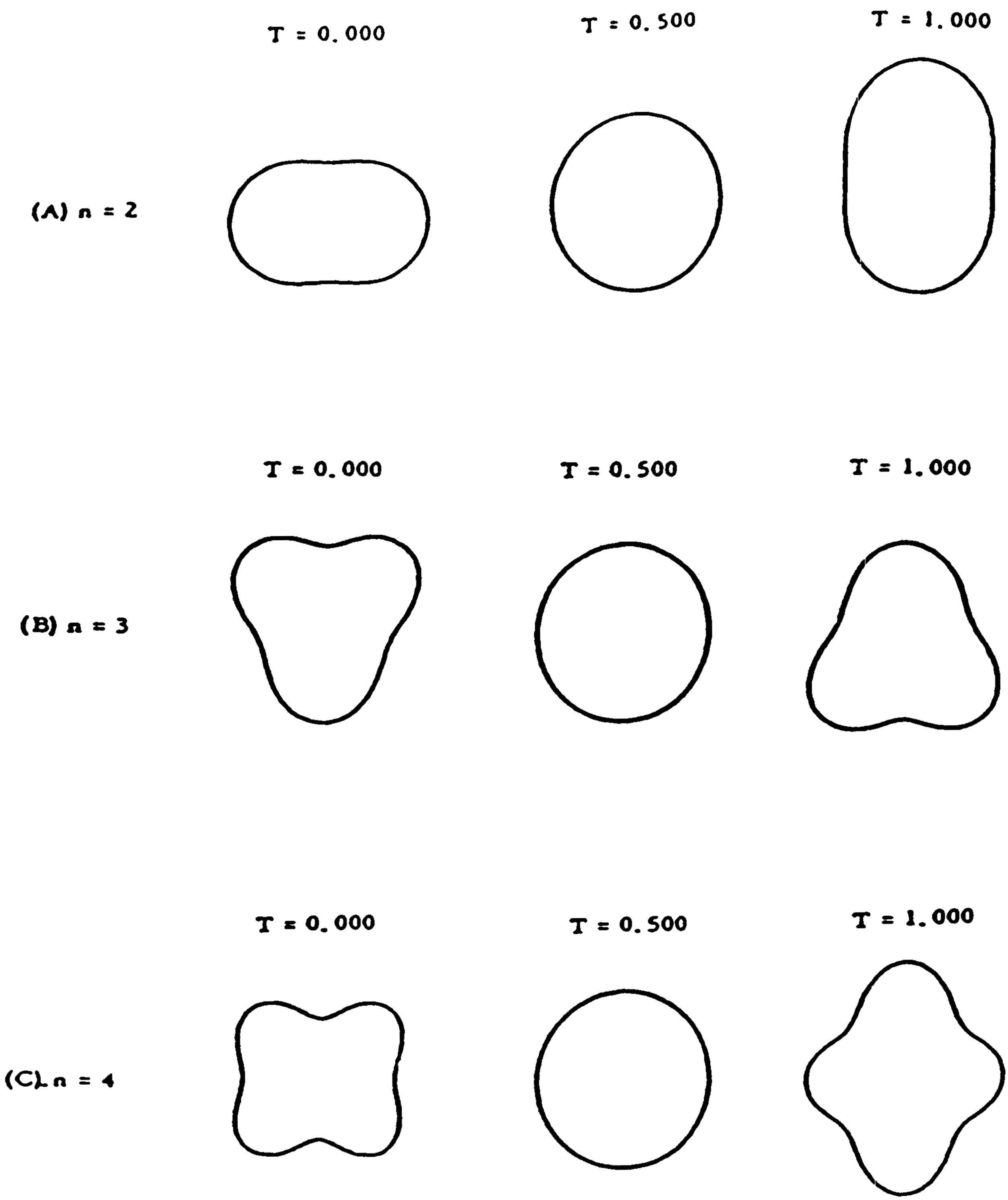
T = 0.000
T = 0.500
T = 1.000
(A) n = 2
T = 0.000
T = 0.500
T = 1.000
(B) n = 3
T = 0.000
T = 0.500
T = 1.000
(C) n = 4

FIGURE 4

AXISYMMETRIC EQUILIBRIUM SHAPES

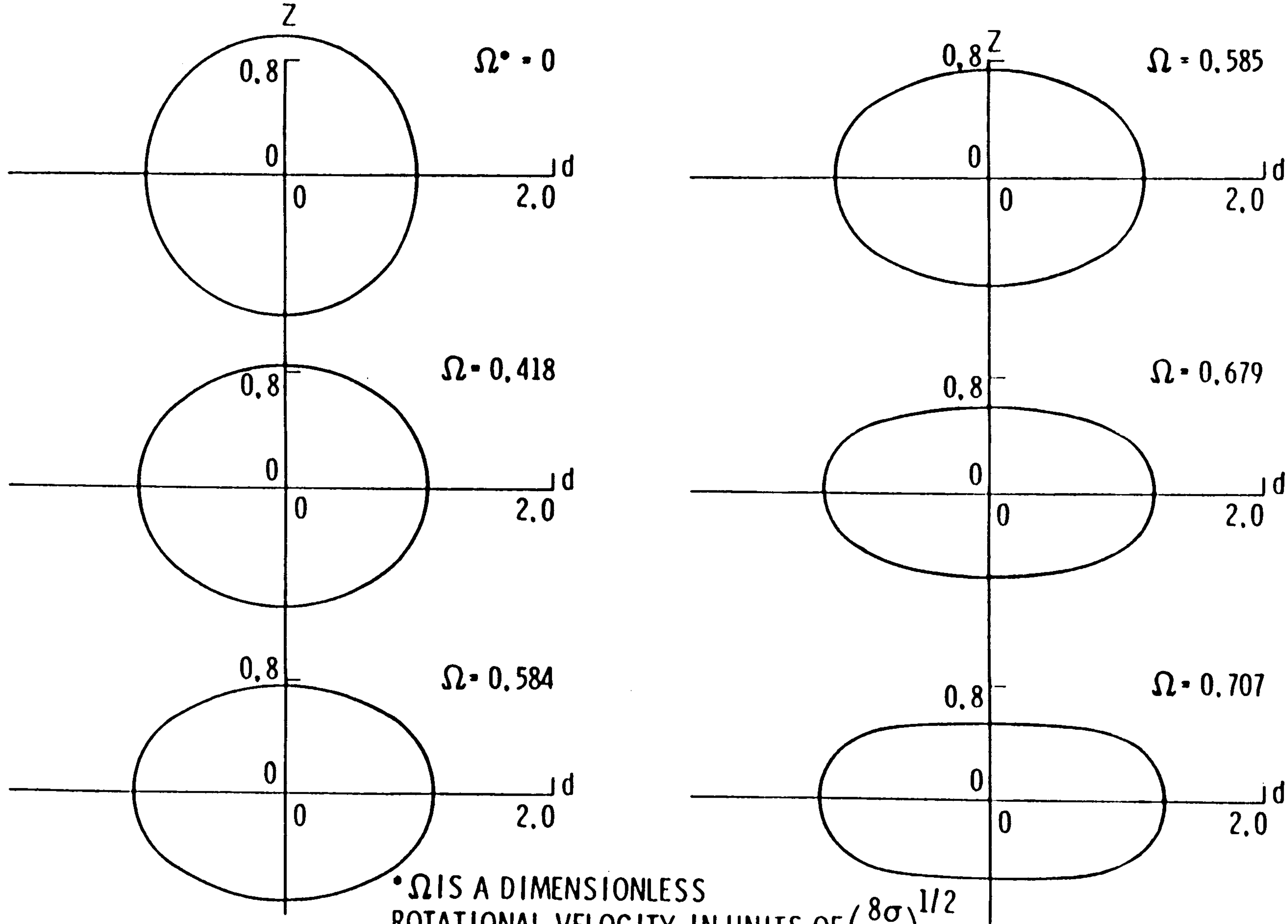

* Ω IS A DIMENSIONLESS ROTATIONAL VELOCITY, IN UNITS OF $\left(\frac{8\sigma}{\rho d^3}\right)^{1/2}$

FIGURE 5

CRYSTAL NUCLEATION IN LITHIUM BORATE GLASS

February 1987

Gary L. Smith, George F. Neilson, and Michael C. Weinberg

Microgravity Science and Materials Group
Jet Propulsion Laboratory
California Institute of Technology
Pasadena, California 91109

ABSTRACT

Crystal nucleation measurements were made on three lithium borate compositions in the vicinity of $Li_2O \cdot 2B_2O_3$. All nucleation measurements were performed at 500°C. Certain aspects of the nucleation behavior indicated (tentatively) that it proceeded by a homogeneous mechanism. The steady state nucleation rate was observed to have the largest value when the Li_2O concentration was slightly in excess of the diborate composition. The change in nucleation rate with composition is controlled by the variation of viscosity as well as the change in free energy with composition. The variation of nucleation rate is explained qualitatively in these terms.

INTRODUCTION

Homogeneous crystal nucleation is a process of extreme scientific interest and technological importance to the field of glass science. It is fundamental to the description of glass forming (1). However, gaps exist in the basic understanding of nucleation phenomena in glasses (2,3). The technological significance of bulk crystal nucleation stems from the central role it plays in glass ceramic formation (4).

Previous studies of homogeneous crystal nucleation in simple glass have involved silicate compositions (5-10). Also, in all cases where quantitative comparisons were made between theory and experiment (7-10), the theoretically predicted rates were many orders of magnitude too small.

Herein, we present our findings on the volume crystal nucleation in a simple binary borate glass system. To our knowledge, it is the first such study performed and reported in the literature.

Borate glasses, in general, do not have the technological importance of silicate glasses, but they are of great interest scientifically. This interest stems in large part from the structural complexity of borate glasses. Although there is not complete agreement concerning the structure of silica (and silicate glasses), the random network theory proposed and substantiated by Zachariasen (11), and Warren (12,13) is widely accepted. The SiO_4 tetrahedron is the basic building block of silica and silicate glasses in the theory. On the other hand, boron may assume 3 or 4 fold coordination in borate glasses. Also, it is believed that borate glasses are constructed with the aid of several basic structural units (14). The number and ratio of structural units present in a given borate is a function of glass composition. Thus, borate glasses exhibit a much richer array of structural configurations than silicates.

It might be expected that these structural differences could produce contrasting crystal nucleation behavior in borate and silicate glasses. For example, the tendency to form short-lived metastable crystalline structures may be quite sensitive to the details of glass structure. Such anticipated possible features stimlated the present study.

EXPERIMENTAL AND AUXILLIARY MEASUREMENTS

Three lithium borate glasses were prepared by standard glassmaking methods. The glasses were chemically analyzed (for Li) with the aid of atomic absorption and refractive index measurements. The composition of the glasses, in mole % Li_2O, were determined as 33.8 (designated as glass Q), 36.8 (glass G), and 38.2 (glass H).

The hydroxyl ion concentration for each glass was measured using IR spectroscopy. It was found that the OH content of the glasses were comparable, and present in low concentration ($\sim$ .05 mol %).

X-ray diffraction measurements were made of the nucleated glasses as well as of the fully crystallized glasses. In all cases, where crystallization could be detected by X-ray analysis, the crystalline species was identified as $Li_2O \cdot 2B_2O_3$.

Differential Scanning Calorimetry (DSC) measurements were made of each composition in the heat-up mode from room temperature to 600°C in an air atmosphere. A portion of a typical DSC scan is shown in Fig. (1), where a heating rate of 5 deg.C/min. was used. A single exotherm, corresponding to crystallization, occurs at approximately 525°C. Also, one notes that the glass transition temperature appears to be located in the vicinity of 469°C.

In view of the above findings a nucleation temperature of 500°C was chosen. Glass samples, free from crystallites as determined via examination with a polarizing microscope, were heated in platinum boats using a tube furnace. The furnace employed has an isothermal zone constant to ± 1°C. The samples were ground and polished after receiving appropriate heat treatment. They were polished to a thickness of 122-290 μm, which was appropriate for the maximum crystallite concentration observed. Diamond stop carriers were used to insure that the faces were parallel and flat. Then, the samples were examined with the aid of an Olympus polarizing microscope, and at least 10 optical micrographs were obtained for each sample. The particle number was determined directly by counting the crystals in from 6 to 10 of the frames from each glass. Knowledge of the magnification and thickness of the glass allowed the determination of the crystallite number density present within it.

NUCLEATION MEASUREMENTS AND RESULTS

Nucleation measurements are usually performed via two stage heat treatments (7). This method consists of a low temperature heating of the glass to produce the nuclei, followed by a high temperature heating to grow the nuclei to an observable size. This procedure is required when the nucleation curve (I(T) vs. T; where T is temperature, and I the nucleation rate) has little overlap with the growth curve. A potential disadvantage of this method is that some of the nuclei may disappear when heated at the growth temperature. This results from the fact that the critical radius is inversely proportional to the bulk free energy difference between crystal and liquid. The magnitude of the latter is smaller at the growth temperature, and thus the critical radius is larger at the growth temperature than at the nucleation temperature. Thus, those particles whose radii fall between these two limits will dissolve. Hence, using a two stage heat treatment tends to underestimate the nucleation rate. James (7), however, has observed that this is not a very serious problem, at least in the case of $Li_2O \cdot 2SiO_2$ crystal nucleation.

In the present situation the particles were observed to grow sufficiently rapidly at the nucleation temperature to grow sufficiently rapidly at the nucleation temperature so that a single stage heating sufficed to determine the particle density (and nucleation rate). This procedure does not suffer from the difficulty described above. However, the single stage heat treatment could potentially lead to underestimation of the particle number, too, since a certain fraction of the nuclei which form will be too small to observe. For the present measurements, it will be demonstrated that this problem will introduce a negligible error in the steady state number density and no error in the measured steady state nucleation rate. Let us assume that particles with radii r less than r_0 cannot be observed. Also, one may divide the actual number density of particles present, N_{true}, into two parts; N_{exp} , the number density measured, and N_x the correction term due to unobservable particles. Thus,

$$N_{true} = N_x + N_{exp} \tag{1}$$

It is clear that at any time, t

$$N_x = \int_{t^*}^{t} I(t')dt' \tag{2a}$$

with t^* defined by

$$g(t-t^*) = r_0 \tag{2b}$$

where g is the crystal growth rate. Since I = dN/dt,

$$I_{true} = I_{exp} + I(t) - I\ (t'-r_0/g) \quad (3a)$$

Also, since $I(t) = I_{true}$,

$$I_{exp} = I(t-r_0/g) \quad (3b)$$

If there are not transient effects at the temperature of measurement, then $I(t-r_0/g)$ is independent of time and is the true nucleation rate. If transient effects are present, but one only considers those experimental points corresponding to steady state nucleation, then I_{exp} is time independent, and clearly equal to the true steady state nucleation rate. Thus, unobserved particles do not contribute to the nucleation rate.

Now the correction to the particle density is considered. Using eqs (1) and (2a),

$$N_{true} = \int_{t^*}^{t} I(t')dt' + N_{exp} \quad (4)$$

However, since it has been shown that $I(t) = I^0$(steady state rate) for $t \geq t^*$, eq (4) reduces to

$$N_{true} = (t-t^*)I^0 + N_{exp} = (r_0/g)I^0 + (t-t_c^e)I^0 \quad (4')$$

where eq (2b) has been used and t_c^e is the experimental value of the intercept on the time axis. In the steady state region $N_{true} = I^0(t-t_c^a)$, where t_c is the true time axis intercept of the steady state line. Hence,

$$t_c^a = t_c^e - r_0/g \tag{5}$$

It will be shown subsequently that $t_c^e \gg r_0/g$, and thus there are negligible corrections to the time axis intercepts and number densities associated with the experimental plots.

The experimentally determined number densities as a function of heating time are shown as the points in figs (2)-(4). The straight lines represent the least squares fit to these data. For glasses H and Q the points for the longest times, 75 and 240 minutes, respectively, were excluded in the calculations of the least-squares lines. This was justified by the significantly higher correlation coefficient values thus obtained. Physically, this may indicate that at the longest times sufficiently rapid and extensive crystallization occurred to raise the sample temperature above the ambient furnace temperature. The equations of these calculated lines and correlation coefficients are shown in Table 1. It is clear that the measurements correspond to the steady state regions. The bars on the points correspond to the root-mean-square errors (standard deviations) of the individual measurements. These were obtained for each point by taking into account the multiple measurements made for N_V at each time corresponding to different optical micrographs of the sample section.

The slopes of the curves are the steady state nucleation rates. They are reported in Table 2, along with the experimentally determined values of t_c^e, the time axis intercepts of the number density vs. time plots. Also, the calculated errors for the latter quantities are indicated. The error analysis was performed by usual statistacal methods, and utilized the calculated standard deviations associated with each number density.

DISCUSSION

It is tempting to proclaim that the bulk nucleation observed in these lithium borate glasses is homogeneous in nature. More nucleation data is required, however, to bolster such a claim. Nevertheless, there does exist one strong indication that the crystal nucleation occurred homogeneously; namely the magnitude of the nucleation rate. For comparative purposes we rely upon the findings of James (2). He noted that for the few silicate glasses which are believed to nucleate homogeneously the ratio of T_d, the temperature at which the nucleation rate is 1 $cm^{-3}sec^{-1}$ (barely detectable) to Tm (the melting temperature) ranges from .62 to .66. For glass Q, T_d/Tm $\approx .64$, and the measured nucleation rate is ≈ 165 $cm^{-3}sec^{-1}$. Hence, the nucleation rate in this glass is comparatively large, which is a leading indication of homogeneous nucleation.

From an inspection of figs (2)-(4), it is noted that the N(t) plots do not intersect the origin, but that they cut the time axis at positive times (see also column 3 of Table 2). This implies the existence of transient nucleation effects. However, eq (5) shows that the actual values of the time axis intercepts are smaller than the observed ones. Thus, in order to demonstrate the existence of transient effects at this temperature, estimates must be made of r_0/g. It may be recalled that r_0 is the smallest visible crystallite. It is estimated that $r_0 \approx 2\ \mu m$. The crystal growth rates, g, have not been measured, but it is possible to obtain lower bounds on the growth rates which will place upper bounds on the magnitude of r_0/g. If one measures the size of the largest crystallite in the sample and assumes that its growth started at t=0, this will yield a lower bound on g. Lower limits to the growth rates determined in this manner are shown in column 4 of Table 2. Then simple calculations show that r_0/g is even smaller than the uncertainty in t_c^e for each glass. This establishes the presence of transient effects.

Finally, the change in nucleation rate with composition is considered. James (15) has discussed the anticipated effects of composition variations upon the nucleation rate based upon the classical nucleation expression

$$I = A/\eta \exp\left(- b\sigma^3/(\Delta G_v)^2 kT\right) \qquad (6)$$

In eq. (6), η is the viscosity, σ is the crystal-glass surface tension, T is the temperature, ΔG_v is the bulk free energy difference between crystal and glass per unit volume, k is the Boltzmann constant, and A and b are constants. Although eq (6) was derived for a one component (or pseudo one component) system and its use is strictly not correct for "off-composition" nucleation, it should be capable of predicting qualitative trends (especially if the composition shift is small). The change in the nucleation rate with composition can be considered by inspecting the anticipated changes in η , ΔG_V, and σ with composition. If one considers a small composition shift away from a compound in a binary system, then by standard thermodynamic arguments (16) it can be shown that the magnitude of ΔG (bulk free energy difference between crystal and liquid) will decrease. In other words, the largest thermodynamic driving force for nucleation will occur at the composition of the compound, and compositional shifts in either direction will tend to make ΔG_V (and thus I) smaller. On the other hand, the nucleation rate is a monotonically decreasing function of viscosity, if all other parameters are held fixed. Therefore, compositonal shifts which decrease (increase) η will increase (decrease) I. For binary alkali silicate systems this implies that a positive compositional shift (adding more R_2O) will tend to increase the nucleation rate while a negative shift will have the opposite effect. Unfortunately, not much is known about the composition dependence of σ , although James speculates that it will be smaller if there is no compositional shift. If this is correct, then this would tend to enhance the nucleation rate of the compound composition in comparison to the rates of compositions with either positive or negative compositional shifts.

There have been several experimental studies on the effects of compositional variations on the nucleation rate in silicate glasses (5,8,9). Gonzalez-Oliver (8) considered the influence on the nucleation rate of small compositional shifts from $Na_2O \cdot 2C_aO \cdot 3SiO_2$ (NC_2S_3) glass. He investigated six glasses, each containing a ±1 mole% variation of one of the major constituents. The largest effect upon the nucleation rate was caused by the Na_2O variation, with an increase in the nucleation rate for the glass with the 1% extra Na_2O and a decrease in I for the -1% Na_2O containing glass. Also, it was observed that these glasses exhibited the smallest and largest viscosities, respectively, too. Thus, for small composition changes from NC_2S_3 the variation in the nucleation rate is primarily controlled by the viscosity change.

Burnett and Douglas (5) investigated the nucleation and crystallization behavior of glass in the Na_2O-BaO-SiO_2 system. They ascertained that nucleation diminished as one moved from the stoichiometric barium disilicate composition. This implies that either a decrease in ΔG_v or an increase in σ is the controlling factor in this system rather than the viscosity.

James (15) has concluded that for the interpretation of the change in nucleation kinetics with composition, one probably must take into account all three factors simultaneously since variations in the nucleation rate are unlikely to be a function of solely one of the variables.

The change in nucleation rate with composition near the $Li_2O \cdot 2B_2O_3$ composition is shown in Table 2. One observes that as the Li_2O content increases the nucleation rate first increases and then decreases. The interpretation of these results is subject to even more uncertainty than in the previous cases because of two additional unknowns. First, viscosity data are not available in the high Li_2O composition glasses due to their rapid crytallization rates. Next, unlike the alkali silicate glasses whose viscosities decrease with increasing alkali concentration, the composition dependence of the viscosities of the alkali borate glasses exhibit minima and maxima (17). Despite these additional uncertainties one may postulate an explanation, albeit speculative, of the present results. Although the behavior of the viscosity as a function of composition of the glasses considered herein is uncertain, it is quite reasonable to assume that it is decreasing with increasing Li_2O content. This assumption results from an inspection of fig (2) of ref (17) which shows that the local maximum in viscosity as a function of R_2O at temperatures of 600, 700, 800, and 900°C all occur in the region of 20 mole%. Therefore, a reasonable explanation of the data is as follows. The change in viscosity with composition is probably greater than the variations in ΔG_v or σ. However, from an inspection of eq. (6) one notes that I is a much more sensitive function of ΔG or σ than of η. Therefore, although the change in η is probably dominant over the entire composition region, the strong dependence of I on ΔG and σ is dominant for larger composition variations causing an eventual decline in nucleation rate. This argument can be given further credence by an inspection of the behavior of the transient time, τ (18). It is easy to demonstrat that τ follows the behavior of t_c (i.e. τ decreases when t_c decreases). Therefore, from column 3 of Table 2, one concludes that τ decreases as the Li_2O concentration increases. However, τ has the following dependence upon the crucial parameters η, ΔG_v, and σ (15),

$$\tau \sim \eta\left(\frac{\sigma}{(\Delta G_v)^2}\right) \quad (7)$$

Since τ decreases with increasing composition, the viscosity change must predominate since ΔG decreases and σ is believed to increase. Thus, the behavior of the transient time with composition is consistent with our interpretation of the variation of the nucleation rate with increasing Li_2O content.

SUMMARY

The bulk nucleation of three glass compositions in the vicinity of $Li_2O \cdot 2B_2O_3$ was examined. Steady state nucleation rates were determined as a function of composition, and it was observed that at + 3% composition variations in Li_2O caused an increase in rate but a +4.2% increase in Li_2O evoked a decline in nucleation rate. This behavior could be plausibly explained in terms of the combined effects of viscosity, free energy, and surface tension changes. It was observed that the nucleation exhibited transient behavior for all compositions. Finally, evidence was provided which led one to suspect that the nucleation occurred homogeneously. However, additional studies are required to confirm this conjecture.

ACKNOWLEDGEMENT

The research described in this paper was performed at the Jet Propulsion Laboratory, California Institute of Technology, under contract with the National Aeronautics and Space Administration (NASA). The authors wish to express their appreciation to the Microgravity Sciences and Application Office of NASA for the financial support of this work.

REFERENCES

1. Uhlmann, D. R. (1972). J. Non-Cryst. Solids 7, 337.

2. James, P. F. (1985). J. Non-Cryst. Solids 73, 517.

3. Neilson, G. F. & Weinberg, M. C. (1974). J. Non-Cryst. Solids 34 137.

4. McMillan, P. W. (1964). Glass Ceramics, Academic Press, London, England.

5. Burnett, D. G. & Douglas, R. W. (1971). Physics Chem. Glasses 12 117.

6. Strnad, Z. & Douglas, R. W. (1973). Physics Chem. Glasses 14 33.

7. Rowlands, E. G. & James, P. F. (1979). Physics Chem. Glasses 20, 1;9.

8. Gonzalez-Oliver, C. J. R. & James, P. F. (1980). J. Non-Cryst. Solids 38-39, 699.

9. James, P. F. & Rowlands, E. G. (1979). In Phase Transformation, Vol. 2. Inst. of Metallurgists, Northway House London. Section III, 27.

10. Zanotto, E. D.(1982). Ph.D. thesis, University of Sheffield.

11. Zachariesen, W. (1932). J. Am. Chem. Soc. 54, 3841.

12. Warren, B., Krutter, H., & Morningstar,O. (1938). J. Amer. Ceram. Soc. 21, 259.

13. Mozzi, R. & Warren, B. (1969). J. Appl. Cryst. 2 164.

14. Kreidl, N. J. (1983). In Glass Science and Technology, Vol. 1. ed. by D. R. Uhlmann & N. J. Kreidl. Academic Press, New York. 105-299.

15. James, P. F.(1982). In Advances in Ceramics, Vol. 4. ed. by J.H. Simmons, D. R. Uhlmann, & G. H. Beall, Amer. Ceram. Soc., Inc., Columbus, Ohio. 1.

16. Christian, J. W.(1965). The Theory of Transformations in Metals and Alloys, Pergamon Press, Oxford, England.

17. Shartsis, L., Capps, W. & Spinner, S. (1953). J. Amer. Ceram. Soc. 36, 319.

18. Kelton, K. F., Greer, A. L. & Thompson, C. V. (1983). J. Chem. Phys. 79, 6261.

TABLE 1

FIT OF EXPERIMENTAL NUMBER DENSITY DATA

Glass	Mole% Li_2O	Equation of line (Figs (2)-(4)) 10^{-4}	Correlation Coefficient
Q	33.8	$N_v = .86t - 72.34$	.943
G	36.8	$N_v = 1.692t - 31.73$	.979
H	38.2	$N_v = .25t - 1.37$	.995

TABLE 2

SUMMARY OF EXPERIMENTAL RESULTS

Glass (Mole% Li_2O)	Nucleation Rate $(cm^3\text{-}min)^{-1}$	t_c^e(min)	Lower Limit to Growth Rate (μm/min)
O (33.8)	$(.86 \pm .14) \times 10^4$	84 ± 4.4	.73
G (36.8)	$(1.69 \pm .26) \times 10^4$	19 ± 2	3.5
H (38.2)	$(.25 \pm .03) \times 10^4$	5.6 ± 1.9	4.2

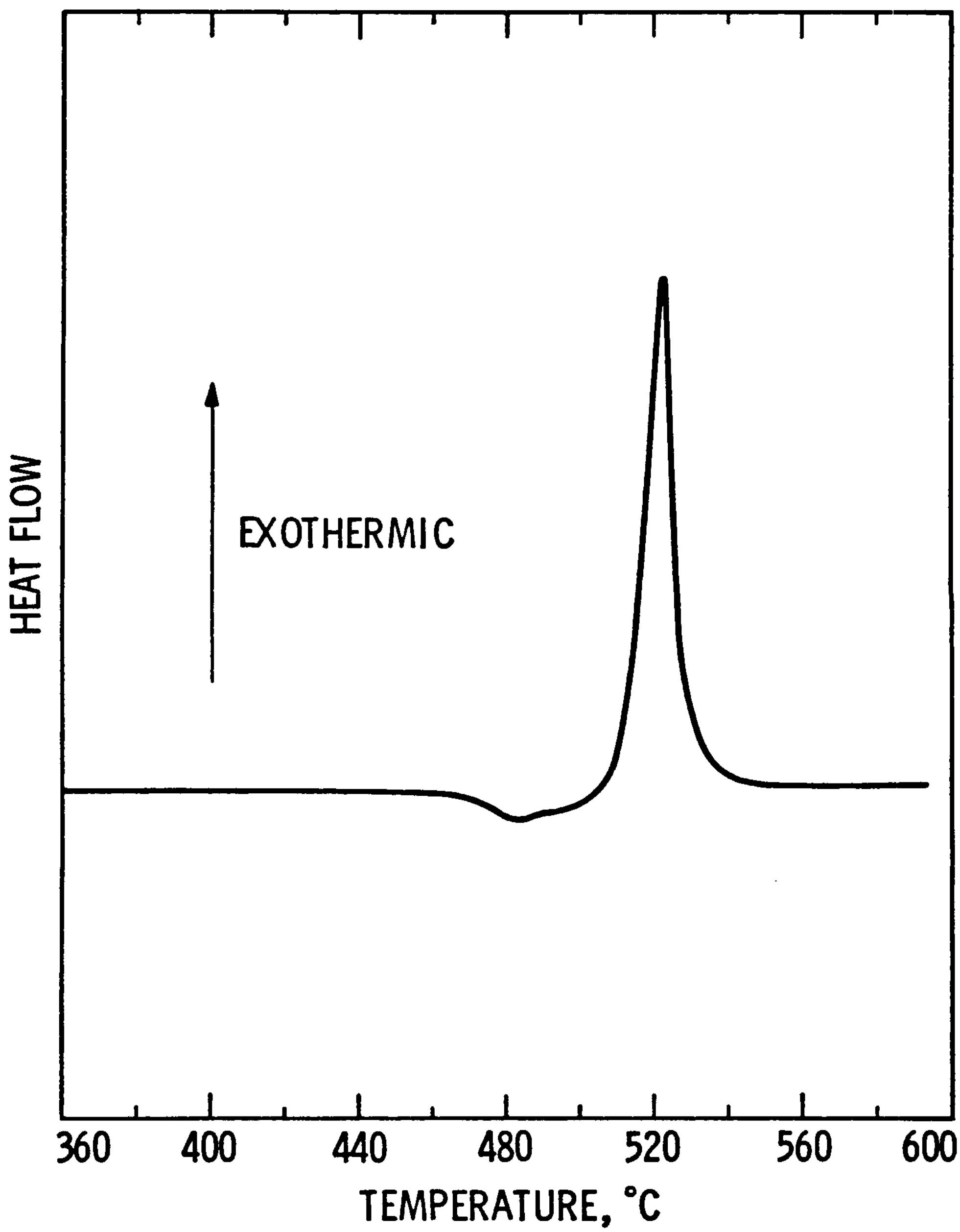

Figure 1 Differential Scanning Calorimetry scan of glass H, heated in air at a rate of 5°C/min.

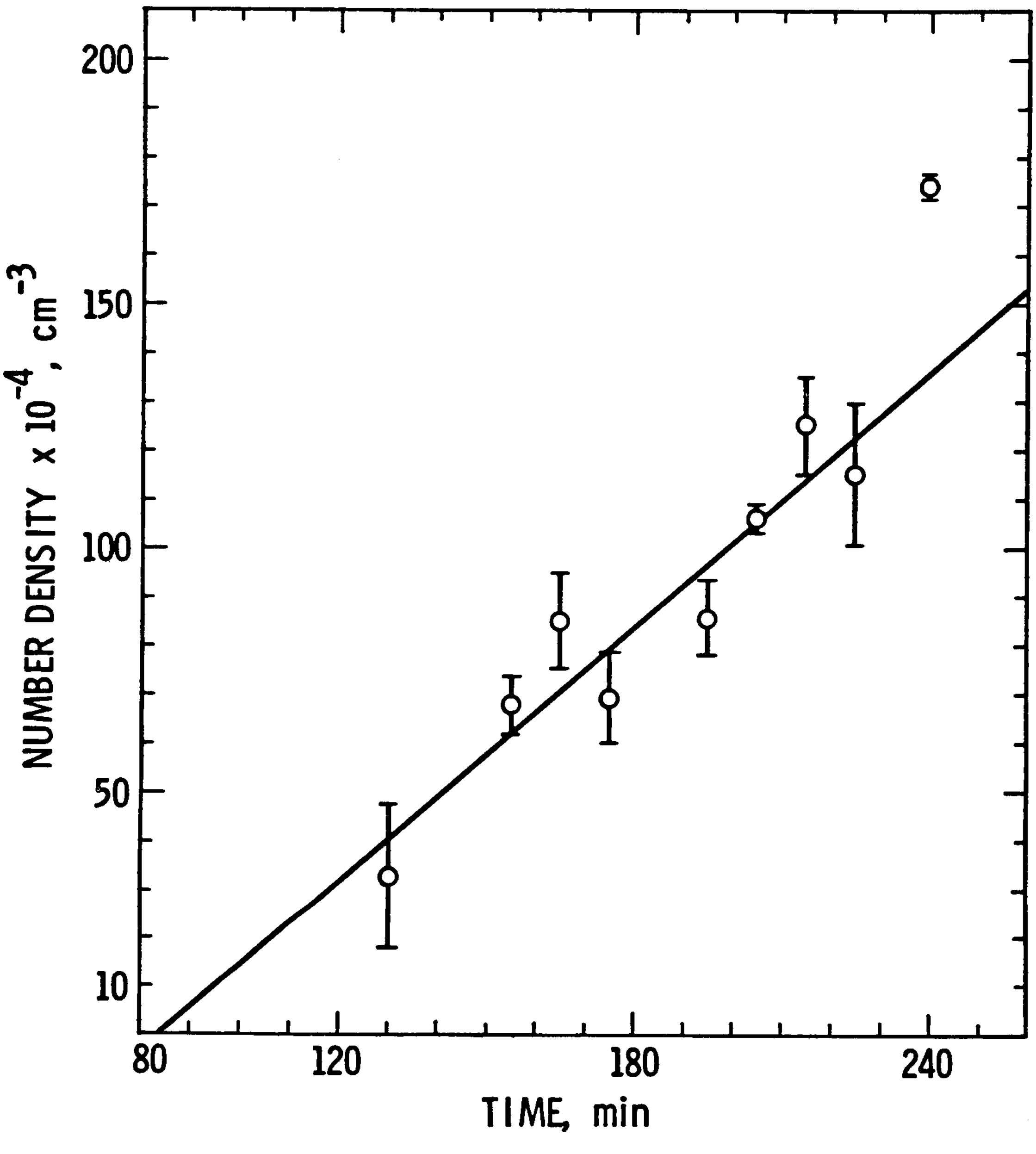

Figure 2 Crystal number density as a function of time for glass Q (33.8 mole% Li_2O). Glass was heated at 500°C.

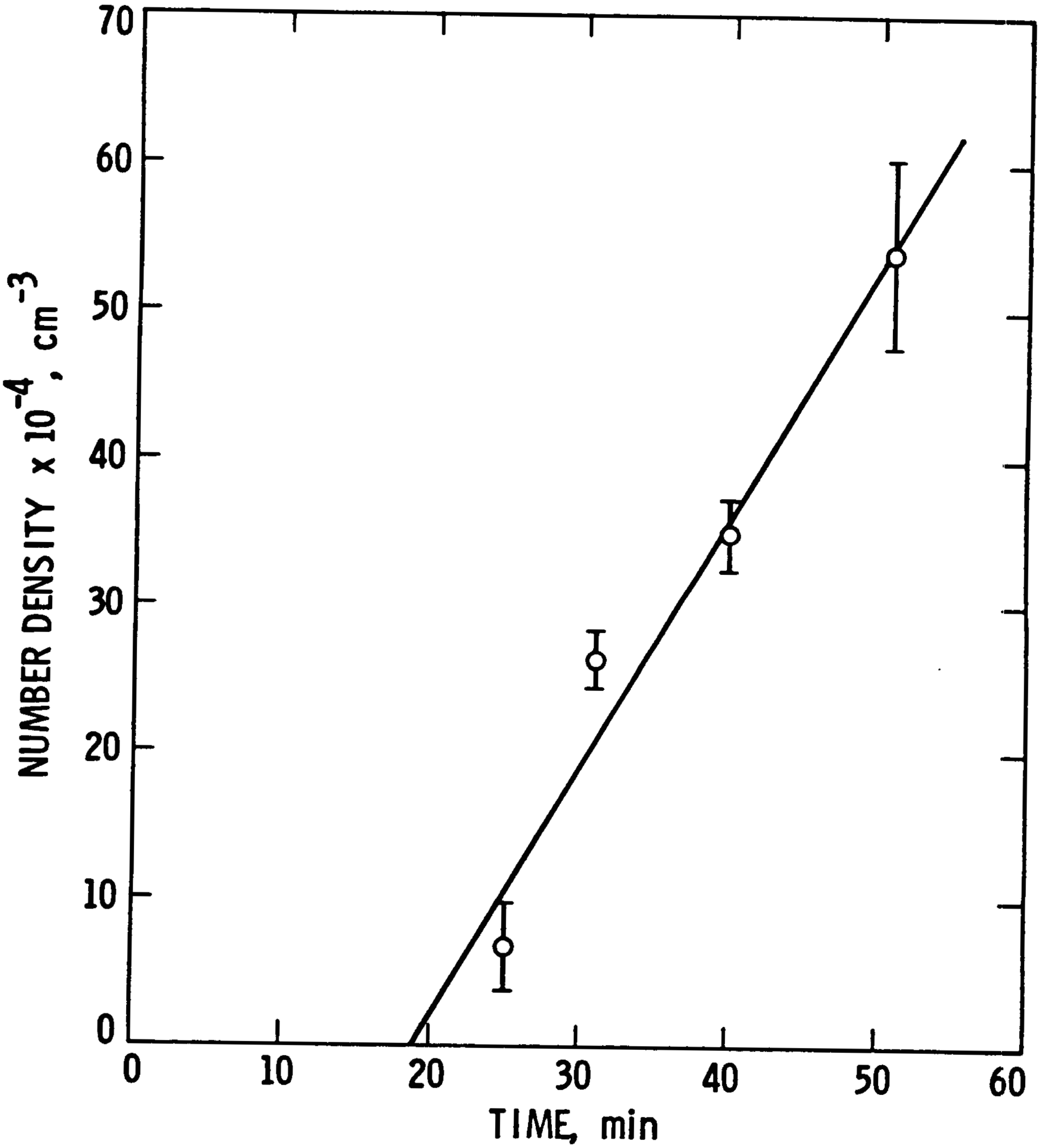

Figure 3 Crystal number density as a function of time for glass G (36.8 mole% Li_2O). Glass was heated at 500°C.

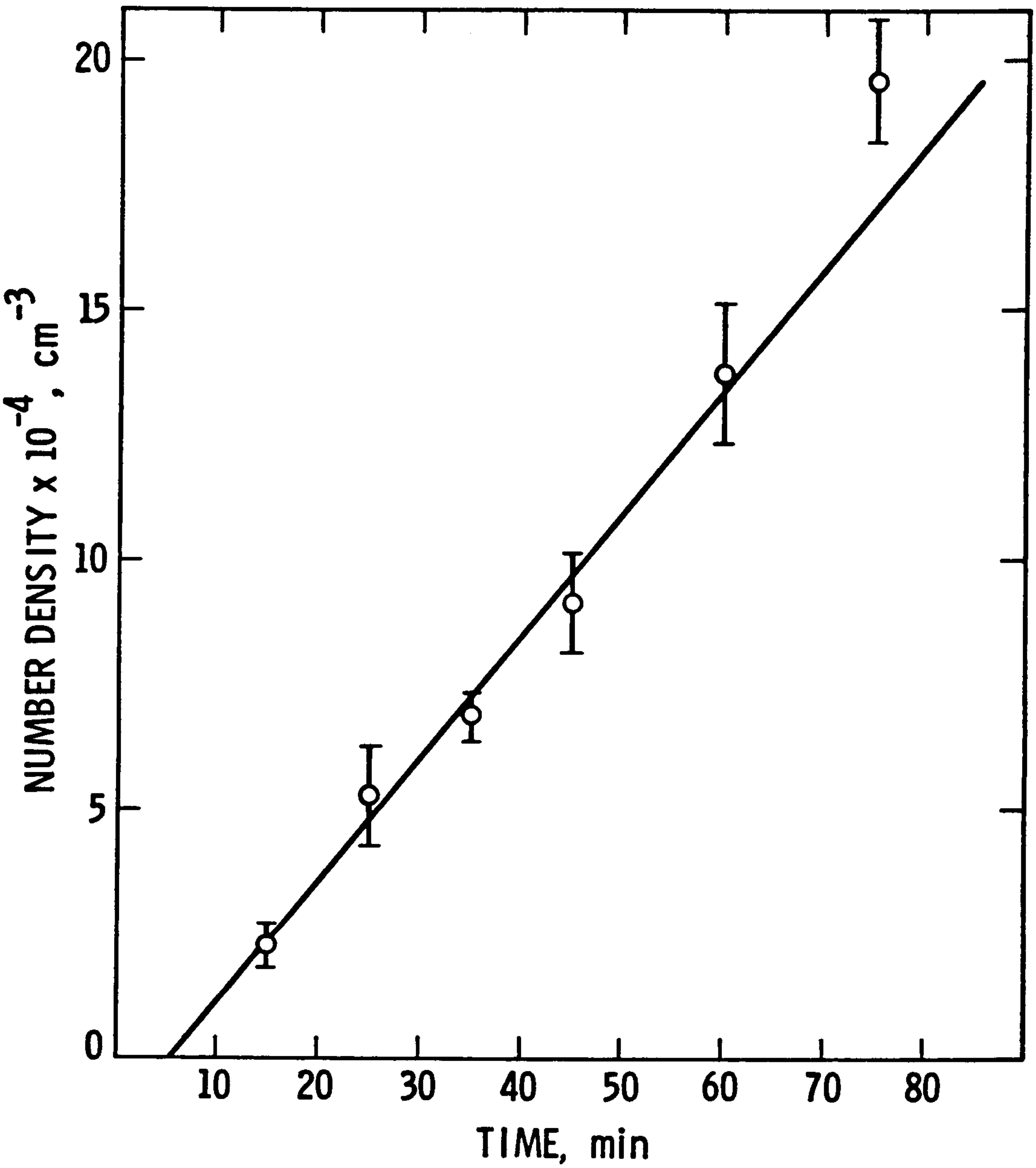

Figure 4 Crystal number density as a function of time for glass H (38.2 mole% Li_2O). Glass was heated at 500°C.

N89-20310

Physical Phenomena in Containerless Glass Processing

R. Shankar Subramanian and Robert Cole
Department of Chemical Engineering
Clarkson University
Potsdam, New York 13676

Introduction

It has been suggested by scientists that certain new and unique glasses can be made in orbital laboratories because drops of liquid can be suspended and cooled without the need for a container (1-2). Glasses are amorphous substances formed by cooling a liquid rapidly enough to avoid the formation of a crystalline material. While common glasses can be made with relative ease, Topol et al. (1) found that certain rare earth oxides could not be cooled into a glass in a container because of container wall induced heterogeneous nucleation. However their experiments using a gas jet levitation scheme showed that the same substances could be cooled into an amorphous material when the container was avoided. Work by Day (3) is currently in progress on studying glass formation in a containerless mode in space.

Gas bubbles are commonly encountered in glass processing. They are released due to chemical reactions, and also are present because of gases trapped in the interstitial region among the grains of the raw materials. The bubbles, on earth, are removed by buoyant rise to the free surface as well as by dissolution. In orbit, the former mechanism is of negligible importance, and it is essential to explore mechanisms other than dissolution for the removal of bubbles from space-processed glasses.

Gas bubbles within liquid drops also are encountered in other applications on earth. For instance, in inertial confinement fusion, a hollow glass shell is filled with the fusion fuel and imploded in a laser or ion beam. The process appears to require shells with a uniform wall thickness. On earth, the shells are made in processes which are incompletely understood. Common to most of these is the appearance, at some point in the process, of a molten drop of liquid containing one or more gas bubbles. The drop typically settles in a gaseous medium in a furnace, and the bubbles within it execute motion and undergo possible size change. The drop solidifies into a glass shell at the bottom of the furnace. A surprisingly large yield of good shells (of relatively uniform wall thickness) apparently has been observed in this process. The reason for this self-centering of the gas bubbles within liquid drops is not clear. Oscillation has been suggested (4) and we have proposed drop rotation (5). Other candidates include expansion and contraction. Other applications in which gas or vapor bubbles might be encountered within drops of liquid include spray drying and encapsulation of volatile materials.

It is difficult to experiment on earth with a relatively large drop of liquid in a gaseous medium with gas bubbles present in it. Using orbital experiments on liquid drops containing gas bubbles it is possible to extract useful information concerning the behavior of bubbles in drops subjected to stimuli. Such information is of technological significance in the above applications.

Objectives

The objectives of this investigation are

To develop an understanding of fluid motion and bubble and droplet motion and interaction when drops containing bubbles are subjected to stimuli such as surface tension gradients, rotation, oscillation, expansion and contraction.

Flight Experiments

It is envisioned that experiments will be conducted in orbit on drops of model liquids containing bubbles in a device which can hold and manipulate drops of liquid at room temperature using acoustic fields. Experiments also are planned on drops of glass melt, to occur at a later stage, in an appropriate apparatus. The model liquids chosen include Dow Corning silicone oils (dimethylsiloxane and similar polymers) and Union Carbide NIAX Polyols (Polypropylene Glycols). These fluids are sufficiently viscous to simulate the fluid mechanical phenomena expected in glass melts. In particular, the ranges of Reynolds and Prandtl numbers will be comparable to those expected in applications involving glass melts.

Initially, two types of experiments are planned, and are schematically illustrated in Figure 1. In one class, drops of liquid, within which one or more gas bubbles have been inserted, will be subjected to a beam of light (of suitable wavelength and intensity) which will be absorbed by the liquid near the surface. The resulting temperature gradients at the drop surface and at the drop-bubble interfaces will lead to surface tension gradients. The consequence will be motion within the drop and migration of the bubbles. The origin of such flows is termed thermocapillarity. It is expected that the bubbles will move toward the heated spot, and might subsequently be extracted from the drop. The shapes of the drop and the bubbles during the experiment also are of interest. The objective of the experiment is to compare the resulting motion of the bubbles with predictions from appropriate theoretical models. Ultimately, it is expected that such experiments might pave the way to the development of practical techniques for managing bubbles within liquid drops in orbit.

In the second category of experiment, similar drops containing bubbles will be subjected to rotation. The resulting pressure fields within the drop will drive the migration of the gas bubbles toward the center of the drop and also deform the shapes of the drop and the bubbles. In this case, the rotation speeds would be chosen to be sufficiently small to avoid shape bifurcations. The objective of this experiment is to compare the resulting trajectories of the bubbles as well as shapes with available theoretical models. This experiment can complement the previous one in providing techniques for bringing several small bubbles within a drop to its center to coalesce into a large bubble which might subsequently be extracted or otherwise manipulated within the drop.

The migration of the bubbles as well as shape information in the above experiments will be recorded via a video camera. Three orthogonal views will be recorded to extract full spatial information from the resulting images. The videotape will be brought back to earth for analysis.

The parameters in the experiments will be varied over a sufficient range either in a single flight or in multiple flights to gain good insight into the physical processes being studied. The experiments will have the best chance of success when they can be performed by a scientist in the space laboratory, and repeated.

The Drop Dynamics Module, designed and built at the Jet Propulsion Laboratory is considered ideal for the conduct of the above experiments. This device was flown on a Shuttle mission in 1985, and experiments on drop dynamics were performed by Dr. Taylor Wang of Jet Propulsion Laboratory who was an astronaut on this mission. His experiments were conducted in a shirt-sleeve environment, and repeated as desired.

The Drop Dynamics Module was not available to this investigation in its initial flight. Since it is well-suited for the conduct of the present experiments, it has been requested that the Clarkson experiments be accommodated on it during its next flight.

Supporting Ground-Based Studies

To date, five Ph.D. theses and five M.S. theses have been completed in support of our flight program. Currently, the program supports two graduate students. In addition, another student working on related problems is being supported as a NASA Graduate Student Researcher.

It is not possible to outline details of the past ground-based research program in this short document. The principal results have been published in the open literature beginning in 1979, and a complete bibliography has been provided separately along with the abstract. The bibliography lists 22 refereed papers published in journals such as J. Colloid and Interface Science, Chemical and Engineering Science, AIChE Journal, Physics of Fluids, J. American Ceramic Society, J. Fluid Mechanics etc., 21 Contributions to Conference Proceedings, and 54 talks presented at various meetings in the United States, Canada, and Western Europe. Copies of all the published papers have been provided routinely to the Microgravity Sciences Division offices at NASA Headquarters as well as to the Marshall Space Flight Center.

In the rest of this document, some interesting scientific problems currently being pursued on ground will be discussed.

Surface Tension Driven Motion

The literature on surface-tension driven motion has been reviewed by Scriven and Sternling (6), Levich and Krylov (7), and Schwabe (8). Some details also are discussed by Ostrach (9). Generally, the fact that gradients in interfacial tension at a fluid-fluid interface can drive fluid motion has been known since the last century. However, experimental measurements of surface tension driven flow velocities and the characteristics of such flows have been relatively rare, and substantially more attention has been devoted to stability problems. Initially in the present program, we undertook the task of making some measurements. The results from our experiments on capillary liquid bridges of silicone oils and glass melts in which flow was generated by surface tension gradients have already been reported in the literature.

In recent years, we have been investigating problems involving gas bubble and liquid drop migration in a temperature gradient. It is known that a gas bubble can be made to move by applying a temperature gradient. Briefly, the interfacial tension depends upon temperature and hence varies around the surface of the bubble. The resulting tangential stress acts upon the neighboring liquid causing it to move toward the cooler side of the bubble. By reaction, the bubble propels itself toward warmer regions.

The motion of gas bubbles due to the action of a temperature gradient was demonstrated by Young, Goldstein, and Block (10) in 1959. By applying a downward temperature gradient on bubbles contained in a capillary liquid bridge, Young et al. were able to arrest the normal buoyant rise of the bubbles, and make them move downward on occasion. These investigators also solved the governing field equations, and from a force balance on the bubble, extracted the steady migration velocity of the bubble. This was done in the limit of negligible convective transport of momentum and energy.

There were difficulties with the Young et al. experiment, not the least of which was the presence of a free liquid surface on the liquid bridge which experienced a temperature gradient and therefore a surface tension gradient. The temperature gradients in the liquid in the lateral direction must also have contributed to overall buoyant convection in it. Several bubbles were present at one time, and finally, the bubbles were observed through a curved liquid surface which must have introduced optical distortion.

Young et al. reported their data in the form of the temperature gradient necessary to arrest the motion of their bubbles plotted against bubble size. The data were considerably scattered, but demonstrated qualitative agreement with their theoretical model. Their experiment was later revived by Hardy (11) who built a refined apparatus at the National Bureau of Standards. Hardy eliminated most of the problems mentioned above.

Short duration (3-5 second) experiments on gas bubbles have been reported by Thompson et al. (12) who performed their study at the NASA Lewis Center's Drop Tower. The experiments, having been done in free fall, correspond to low gravity conditions. It is surprising that Thompson et al. report agreement of the migration velocity with the prediction of Young et al. for values of the Marangoni number as large as 1,200. The Marangoni number is a parameter which describes the relative importance of convective transport of energy to its molecular transport. The theory of Young et al. was developed for <u>negligible</u> values of the Marangoni number. We have extended the theory to accommodate moderate values of the Marangoni number, and our predictions indicate a substantial influence at these values of this parameter. Our predictions ignore inertial effects which were probably significant in the experiments of Thompson et al. The role of such effects would be to increase the deviation of the data from the predictions of Young et al. Further low gravity experiments are necessary to resolve the above discrepancy.

At Clarkson, an apparatus has been built which is modelled after the one used by Hardy. Air bubbles in the diameter range 50-200 micrometers are introduced into liquid contained in a rectangular cavity (20 x 20 mm cross-section, 5 mm high) and subjected to a vertical temperature gradient which can be as high as 10 K/mm. The refinements over Hardy's apparatus include active temperature control, the use of a nanoliter pump to inject bubbles reproducibly, and the facility to perform experiments on bubbles in the vicinity of a horizontal surface. Also, experiments are videotaped through a microscope and analyzed later on a frame-by-frame basis for bubble size and position as functions of time. Free convection velocities have been measured in the cell using a neutrally buoyant tracer to assure that such velocities are negligible compared to the bubble migration velocities.

Initially, experiments were performed on air bubbles in a Dow-Corning DC-200 series silicone oil of viscosity approximately three Poise. Data were taken on several isolated bubbles migrating in a downward temperature gradient. The bubbles, after injection, were found to grow throughout the experiment, roughly doubling in size over a two minute interval. In spite of this substantial size change, the experimental data on several bubbles were found to be consistent with predictions from the theory of Young et al. The Reynolds and Peclet numbers in these experiments were negligibly small. The growth of the bubbles is caused by the supersaturation of gas in the liquid, and will be an integral aspect of such experiments in space applications.

More recently, some preliminary experiments have been performed on air bubbles introduced in the vicinity of the bottom surface of the cell. A downward temperature gradient was used. The bubbles were found to grow as before as they migrated downward. Often they proceeded to become attached to the surface, grew further, and then became detached when sufficiently large. At this point they rose rapidly out of the field of view. The downward velocities have been observed to be substantially <u>larger</u> than those predicted by the theory of Young et al. The explanation lies in the nature of the influence of the surface on the velocity field components generated from the body force (gravity) and from the thermocapillary effect. A full quasi-steady theoretical analysis is planned and the results will be compared with the data. Additional experiments also are planned on interactions with a surface wherein the bubble moves upward.

Finally, it should be mentioned that we are continuing to develop new theoretical predictions on the subject of thermocapillary motion of drops and bubbles. An analysis of the thermocapillary motion of an isolated bubble/drop in the presence of an insoluble surfactant which forms a stagnant cap is in progress. Numerical work is under way for predicting the migration speed of a gas bubble in a vertical temperature gradient on earth under conditions of moderate Peclet number and negligible Reynolds number. The problem of predicting the migration speed of an isolated bubble in a temperature gradient under conditions of large Peclet number and no gravity is still unresolved. This is a difficult singular perturbation problem and the solution is not in sight yet. Finally, it is planned to begin posing the problem of predicting the direction and magnitude of the velocity of a bubble present in a drop subjected to an arbitrary non-uniform temperature field on its surface under conditions of negligible Reynolds and Peclet numbers. We solved the problem for axisymmetric fields in 1982, but are just beginning to consider the non-axisymmetric case.

Compound Drops

In another apparatus, drops of liquid are formed in a second immiscible liquid. While the drops are held at the tip of the injector, a gas bubble or an immiscible liquid droplet is introduced within the drop. Then the entire compound drop (drop containing droplet/bubble) is released. The resulting motion of the drop is recorded using an orthogonal pair of video cameras, and observation time is extended using a motorized platform which is moved upward at nearly the same velocity as that of the settling drop. An optical analysis has been developed to correct for the refraction effects through the drop's curved surface. Thus, from a frame by frame analysis of the videotape, suitably corrected, the bubble size and velocity (relative to the drop) can be obtained.

There are several reasons for initiating the compound drop experiments. Sadhal and Oguz (13) recently predicted that for certain ranges of parameters, the bubble velocity along a vertical drop axis can be zero. Some of these locations can be stable while others are unstable. This is an interesting prediction which can have important consequences on mass transfer to and from droplets/bubbles within a drop in various applications. Also, surface active agents (surfactants), if present, can influence the motion of the bubble within the drop. We have already observed, with certain fluid-fluid combinations, classical surfactant cap formation on the settling drops. Finally, the system also permits us to gain valuable experience on drop-bubble combinations of the types we expect to use in the flight experiments.

Bubble Migration in Rotating Fluids

A rotating fluid provides a gyrostatic pressure field which will cause less dense material such as bubbles to move inward toward the rotation axis. Experimental evidence of this fact was provided by Schrage and Perkins (14) who photographed the inward spiralling motion of gas bubbles in liquid contained within a cylinder. Our initial work on this topic was centered on confirming that this will happen in a fluid spun up from rest about a horizontal axis, and contained in a sphere. On earth, the trajectory of the bubble is influenced by gravity resulting in interesting oscillations of the radial position of the bubble as it approaches the axis of rotation. The final position of the bubble is determined by equilibrium among the forces acting on the bubble and may not be on the rotation axis, but some position off-set from it. Over the years, we have developed suitable theoretical descriptions of the trajectory of the bubble as well as its ultimate location. The predictions have generally been confirmed by the observations and the results have been reported in the open literature.

The shape of a rotating liquid drop has interested several prominent scientists since the last century. Initially studied by Plateau, the problem has been investigated analytically by Chandrasekhar (15) who studied the stability of equilibrium drop shapes. Brown and Scriven (16) have more recently constructed an exhaustive map of the stability diagram for a rotating drop using finite element methods.

Our plans are to work with relatively low rotation speeds so that in the experiments in orbit, there is sufficient time for observation of the bubble trajectories and drop and bubble shape changes. For such speeds, we do not expect complications from drop shape bifurcations. While a thorough stability analysis of the shapes of drops containing bubbles still has not been performed, the rotation speeds to be used will be an order of magnitude smaller than the speed required for liquid drops to exhibit shape bifurcation.

Serendipitously, it was observed that spin-up flows can cause a drop more dense than the surrounding fluid to migrate toward the rotation axis. After spending some time spinning at a location close to the rotation axis, the drop would migrate back toward the wall of the container. By using tracer particles to follow the shear front during spin-up, we have determined that the initial "wrong direction" motion of the more dense drops is due to the spin-up flows.

We also have performed bubble and drop migration experiments under low gravity conditions through the Marshall Space Flight Center KC-135 reduced gravity program. The bubble migration experiments provided data at low rotation rates on the shape and trajectories of large bubbles in a liquid-filled rotating sphere which were unobtainable in 1-g. Experiments on more dense liquid drops in a liquid-filled rotating sphere showed conclusively that gravity assists the process.

Because of the nature of the KC135 aircraft flight path, it was possible to conduct both sets of experiments repeatedly in alternating low-g and 1-g environments. The gas bubbles which adhered to the wall in 1-g were easily detached in low-g. The more dense drops which left the wall in 1-g adhered to the wall in low-g, and hence did not migrate at all.

Future experiments will focus on bubble and drop migration within contained rotating fluids wherein the size of the bubble/drop is not small compared to that of the container. Preliminary experiments on this subject have provided information on the shapes assumed by a bubble while it migrates toward the axis and reaches a stable equilibrium location. These shapes, determined by the complex flows within the system, are probably similar to those one might expect in the flight experiments. Another experiment currently being pursued involves a compound drop present in a more dense liquid contained in a sphere. As the sphere is spun up about a horizontal axis, the drop migrates toward the rotation axis, and upon reaching it, starts rotating. At this point, the bubble begins to spiral in toward the axis of the rotating drop. Work on this experiment has been at a preliminary stage for a long time due to wetting problems as well as problems with drop breakup. These problems are gradually being resolved.

SUMMARY

Flight experiments are planned on drops containing bubbles. The experiments involve stimulating the drop via non-uniform heating and rotation. The resulting trajectories of the bubbles as well as the shapes of the drops and bubbles will be videotaped and analyzed later frame-by-frame on ground.

Supporting ground based experiments are planned in the area of surface tension driven motion of bubbles, the behavior of compound drops settling in an immiscible liquid and the shapes and trajectories of large bubbles and drops in a rotating liquid.

Theoretical efforts will be directed at thermocapillary migration of drops and bubbles, surfactant effects on such migration, and the behavior of compound drops.

REFERENCES

1. L.E. Topol, D.H. Dengstenberg, M. Blander, R.A. Happe, N.L. Richardson, and L.S. Nelson, "Formation of New Oxide Glasses by Laser Spin Melting and Free Fall Cooling," J. Non-Crystalline Solids 12, 377 (1973).

2. M.C. Weinberg, "Glass Processing in Space," Glass Industry, 59, 22 (1978).

3. D.E. Day, "Containerless Processing of Glass Forming Melts, NASA Contract NAS8-34758 Final Report For MEA/A-1 Experiment 81F01," NASA Marshall Space Flight Center, Huntsville, Alabama (1984).

4. M.C. Lee, J.M. Kendall, D.D. Elleman, W-K Rhim, R.S. Helizon, C.L. Youngberg, I-A Feng, and T.G. Wang, "Application of Microgravity and Containerless Environments to the Investigation of Fusion Target Fabrication Technology," in Materials Processing in the Reduced Gravity Environment of Space, Ed. G.E. Rindone, North-Holland, New York, 1982, p. 95.

5. R.S. Subramanian and R. Cole, "Physical Phenomena in Containerless Glass Processing," Proposal submitted to NASA, 1977; see also, P. Annamalai, N. Shankar, R. Cole, and R.S. Subramanian, "Bubble Migration Inside a Liquid Drop in a Space Laboratory," App. Sci. Res. 38, 179 (1982).

6. L.E. Scriven and C.V. Sternling, "The Marangoni Effects," Nature 187, 186 (1960).

7. V.G. Levich and V.S. Krylov, "Surface-Tension-Driven Phenomena," in Annual Reviews of Fluid Mechanics, Volume I, Ed. W.R. Sears and M. Van Dyke, 1969, p. 293.

8. D. Schwabe, "Marangoni Effects in Crystal Growth Melts," Physicochemical Hydrodynamics 2, 263 (1981).

9. S. Ostrach, "Low-Gravity Fluid Flows," in Annual Reviews of Fluid Mechanics, Vol. 14, Ed. M. Van Dyke, J.V. Wehausen, and J.L. Lumley, 1982, p. 313.

10. N.O. Young, J.S. Goldstein and M.J. Block, "The Motion of Bubbles in a Vertical Temperature Gradient," J. Fluid Mech. 6, 350 (1959).

11. S.C. Hardy, "The Motion of Bubbles in a Vertical Temperature Gradient," J. Colloid Interface Sci. 69, 157 (1979).

12. R.L. Thompson, K.J. DeWitt and T.L. Labus, "Marangoni Bubble Motion Phenomenon in Zero Gravity," Chem. Eng. Commun. 5, 299 (1980).

13. S.S. Sadhal and H.N. Oguz, "Stokes Flow Past Compound Multiphase Drops: The Case of Completely Engulfed Drops/Bubbles," J. Fluid Mech. 160, 511 (1985).

14. D.L. Schrage and H.C. Perkins, "Isothermal Bubble Motion Through a Rotating Liquid," ASME J. Basic Engineering March 1972, p. 187.

15. S. Chandrasekhar, "The Stability of a Rotating Liquid Drop," Proc. Roy. Soc. Lond. A286, 1 (1965).

16. R.A. Brown and L.E. Scriven, "The Shape and Stability of Rotating Liquid Drops," Proc. Roy. Soc. Lond. A371, 331 (1980).

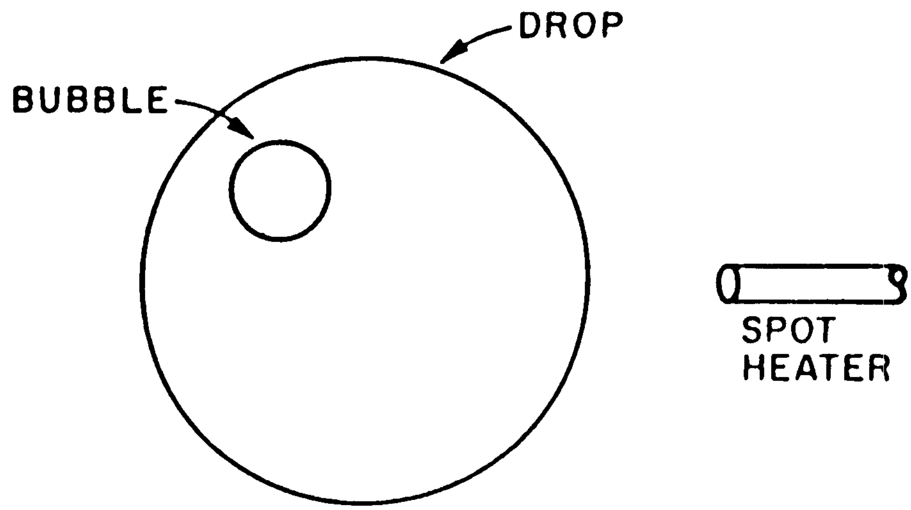

BUBBLE MIGRATION DUE TO THERMOCAPILLARITY

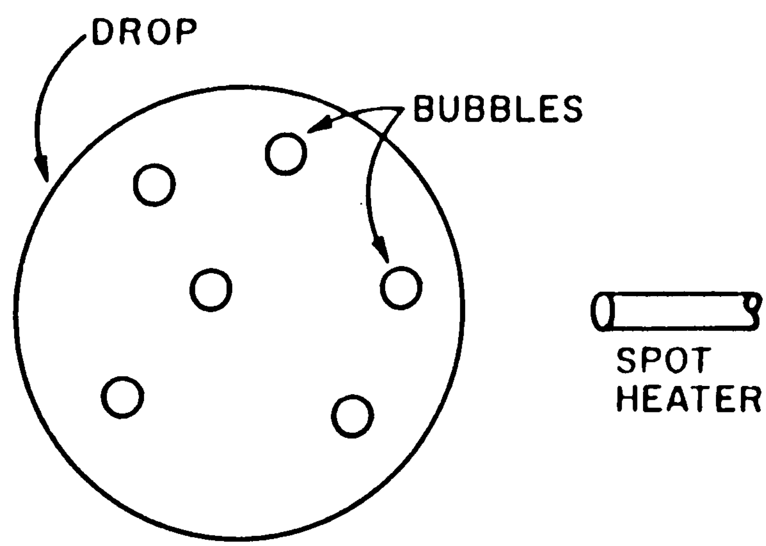

CENTRIFUGAL FINING TECHNIQUE

Figure 1. Flight Experiments

COMBUSTION SCIENCES

PARTICLE CLOUD COMBUSTION IN REDUCED GRAVITY

by

A. L. Berlad

Department of Applied Mechanics and Engineering Science
University of California, San Diego
La Jolla, California 92093

March, 1987

N89-20311

ABSTRACT

Particle Cloud Combustion In Reduced Gravity

by

A. L. Berlad

Dept. of Applied Mechanics and Engineering Science
University of California, San Diego
La Jolla, California 92093

Study of flame propagation and extinction for premixed flames has occupied a position of central interest in combustion science. Despite the substantial body of experimental and theoretical work achieved to date, experiments aimed at determining these properties for quiescent premixed particle clouds in a gaseous oxidizer suffer from a number of serious deficiencies. The experiments cannot be conducted in normal gravity because:

(1) gravity causes the sedimentation of particles of significant size, thereby rendering spatial and temporal uniformity of a quiescent reactive particle cloud impossible.

(2) mixing-induced turbulence and secondary flows used to suppress sedimentation and to create uniform particle clouds imply ill-defined transport properties. Such mixtures sustain the problems of item (1), above, when particle-uniformity-promoting stirring ceases.

(3) fuel-oxidizer ratio fluxes through freely propagating flame fronts are functions of the gravity vector, and

(4) gravity induced natural convection processes modify the underlying flame propagation and extinction phenomena.

The principal objectives of this microgravity experimental program are to obtain flame propagation rate and flame extinction limit data for several important premixed, quiescent particle cloud combustion systems under near zero-gravity conditions. The data resulting from these experiments are needed for utilization with currently available and tractable flame propagation and extinction theory. These data are also expected to provide new standards for the evaluation of fire hazards in particle suspensions in both Earth-based and Space-based applications. Both terrestrial and Space-based fire safety criteria require the identification of the critical concentrations of particulate fuels and inerts at the flame extinction conditions.

The Particle Cloud Combustion Experiment (PCCE) employs a circular array of flame tubes. Within each flame tube, a uniform quiescent cloud of particles (of selected stoichiometry) is to be suspended in near zero-gravity. The successful establishment of these initial conditions is essential to the successful observation of well-defined flame propagation and extinction processes. Cloud preparation and flame observation elements include: acoustic sources to promote macro-mixing; arrays of weak α-particle sources to prevent significant par-

ticle-particle agglomeration and particle-wall attachment; arrays of optical sources and detectors to measure particle cloud concentrations and flame propagation rates; igniters, photographic recording of flame propagation and extinction phenomena, and associated electronic control and data acquisition and storage devices. Once a suitably uniform and quiescent particle cloud is established in a flame tube, ignition, flame propagation and extinction characteristics are examined through use of photographic and other optical means.

Fuel particulates to be studied in the PCCE include lycopodium, coal, cellulose, and a number of inerts. Lean flammability limit determination is particularly important and is needed for both fundamental and applied purposes. The long mixing and combustion times for lean flammability limit studies are expected to require STS experimentation. Flame propagation studies of fuel-rich mixtures involve shorter mixing and combustion times and selected data of this kind may be obtained through use of ground-based facilities (e.g., flame propagation studies in airplane-established Keplerian trajectories).

Completed and ongoing studies support the PCCE effort. These have been performed in various ground-based facilities and include studies of: (1) premixed, stabilized lycopodium-air flames under conditions of near zero gravity as well as upward (g=+1) and downward (g=-1) flame propagation in normal gravity.

(2) particle cloud mixing methods, with provision for inhibition of particle-particle and particle-wall attachment processes.

(3) effects of vaporization-pyrolysis endothermicities and radiation-conduction transport on flame propagation and extinction characteristics.

Observations and deductions include the following: Stabilized, upward flame propagation (g=+1) is much more stable than downward flame propagation (g=-1). Omnidirectional radiative losses from lycopodium-air flames are much larger than conductive losses to the cold boundary. Flame structures for the three cases ($g=0, \pm 1$) are substantially different. Additionally, acoustic mixing methods, combined with distributed α-particle sources have been uniquely successful in assuring that planned and optically characterized suspensions of particulates (in air) are meaningful. The success of these methods is essential for the proper establishment of a quiescent cloud in any given flame tube of the PCCE apparatus.

1. INTRODUCTION AND BACKGROUND

The characteristic flame propagation and flame extinction processes sustained by a uniformly premixed, quiescent fuel and oxidizer are of central interest in the fundamental and applied combustion sciences. Treatises on Fire Safety for gaseous systems feature experimental data describing the range of fuel-oxidizer ratios within which quasi-steady flame propagation can (or cannot) occur (Ref. 1). Corresponding combustion theory attempts to describe the flame's structure, its propagation speed, the extinction process, and other conditions that may limit quasi-steady flame propagation (2). Fundamental to this experimental and theoretical correspondence is the requirement that the unburned combustible medium is initially quasi-steady. For premixed combustible gaseous systems, initial spatial and temporal uniformity of a combustible system's chemical, transport, and thermophysical properties is easily achieved, prior to combustion experimentation. At normal gravitational conditions, the corresponding quasi-steady requirements for particulate fuel clouds is not achieved (3-6). Accordingly, the extensive body of experimental observations characteristic for premixed gaseous combustion (autoignition, ignition, laminar flame propagation, extinction, oscillatory oxidation, and other phenomena) is not matched by a corresponding body of combustion data characteristic for initially quasi-steady premixed particle clouds. At normal gravitational conditions, uniform, quiescent particle clouds cannot be established because:

(1) Gravity causes the sedimentation of particles of significant size, thereby rendering spatial and temporal uniformity of a quiescent fuel particle cloud impossible.

(2) Mixing-induced turbulence and secondary flows, used to suppress sedimentation and to create uniform particle clouds, imply ill-defined transport properties. Such mixtures sustain the problems of item (1) when particle-uniformity-promoting stirring ceases.

(3) Fuel-oxidizer ratio fluxes through freely propagating flame fronts are functions of the gravity vector.

The systematic experimental study of freely propagating flames through clouds of uniform, quiescent particulates is thus not feasible at normal gravity. However, premixed particle cloud flames have been stabilized on burners and studied at normal gravity.

Premixed coal-air flames have been stabilized on burners and their properties in the upwards propagation mode observed (7-9) at normal gravity. More recent experiments with burner-stabilized premixed lycopodium-air flames have been carried out in upwards propagation (g = +1), in downwards propagation (g = -1) and in reduced gravity ($g \simeq 0$). These latter studies (10,11) show that the stability and structures of these three flame propagation modes are substantially different. Premixed, stabilized particle cloud flame characteristics are related to those for freely propagating flames. However, burner-stabilized flame propagation rates and existence limits depend importantly on experimentally predetermined flow and burner conditions. Freely propagating flames (sustained by initially quiescent, uniform combustible media) display characteristic flame speeds and existence limits. Thus, it is the limiting, fuel-lean concentrations of freely propagating flames that are associated with the "lean flammability limit" for any given premixed fuel-oxidizer system. (1,2,12).

In the neighborhood of lean flammability limit fuel concentrations, normal gravity buoyancy effects on the slowly propagating flame structures are most pronounced. This is widely observed for premixed, freely propagating gaseous flames (1,12-14). It is observed for both stabilized and for freely propagating (4) particle cloud flames. Oddly enough, stabilized premixed gaseous flame studies analogous to those done recently (at $g = 0, \pm 1$) for particle clouds (10,11) have not been reported. Nevertheless, the experimental combustion literature shows that normal gravity buoyancy effects are most pronounced for the cases of near lean limit fuel concentrations. This is observed for premixed gaseous systems as well as for premixed particle cloud flames. It is observed for burner stabilized as well as for freely propagating flame systems.

Fundamental flame theory seeks to describe flame structure, flame propagation speeds, and flame existence limits (2,15-21). Currently tractable fundamental flame theory generally neglects gravitational (and other body force) effects of flame propagation characteristics (2,15-21). Heavily truncated phenomenological theories are generally used to characterize experimental flame propagation and extinction data where buoyancy plays a substantial role (12,13).

For premixed flame systems in general, the available $g \simeq 0$ theoretical formulations do not correspond satisfactorily to the available $g = \pm 1$ experimental observations, for freely propagating flames sustained by near-lean-limit fuel concentrations. For premixed particle cloud flames, sedimentation as well as buoyancy effects further degrade the correspondence between $g = \pm 1$ experimentation and $g \simeq 0$ theory.

The studies described in this paper are concerned with understanding the experimental behavior of particle cloud flame propagation and extinction processes under reduced gravity conditions where sedimentation and buoyancy effects do not significantly modify the underlying $g \simeq$ zero combustion processes. Such experimental observations are associated with initially quasi-steady, defined combustible particle clouds. These experimental data may then be utilized, together with existing fundamental flame theory, to help provide an understanding of the underlying $g \simeq 0$ flame processes of interest. Understanding of these underlying $g \simeq 0$ flame propagation and extinction characteristics are needed as a basis for understanding general particle-cloud flame processes, including the effects of gravitational, transport, compositional, and other combustion parameters.

2. GRAVITATIONAL EFFECTS AND THE PARTICLE CLOUD COMBUSTION EXPERIMENT

The principal objective of the Particle Cloud Combustion Experiment (PCCE) is to provide flame propagation rate and extinction condition data for quiescent uniform fuel particle clouds. At normal gravity, particle sedimentation processes compromise our ability to properly prepare a combustible system for meaningful study of freely propagating flames and their limiting conditions for propagation. During combustion experimentation, buoyancy effects (as well as continuing sedimentation processes) further compromise our ability to understand the experimental observations (3-6,10-14). An examination of the character and magnitude of these gravitational effects is useful. Normal gravity difficulties as well as the unique research opportunities afforded by reduced gravity are thereby characterized.

Particles of initial interest in this investigation have maximum densities (~ 1.35) and maximum diameters ($\sim 70\mu m$) such that their settling speeds, at normal gravity, are in the Stokes regime. In this regime, the particle settling speed (in air) is given by

$$V_t = gr^2 \left[\frac{2}{9}\right]\left[\rho_p/\mu_g\right] \qquad (1)$$

where g is the acceleration due to gravity, r the particle diameter, ρ_p the particle density and μ_g the gas (air) viscosity. The first fuel particulate under study is the lycopodium spore, which has a mean diameter of about 27μm and a density very close to unity. Some properties of lycopodium are given in Table (1). Pocahontas coal particles (also to be studied) have a density that is about one third higher than that for lycopodium.

At normal gravity, lycopodium has a settling speed of about 3 cm/sec. If one attempts to mix lycopodium with air in a 5 cm. i.d. tube (classically, the inside diameter of a flame tube selected for flammability limit measurements) (1), to create a uniformly mixed cloud, the quiescent uniformity criterion for the combustion experiment cannot be met. Mixing-induced turbulence and secondary flows must be allowed to decay, prior to flame initiation (ignition occurs at one end of a 75 cm. long flame tube). The unburned combustible medium must display time invariant properties, prior to arrival of the flame front. Near fuel-lean flammability limits (the minimum fuel-air ratio capable of supporting quasi-steady flame propagation), flame speeds of the order of 10 cm/sec., or less, may be characteristic. Any reasonable criterion of both quiescence and uniformity

Lycopodium Spore Diameter		
Major Axis	:	30 $\mu m \pm$ 1.5 μm
Minor Axis	:	25 $\mu m \pm$ 1.5 μm
Stoichiometric Ratio	:	124 mg / liter
Combustion Enthalpy	:	30.25 Mj / Kg
Density		
Single Particle	:	1015 Kg / m^3
Bulk Density	:	400 Kg / m^3
Adiabatic Flame Temperature	:	1975 ^oK
Analyais		
Carbon	:	65.8 %
Oxygen	:	21.9 %
Hydrogen	:	9.6 %
Nitrogen	:	1.2 %
Sulphur	:	0.2 %

Table I : Some Properties of Lycopodium Particles.

cannot be met. Post-mixing periods needed to achieve quiescence have been estimated to be of the order of 10 seconds, for energetic acoustically-induced mixing processes. Minimum time requirements for maintenance of a quiescent cloud, prior to flame front arrival, is of the order of 10 seconds, or more. If the cloud of vigorously mixed particles is to be allowed to settle (or drift) by no more than 10 percent of a tube diameter during a total experimental time of some 50 seconds, utilization of equation (1) implies the need for a reduced gravity environment (g^*) of about $10^{-3} g_0$ to $5 \times 10^{-4} g_0$ where g_0 is the acceleration due to normal gravity. It is clear that mixing of lycopodium (to uniformity) in reduced gravity is an easier and shorter task than mixing attempts at g_0. This requirement for a reduced gravity environment is one of three shown in Table (2).

Another normal gravity obstacle to achievement of the experimental objectives relates to the effective number of particulates, consumed by a flame front which propagates upwards (g_0 = +1) or downwards (g_0 = -1) at normal gravity. Even if the particle cloud were uniform and quiescent (at normal gravity) the particle number swept out per unit time by a given quasi-steady flame front (propagating upwards or downwards) is different. The effective concentration of such a flame front is given by (4)

$$c^* \approx c_0 \left[1 \pm \frac{V_t}{U_f} \right] \qquad (2)$$

where c^* is the effective concentration, c_0 the actual concentration, V_t the settling speed, and U_f the flame speed. The positive sign corresponds to upwards propagation and the negative sign corresponds to downwards propagation. The upwards propagating front enjoys an enriched fuel concentration. The downwards propagating front experiences a depleted fuel concentration. This effect is particularly troublesome for large dense particles and for the very slow flames anticipated in the neighborhood of flammability limits. For example, a lycopodium-air flame speed of 3 cm/sec., observed in upwards propagation would correspond to an enriched particle concentration of $c_+^* \sim 2c_0$. The same flame speed in downwards propagation is a physical impossibility. In the latter case $c_-^* \sim 0$. Here again, use of the reduced gravity environment allows the imposition of effective limits on the difference between c^* and c_0, regardless of the direction of the gravity vector. If we require that $(V_t/U_f) \leq 0.02$, we find that the required range of reduced gravity conditions is of the order $g_* \approx 10^{-2} g_0 - 10^{-3} g_0$. This requirement for a reduced gravity environment is one of three shown in Table (2).

Another normal gravity obstacle to achievement of an important experimental objective relates to the effects of buoyancy in flames. These effects are well-known for purely gaseous flames (1,12-14) and are also observed for particle-cloud flames. Lovachev (12) has discussed the relation between a characteristic time and other parameters

1	Reaction zone's effective concentration is to be kept close to actual: where $C^* = C_0 (1 \pm V_t / U_f)$ and $V_t / U_f \leq 0.02$	$\boxed{g^* \approx 10^{-2} g_0 - 10^{-3} g_0}$
2	The dispersed cloud is to be restricted to small drift during a 50 second combustion process, where $\delta \approx 0.5$ cm. and $\rho = 1.0$ gm/cc	$\boxed{g^* \approx 10^{-3} g_0 - 5.0 \times 10^{-4} g_0}$
3	Buoyancy-induced flows due to post-reaction zone products are to be inhibited during the combustion process. $[t_s^3 g^2 / \nu] \approx$ constant Ref. : Lovachev, Comb. & Flame, 20, 259 (1973)	$\boxed{g^* \approx 10^{-2} g_0}$

Table 2: Experimentally Required g-Values.

for hot combustion product buoyancy effects on premixed flame propagation rates. His studies lead to the relation

$$\frac{t_k^3 g^2}{\nu} \approx \text{constant} \qquad (3)$$

where t_k is the time (after ignition) necessary for the development of significant buoyancy effects on flame propagation, g the gravitational constant, and ν the kinematic viscosity. The characteristic group of equation (3) was developed through observation of hot product buoyancy effects of premixed gaseous flames as a function of pressure, at normal gravity. Lovachev finds that an ambient pressure of one-tenth atmospheric is adequate for virtual suppression of this buoyancy effect. Based on the Lovachev data (12) and a conservative estimate of some 50 sec.-100 sec. needed for a particle-cloud combustion experiment at reduced gravity, it follows that a value of $g^* \approx 10^{-2} g_0$ is needed to achieve about the same buoyancy-suppression effects for particle-cloud flames at reduced gravity. This requirement for a reduced gravity environment is one of three shown in Table (2).

Finally, we note a flame reaction zone buoyancy effect whose significance has not yet been evaluated. It has been noted (14) that the reaction zone ratio of the gravitational to pressure terms for a flat freely propagating gaseous flame is given by the ratio

$$\frac{(\rho_1 + \rho_2)\, gh}{2\,(p_2 - p_1)} = \sigma \qquad (4)$$

where ρ_1 and ρ_2 are the respective densities downstream and upstream of the reaction zone, h the reaction zone depth, and $(p_2 - p_1)$ is the pressure drop across the reaction zone. The reaction zone thickness varies inversely with flame speed. Near the flammability limits, it is expected that (h) may become a relatively large value. Inasmuch as the near-lean-limit flame speed for experiments of interest (in this study) are not known, the value of σ is not known and its possible significance cannot be fully assessed. However, the observations (12) that led to equation (3) suggest that the reaction zone buoyancy effects are no more significant than the combustion product buoyancy effects, for the range of stoichiometries studied and reported in reference (12). A plot of (σ) versus equivalence ratio for Methane-air flames in shown in reference 14.

Based on the above cited considerations, it is concluded that gravitational conditions of the order of $g^* = 10^{-3} g_0$ are adequate to fulfill virtually all requirements for suppression of sedimentation and buoyancy effects.

3. PARTICLE CLOUD COMBUSTION EXPERIMENTS

The principal objectives of the microgravity experimental program are to obtain flame property and flame extinction limit data for a variety of premixed, quiescent two-phase combustion systems under near zero gravity conditions. In a previous section, the essential need for reduced gravity conditions was discussed. In subsequent parts of this report, ongoing complementary experimental and theoretical studies are discussed. We here discuss the principal features of these particle cloud combustion experiments as well as the needed use of NASA's reduced gravity facilities.

It is anticipated that several of the NASA reduced gravity facilities must be employed to help gather the scientific data required. The study of extinction phenomena and flame propagation rates of fuel-lean systems requires both the long reduced gravity time and the low values of the gravity levels offered by STS. Near the lean flammability limits, flame speeds are at their slowest (perhaps significantly less than 10 cm./sec) and the rate of change of flame speed with fuel concentration is at its highest (9-14). Accordingly, mixing times and flame propagation times associated with a 75 cm. long flame tube are expected to require STS conditions. However, the higher flame propagation rates of fuel-rich mixtures (which could be studied in STS) may also permit the collection of needed scientific data in ground-based facilities (e.g., airplane flights in Keplerian trajectories).

Experiments to be studied emphasize the following features:

(1) Establishment and certification of an adequately quiescent, uniform particle cloud in a 5 cm. i.d. tube, for purposes of measuring the characteristic flame propagation rates and extinction conditions.

(2) Determination of the characteristic lean extinction limits for such systems requires a series of experiments, each corresponding to a different stoichiometry.

(3) Several prototypical particulates are to be studied. The first of these is to be lycopodium. Particle size uniformity, batch reproducibility, low ash content, and compositional correspondence to coals of interest make this particle type our first choice for study. Subsequent studies of coal particulate clouds and of cellulose particulates are planned.

(4) For any experiment conducted, flame initiation, flame extinction, and end gas combustion sequences are time dependent processes. Photographic and localized flame detectors are needed to establish these properties as well as spatial regimes of quasi-steady flame propagation. These also establish flame structure properties. The same localized detector arrays are to be used to help characterize particle

cloud uniformity prior to ignition. Information on unsteady, multidimensional features of the phenomena is to be recorded photographically.

Detailed preliminary design information regarding these experiments is given in references 4,22,23. Nevertheless, it is important to identify here the experiments that are considered to be primary. The STS experiments are to be supported importantly by complementary ground-based studies. Both classes of studies involve the sequential study of varied concentrations of lycopodium suspended in an oxidizing gaseous atmosphere (air).

The study of low burning velocities (less than 10 cm/seconds) and the rapid changes in burning velocity in the neighborhood of lean flammability limits requires the long microgravity conditions of STS. For a range of fuel-rich flames, burning velocities are high, probably on the order of or greater than 15 cm/second. These flame speeds are relatively insensitive to stoichiometry variations, and extinction conditions are not approached. For such flames, ground-based facilities may be advantageously employed. For these latter studies, combustion times are less than 5 seconds which, under ideal aircraft microgravity conditions, then allows some 10 to 15 seconds for completion of a mixing process. Aircraft-based experiments also permit extensive involvement of an expert combustion scientist. The anticipated simple dependence of rich mixture burning velocity on stoichiometry permits the experimental study of these relationships with only a small number of experiments. The experimental test matrix for lean and near stoichiometric mixture experiments is shown in Table (3). The experimental test matrix for richer mixture experiments is shown in Table (4). The "Equivalence Ratio", shown in Tables 3 and 4, is a measure of the suspended particle concentration and is defined as the actual fuel-air mass ratio divided by the stoichiometric fuel-air mass ratio. It is anticipated that the experimental test matrix displayed on Table 3 requires the use of the STS. However, the experimental test matrix of Table 4 may be conducted in ground-based facilities, if acceptable cloud uniformity can be achieved in a short time period of microgravity.

The matrices of target equivalence ratios were selected on the basis of studies to date and the requirement that the equivalence ratio of the extinction limit be determined to an accuracy of about five percent.

It appears certain that these will lead to quasi-steady flame propagation. Although the lean extinction limit is not well known, it is expected that the lean flammability will be encountered for $\Phi < 1.0$ but above $\Phi \sim 0.5$. Accordingly, for lean mixture studies, we would choose to give first priority to the cloud stoichiometries shown in Table. 3.

In subsequent lean mixture experiments, it is expected that

Particle Type	ϕ_1	ϕ_2	ϕ_3	ϕ_4	ϕ_5	ϕ_6	ϕ_7	ϕ_8
• Lycopodium	1.3	1.2	1.1	1.0	0.92	0.84	0.78	0.72
** Lycopodium Plus Inert Particles	TBD	TBD	TBD	TBD	TBD	TBD	TBD	TBD
• 25 µm Pocahontas Coal	2.0	1.8	1.6	1.4	1.2	1.0	0.85	0.75
* 40 µm Pocahontas Coal	2.4	2.0	1.6	1.4	1.2	1.0	0.85	0.75
* 55 µm Pocahontas Coal	2.8	2.4	2.0	1.6	1.4	1.2	1.00	0.90
** 25 µm Pocahontas Plus Inert Particles	TBD	TBD	TBD	TBD	TBD	TBD	TBD	TBD
• 25 µm Cellulose	2.0	1.8	1.6	1.4	1.2	1.0	0.85	0.75

Table (3) : Experimental Test Matrix For PCCE Studies of Lean and Near-Stoichiometric Mixtures.

* Eight experiments are anticipated for each particle type. Each of these experiments is for a different stoichiometry.

** Two differnt fuel-to-inert mass ratios are to be investigated for each stoichiometry and fuel-to-inert mass ratios will be selected on the basis of results of earlier inert-free studies.

Particle Type	ϕ_A	ϕ_B	ϕ_C	ϕ_D	ϕ_E	ϕ_F
Lycopodium	1.3	2.0	3.0	4.0	5.0	6.0
Lycopodium Plus Inert Particles	TBD	TBD	TBD	TBD	TBD	TBD
25 μm Pocahontas Coal	2.0	3.2	4.0	5.0	6.0	7.0
40 μm Pocahontas Coal	2.4	3.2	4.0	5.0	6.0	7.0
55 μm Pocahontas Coal	2.8	3.2	4.0	5.0	6.0	7.0
25 μm Pocahontas Plus Inert Particles	TBD	TBD	TBD	TBD	TBD	TBD
25 μm Cellulose	2.0	3.0	4.0	5.0	6.0	7.0

Table (4) : Experimental Test Matrix For PCCE Studies of Rich Mixtures other particulate species (e.g., coal, cellulose) and larger particle sizes will be studied. Nevertheless, it is expected that a single sequence of experiments will be sufficient to determine flame propagation and extinction characteristics for any particle cloud type to accuracies of five percent or better.

Should subsequent flight opportunities permit, particle mixtures and particle size mixtures would be proposed for similar studies of flame propagation and extinction conditions. The roles of inert particulate constituents are of special fundamental interest in questions of industrial safety and dust flammability (Refs. 6,31).

An experimental test matrix for the proposed 56 STS tests is given in Table 3. Although it has been assumed here that there will be 8 tests per flight, design considerations may prescribe a smaller/larger number. Figures (1) and (2) give the apparatus schematics.

The rich mixture experiments proposed for aircraft tests (shown in Table 4) will permit the experimental study to determine kinetics of pyrolysis effects on flame propagation theory and to determine burning velocity behavior over a wide equivalence ratio range.

A number of generic apparatus, probe, fuel, data recorder and mission specialist support features are required by the experiments planned. Detailed arguments supporting the specification of these generic elements of the experimental program are given in the science requirements (Reference 24). The major science requirements and their possible implications regarding engineering design are discussed in the following subsections:

(1) A flame tube of 0.05 ± 0.002 meter i.d. is selected, by definition and by conventional practice, to help define flame propagation and extinction conditions for any quiescent fuel-air mixture. The tube must be long enough to assure observable quasi-steady flame propagation (within the extinction limits) and strong enough to safely contain all possible combustion processes. Preliminary experiments indicate that a tube length of about 0.75 ± 0.002 meters is suitable. Gold-coated tubes are necessary in order to adequately impose radial boundary conditions. In some cases, the electrically conductive properties of gold-coated tubes may also be necessary to suppress particle-wall adhesion. Aircraft studies of rich mixtures with both gold-coated and uncoated tubes will permit subsequent selection of tube coatings for STS flights.

(2) Test fuel particle types are lycopodium, selected coal, and cellulose. Lycopodium particle clouds are to be studied first.

(3) Particle cloud equivalence ratios are determined by the concentration of suspended particulates, rather than the total num- of particulates within the flame tube. Methods of reducing the

wall surface density of particulates have been identified. Even for extremely small wall saturation effects, wall surface densities must be known in order that suspended particulate concentrations can be determined. During in-flight experimentation, in situ determination of fuel-air equivalence ratio is to be derived from cloud optical attenuation measurements. To achieve adequate accuracy in the determination of flammability limits, a precision of ± 5 percent is required in the measurement of particle concentration. In this regard, optical probe source and detector windows may employ special wall saturation suppression techniques. The ± 5 percent precision requirement relates both to mean variation observed at any one optical attenuation station and the deviation from the mean, taken for the several optical attenuation measurements over a 10-second time period (during orbital flight).

(4) Preparation of the particle cloud in microgravity requires that particle mixing techniques be employed. Where vigorous acoustic mixing is employed, turbulence and secondary flow decay times are on the order of 10 seconds.

(5) The desired value of pressure for the experiment is p=1 atm, to directly relate to normal gravity experiments. Although the combustion processes under investigation do not vary substantially over a small initial pressure range in the neighborhood of p = 1 atm, it is important that pressure be constant during the combustion event. A pressure stability of approximately ± 0.2 psi/second is needed during the combustion event.

(6) Successful ignition of a quasi-steady flame is best achieved and identified when an energetic igniter (e.g., nitrocellulose) and an oversized ignition section (e.g., 7.5 cm. i.d. x 12 cm. long) are employed.

(7) Ambient temperature conditions should be stable during experimentation. Initial temperature should be 294°K $\pm$6°K with a stability of $\pm$2°K per minute during the experiment. A uniformity of $\pm$4°K over the tube length is required.

(8) Effective gravitational conditions should be small and steady. A g-level environment, of 5×10^{-4} g is desired with a stability of $\pm 1 \times 10^{-4}$ g. Higher g-levels up to 5×10^{-2} g can be tolerated in the aircraft experiments. It is recognized that the desired g-level may not be satisfied at all times on the STS. Therefore, for STS experiments, tests should be conducted during "quiet periods", and the synchronized g-level recorded at a frequency of 1 HZ during the entire experiment.

(9) Air composition should be "normal" and "dry" with 79 percent N_2 and 21 percent O_2.

(10) Near-field camera framing rates are to be 100/second in order to achieve sufficient resolution in time. It is desired to have a camera field of view such that the entire flame tube is contained therein. A full view of the tube's length, including

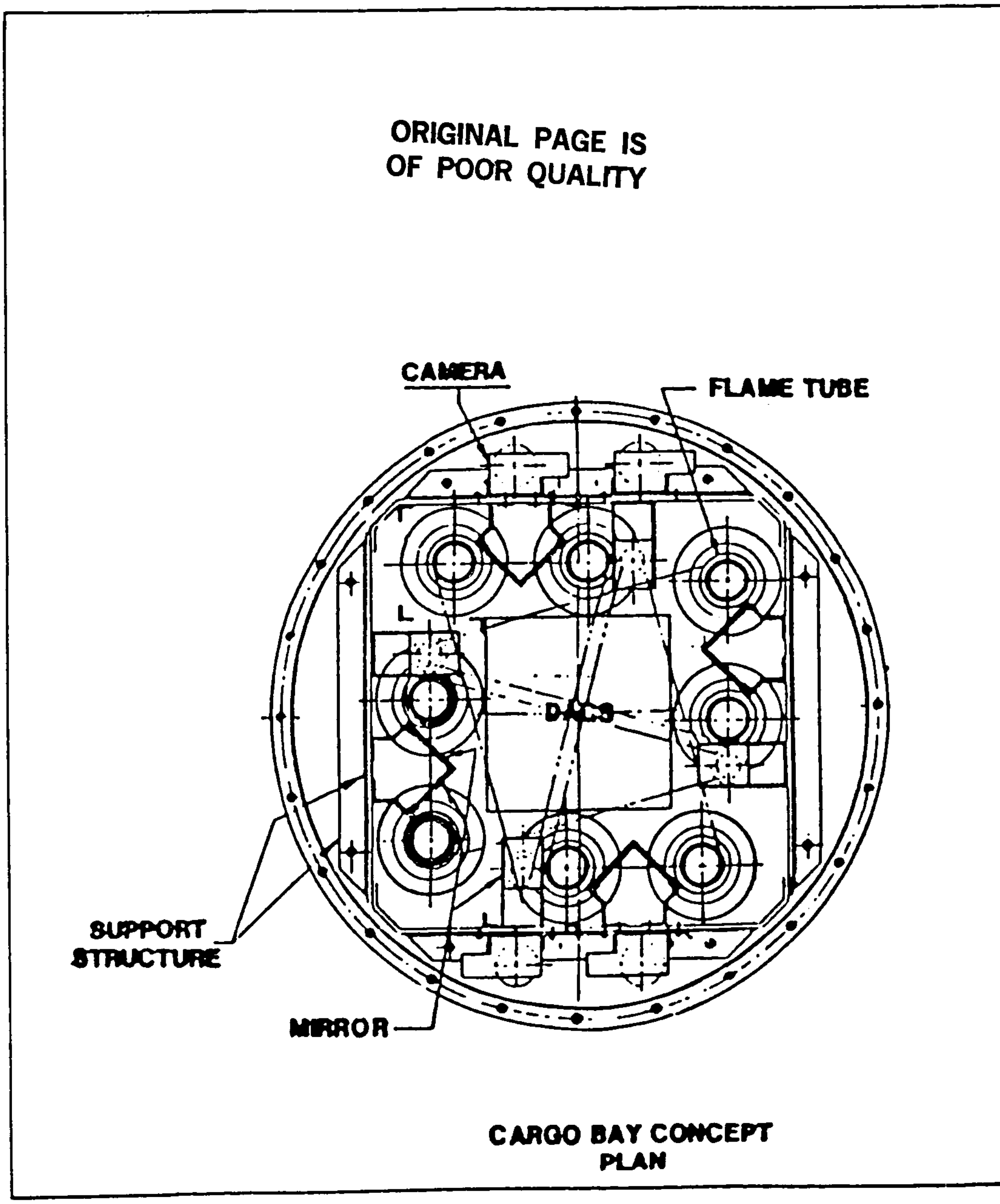

Figure 1: Flame Tube Assembly, Particulate Cloud Combustion Experiment.

ORIGINAL PAGE IS
OF POOR QUALITY

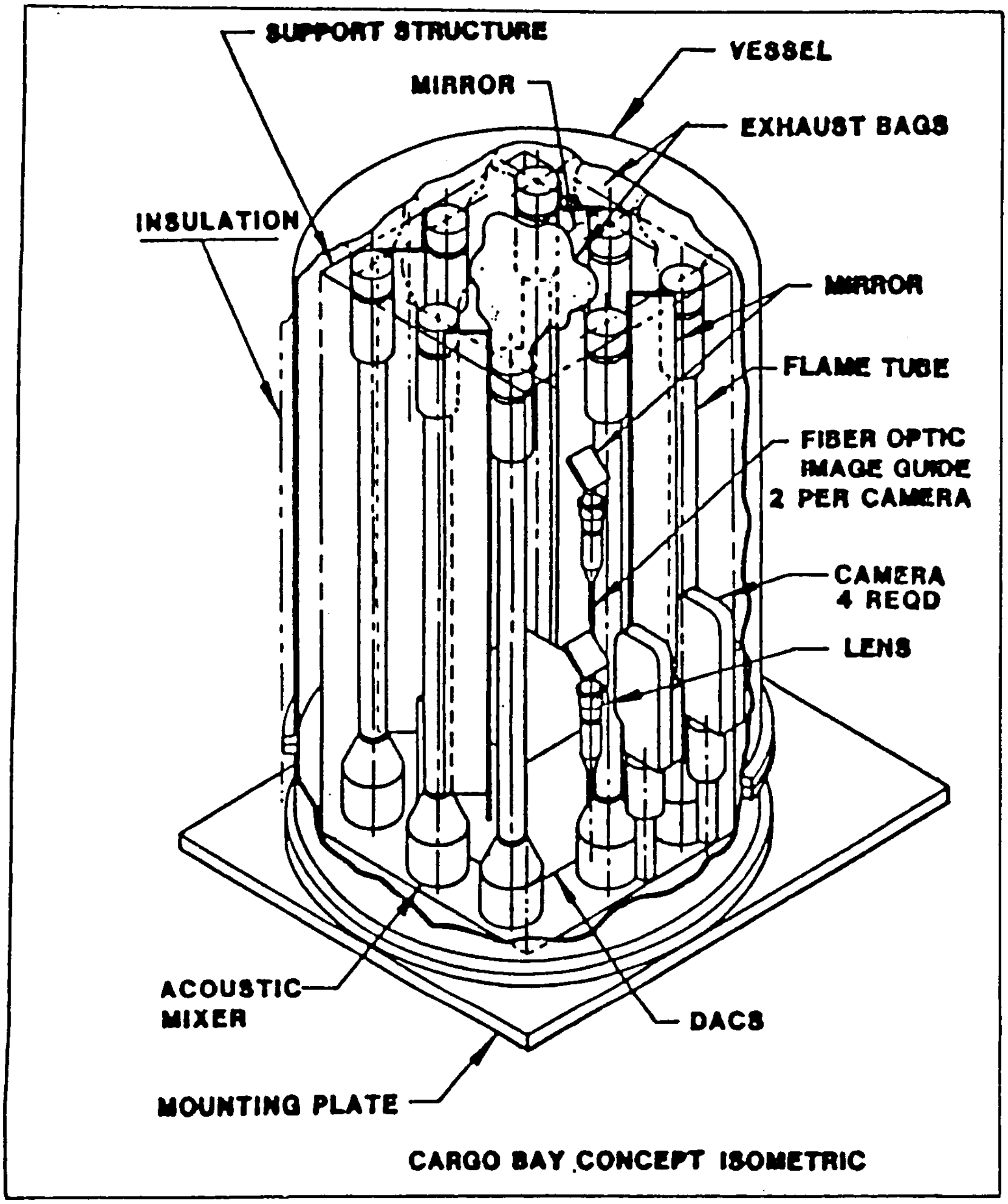

Figure 2: Cargo Bay Isometric, Particulate Cloud Combustion Experiment.

the ignition zone, must be within the field of view in order to adequately establish the steadiness properties of the flame. Film records must be synchronized to 0.005 seconds with the measured data.

(11) Mission specialist involvement, wherever possible, is desired. Three dimensional and time-dependent combustion effects may be observed by the mission specialist directly, and by long focal length motion picture photography (mission specialist operated). In the neighborhood of extinction limits, it is necessary to distinguish an inadequate ignition attempt from an extinguished flame phenomenon. A mission specialist (with minimal training) can provide invaluable help in making these observations. In the absence of a mission specialist, two photographic views of the flame tube, 90 offset (approximately) from each other is required.

The schematics of an individual flame tube assemby as well as an eight flame tube experimental arrangement is shown in Figures (1) and (2). Detailed summaries of the essential experimental apparatus requirements (for both STS experiments and aircraft flights) are given in reference (24).

4. SOME ADDITIONAL CONSIDERATIONS FOR PARTICLE CLOUD COMBUSTION EXPERIMENTS

A combustible system's experimentally-determined flammability limits, quenching limits and pressure limits are not completely independent of one another (1-4, 18-20). Comprehensive theoretical consideration of premixed flame existence limits is complicated by the substantial effects that gravitational conditions may impose. Tractable combustion theory is rarely more than one-dimensional. Free convective flows are generally three-dimensional. Upward ($g = +1$) flame propagation limits are generally wider than downward ($g = -1$) propagation limits. Findings to date show that this general combustion limit behavior obtains for both premixed gaseous and premixed particle cloud flames (10). This behavior also obtains for burner-stabilized (10) as well as for freely propagating flames (1-4, 10-14).

Recent studies (10) of burner-stabilized lycopodium-air flames have been carried out under all three conditions of interest, $g = 0, \pm 1$. A single, fully self-contained apparatus was used for all three gravitational conditions. The $g = 0$ data (10,11) were obtained at the NASA-Lewis Research Center 2.2 second drop tower facility. It may be surprising that no similar studies of other $g = 0, \pm 1$ stabilized flames have been reported, either for premixed gaseous systems or for premixed particle cloud systems. These recent findings (10,11) are derived from a burner apparatus capable of measuring heat transfer rates to the burner lip and capable of thermocouple probing of flame structure. Figure (3) is a schematic of the burner apparatus. Figure (4), (5), and (6) show the measured heat transfer rates from stabilized lycopodium-air flames to the burner lip. Figure (7) shows three flame temperature structures, for the three conditions, $g = 0, \pm 1$. The findings of references (10) and (11) for stabilized lycopodium-air flames appear to describe stabilized flame properties expected for both premixed particle cloud flames as well as for many premixed gaseous flame systems. These findings include the following:

(1) Omnidirectional heat losses sustained by the upstream flame structure at $g = 0$ are smaller than those for the other two modes ($g = \pm 1$) and results in substantially higher peak temperatures for the $g = 0$ case.

(2) Omnidirectional heat losses sustained by the upstream flame structure at $g = +1$ are smaller than those for the $g = -1$ case. This helps to account for the wider stability limits at $g = +1$ than are observed at $g = -1$.

(3) Buoyancy effects move the $g = +1$ flame closer to the cold boundary (than is the case for $g = 0$). Buoyancy effects move the $g = -1$ flame further away from the cold boundary. This helps to account for

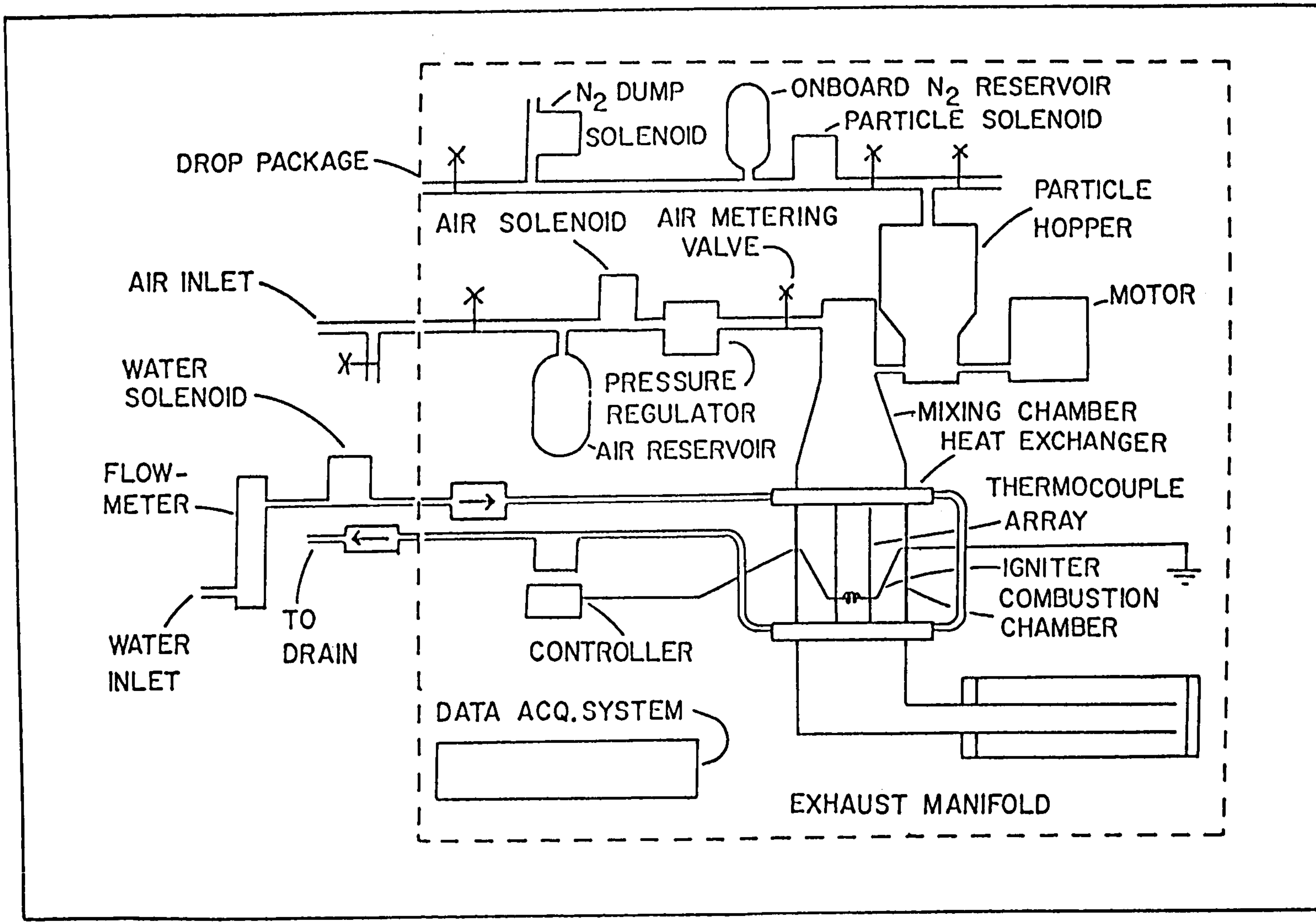

Figure 3: Schematic of the Burner Apparatus Used for the Study of Stabilized Lycopodium-Air Flames at g = 0, ± 1.

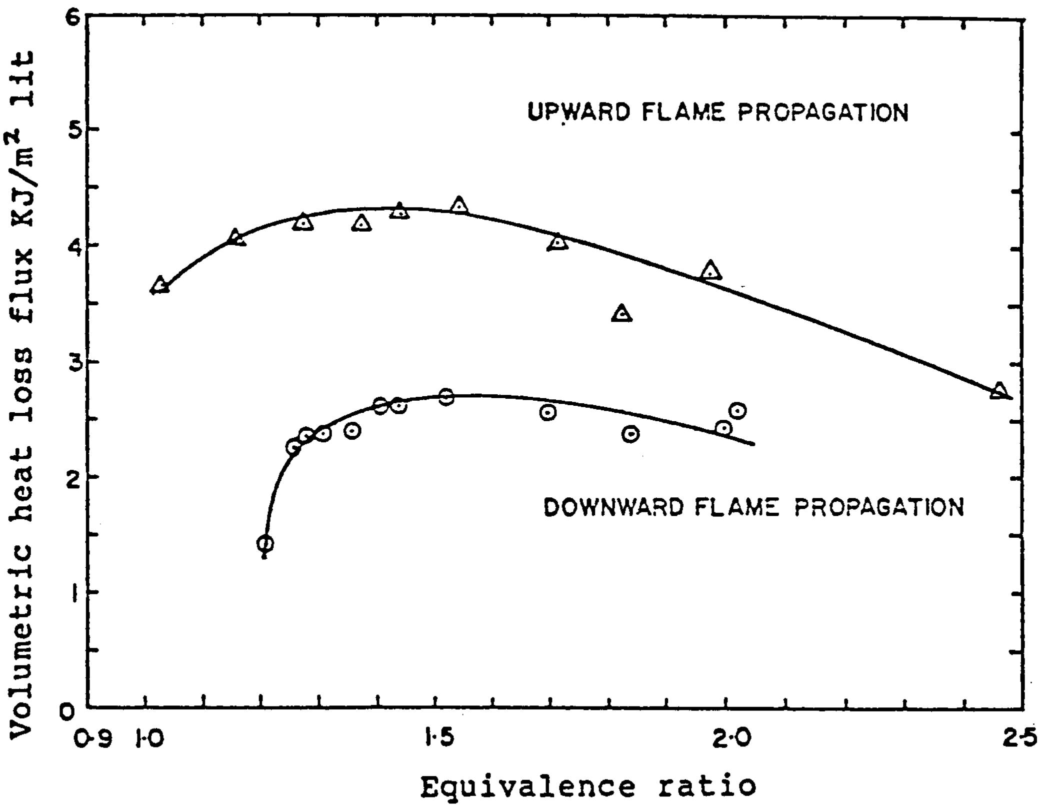

Figure 4: Volumetric Heat Loss Flux for Stabilized Lycopodium-Air Flames for a Flame Velocity of 17.1 cm/sec.

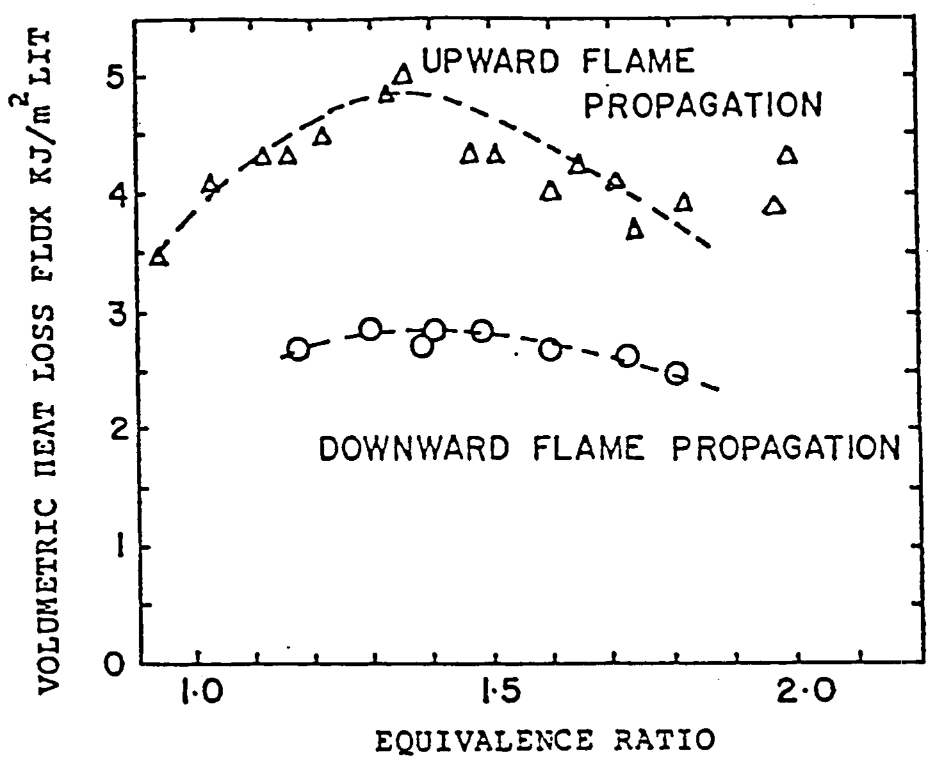

Figure 5: Volumetric Heat Loss Flux for Stabilized Lycopodium-Air Flames for a Flame Velocity of 13.9 cm/sec.

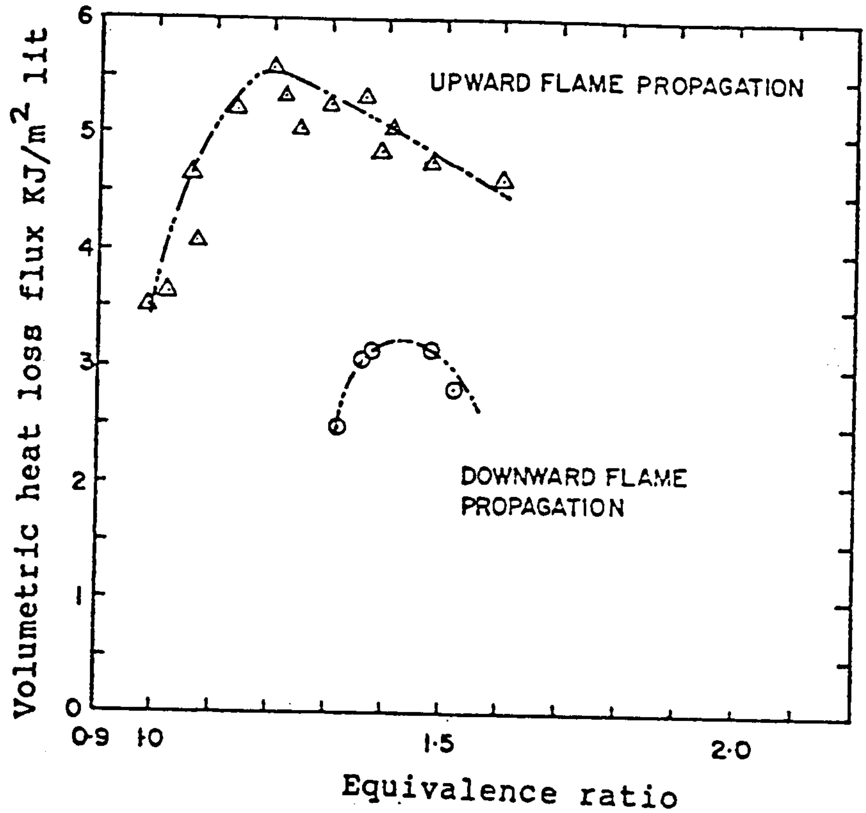

Figure 6: Volumetric Heat Loss Flux for Stabilized Lycopodium-Air Flames for a Flame Velocity of 11.4 cm/sec.

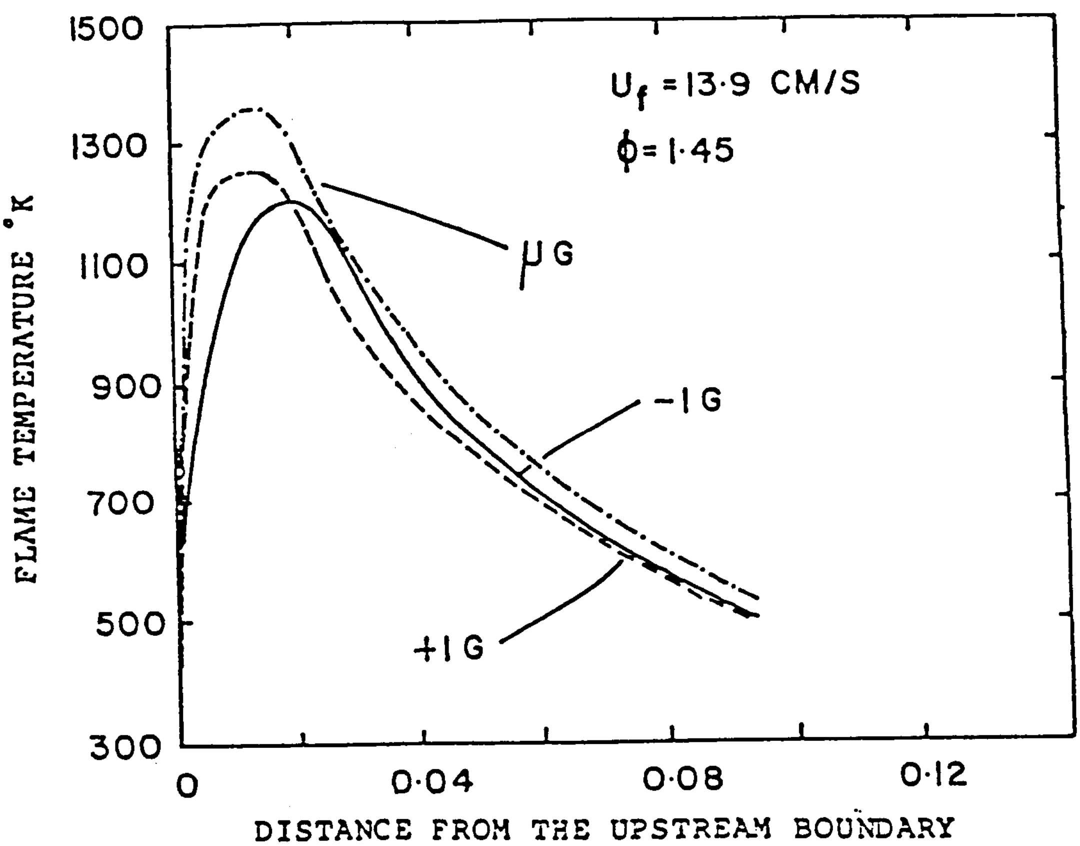

Figure 7: Measured Flame Temperature Profiles for Stabilized Lycopodium-Air Flames for Upward (+1g), Downward (-1g) and Microgravity Flames.

the larger cold boundary heat losses at $g = +1$ than are observed for $g = -1$.

(4) From (2) and (3), above, it follows that upstream transverse hear losses at $g = -1$ are larger than those at $g = +1$.

(5) From (2) - (4), above, it follows that large omnidirectional heat losses (rather than simply cold boundary heat losses) lead to narrowing of these flame stability limits.

(6) From (1) - (5), above, it follows that flame stability limit theory requires inclusion of omnidirectional heat loss rates. This general observation applies to both purely gaseous flames as well as to particle-cloud flames.

(7) The data show that cold boundary heat losses due to molecular conductive processes are a small fraction of the total heat loss rate to the cold boundary. These data, taken together with the observed temperature structures show that radiative omnidirectional losses are large and that gravitationally induced transverse losses can be significant.

Commonly employed non-adiabatic flame theory (2) (for stabilized flames) is generally one-dimensional and does not take account of gravitational effects. Recent theoretical efforts to consider gravitational effects (25) (in one dimension) and to consider two-dimensional flows (18,26) (without gravitational effects) represent promising starts to more general representations. Flame propagation and extinction theory recently employed for particle cloud combustion generally fails to account for transverse radiative losses (9,19,20, 27).

An interesting aspect of other studies of quasi-steady, burner-stabilized particle cloud flames concerns the effects of particle sedimentation. In general, the experimenter fixes the particle number flux that is to support the steady, stabilized flame. Cold gas particle concentrations are gravitationally influenced and are determined from

$$c_0 = \frac{\dot{n}''}{V_t \pm V_g} \qquad (5)$$

where $\dot{n}''$ is the number flux per unit area, V_t the settling speed, V_g the experimenter-imposed gas speed, and c_0 is the volumetric number concentration of particulates. The positive sign is used where settling velocities and gas velocities are parallel. The gaseous flux is given by

$$\dot{m}''_g = V_g \cdot \rho_g \qquad (6)$$

and the equivalence ratio (defined to be the fuel/oxidizer mass fluxes divided by the stoichiometric fuel/oxidizer mass flux ratio) is given by

$$\phi = \frac{c_0(V_g \pm V_t)}{\rho_g V_g M_p} \qquad (7)$$

where M_p is a (stoichiometric factor) constant. We may also define ϕ^* as the ratio of fuel to oxidizer mass densities divided by the stoichiometric fuel/oxidizer mass density ratio

$$\phi^* = \frac{c_0}{\rho_g M_p} \qquad (8)$$

For purely gas phase systems, ϕ and ϕ^* are identical. This is generally not the case for flowing particle cloud systems. The magnitudes and directions of V_t and V_g becomes exceedingly important as experiments are carried out near flammability limits (low values of V_g) and for large particle sizes (high values of V_t). These effects are generally important but not analyzed in the body of data provided by g = -1 burner stabilized studies. Consider, for example, the data derived from the very careful experimental studies reported in ref. (8). Those data (8) are shown in Figure (8) and show flame speed versus particle concentration for burner-stabilized pocahontas coal dust-air flames. Flow was downward, flame propagation upward. The apparatus used (8) was not capable of performing downward flame propagation studies. Left unresolved are the following experimental (and theoretical) issues: What downward propagating flame speeds would be measured, if the apparatus could accomodate the observations? What are the effects of sedimentation, particularly where flame speed values are lowest (and flame stability is marginal)? As one investigates larger and larger particle sizes, a particle size regime is reached where no flame propagation is observable in <u>downward</u> flame propagation ($V_g - V_t$) $\simeq$ 0. To what extent is flame extinction due to buoyancy effects? To what extent is this due to sedimentation effects? To what extent is this due to low volumetric vaporization-pyrolysis rates associated with increased particle size heat transfer effects? Clearly, mixed particle size, burner-stabilized flames are impossible to study at g = -1, where particle settling speeds are a significant fraction of the fundamental flame speeds.

Our forthcoming reduced gravity experiments (starting with Keplerian trajectories in aircraft) are planned (24) to include the use of both infrared reflective wall coatings and in other cases, infrared absorbing flame tube surfaces. Computational methods recently employed for two-dimensional, time-dependent reactive flows (21,28) show great promise for delineating characteristic flame details that are not derivable from steady state flame formulations. Time-dependent computational studies of particle cloud flames involving UCSD-NRL collaborative efforts have been initiated. We note that the constituative equations of particle cloud combustion are generally well known (2,8,9,10,19,20,27). Analytic and/or computational success rests heavily on wise selections of those physicochemical parameters that may significantly influence results -- and neglect of those physicochemical parameters that play insignificant roles. Particle cloud combustion experiments are needed to identify and assess the underlying combustion processes, phenomena, and parameters which are important.

5. PARTICLE CLOUD DISPERSION AND CHARACTERIZATION ISSUES

Fuel particle dispersion in a gas, for purposes of particle cloud combustion experimentation, has been carried out in a number of experiments (5,6,29,30). At normal gravity, these experiments are generally concerned with studies of ignition and explosion in turbulent particle clouds. Time for decay of turbulence and secondary flows is generally longer than the time during which sedimentation compromises the needed particle uniformity.

Joint UCSD-Lewis Research Center studies of mixing methods (to be used in reduced gravity environments) currently emphasize acoustically induced flows to assist in mixing and the establishment of particle cloud uniformity. A problem which appears important to all particle cloud combustion experiments ($g = 0, \pm 1$) concerns the consequences of triboelectrically-induced charge separation processes which derive from vigorous mixing. Charge separation processes sustained by dielectric particles in air can lead to unwanted effects such as the agglomerative growth of particle clusters and the attachment of particulate clusters to combustion chambers walls (22).

UCSD-Lewis Research Center studies have focused on methods of mitigating these unwanted effects. During vigorous mixing (by acoustic or other sources),charge neutralization can be promoted through use of ionizing sources. We have employed arrays of ionizing sources (the active source component is Polonium-210, a weak α-source). Studies to date show that during several minutes of vigorous mixing, particle-particle and particle-wall interactions can be controlled to achieve (22) the following two important objectives:

(1) The vigorously-mixed cloud of particulates remains essentially monomeric.

(2) Particle-wall attachment rates are small. Particle surface densities of the order of 1 particle per square millimeter have been achieved. This corresponds to no more than a one or two percent depletion of the particles to be contained in a flame tube's volume.

Figure (8) is a schematic of the test apparatus used to carry out the aforementioned mixing experiments. Figure (9) shows the arrangement of Polonium strip sources along the inside surfaces of the 15 cm. long by 5 cm. i.d. test chamber. Figure (10) shows the results of particle-particle agglomeration and particle-cluster wall attachment for three different test conditions. Where no ionizing sources were employed, Figure (10-a) shows a wall density of particles that is several orders of magnitude greater than that shown in Figures (10-b) and (11). The experiment that yielded the Figure (10-a) results was

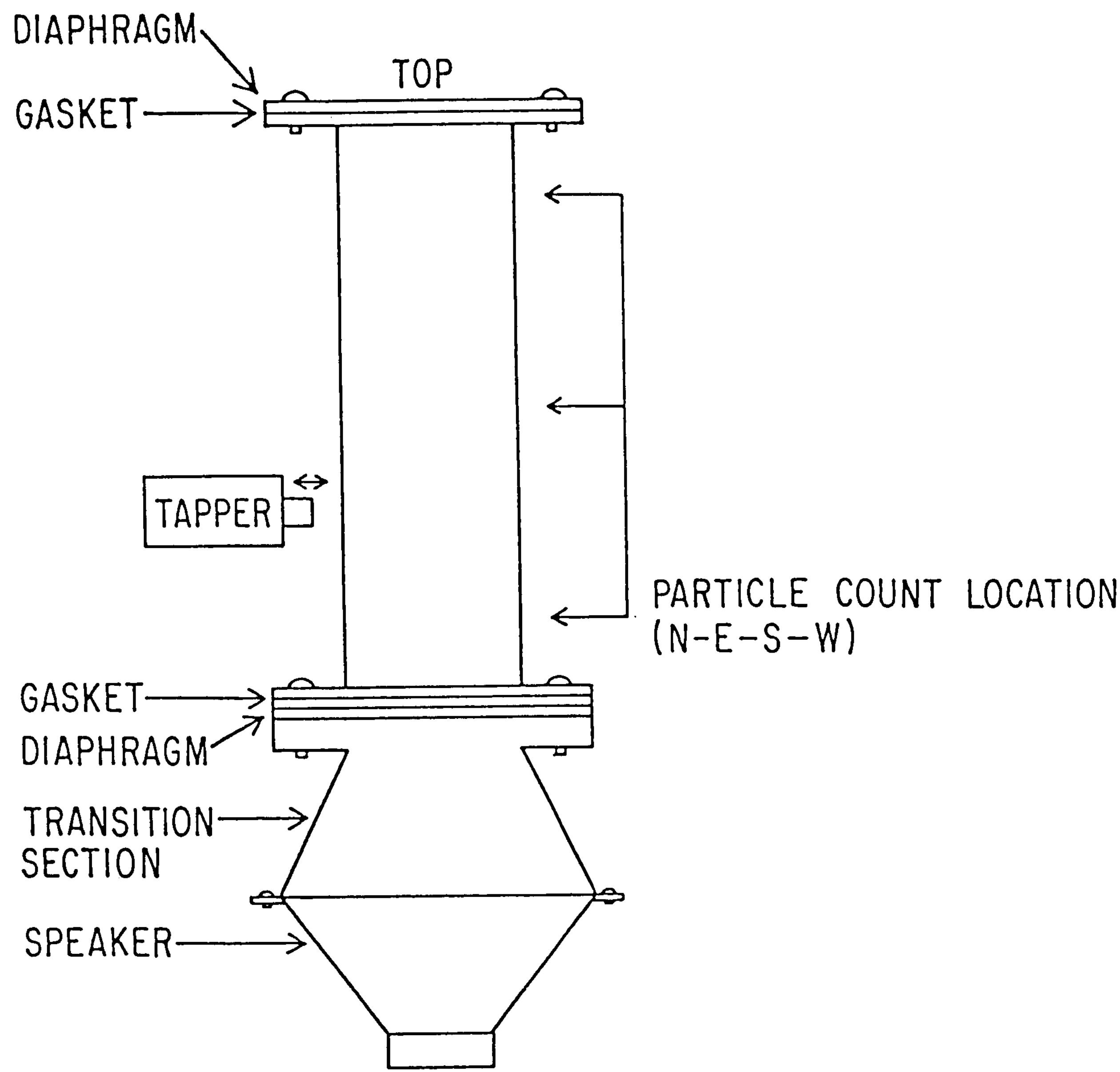

Figure 8: Diagram of Lycopodium Particle Adhesion Test Apparatus.

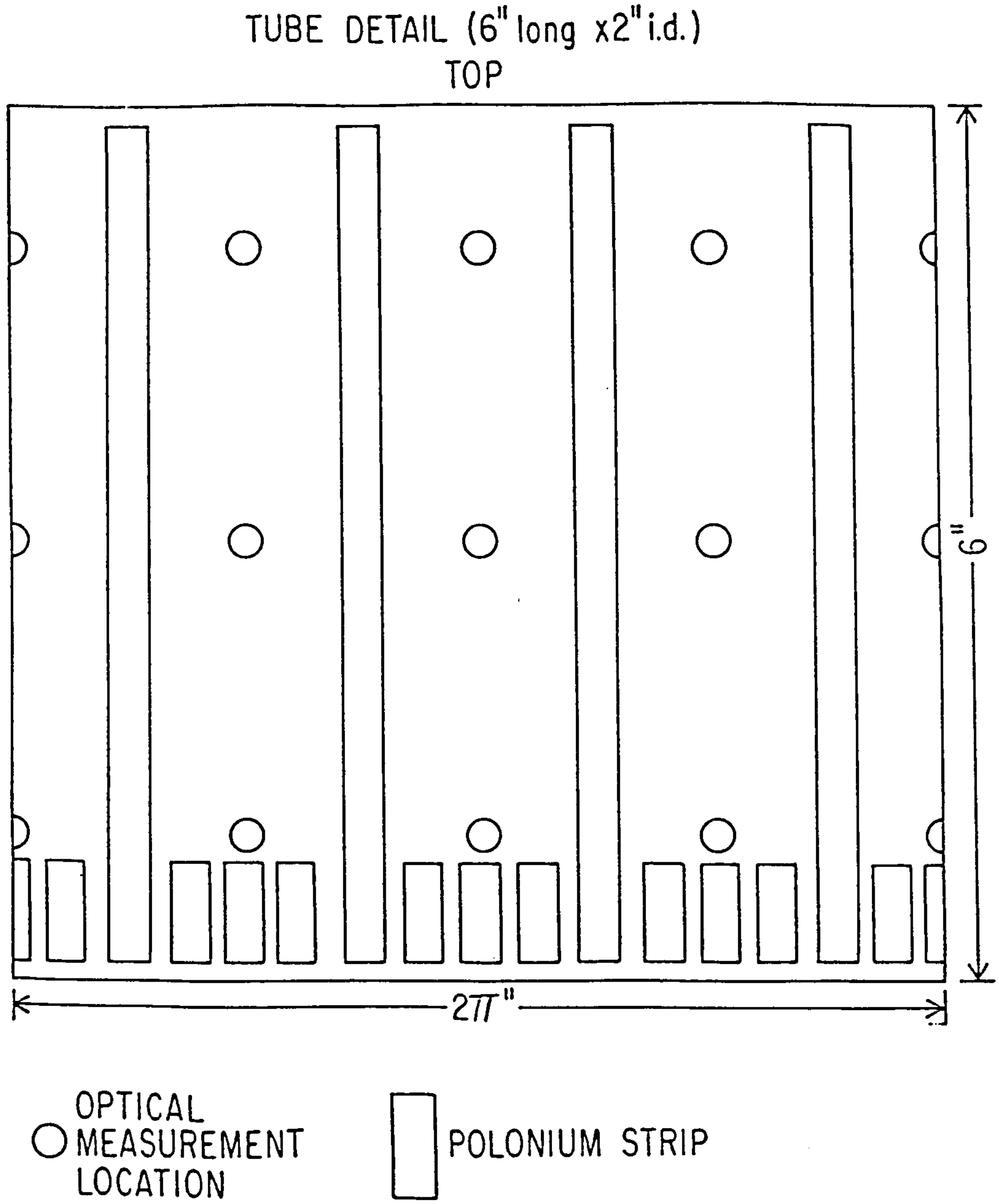

Figure 9: Test Apparatus Tube Detail Showing Wall Placement of Polonium 210 Strip Sources.

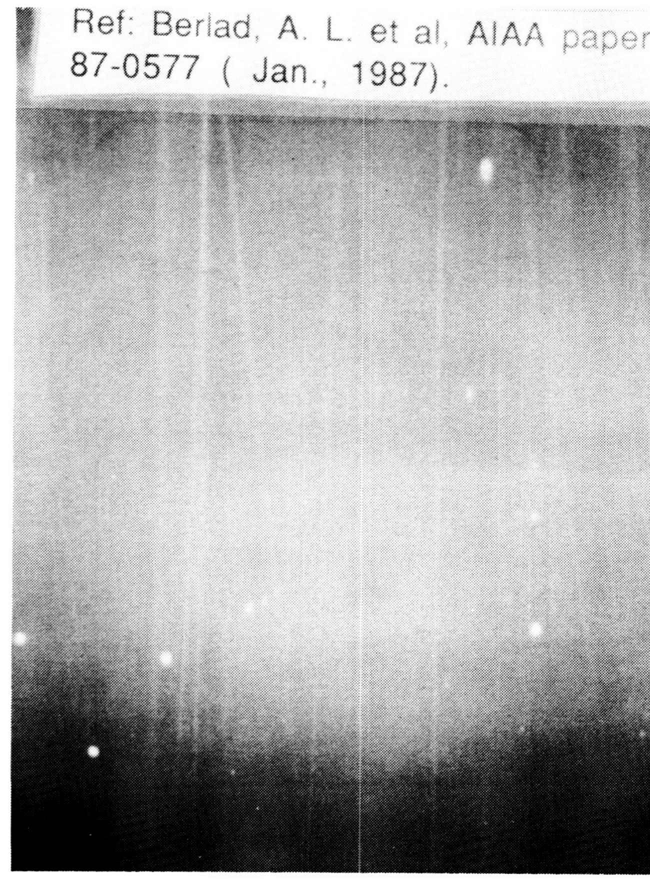

(a)
Radioactive Sources not in Use

(b)
Polonium-210 Sources in Use

Figure 10: Wall Particle Adhesion for a Gold Coated (ungrounded) Tube.

Mixing: 2.5×10^{-8} Kg Lycopodium at 13 W and 200 Hz for 60 seconds.

Figure 11: Wall Particle Adhesion for a Clear Lexan (ungrounded) Tube.

Mixing: 2.5×10^{-8} Kg Lycopodium at 13 W and 200 Hz for 60 seconds.

conducted without aid of ionizing strip sources. The Figure (10-b) and Figure (11) results derive from experiments with the Polonium-210-containing strips arranged along the inner surface of the test chamber. Further details concering these findings (as well as the dynmamics of particle-particle and particle-wall attachment/detachment processes) are given in reference (22).

It is important to note that the successful mitigation of particle-particle and particle-wall attachment processes is essential to all particle cloud experiments which involve vigorous mixing processes. This includes the body of normal gravity experiments reported previously (e.g., 6, 29,30), as well as our own reduced gravity experiments. It is not evident that previous studies have taken adequate account of mixing-induced agglomerative growth and cloud concentration depletion through surface attachment of particles. Although the use of ionizing sources to inhibit particle-wall attachment is well known, the technique appears not to have been employed previously in particle cloud combustion experiments.

6. LIST OF TABLES

7. LIST OF FIGURES

8. REFERENCES

1. Coward, H. F. and Jones, G. W.: Limits of Flammability of Gases and Vapors. U.S. Bureau of Mines Bulletin 503 (1952).

2. Williams, F. A.: Combustion Theory. 2nd edition. Benjamin Cummings (1985).

3. Berlad, A. L., Huggett, C., Kaufman, F., Markstein, G., Palmer, H. B., and Yang, C. H.: Study of Combustion Experiments In Space. NASA CR-134744 (Nov., 1974).

4. Berlad, A. L.: Combustion of Particle Clouds: in Combustion Experiments in a Zero-Gravity Laboratory, T. H. Cochran (Ed.). Progress in Aeronautics and Astronautics 73, 91 (1981).

5. Hertzberg, M., Conti, R. S., and Cashdollar, K. L.: Spark Ignition Energies for Dust-Air Mixtures: Temperature and Concentration Dependences. Twentieth Symposium (Int'l) on Combustion/The Combustion Institute 1984 (p.1681).

6. Palmer, K. N.: Dust Explosions and Fires. Chapman and Hall, London (1973).

7. Smoot, L. D., Horton, M. D., and Williams, G. A.: Propagation of Laminar Pulverized Coal-Air Flames. Sixteenth Symp. (Int'l) on Combustion, The Combustion Institute, 1976 (p. 375).

8. Horton, M. D., Goodson, F. P., and Smoot, L. D.: Characteristics of Flat, Laminar Coal Dust Flames. Combustion and Flame 28, 187 (1977).

9. Smoot, D. and Horton, M.: Propagation of Laminar Coal-Air Flames. Progress In Energy and Combustion Science 1, 235 (1977).

10. Berlad, A. L. and Joshi, N. D.: Gravitational Effects On The Extinction Conditions for Premixed Flames. Acta Astronautica 12, 539 (1985).

11. Joshi, N. D. and Berlad, A. L.: Gravitational Effects On Stabilized, Premixed, Lycopodium-Air Flames. Comb. Sci. & Tech. 47, 55 (1986).

12. Lovachev, L. A., et. al.: Flammability Limits: An Invited Review. Combustion and Flames 20, 259 (1973).

13. Levy, A.: An Optical Study of Flammability Limits. Proc. Roy. Soc., London A283, 134 (1965).

14. Hamins, A., Heitor, M., and Libby, P.A.: Gravitational Effects On The Structure and Propagation of Premixed Flames. IAF paper 86-279. International Astronautical Congress (1986).

15. Spalding, D. B.: A Theory of Inflammability Limits and Flame Quenching. Proc. Roy. Soc. A240, 83 (1956).

16. Berlad, A. L. and Yang, C. H.: On The Existence of Steady State Flames. Combustion and Flame 3, 447 (1959).

17. Essenhigh, R. H. and Csaba, J.: The Thermal Radiation Theory For Flame Propagation In Coal Dust Clouds. Ninth Symposium (Int'l) on Combustion/Combustion Institute (1963), p. 111.

18. Aly, S. L. and Hermance, C. E.: A Two-Dimensional Theory of Laminar Flame Quenching. Combustion and Flame 40, 173 (1981).

19. Mitani, T.: A Flame Inhibition Theory By Inert Dust and Spray. Combustion and Flame 43, 243 (1981).

20. Joulin, G.: Asymptotic Analysis of Non-Adiabatic Flames. Heat Losses Towards Small Inert Particles. Eighteenth Symposium (Int'l) on Combustion/The Combustion Institute (1981), p. 1395.

21. Kailasnath, K. and Oran, E.: Effects of Curvature and Dilution On Unsteady, Premixed Laminar Flame Propagation. NRL Report #5659 (1985).

22. Berlad, A. L., Joshi, N., Ross, H. and Klimek, R.: Particle Cloud Kinetics In Microgravity. AIAA Paper No. 87-0577 (1987).

23. Gat, N. and Kropp, J. L.: Summary of Activities On The Zero-Gravity Particle Cloud Combustion Experiment. Summary Report on NASA Contract NAS3-23254 (1983).

24. Berlad, A. L., Burns, R. J. and Ross, H. D.: Science Requirements For The Particle Cloud Combustion Experiment (Revision A). NASA document (Jan., 1987).

25. Clavin, P. and Nicoli, C.: Effects of Heat Losses On The Limits of Stability of Premixed Flames Propagating Downwards. Combustion and Flame 60, 1(1985).

26. Oran, E. S., et. al.: A Study of Detonation Structure: The Formation of Unreacted Gas Pockets. Nineteenth Symposium (Int'l) on Combustion/The Combustion Institute (1982), p. 573.

27. Smoot, L. D., Horton, M. D., and Williams, G. A.: Propagation of Laminar Pulverized Coal-Air Flames. Sixteenth Symposium (Int'l) on Combustion (1976), p. 375.

28. Oran, E. S. and Boris, J. P.: Numerical Simulation of Reactive Flows. Monograph, To Be Published (1987).

29. Nagy, John, et. al.: Explosibility of Miscellaneous Dusts. U.S. Bureau of Mines Report on Investigations 7208 (Dec., 1968).

30. Hertzberg, M., Cashdollar, K. L., Zlochower, I., and Ng, D. L.: Inhibition and Extinction of Explosions In Heterogeneous Mixtures. Twentieth Symposium (Int'l) on Combustion/The Combustion Institute, (1984), p. 1691.

31. Berlad, A. L.; On Characterization and Mitigation of Combustion Hazards Involved in the Handling of Particulate Materials. Invited Review. Drying Technology 3, 123 (1985).

N89-20312

Scientific Support for an Orbiter Middeck Experiment on Solid Surface Combustion

Robert A. Altenkirch (PI), M. Vedha-Nayagam (Postdoctoral Fellow), and Nataraj Srikantaiah (Graduate Student)
Department of Mechanical Engineering
University of Kentucky
Lexington, KY 40506

Abstract

The objective of the current study is to determine the mechanism of gas-phase flame spread over solid fuel surfaces in the absence of any buoyancy or externally imposed gas-phase flow. Such understanding can be used to improve the fire safety aspects of space travel by providing information that will allow judicious selections of spacecraft materials and environments to be made.

The planned experiment consists of measuring the flame spread rate over thermally thin and thermally thick fuels in a closed container in the low-gravity environment of the Space Shuttle. The Shuttle provides sufficient time for the spread process to be studied and to evolve to a steady state. Steady spread can be achieved only if the experimental time is long compared to the ratio of the gas-phase kinematic viscosity to the product of the spread rate and a velocity characteristic of the gas. Measurements consist of flame spread rate and shape obtained from two views of the process as recorded on movie film and surface and gas-phase temperatures obtained from fine-wire thermocouples. The temperature measurements along with appropriate modelling provide information about the gas-to-solid heat flux. Environmental parameters to be varied are the oxygen concentration and pressure.

In support of the proposed space-based experiments, ground-based experiments have been used to prove the sample ignition system and provide limited information about flame shapes and spread rates in the experimental time available in the droptower facilities at Lewis Research Center. Additionally, a theoretical modelling effort is being conducted to aid in elucidating the physics of the flame spread process.

Numerical computations of the theoretical problem appear to show that it is necessary to account for the fact that, with respect to the quiescent oxidizer, the flame is moving. In flame-fixed coordinates then, the flame sees a gentle forced flow of speed equal to the spread rate. Attempts to neglect this flow as being unimportant with respect to the flow established by the interfacial velocity appear to indicate that a consistent, steady-state coupling between the gas and solid phases is not possible under this circumstance. The relative flow is responsible for removing convectively the energy released by chemical reaction in the gas to allow the steady-state to be maintained.

Introduction

A gas-phase flame spreads over the surface of a solid, pyrolyzing combustible by tranferring heat, either through the gas or the solid, ahead of itself to raise the temperature of the virgin fuel to a pyrolysis temperature [1]. The characteristics of the spreading flame and the forward heat transfer depend on the gas-phase flow field in which the flame is embedded. In most flame spread studies, the flow field is established by natural (see, e.g., [2-4]) or externally imposed forced (see, e.g., [5,6]) convection superimposed on the flow resulting from the phase change at the fuel-gas interface. Little is known about the physics of the process as it would occur in a flow field established by the phase change alone.

The flow induced by flames spreading in the Earth's gravitational environment may be either in the same or opposite direction to that of spread depending on the direction of spread with respect to the Earth's gravity. In upward propagating flames, that is those oriented so that a component of gravity is in the direction of spread, the spread process is rapid and acceleratory [7]. The induced flow is in the direction of spread, and the hot combustion products form a plume that bathes the unburnt fuel, heating it by conduction and, if the optical depth of the flame is large enough, by radiation as well. In downward flame spread, buoyancy induces a flow of ambient fluid that opposes the spreading flame as shown in Fig. 1 where U_∞ is the speed of the induced flow. The result is that the forward heat transfer occurs either by heat conduction through the gas or solid (or both) [3,4]. Radiation heat transfer is usually unimportant because the flame, due to the buoyant flow, lies close to the fuel surface resulting in a small view factor. And, the convective motion cools the unburnt fuel rather than heating it.

Horizontally spreading flames possess some of the same characteristics as both downward and upward spreading flames do. Topside flames must spread into an opposing flow of oxidizer that is induced by the flame plume as in downward spread, but unlike downward spread, the flame plume extends above the pyrolyzing surface of the fuel to provide a favorable view factor for forward radiation heat transfer [8,9]. Underside flames induce a flow in the direction of spread. They tend to propagate unsteadily and race ahead of the topside flame [10,11].

Photographs of flames spreading over thin cellulose acetate sheets at nearly zero gravity show that these low-gravity flames are similar in appearance to downward spreading flames at normal gravity [12,13]. They do not exhibit a plume that precedes the leading edge of the flame as in upward spread, and the flames on both sides of the fuel bed look the same, as they do in downward spread, in contrast to horizontal spread. It is likely then that the physics of flame spreading in low gravity is more akin to that of downward spread in normal gravity rather than either upward or horizontal spread. Further support of this speculation is given by the fact that low-gravity spread rates are just less than downward spread rates at normal gravity, which in turn are lower than either horizontal or upward spread rates, upward ones being the highest [7,12].

Downward Flame Spread

Gas-phase conduction is the dominant mode of forward heat transfer in downward flame spread (and for spreading into a forced flow) for fuels that are heated across their entire thickness (thermally thin) downstream of the leading edge of the flame and also have a large ratio of the gas-phase conduction length (gas thermal diffusivity divided by opposing flow velocity) to the solid-phase forward conduction length (solid thermal diffusivity divided by flame spread rate). In this case, an increase in the strength of the buoyant flow can only cause the spread rate to fall. The reason for this is that the residence time of the fuel vapors near the leading edge of the flame is reduced relative to the time that the exothermic reactions require for completion so that the flame temperature drops, reducing the forward heat tranfer and hence the spread rate. This phenomenon can be expressed in terms of the Damkohler number, a ratio of the residence time to the reaction time. For large Damkohler number, the spread rate is unaffected by changes in the Damkohler number because sufficient reaction time is provided for the production of the highest temperature attainable. For small Damkohler number, the spread rate decreases as the Damkohler number decreases [3].

The dominant heat transfer mode depends on the Damkohler number for fuels that are thick enough so that they may or may not be heated across their entire thickness [4]. At large Damkohler number, the heated layer thickness in the fuel is small compared to the fuel's thickness (thermally thick), and the ratio of the gas-phase to solid-phase conduction length exceeds unity; heat transfer occurs then by gas-phase conduction.

Increasing the strength of the opposing flow does not change the flame temperature or the heat conducted upstream in the gas because the conduction length scale in the gas is the same parallel and normal to the fuel surface, but it decreases the heated layer depth in the solid. The reduced in-depth heating results in more of the forward heat transfer being available for vaporization with a concomitant increase in spread rate [4]. At small Damkohler number, as the flame nears extinction, nearly the entire fuel thickness is heated, and forward heat transfer is by solid-phase conduction [1,14]. Increasing the buoyant flow here decreases the flame temperature causing a reduction in the forward heat transfer and hence a reduction in the spread rate.

As is evident from the above discussion, the direction and strength of the gas-phase flow are of signal importance in establishing the spread rate. For downward spread, the character of the flow field and the physics of the process are reasonably well understood. The degree of this understanding is demonstrated by the success with which dimensionless downward flame spread rates, $\bar{V}_F$ where

$$\bar{V}_F = \frac{\rho_s C_s V_F \tau}{2^{1/2}\ k} \quad \left(\frac{T_v - T_\infty}{T_f - T_v} \right) \tag{1}$$

are correlated against a Damkohler number [3-5], $\bar{B}$, where

$$\bar{B} = \frac{B\ k\ m_{ox,\infty}}{M_{ox} C_p v_c^2} \quad \left(\frac{\bar{T}_f^2}{\bar{T}_a} \right)^3 \quad e^{-(\bar{T}_a/\bar{T}_f)} \tag{2}$$

The dimensionless spread rate $\bar{V}_F$ is a ratio of the actual heat transferred forward of the flame to the maximum that could be transferred if $\bar{B}$ were large and the flame were at its maximum temperature [3]. In the above, ρ_s is the solid-phase density, C_s is the solid-phase specific heat, V_F is the spread rate, k is the gas-phase thermal conductivity, T_v is the vaporization temperature, T_∞ is the ambient temperature, T_f is the flame temperature for adiabatic stoichiometric combustion, τ is the heated layer depth in the solid, B is the preexponential factor for an assumed second-order reaction, $m_{ox,\infty}$ is the ambient oxygen mass fraction, M_{ox} is the molecular weight of oxygen, C_p is the gas-phase specific heat at constant pressure, v_c is the characteristic, gas-phase velocity, which in Fig. 1 would be U_∞, and $\bar{T}_f$ and $\bar{T}_a$ are the flame and activation temperature, respectively, measured in the units of $\Delta H_c m_{ox,\infty}/iC_p$ where ΔH_c is the heat of combustion of gas-phase fuel, and i is the mass of oxygen needed to oxidize a unit mass of fuel. For thermally thin fuels, τ is the fuel bed half-thickness while for thick fuels, τ depends on v_c but is independent of the fuel bed thickness [4].

The expression for $\bar{V}_F$ above derives from a solution to the constitutive equations that govern flame spread into an opposing flow of oxidizer of uniform speed v_c when $\bar{B}\rightarrow\infty$ [6] such that $\bar{V}_F$ is unity. The parameter $\bar{B}$, with which $\bar{V}_F$ correlates for finite $\bar{B}$, obtains, in part, from dimensional analysis [3]. Examples of the manner in which $\bar{V}_F$ correlates with $\bar{B}$ are shown in Figs. 2 and 3 for downward spread over thin paper samples and thick samples of polymethlymethacryalate (PMMA) where τ has been set equal to $[2^{1/2}k_s\ (T_v - T_\infty)]/[\rho C_p v_c (T_f - T_v)]\ (1 + 0.5\tan\phi)$ with k_s the solid-phase thermal conductivity, and ρ the gas-phase density [6]. The item in parentheses that contains ϕ, where ϕ is the regression angle in the pyrolyzing region measured with respect to the plane in which the unburnt fuel surface lies, accounts for surface regression [14]. The characteristic, gas-phase velocity for downward spread that was used in Figs. 2 and 3 is v_b, the buoyant velocity $(\nu g \Delta H_c m_{ox,\infty}/T_\infty i C_p)^{1/3}$ where ν is the kinematic viscosity, and g is the acceleration of gravity. This form for v_c reflects the fact that the important induced flow velocity is that near the leading edge of the flame, where boundary layer assumptions are invalid. As a result, the Peclet number there must be of order unity such that there is no independently specifiable length [15]. Dimensional analysis then leads to the expression given for v_b [3].

Changes in $\bar{B}$ in Figs. 2 and 3 were brought about by changes in $m_{ox,\infty}$, the environmental pressure, P, and the acceleration of gravity, the major controllable dimensional parameters that affect the buoyant flow. Parameter variation was accomplished by performing the spread rate experiments in a closed chamber that was swung on a centrifuge so that gravitational accelerations above those of the Earth's normal acceleration, g_E, were obtained. Increases in v_b, e.g., through increases in g, cause $\bar{B}$ to decrease, which results in a decrease in flame temperature for small $\bar{B}$. As $\bar{B}$ decreases, $\bar{V}_F$ decreases for small $\bar{B}$ indicating a reduction in the forward heat transfer compared to the maximum that could be transferred if $\bar{B}$ were large.

Flame Spreading at Reduced Gravity

Results in Figs. 2 and 3 can be used to estimate spread rates at reduced gravity. In Fig. 4 we compare spread rates for flame spread down thick PMMA fuel beds determined from the correlation of Fig. 3 and computed from the theoretical treatment of Refs. [16] and [17]. The discrepancy between measured spread rates and those determined from the correlation, which derives from experiment, is because of a slightly different definition of the vaporization temperature in Figs. 3 and 4 [17].

In the theory, it is assumed that the gas-phase chemistry is infinitely fast and that an appropriately defined Grashof number is large. The gas-phase flow, temperature, and species fields were determined through the application of matched asymptotic expansion for large Grashof number [17]. The flow then is taken to be established by buoyancy, and for the conditions shown, $\bar{B}$ is large enough for g less than about 10^{-1} g_E to make the assumption of infinite-rate chemistry valid. Beyond 10^{-1} g_E, the discrepancy between theory and correlation is due to finite-rate chemistry effects, and below 10^{-3} g_E the theory fails because the Grashof number is not large. The flow then for $g < 10^{-3}$ g_E is not dominated by buoyancy, and the normal flow at the surface with velocity v_s due to pyrolysis becomes important. In this circumstance, the correlations of Figs. 2 and 3 are no longer valid because of the use of v_b for v_c.

With the characteristic length in the Grashof number set equal to ν/v_s, whether or not buoyancy induced flows are important depends on the magnitude of $(v_b/v_s)^3$ [18]. Realizing that the fuel pyrolyzes according to an Arrhenius decomposition law, we get approximately that

$$(v_b/v_s)^3 \propto g m_{ox,\infty} P^2 \exp(E_s/RT_s) \qquad (3)$$

where in the above proportionally E_s is the activation energy for pyrolysis, R is the gas constant, T_s is the surface temperature, and the temperature dependence of gas-phase properties such as viscosity, density, specific heat, etc. have been neglected because their effect is overwhelmed by the temperature dependence of the Arrhenius term. The controllable parameters in Eqn. (3) are g, $m_{ox,\infty}$, and P, and T_s is determined by these controllable parameters. Buoyancy can be rendered unimportant then if $(v_b/v_s)^3$ can be made small compared to unity by conducting experiments at reduced $m_{ox,\infty}$, P, and/or g.

Reducing $m_{ox,\infty}$ to minimize buoyancy is impractical because approximately less than an order of magnitude reduction can be achieved from pure oxygen before extinction is encountered. Additionally, a reduction of $m_{ox,\infty}$ results in a reduction of T_s because of the reduced flame temperature and resultant heat flux back to the fuel bed. The reduction in T_s causes the exponential term in $(v_b/v_s)^3$ to increase such that, practically, it is unclear whether or not a decrease in the velocity ratio is achieved by a decrease in $m_{ox,\infty}$.

Reducing pressure to achieve a small value of the velocity ratio is more attractive than reducing $m_{ox,\infty}$ because the ratio is more sensitive to pressure. A three order of magnitude change in $(v_b/v_s)^3$ can be achieved by changes in pressure, but at low pressures, extinction is encountered at the lower oxygen concentrations.

Reductions in gravitational acceleration can be used to acheive the desired goal, and it would appear that the largest reductions in $(v_b/v_s)^3$ can be had, about five to six orders of magnitude, through reductions in g. Uncertainties in the kinetic constants of pyrolysis make it difficult to determine quantitatively accurate values of the gravitational acceleration necessary to achieve small values of $(v_b/v_s)^3$, but for the conditions of

Fig. 4, levels below 10^{-3} g_E are needed.

Based on a detailed assessment of the gas-phase physics of flame spreading as described above, a Space Shuttle-based experimental program has been developed [19]. Although ground-based techniques for conducting reduced-gravity experiments can be used to obtain some useful information, the time available in a droptower is, in general, not sufficient to study the process adequately or develop a steady state. Aircraft flying parabolic trajectories do not appear to provide a sufficiently low gravitational acceleration to yield quantitative results, and the acceleration present can exist in more than one direction. Below we briefly describe the experiment and the modelling effort that is being conducted to support it. Detailed requirements of the experimental design can be found in Refs. [18] and [19].

Experiment

The experiment consists of measuring the flame spread rate, the surface temperature, and the gas-phase temperature, at two locations at different distances from the fuel bed surface, for rectangular samples of ashless filter paper, a thermally thin fuel, and PMMA, a thermally thick fuel. These fuels were chosen because of the flame spread data that are available on them. Additionally, ashless filter paper is about the thinnest sample for which the solid temperature can be measured using fine-wire thermocouples, which is the technique used for measuring temperatures.

Spread rates are obtained from color movies of the spread process. Two cameras are used to obtain an edge view of the flame and a view of the fuel surface over which the flame is spreading. The sample is held in the center of an environmental chamber as shown schematically in Fig. 5. It is ignited at one end using a heated nichrome wire coated with nitrocellulose.

Chamber volume, which is about 0.039 m^3, was chosen such that the oxygen present in the chamber would not be depleted more than 5% as a result of the combustion of the fuel. Sample size, which is 10 cm by 3 cm for the filter paper and 0.318 cm thick by 2 cm long by 0.635 cm wide for the PMMA, was chosen in conjunction with the chamber sizing and is typical of sample sizes that have been used in ground-based experiments [3,4]. The paper sample is clamped between thin metal plates while the sides and bottom of the PMMA sample are to be insulated.

In addition to oxygen depletion considerations, heat loss from the sides of the paper sample was taken into account in choosing the size of the sample. Ideally, the sides should be insulated so as not to complicate the process with heat loss to the sample holder. Insulating the sides of the paper sample is impractical, so it is made wide enough so that the heat lost to the sample holder is unimportant. The data in Fig. 2 for $m_{ox,\infty} = 0.329$ and $m_{ox,\infty} = 0.774$ that seem not to follow the general correlation between $\bar{V}_F$ and $\bar{B}$ were obtained under conditions where heat loss to the sample holder was not insignificant. The result is that another dimensionless parameter is introduced such that $\bar{V}_F$ is no longer a function of $\bar{B}$ alone [3].

The experimental apparatus for the paper samples has been tested in the NASA-Lewis Research Center 5 s droptower facility. Tests were completed to prove the ignition system and choose an experimental matrix. The proposed test matrix consists of environments composed of 30% to 50% O_2 in N_2 and pressures from 1.0 to 2.0 atm.

Some preliminary results for the ashless filter from the droptower experiments are shown in Figs. 6 and 7. In Fig. 6, an edge photo of three flames spreading from left to right is shown. The scale is that 1 cm on the figure is 0.625 cm of actual length. The light region in the photos is due to luminous radiation. There is a faint, blue flame at the leading edge that is visible in the color photos but does not show in the black-and-white copy.

In Fig. 6, the progression of the pyrolysis front as a function of time for what is labelled Case 1 in Fig. 6 is shown. From the figure, the spread rate, which can be calculated to be about 0.32 cm/s for comparison to the measured downward spread rate of 0.86 cm/s, appears rather steady.

Some unsteadiness in the overall process was present though in that the distance between the pyrolysis front and the luminous portion of the flame was increasing, indicating that the blue flame region at the leading edge of the flame was growing.

Modelling

In support of the experimental effort, a modelling effort is being conducted to provide insight for interpretation of the experimental results. The mathematical problem in dimensionless form for steady flame spreading in the absence of buoyancy over a thermally thin fuel in which solid-phase conduction is neglected is given below. A schematic of the region to which the equations apply is shown in Fig. 8.

Line S is an approximate line of symmetry through the pyrolysis region that we use in one version of the problem that we have investigated. Assumptions inherent in the formulation, which is for properties evaluated at a reference temperature intermediate between the ambient temperature and the flame temperature, are the usual ones (see, e.g., Ref. [20]) and will not be discussed here.

Continuity

$$\frac{\partial \rho u}{\partial x} + \frac{\partial \rho v}{\partial y} = 0 \tag{4}$$

Momentum

$$\rho u \frac{\partial u}{\partial x} + \rho v \frac{\partial u}{\partial y} = - \frac{\partial P}{\partial x} + \frac{\mu}{Re} \left(\frac{\partial^2 u}{\partial x^2} + \frac{\partial^2 u}{\partial y^2} \right) \tag{5}$$

$$\rho u \frac{\partial v}{\partial x} + \rho v \frac{\partial v}{\partial y} = - \frac{\partial P}{\partial y} + \frac{\mu}{Re} \left(\frac{\partial^2 v}{\partial x^2} + \frac{\partial^2 v}{\partial y^2} \right) \tag{6}$$

Energy

$$\rho u \frac{\partial T}{\partial x} + \rho v \frac{\partial T}{\partial y} = \frac{k}{Re\ Pr} \left(\frac{\partial^2 T}{\partial x^2} + \frac{\partial^2 T}{\partial y^2} \right) + Q\, \dot{W}_f''' \tag{7}$$

Species (fuel and oxygen)

$$\rho u \frac{\partial m_f}{\partial x} + \rho v \frac{\partial m_f}{\partial y} = \frac{\rho D}{Re\ Pr\ Le} \left(\frac{\partial^2 m_f}{\partial x^2} + \frac{\partial^2 m_f}{\partial y^2} \right) + \dot{W}_f''' \tag{8}$$

$$\rho u \frac{\partial m_{ox}}{\partial x} + \rho v \frac{\partial m_{ox}}{\partial y} = \frac{\rho D}{Re\ Pr\ Le} \left(\frac{\partial^2 m_{ox}}{\partial x^2} + \frac{\partial^2 m_{ox}}{\partial y^2} \right) + i\dot{W}_f''' \tag{9}$$

In the above, the density, ρ, viscosity, μ, temperature, T, and mass diffusivity, D, are measured in the units of their ambient values, i.e., at ∞. The pressure, P, is measured in the units of $\rho_\infty v_c^2$. The Reynolds number, Re, Prandtl number, Pr, and Lewis number, Le are

$$Re = \frac{v_c L}{\nu_\infty}; \quad Pr = \frac{\nu_\infty}{\alpha_\infty}; \quad Le = \frac{\alpha_\infty}{D_\infty} \tag{10}$$

with α the thermal diffusivity, and L an arbitrary length. Distances x and y are measured in the units of L. The dimensionless reaction rate is

$$\dot{W}_f''' = -\tilde{B}\rho^2 m_{ox} m_f e^{-T_a/T} \tag{11}$$

with $\tilde{B}$ a Damkohler number defined as

$$\tilde{B} = \frac{BL\rho_\infty}{M_{ox} v_c} \tag{12}$$

M_{ox} is the molecular weight of oxygen, and Q is the heat of combustion divided by $C_p T_\infty$. The equation of state is that $\rho T=1$.

The boundary conditions are:

Right side (R)

$$u = \frac{-V_F}{v_c}; \quad v = m_f = 0; \; m_{ox} = m_{ox,\infty}; \; T = 1 \tag{13}$$

Left side (L)

$$\frac{\partial u}{\partial x} = \frac{\partial v}{\partial x} = \frac{\partial m_f}{\partial x} = \frac{\partial m_{ox}}{\partial x} = \frac{\partial T}{\partial x} = 0 \; ; \; P = \text{constant} \tag{14}$$

Top (T)

$$u = \frac{-V_F}{v_c} \; ; \; \frac{\partial v}{\partial y} = m_f = 0 \; ; \; m_{ox} = m_{ox,\infty} \; ; \; T = 1 \; ; \; P = \text{constant} \tag{15}$$

Upstream fuel surface (U)

$$u = \frac{-V_F}{v_c} \; ; \; v = \frac{\partial m_f}{\partial y} = \frac{\partial m_{ox}}{\partial y} = 0 \; ; \; T = T_s \tag{16}$$

Pyrolysis region (P)

$$u = \frac{-V_F}{v_c} \; ; \; v = \frac{v_s}{v_c} \; ; \; T = T_s \tag{17}$$

$$\dot{m}''(1 - m_{f,s}) = \frac{\rho D}{\text{Re Pr Le}} \left. \frac{\partial m_f}{\partial y} \right|_s \tag{18}$$

$$\dot{m}'' \, m_{ox,s} = - \frac{\rho D}{\text{Re Pr Le}} \left. \frac{\partial m_{ox}}{\partial y} \right|_s \tag{19}$$

Downstream of burnout (D)

$$\frac{\partial u}{\partial y} = v = \frac{\partial m_f}{\partial y} = \frac{\partial m_{ox}}{\partial y} = \frac{\partial T}{\partial y} = 0 \tag{20}$$

The dimensionless pyrolysis flux, $\dot{m}''$, is taken to be

$$\dot{m}'' = \frac{\rho_s \tau B_s e^{-E_s/RT_s}}{\rho_\infty v_c} \tag{21}$$

where B_s is the preexponential factor for the Arrhenius decomposition.

For the solid phase, the energy and mass conservation equations with x, y, T_s, $\dot{m}''$, and k defined as above are

$$\rho_s \left(\frac{V_F}{v_c}\right) \frac{\partial T_s}{\partial x} = \dot{m}'' \left(\frac{\rho_\infty}{\rho_{s,\infty}}\right) \left(\frac{L}{\tau}\right) (\Delta H_v + (1 - C_p)(T_s - 1)) + \left(\frac{k_\infty}{\tau C_s v_c \rho_{s,\infty}}\right) k \left.\frac{\partial T}{\partial y}\right|_s \tag{22}$$

$$\left(\frac{V_F}{v_c}\right) \frac{\partial \rho_s}{\partial x} = - \dot{m}'' \left(\frac{\rho_\infty}{\rho_{s,\infty}}\right) \left(\frac{L}{\tau}\right) \tag{23}$$

where ρ_s is measured in the units of the original solid density, $\rho_{s,\infty}$, C_p is measured in the units of C_s, and ΔH_v is the heat of vaporization divided by $C_s T_\infty$. The fuel enters at the right where $\rho_s = T_s = 1$.

If the gas-phase chemistry is infinitely fast, it is convenient to combine the energy and species equations by defining the coupling functions [21]

$$b_{fo} = m_f - \frac{(m_{ox} - m_{ox,\infty})}{i} \; ; \; b_{to} = \frac{T}{Q} + \frac{(m_{ox} - m_{ox,\infty})}{i} \tag{24}$$

The b_i then satisfy, with unity Lewis number,

$$\rho u \frac{\partial b_i}{\partial x} + \rho v \frac{\partial b_i}{\partial y} = \frac{k}{RePr} \left(\frac{\partial^2 b_i}{\partial x^2} + \frac{\partial^2 b_i}{\partial y^2} \right) \tag{25}$$

The boundary conditions on b_i derive from the above, but they are modified to account for the fact that, for infinite-rate chemistry, inside the flame there is no oxygen, and outside the flame there is no fuel. The flame is located where $m_f = m_{ox} = 0$.

There are not a large number of solutions of similar problems in the literature because of the complexity of the problem and the difficulties in determining the eigenvalue spread rate, but some noteworthy examples are given in Refs. [6,17] and [22] through [25]. We have solved several versions of the above problem using the numerical scheme SIMPLER [26]. The cases that we have considered to date are i) infinite-rate chemistry in the "half-region" in which symmetry conditions are written along S, ii) infinite-rate chemistry in the entire domain, and iii) finite-rate chemistry in the "half-region" and entire domain.

In Problem i), the flame is taken to be symmetrical about the line S, and a unique surface temperature in the pyrolysis region is specified. This decouples the gas and solid phases such that the gas-phase problem is computed as though the flame were stationary, i.e., $V_F \ll v_s$, and as a function of surface temperature. The length L that appears in the problem is set equal to one-half the length of the pyrolysis region, which is estimated from the experiment. Additionally, v_c is set equal to v_s, and along R $\partial(u,v)/\partial x = 0$, and b_i are their ambient values. Along T, y-direction derivatives are zero. We have used this problem to investigate the characteristics of the fluid mechanics and compute flame shapes for comparison to the droptower experiments, even though the experiments may not have reached steady state.

Coupling function contours for the half-region for Case 1 of Fig. 6 are shown in Fig. 9. The heavy contour is the flame. The scale in Figs. 6 and 9 are the same so that a direct comparison can be made. A surface temperature of 650 K, which is comparable to measured temperatures under similar conditions [27], gives a flame shape that matches the experimental shape adequately.

Using the entire domain and infinite-rate chemistry, (Problem ii) attempts to predict the spread rate with L identified as the length of the pyrolysis region, $v_c = v_s$, and conditions along R, L, and T as in the symmetrical problem failed. If the requirement is made that the the fuel density at burnout drop to some small percentage of its original value, no pyrolysis temperature can be found that is consistent with the gas and solid-phase conservation equations. The reason for this is that the flow in the gas, which is generated solely by the flow in the pyrolysis region, is insufficient to remove the chemical energy that is released in the gas to maintain a steady state. Because the fuel, which is moving at speed V_F in flame-fixed coordinates, contains little mass after the burnout location, it cannot remove the energy either. The result is that no consistent steady-state can be found.

It would appear necessary to include the forced flow of speed V_F that the flame sees in flame fixed coordinates, even though V_F may be small compared to v_s, to remove the chemical energy released. Solving Problem ii) with v_c defined as an arbitrary reference velocity, v_r, such that u along R is equal to $-V_F/v_r$ and L set equal to α/v_r, steady spread rates can be found. The process is an iterative one of guessing the solution and iterating back and forth betwen the phases until the surface temperature and spread rate do not change substantially from one iteration to another. The resulting spread rate will be valid as long as V_F is approximately equal to v_r. Coupling function contours and a velocity vector field for Case 1 of Fig. 5 are shown in Figs. 10 and 11. The computed spread rate is 2.35 cm/s, as compared to the value gotten from Fig. 7 of 0.32 cm/s. The computed spread rate is larger than what we expect ultimately to measure because of the use of infinite-rate chemistry. We are in the process now of making computations that include the effects of finite-rate chemistry with all other aspects of the procedure the same, i.e., Problem iii).

Summary

Based on a review of the flame spread literature, an experiment to investigate flame spreading in reduced gravity has been designed. Construction of the experiment is, for all practical purposes, complete. The modelling effort that is being conducted in support of the experiment is continuing. To date it has demonstrated the importance of the convective motion that results from the fact that the flame is moving into the oxidizing environment.

References

1. Williams, F.A. (1977). Mechanisms of fire spread, Sixteenth Symposium (International) on Combustion, The Combustion Institute, pp. 1281-1294.

2. Fernandez-Pello, A.C. and Santoro, R.J. (1979). On the dominant mode of heat transfer in downward flame spread, Seventeenth Symposium (International) on Combustion, The Combustion Institute, Pittsburgh, pp. 1201-1209.

3. Altenkirch, R.A., Eichhorn, R., and Shang, P.C. (1980). Buoyancy effects on flames spreading down thermally thin fuels, Combustion and Flame, 37, pp. 71-83.

4. Altenkirch, R.A., Eichhorn, R., and Rizvi, A.R. (1983). Correlating downward flame spread rates for thick fuel beds, Combustion Science and Technology, 32, pp. 49-66.

5. Fernandez-Pello, A.C., Ray, S.R., and Glassman, I. (1981). Flame spread in an opposed forced flow: the effect of ambient oxygen concentration, Eighteenth Symposium (International) on Combustion, The Combustion Institute, pp. 579-589.

6. de Ris, J.N. (1969). Spread of a laminar diffusion flame, Twelfth Symposium (International) on Combustion, The Combustion Institute, Pittsburgh, pp. 241-252.

7. Fernandez-Pello, A.C. (1978). A theoretical model for the upward laminar spread of flames over vertical fuel surfaces, Combustion and Flame, 31, pp. 135-148.

8. Ray, S.R., Fernandez-Pello, A.C., and Glassman, I. (1980). A study of the heat transfer mechanisms in horizontal flame propagation, Journal of Heat Transfer, 107, pp. 357-363.

9. Altenkirch, R.A., Short, J.L., Vedha-Nayagam, M., and Padgaonkar, A.M. (1985). Including radiation heat transfer effects in dimensionless flame spread correlations, Central States-Western States Section/The Combustion Institute.

10. Kashiwagi, T. and Newman, D.L. (1976). Flame spread over an inclined thin fuel surface, Combustion and Flame, 26, 163-177.

11. Hirano, T., Noreikis, S.E., and Waterman, T.E. (1973). Measured velocity and temperature profiles of flames spreading over a thin combustible solid, IIT Research Institute, Interim Technical Report No. 2, Project J-1139.

12. Andracchio, C.R. and Cochran, T.H. (1976). Gravity effects on flame spreading over solid surfaces, NASA TN D-8828.

13. Andracchio, C.R. and Cochran, T.H. (1974). Burning of solids in oxygen-rich environments in normal and reduced gravity, NASA TM X-3055.

14. Altenkirch, R.A., Rezayat, M., Eichhorn, R., and Rizzo, F.J. (1982). Boundary integral equation method calculations of surface regression effects in flame spreading, Journal of Heat Transfer, 104, pp. 734-740.

15. Hellums, J.D. and Churchill, S.W. (1961). Dimensional analysis and natural circulation, Chemical Engineering Progress Symposium Series, 57, pp. 75-80.

16. Vedha-Nayagam, M. and Altenkirch, R.A. (1985). Backward boundary layers in downward flame spread, Twentieth Symposium (International on Combustion, The Combustion Institute, Pittsburgh, pp. 1583-1590.

17. Altenkirch, R.A. and Vedha-Nayagam, M. (1985). Gravitational effects on flames spreading over thick solid surfaces, Acta Astronautica, 12, pp. 565-572.

18. Altenkirch, R.A. and Vedha-Nayagam, M. (1985). Gravitational effects in flame spreading, NASA report on Grants NAG 3-258 and NAG 3-114.

19. Altenkirch, R.A. (1985). Science requirements document for a solid surface combustion experiment, NASA-Lewis Research Center.

20. T'ien, J.S. (1986). The flame front problem: combustion in low-Reynolds-number flow, ASME Paper 86-WA/HT-49.

21. Williams, F.A. (1985). Combustion Theory, Benjamin/Cummings.

22. Frey, A.E., Jr. and T'ien, J.S. (1979). A theory of flame spread over a solid fuel including finite-rate chemical kinetics, Combustion and flame, 36, pp. 263-289.

23. Fernandez-Pello, A.C. and Williams, F.A. (1977). A theory of laminar flame spread over flat surfaces of solid combustibles, Combustion and Flame, 28, pp. 251-277.

24. Sirignano, W.A. (1974). Theory of flame spread above solids, Acta Astronautica, 1, pp. 1285-1299.

25. Chen, C. (1986). Flame propagation: effect of solid-phase heat conduction, Eastern Section/The Combustion Institute.

26. Patankar, S.V. (1980). Numerical Heat Transfer and Fluid Flow, McGraw-Hill.

27. Parker, W.J. (1972). Flame spread model for cellulosic materials, Journal of Fire and Flammability, 3, pp. 254-269.

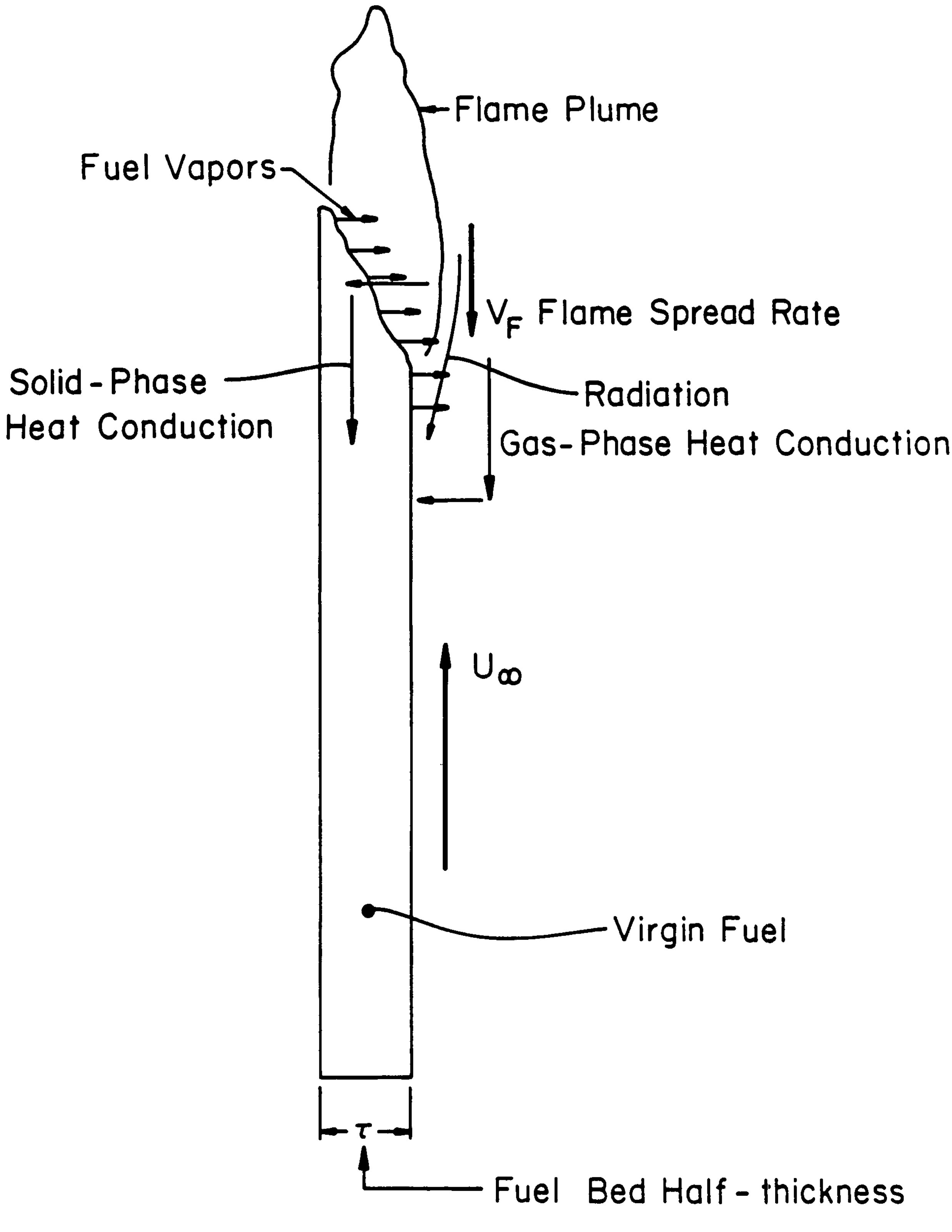

Figure 1 Downward flame spread process.

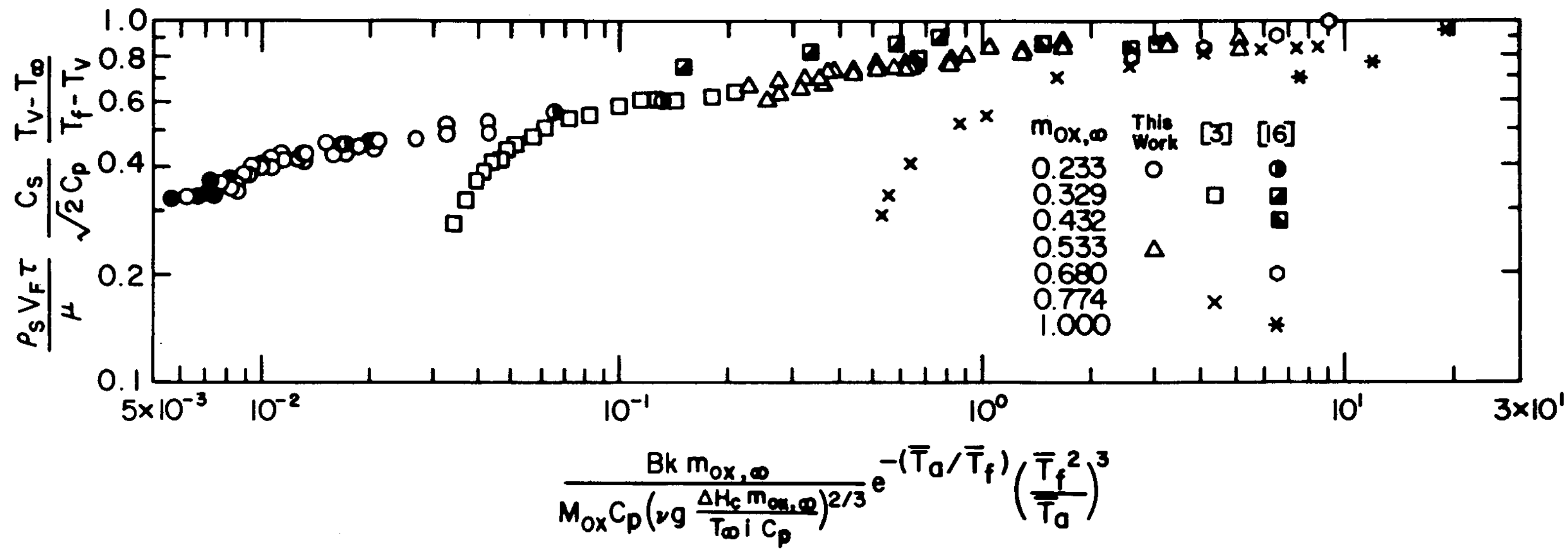

Figure 2 Dimensionless downward flame spread correlation for thin fuels [3]

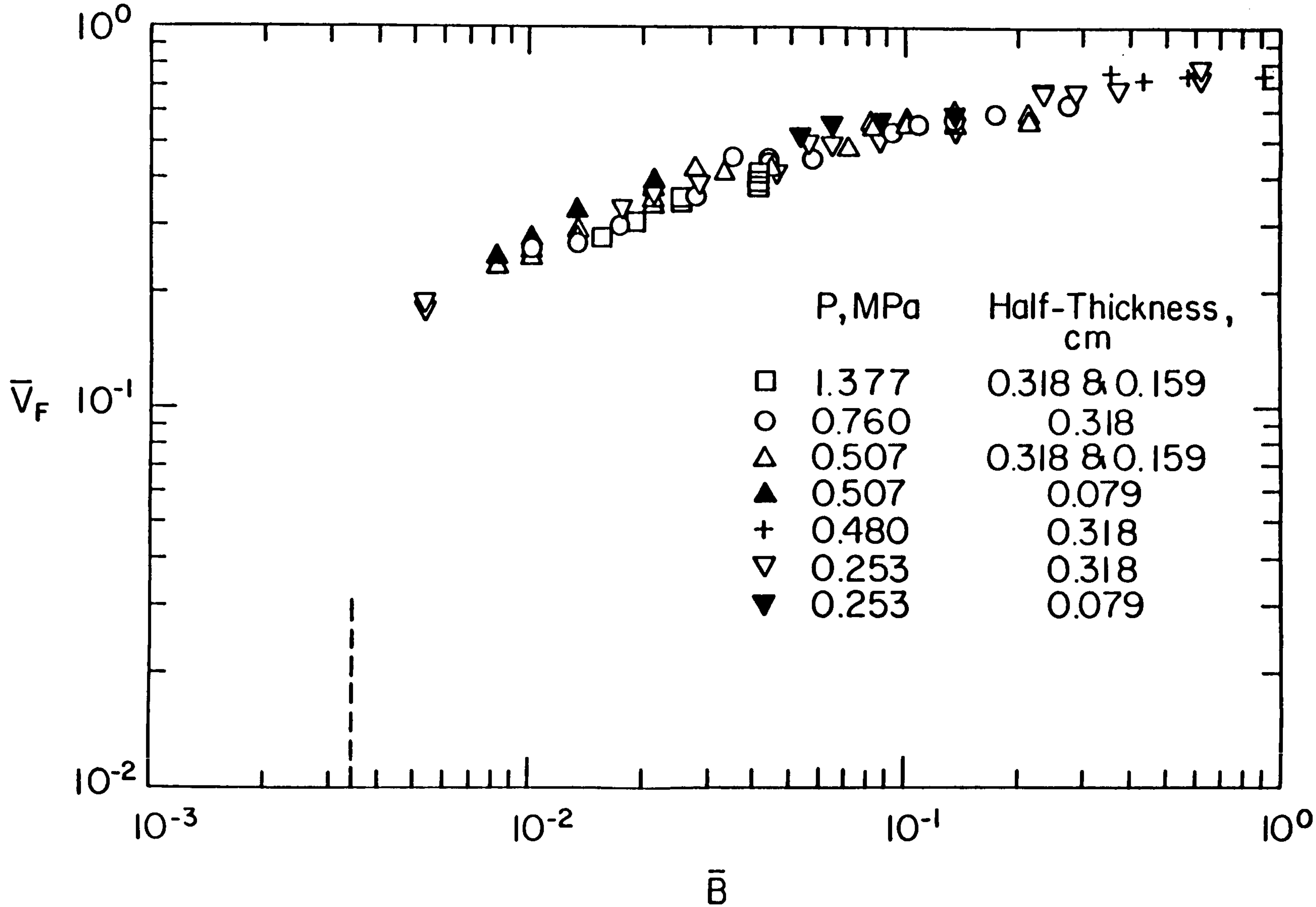

Figure 3 Dimensionless downward flame spread correlation for thick fuels [4]

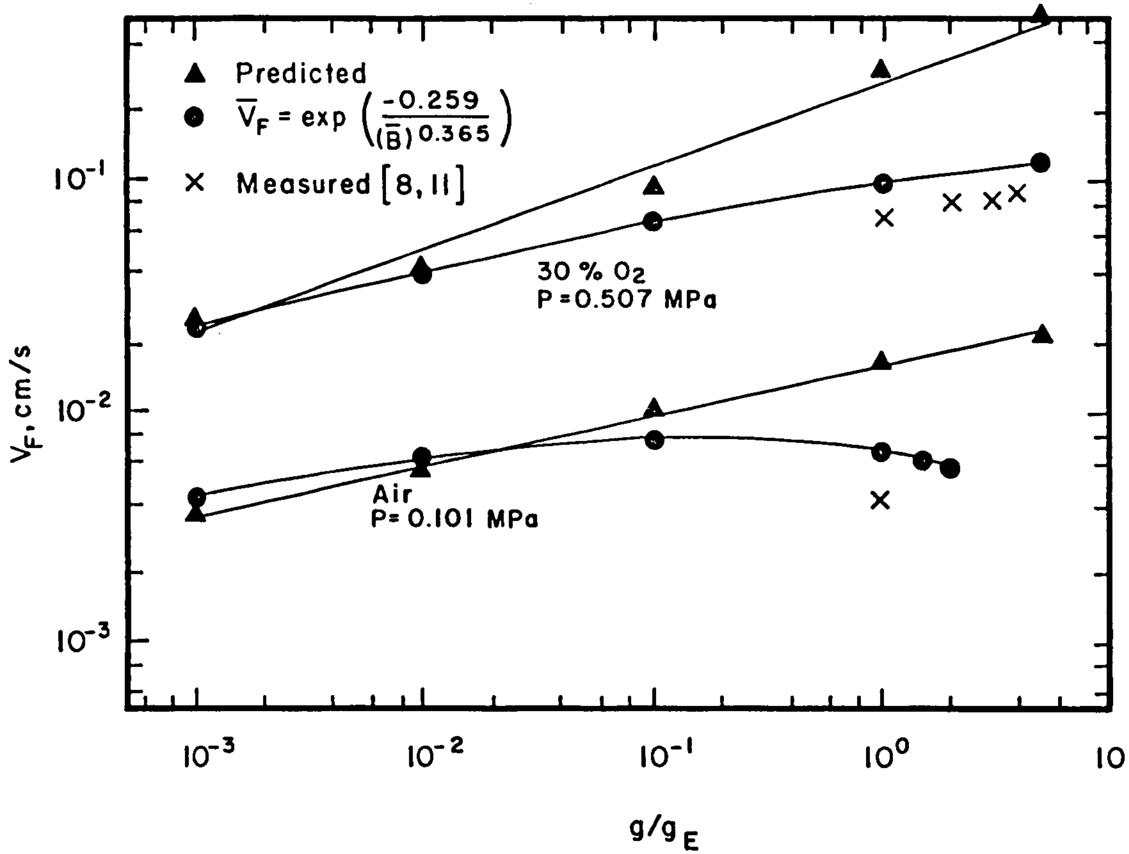

Figure 4 Predicted and Experimental Spread Rates for Spread Down a Semi-infinitely Thick, PMMA Fuel Bed as a Function of Gravitational Acceleration [17]

SOLID SURFACE COMBUSTION EXPERIMENT

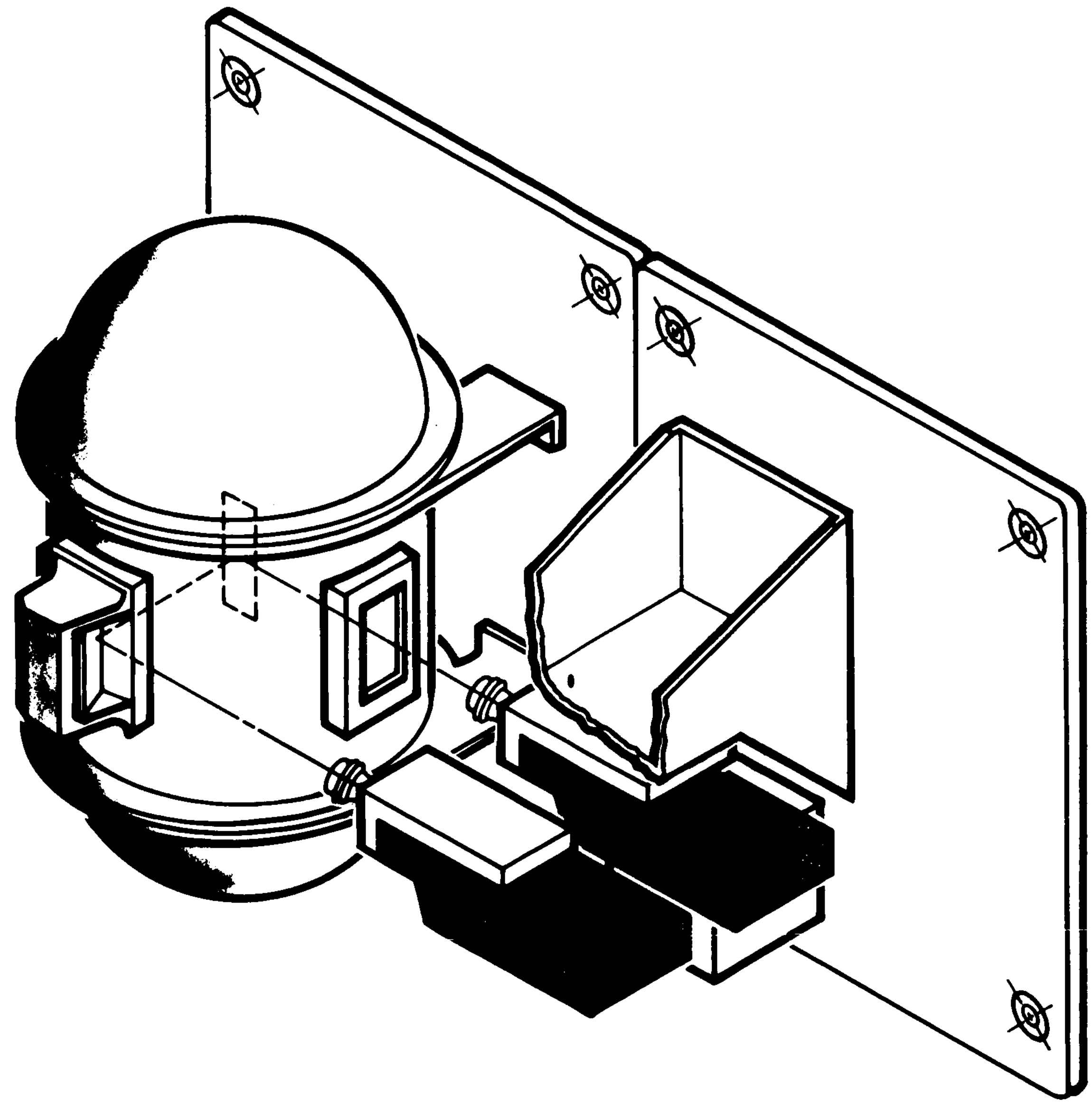

CD-84-14426

Case 1
50% O_2
0.152 MPa

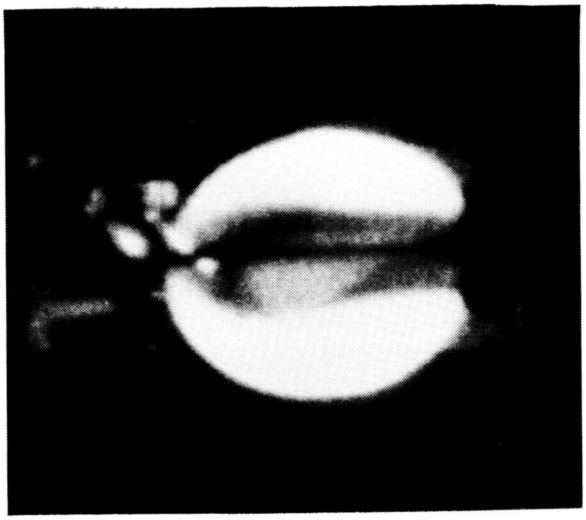

Case 2
30% O_2
0.152 MPa

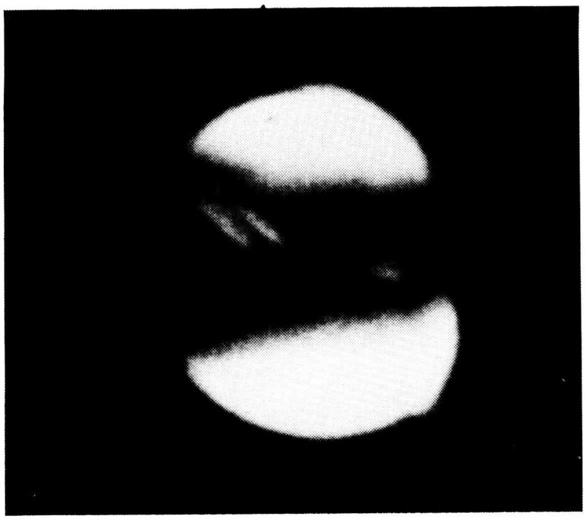

Case 3
30% O_2
0.203 MPa

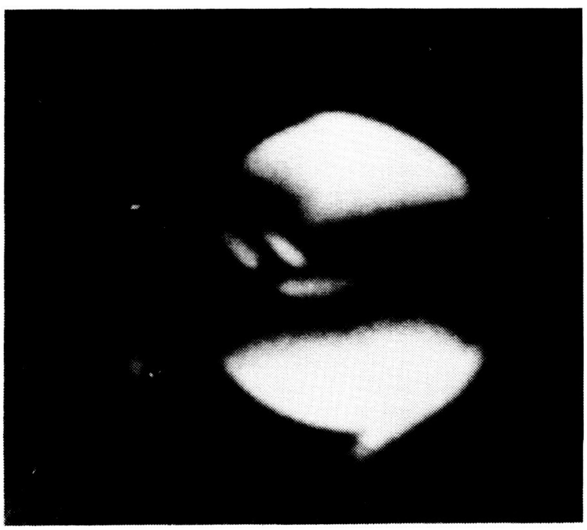

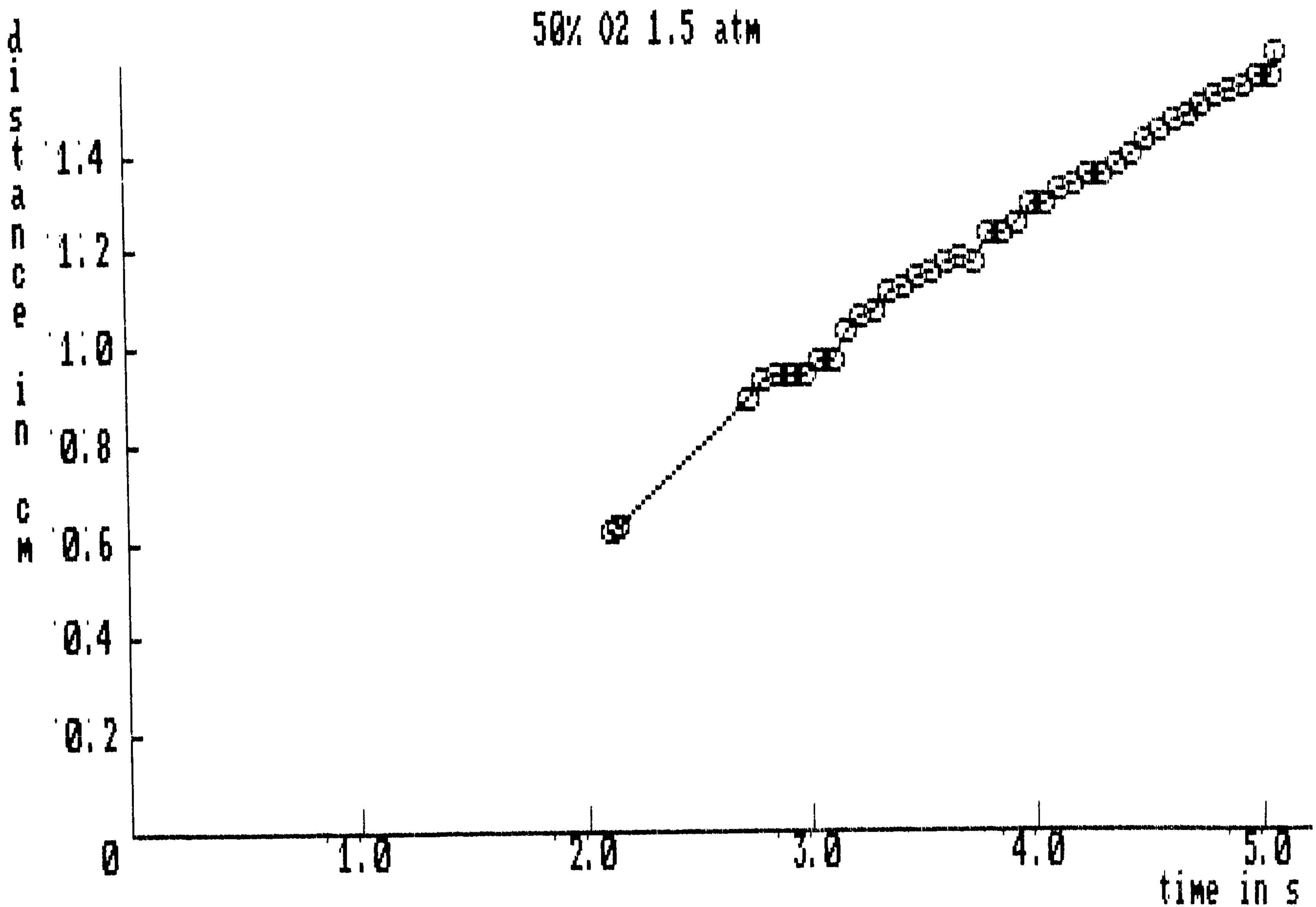

Figure 7 Position vs time for flame spreading in the 5 s droptower.

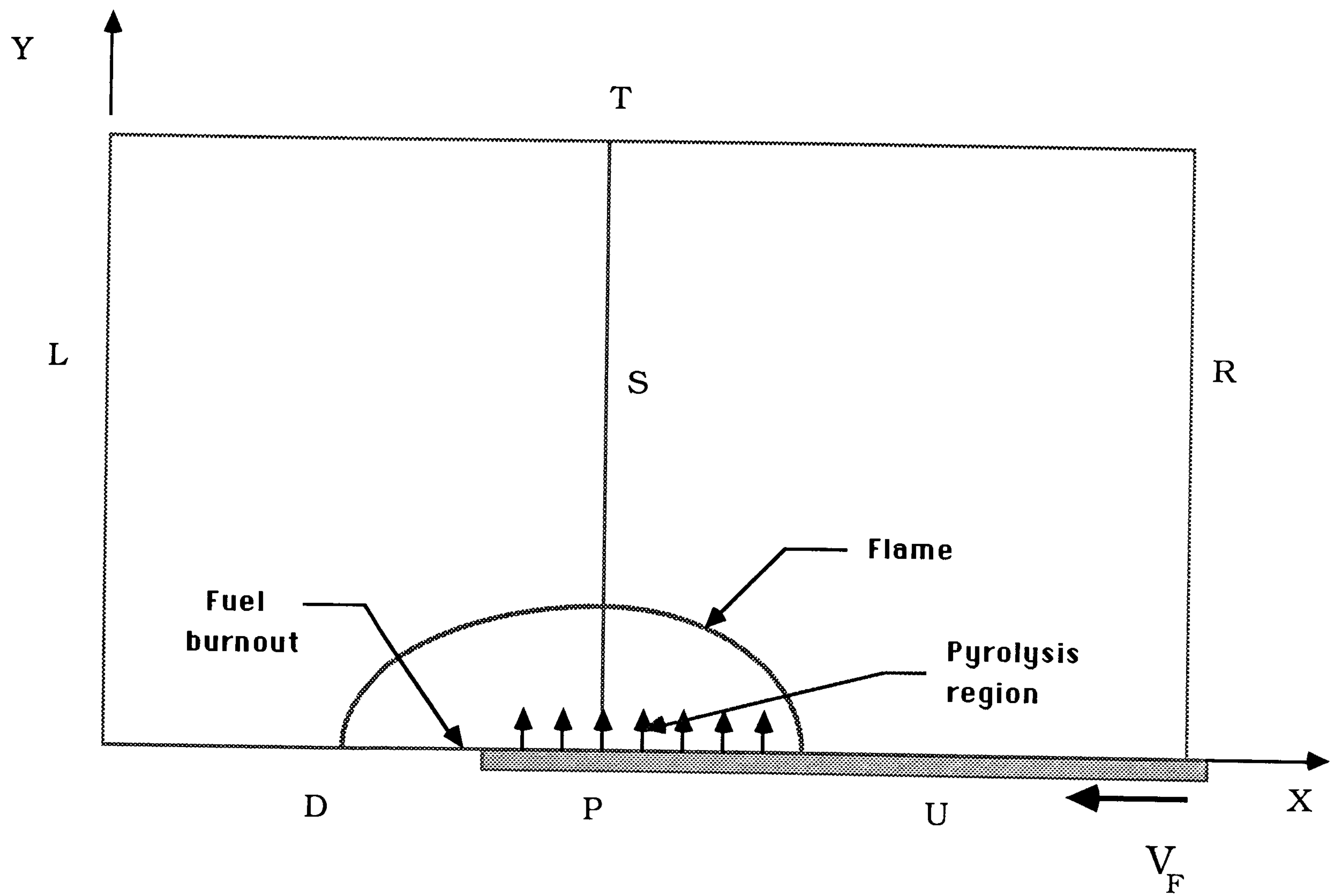

Figure 8 Computational domain.

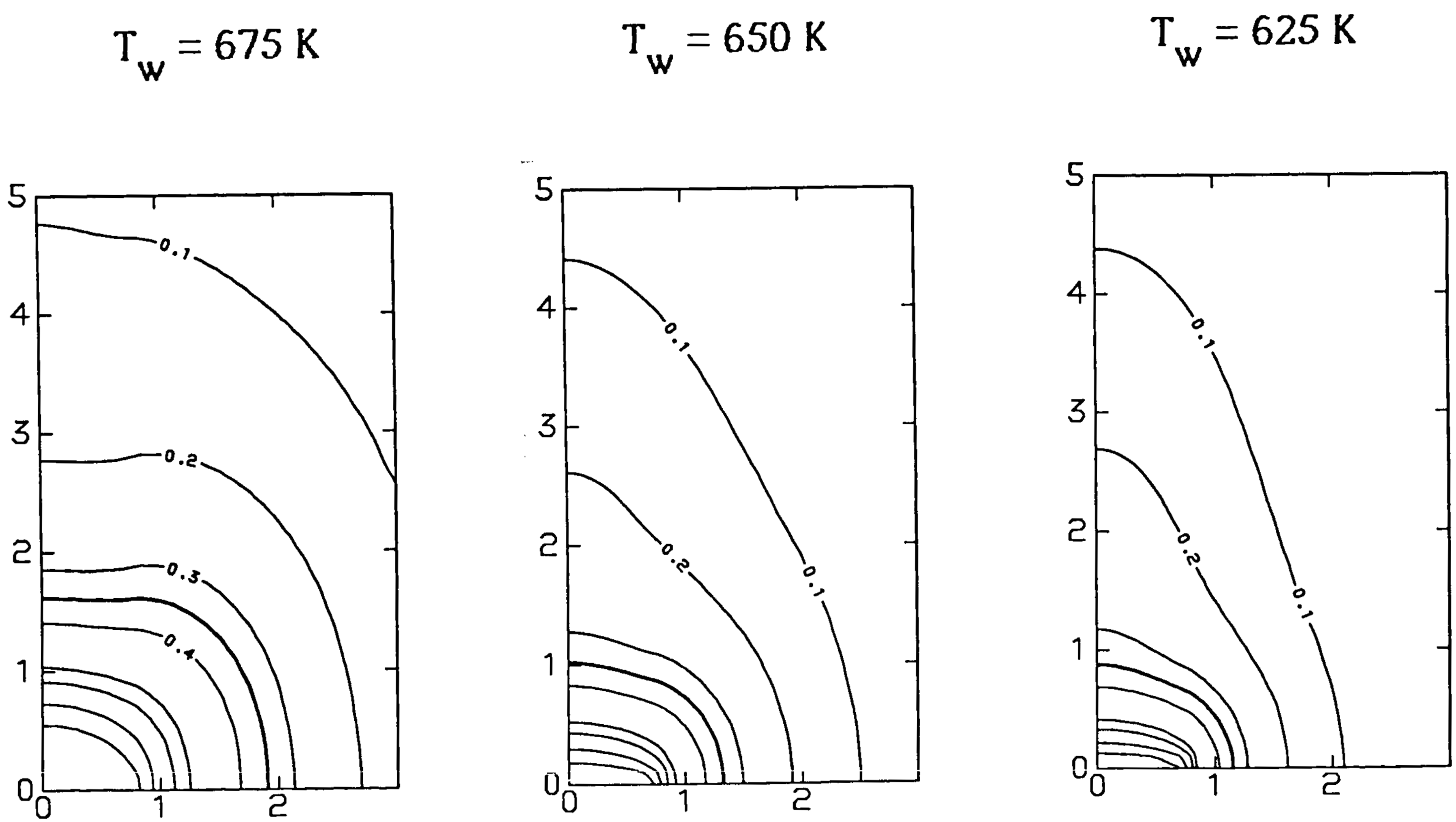

Figure 9 Coupling Function Contours for 50% O_2 , 1.5 atm (Case 1).

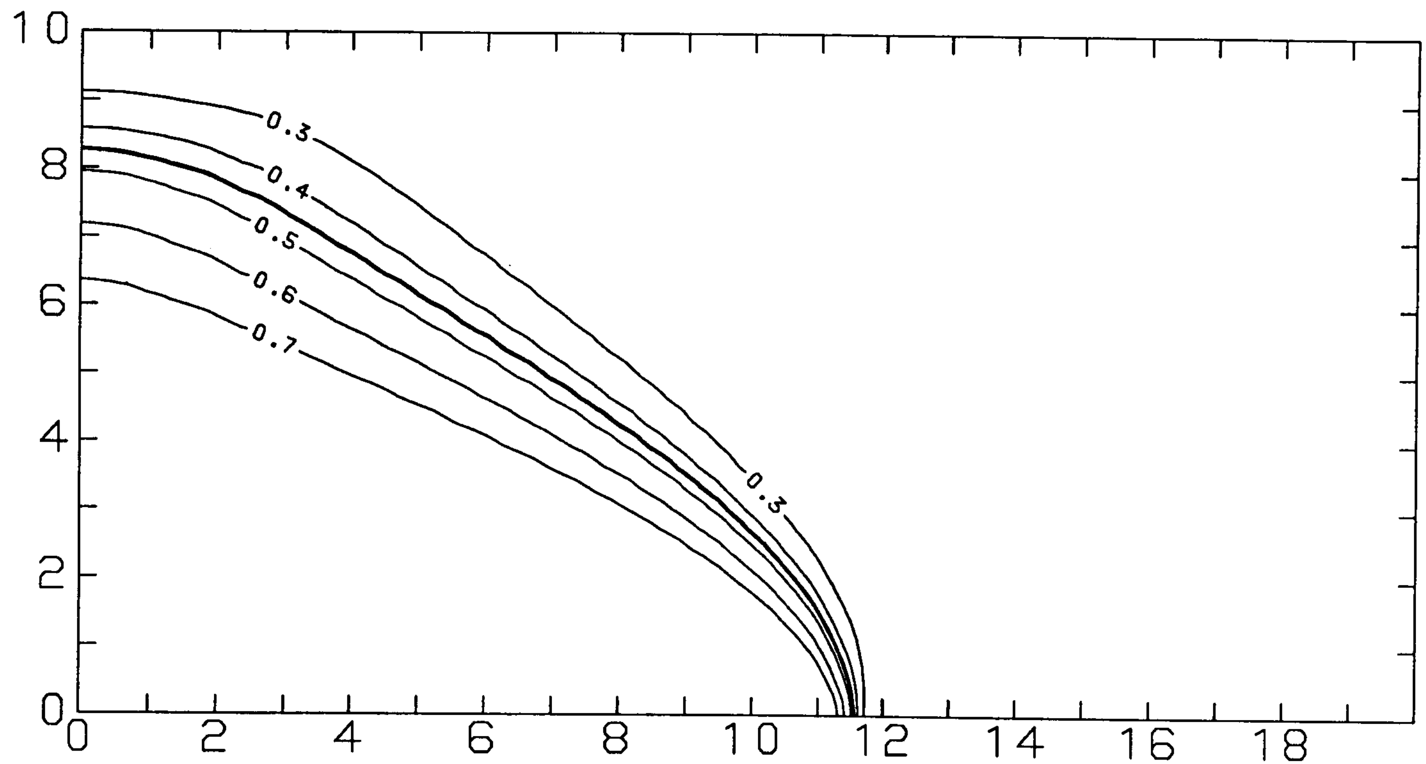

Figure 10 Coupling function field for Case 1 of Fig. 6. The length scale is α/v_r.

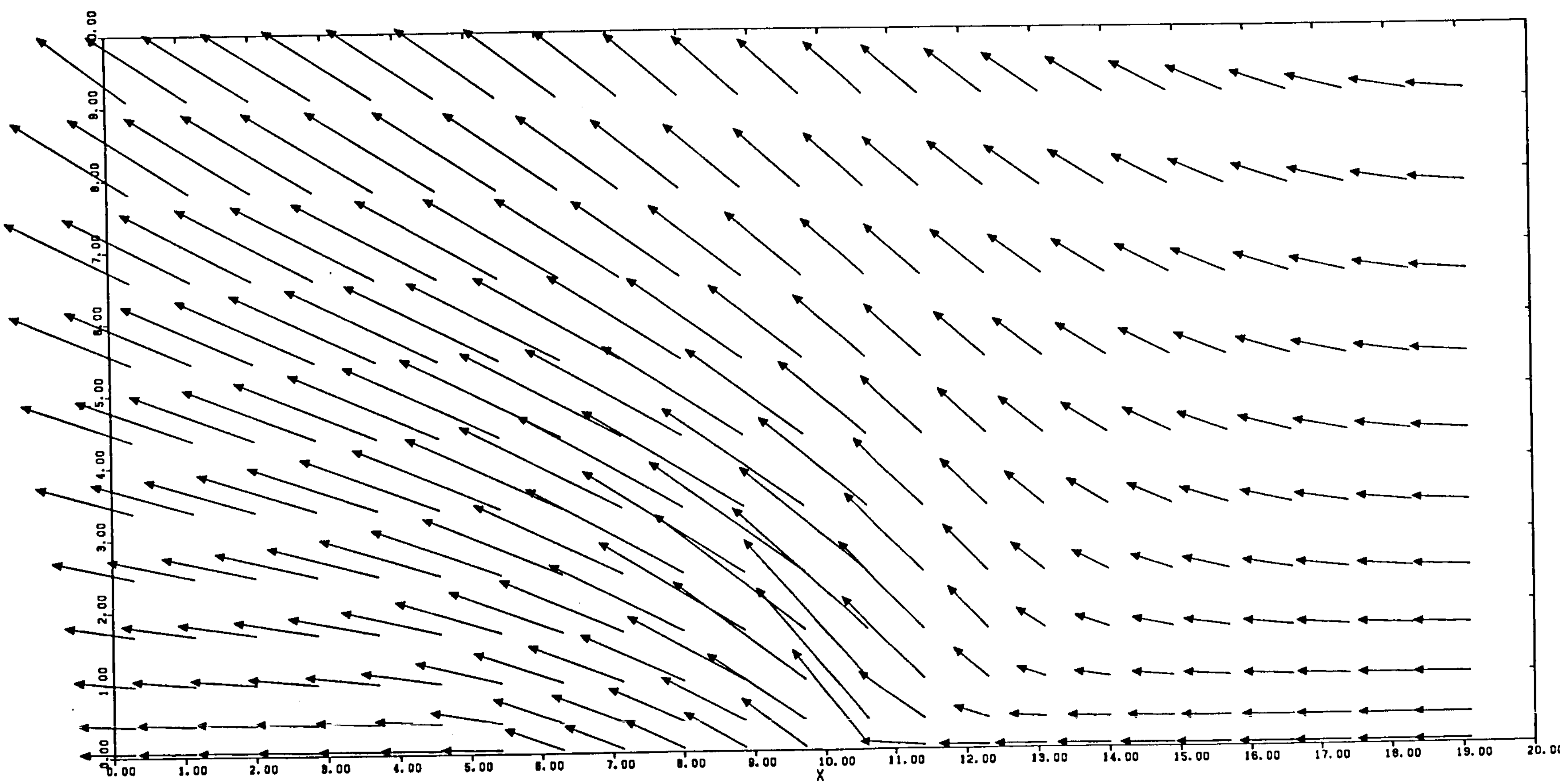

Figure 11 Velocity vector field for Case 1 of Fig. 6. The length scale α/v_r.

ORIGINAL PAGE IS
OF POOR QUALITY

N89-20313

DROPLET COMBUSTION AT REDUCED GRAVITY

by

F. L. Dryer and F. A. Williams
Princeton University
Princeton, NJ 08544

Extended Abstract

The science of droplet combustion is an applied science of current interest. Improvements in understanding of droplet combustion could lead to enhanced performance of combustors that employ liquid or slurry fuels. Although much is known about droplet combustion, various aspects of the subject are in need of additional fundamental knowledge. The research in progress addresses some of these aspects.

In applications of droplet combustion use is made of the now-classical theory developed in the early 1950's. Properties are approximated as uniform throughout the liquid, and steady-state conservation equations in spherical symmetry are employed to describe the gas on the basis of a reaction-sheet approximation, in which the combustion occurs at a spherical surface (the flame) surrounding the droplet. Fuel and oxygen diffuse into this surface from opposite sides, and heat liberated there is conducted back to the liquid to cause fuel vaporization. It is predicted that the square of the droplet diameter decreases linearly with time, and the ratio of the flame diameter to the droplet diameter remains constant during combustion.

The classical theory provides a good approximation to reality in many circumstances. However, phenomena neglected by this theory can be important in practical situations. The research is addressing various aspects of departures from the classical theory. These aspects include heating transients in the liquid, unsteady evolution of the gas-phase reaction zone, extinction of the gas-phase reactions, disruption of the liquid during combustion, and sooting behavior in the gas. The last three of these can be especially significant in applications; for example, liquid disruption through generation of gases in the droplet interior reduces burning times by producing collections of smaller droplets and can decrease yields of unburnt hydrocarbons and oxides of nitrogen.

Experiments under reduced gravity can aid in investigating many of these aspects of droplet combustion by decreasing buoyant convection. Although the individual combustion of each of the small droplets in sprays in practical combustion chambers often occurs with nearly spherical symmetry, for ease in data acquisition laboratory experiments on burning of individual droplets usually must employ larger droplets whose flames are displaced and elongated by buoyancy. Research taking advantage of reduced-gravity facilities, such as drop towers and space vehicles, affords the opportunity to study combustion of larger droplets with decreased buoyant influences. In the present studies, burning of individual droplets having diameters between 0.8 and 2.5 mm is being investigated at pressures between 0.5 and 2 atm in oxygen-nitrogen atmospheres having oxygen mole fractions between 0.18 and 0.50. The fuels are alkanes (initially decane and heptane), alcohols and (later) possibly mixtures, slurries and emulsions.

The current work involves theoretical analyses of the effects identified, experiments in the NASA Lewis drop towers and design of a flight apparatus for experiments to be performed in the middeck area of the Space Shuttle. In addition, there is laboratory work associated with the design of the flight apparatus. Calculations have shown that some of the test-matrix data can be obtained in drop towers, and some are achievable only in the space experiments. The apparatus consists of a droplet dispensing device (syringes), a droplet positioning device (opposing, retractable, hollow needles), a droplet ignition device (two matched pairs of retractable spark electrodes), gas and liquid handling systems, a data acquisition system (mainly giving motion-picture records of the combustion in two orthogonal views, one with backlighting for droplet resolution), and associated electronics.

Recent results from drop-tower testing of decane droplet combustion exhibit unexpected instances of disruptive burning. Theoretically, disruption does not occur for pure fuels. Earlier drop-tower tests encountered only two such events, both with small and unresolved satellite droplets burning in atmospheres having an oxygen mole fraction of 0.50. The recent tests demonstrate disruptions of larger, resolved droplets burning in air and suggest that disruption may be the rule rather than the exception under the experimental conditions. One hypothesis attributes the new results to improved achievement of spherical symmetry, allowing increased absorption of gas-phase fuel pyrolysis products in the liquid to form a multicomponent mixture susceptible to disruption. Future work includes evaluation of this hypothesis, further developments of theory for disruption, and exploration of ranges of conditions over which this mode of combustion occurs.

Theoretical studies have identified transient evolution of temperature profiles within droplets during combustion, through use of asymptotic analyses. Impulses delivered to droplets by sparks and by g-jitter have been calculated theoretically. Further theoretical investigations are planned on thermophoretic motion of soot particles formed around burning droplets, e.g. in relationship to disruptive burning.

Laboratory experiments have characterized spark transients and measured impulses delivered to droplets by sparks. Clarification of aspects of droplet formation on opposing needles also has been achieved in the laboratory. Future laboratory work will extend information on individual droplet ignition by sparks with attention paid to influences of fuel type, oxygen content of the atmosphere, and pressure. Analyses of soots collected under different laboratory combustion conditions also are planned. Future studies will devote special consideration to transients, extinction, soot and disruption.

Introduction

Droplet burning has been the subject of intensive study over many years. The practical motivations for such investigations come mainly from a desire to achieve clean and efficient production of power through the combustion of liquid fuels. The fact that studies are continuing demonstrates that unknown factors remain at the basis of the subject.

Scientific studies of the topic first appeared at the Fourth International Combustion Symposium in 1953 [1,2,3]. A number of review articles on the subject have been prepared in recent years [4-8]. Much is known about the fundamentals of the subject, and good methods for calculating burning rates of droplets are available [9]. That these methods involve semiempirical procedures illustrates the need for further fundamental studies.

In the now-classical theory of droplet combustion, properties are approximated as uniform throughout the liquid, and steady-state conservation equations in spherical symmetry are employed to describe the gas on the basis of a reaction-sheet approximation, in which the combustion occurs at a spherical surface (the flame) surrounding the droplet. Fuel and oxygen diffuse into this surface from opposite sides, and part of the heat liberated there is conducted back to the liquid to cause fuel vaporization.

It is predicted that the square of the droplet diameter decreases linearly with time, and the ratio of the flame diameter to the droplet diameter remains constant during combustion. Specifically, the dependence of the droplet diameter d on time t is given by the "d-square law",

$$d^2 = d_0^2 - Kt \ , \tag{1}$$

where K is called the burning-rate constant. In terms of the thermal diffusivity α of the gas, the ratio ρ of the density of the gas to that of the liquid and the transfer number B, it was found that theoretically

$$K = 8\alpha\, \rho\, \ell n(1+B) \ . \tag{2}$$

The transfer number is a thermodynamic quantity measuring the ease with which mass transfer can occur, viz.,

$$B = H/L \quad , \tag{3}$$

where H is the enthalpy difference driving mass transfer and L is the enthalpy difference resisting it. The ratio of the flame diameter to the droplet diameter is predicted to be

$$R = \ell n(1+B)/\ell n(1+\nu) \quad , \tag{4}$$

where ν is the product of the ambient oxygen mass fraction with the stoichiometric mass ratio of fuel to oxygen.

The classical theory provides a good approximation to reality in many circumstances. However, phenomena neglected by this theory can be important in practical situations. The current low-gravity research is addressing various aspects of departures from the classical theory. These aspects include heating transients in the liquid, unsteady evolution of the gas-phase reaction zone, extinction of the gas-phase reactions, disruption of the liquid during combustion, and sooting behavior in the gas. The last three of these can be especially significant in applications; for example, liquid disruption through generation of gases in the droplet interior reduces burning times by producing collections of smaller droplets and can decrease yields of unburnt hydrocarbons and oxides of nitrogen, thereby decreasing pollutant production.

Liquid Heating Transients

The burning-rate constant K is affected by unsteady heat transfer within the liquid because the resistance enthalpy L includes, in addition to the heat of vaporization, the enthalpy conducted into the droplet interior. The variation of the latter with time introduces departures from the d-square law. Theories [10-12] have suggested that consequently K will gradually increase over the first 10% of the burning history, but recent studies [13-15] have identified the thermal diffusivity β of the liquid and the ratio ϵ of sensible to latent enthalpy change of the liquid as parameters influencing this prediction. If $\beta < \alpha\rho\ell n(1+B)$ and $\epsilon > 1$, a thermal wave develops in the liquid at the droplet surface during combustion and causes L to increase with time, so that K decreases, contrary to expectation; instead of "heating up", the droplet "cools down". Experiments have shown heat-up behavior but have not been performed with parameters for which cool-down is predicted.

Reaction-Zone Motion

There have been theoretical examinations of the classical result that the ratio R of flame to droplet radius remains constant during combustion [16-19]. In droplet burning, after an initial transient there is an outer transient-diffusive zone and an inner quasisteady convective-diffusive zone in the gas [16,17], and the flame should lie in the outer zone for low ambient oxidizer concentrations and in the inner zone for high concentrations, the specific condition for the latter being approximately $8\rho[\ell n(1+B)]^3 < [\ell n(1+\nu)]^2$. Thus, the theory predicts that the flame will remain unsteady in some cases but will achieve quasisteady behavior (flame radius proportional to droplet radius) in others. *Good experimental tests of these* theoretical predictions are unavailable. The burning rate of the droplet is influenced by this effect [17-19] such that, on the average, an additional factor $1 + [(2/\pi)\rho\ell n(1+B)]^{1/2}$ appears in the equation for K[8]. This result too lacks experimental scrutiny. The best available experimental *indications* are that under gravity-free conditions the ratio *R* usually increases with time, at least initially [20-22].

Reaction-Zone Extinction

The flame extinguishes if a Damkohler number D, the ratio of a residence time to a reaction time in the reaction zone, becomes too small. Since the reaction time is independent of the droplet diameter but the residence time is proportional to the square of the diameter, extinction is predicted to occur when the droplet becomes sufficiently small. Although extinctions have been observed in experiments with droplets suspended on fibers [9,23,24], interpretation of the results is difficult because of interference by the fiber. Depending on conditions, extinction is predicted to occur either before or after complete vaporization of the fuel [17,25]. Experimental tests of these extinction predictions for droplets currently are unavailable.

Extinctions in configurations of counterflowing fuel and oxidizer have been analyzed theoretically [26,27], and the results have been employed in conjunction with experiments to extract overall rate parameters [27-29]. Extinctions by convection have been inferred for free droplets [30], but data are insufficient to extract rate parameters. Published extinction analyses employ activation-energy asymptotics in a one-step approximation for the chemistry. More recent analyses [31,32] are addressing influences of full kinetic mechanisms on extinction. Since existing experimental methods for studying extinction can be applied only over a limited range of residence times, measurements of extinction for droplets burning with spherical symmetry as can be obtained in gravity-free conditions could extend capabilities of testing extinction theories.

Liquid Disruption

Disruptive burning is a phenomenon whereby the fuel droplet disintegrates abruptly prior to completion of combustion. Experimental studies of the phenomenon have been performed, e.g. [30,33-35], and some theoretical understanding of the mechanisms of disruption has been obtained, e.g. [7,13,30,36], on the basis of ideas of homogeneous nucleation.

Deficiencies remain in abilities to predict disruption, and experiments at reduced gravity afford a means for addressing these deficiencies, as will be demonstrated below.

Soot

Soot production in diffusion flames is a complicated chemical-kinetic process about which some qualitative concepts are available. The literature on the subject is vast, as may be seen from the citations in a recent publication [37], for example. In liquid-fuel combustors soot production in droplet burning may be a contributor to the soot levels in the combustion chamber. The soot may be beneficial for radiant energy transfer but detrimental for pollutant emissions. Soot formation has been observed in droplet-burning experiments, but quantitative measurements of soot concentrations or of rates of soot production in droplet burning are unavailable.

The Role of Reduced Gravity

Experiments under reduced gravity can aid in investigating these aspects of droplet combustion by decreasing buoyant convection. Although the individual combustion of each of the small droplets in sprays in practical combustion chambers often occurs with nearly spherical symmetry, for ease in data acquisition laboratory experiments on burning of individual droplets usually must employ larger droplets whose flames are displaced and elongated by buoyancy. Research taking advantage of reduced-gravity facilities, such as drop towers and space vehicles, affords the opportunity to study combustion of larger droplets with decreased buoyant influences.

A droplet of diameter d exposed to an acceleration of magnitude g has an associated buoyancy-controlled residence time of order $\sqrt{d/g}$, which may be compared with the diffusion-controlled residence time d^2/α. The square of the ratio of the second of these times to the first (viz. $d^3 g/\alpha^2$) is proportional to a Grashof number that measures the importance of free convection relative to diffusive processes. Estimates show this number to be about unity under normal laboratory combustion conditions for $d \approx 1$ mm. Since gas diffusivities α vary inversely with the pressure p, reducing d, p or g decreases effects of buoyancy. Changing p also affects chemical-kinetic rates and mechanisms; reduction in g therefore is a more attractive way to achieve $d^3 g/\alpha^2 \ll 1$.

With this last inequality enforced, changing d by a factor of five changes residence times by a factor of 25, which should be sufficient for investigating chemical-kinetic effects associated with extinction and soot production, for example. Changing d by a factor of three (as planned in the initial phase of the present program) changes residence times by a factor of nine, which still could reveal interesting phenomena.

To achieve these ranges of residence times, corresponding ranges of *burning times are needed.* The short-duration tests can be performed with drop towers, but the long-duration tests require the times available in space vehicles. Possible changes in controlling mechanisms, for example through changes in chemical-kinetic mechanisms, provide incentive for exploring the *residence-time range indicated.* The long-duration end of these residence times is relatively unexplored and therefore more likely to uncover unanticipated phenomena.

Reasons for Shuttle Tests

The present project involves plans to use the Space Shuttle, as a vehicle in which droplet combustion experiments are performed, primarily because of the extended test duration that it provides, at sufficiently low g-levels, with a hands-on observer present. The longer test durations afforded by the Space Shuttle are helpful for a number of reasons.

With respect to liquid heating transients, for example, experimental discrimination between heat-up and cool-down behavior is facilitated if the entire droplet burning history is accessible experimentally for droplets suffciently large to manifest anticipated differences. In tests where the reaction-zone motion is expected to approach quasisteady behavior, most or all of the combustion history of sufficiently large droplets must be observed to establish the quasisteadiness clearly; this could not be achieved in the earliest tests [20-22], but the planned use of larger drop towers can alleviate the difficulty, at least partially. To investigate reaction-zone extinction, the combustion history must be observed until extinction occurs. In sufficiently reduced-oxygen atmospheres, extinction times are accessible in drop towers (although the increased severity of ignition difficulties could degrade data), but interest in extraction of overall chemical-kinetic information dictates experiments in increased-oxygen atmospheres as well, at the same initial diameters d_o used in reduced-oxygen tests, and this increases test times beyond drop-tower capabilities. Disruption shortens burning times, thereby promoting possibilities of full-data acquisition in drop towers, although use of larger droplets under conditions of slower onset of disruption (as would be possible in the Space Shuttle) could enhance resolution of the *instabilities and other processes occurring.* Observations of sooting behavior similarly could benefit from improved resolution afforded by study of larger droplets, and, moreover the residence-time variations achievable by use of the Space Shuttle can be beneficial in studying the chemical kinetics of sooting. *Finally,* at the longer test times approachable in the Space Shuttle, the observer may encounter unexpected and as yet unknown combustion events that may prove to be of fundamental scientific interest.

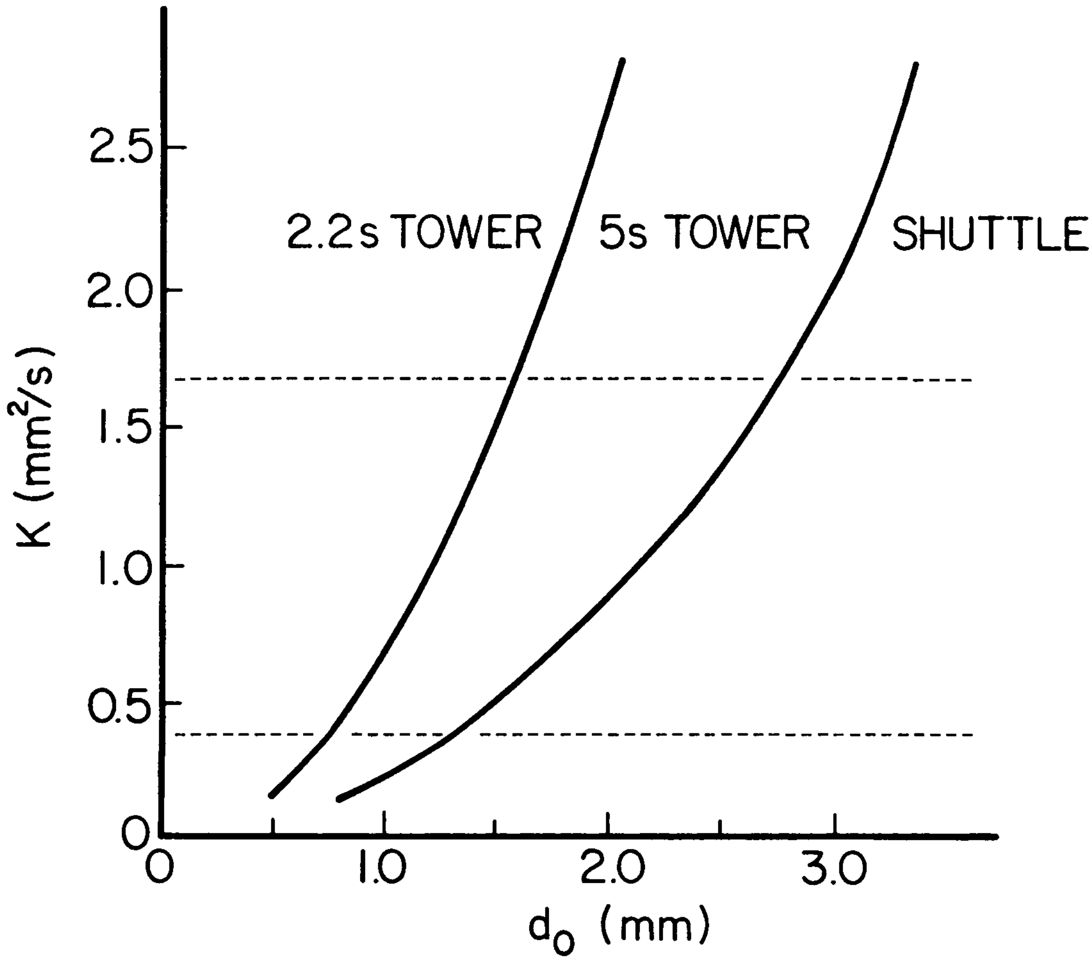

FIGURE 1. Ranges of conditions accessible to drop towers and to the Space Shuttle.

The easiest of the preceding considerations to quantify is a presumed requirement to observe the entire burning history of a droplet, with a specified initial diameter d_o, having a known burning-rate constant K. Figure 1 shows the ranges of d_o and K accessible to the two NASA-Lewis drop towers and to the Space Shuttle. This figure allows for a preparation time of about 0.5 s prior to ignition. The range of values of K of interest is from about 0.4 mm^2/s (a value estimated for the early period in recent drop-tower testing of decane in air) to about 1.5 mm^2/s (a value representative of relatively volatile fuels in oxygen-enriched environments), as indicated by dashes in Fig. 1. In view of this range and the range of d_o of interest, it is seen from Fig. 1 that some tests can be run in each of the drop towers, while some need the Space Shuttle.

Consideration was given to alternative options for obtaining the longer-duration test times assigned to the Space Shuttle in Fig. 1. Larger drop towers do not exist since the complexity and expense of drop tower operation increases rapidly with tower size (for example, more than ten drops per day have been made in the 2.2 s tower, but no more than two in the 5 s tower). Use of ballistic missiles would entail great expense for each data point. Aircraft flying "zero-g" trajectories offer the most attractive alternative to the Space Shuttle but pose special difficulties that render their utility problematic. Although reduced-gravity times on the order of 30 s or more are routinely achieved in such aircraft, their g-level fluctuations are appreciably greater than those in drop towers or in the Space Shuttle. Consideration of acceleration, velocity and displacement effects in the conservation equations for droplet combustion have indicated that g-levels on the order of 10^{-3} times normal earth gravity or less are needed in the droplet-burning experiments. These levels are readily obtained in drop towers and in the Space Shuttle, but in aircraft they would necessitate "free-floating" the experiment in the cabin (i.e., the apparatus could not be fastened to the wall). Free-floating reduces the test time appreciably, and moreover in these experiments the preparation time would be increased since the droplet would have to be formed as well as ignited during free-floating, and the formation time is on the order of 10 s. Thus it is uncertain that longer high-quality low-g burning times can be achieved in aircraft than in drop towers.

History of the Program

The idea of an experiment on droplet combustion at reduced gravity was conceived in the early to middle 1970's when NASA-Lewis became interested in developing basic science of combustion experiments for the Shuttle. An overview committee was established which canvassed the combustion community to identify research areas benefiting from extended periods of near weightlessness or a buoyancy-free environment. The committee report [38] found ten major research areas including single-droplet combustion.

Kumagai [20-22] had pioneered gravity-free droplet-burning experiments with a drop tower giving 0.9 s test time. He had found in his experiments that the burning-rate constants were, in units of mm^2/s, 0.8 for benzene, 0.64 for ethyl alcohol, and 0.78 for n-heptane, approximately 82% of the corresponding normal-gravity rate constants. In an attempt to augment Kumagai's results on zero-gravity burning times, to test his burning-rate constants over a greater part of the droplet-burning history, and to extend the data base to other fuels (first decane), a test program (that acquired approximately 50 to 75 points) was undertaken in the 2.2 s NASA-Lewis drop tower [39]. These tests failed to produce burning droplets with less than 3 cm/s residual velocity upon deployment. The droplet deployment system used, a single-fiber-withdrawal technique, represented an attempt to implement the techniques that had been introduced by Kumagai. Critical timing difficulties between the instant of fiber withdrawal vertically upward and the subsequent instant of entry into zero-g is cited as the difficulty.

In 1984, after continuing investigations [39,40] and definition of droplet experiments to be flown in the Space Shuttle, a flight-hardware-development program was initiated with the award of a contract to TRW (NAS 3-23887). At the start of this hardware-development program the key feasibility issue of obtaining a single burning droplet in zero gravity with little or no residual motion was unresolved. This feasibility issue has now been solved by use of systems developed by TRW and testing accomplished in the NASA-Lewis drop tower, and the hardware has proceeded through a recently successful Preliminary Design Review.

The Current Program

The current program involves continuation of the TRW work on development of a flight apparatus for experiments to be performed in the middeck area of the Space Shuttle, further testing in the NASA-Lewis 2.2 s and 5 s drop towers, and both theoretical studies and laboratory experiments at Princeton, associated with design of the flight apparatus and with the previously discussed outstanding problems in droplet combustion. In the present studies, burning of individual droplets having diameters between 0.8 and 2.5 mm is being investigated at pressures between 0.5 and 2 atm in oxygen-nitrogen atmospheres having oxygen mole fractions between 0.18 and 0.50. The fuels are alkanes (initially decane and heptane), alcohols and (later) possibly mixtures, slurries and emulsions. The current representative science-requirement test matrix is shown in Table I. Some of the entries in this matrix can be obtained from drop-tower tests, while others require longer test times. Continuing drop-tower studies are intended to lead to revisions of Table I, to identify those tests that are the best to be planned for a few flights of the Space Shuttle.

Design of the Flight Experiment

Elements of the current design of the flight experiment for the Space Shuttle are shown in Fig. 2. The apparatus consists in general of a droplet dispensing device (special syringe mechanisms), a droplet positioning device (opposing, retractable, hollow needles), a droplet ignition device (two matched pairs of retractable spark electrodes), a gas handling system, a data acquisition system (mainly giving motion-picture records of the combustion in two orthogonal views, one with backlighting for droplet resolution), and associated

Table I

ORIGINAL PAGE IS OF POOR QUALITY

TEST MATRIX

FLIGHT #1 - n-Decane fuel at 14.7 psia and cabin temperature.

Test #	Oxygen Concentration (mol %)	Drop Diameter - mm
1	.21	1.
2	.21 - Amt. consumed	1.2
3	.21 - " "	1.4
4	.21 - " "	1.6
5	.21 - " "	.8
6	.21 - " "	1.
7	.21 - " "	1.6
8	.21 - " "	1.2
9	.21 - " "	.8
10	.21 - .021 = .189	1.4

FLIGHT #2 - n-Decane at cabin temperature.

Test #	Oxygen Concentration (mol %)	Pressure - Atm.	Drop Diameter - mm
1	.21	.5	1.
2	.21 - Amt. consumed	.5	1.5
3	.21 - " "	.5	.8
4	.21 - " "	.5	1.
5	.5	.5	1.
6	.5 - Amt. consumed	.5	1.5
7	.5 - " "	.5	.8
8	.5 - " "	.5	2.5
9	.5 - " "	.5	1.
10	.5 - " "	.5	1.6
11	.18	1.	1.
12	.18 - Amt. consumed	1.	1.5
13	.18 - " "	1.	.8
14	.18 - " "	1.	1.
15	.25	2.	1.
16	.25 - Amt. consumed	2.	1.5
17	.25 - " "	2.	.8
18	.25 - " "	2.	2.5
19	.25 - " "	2.	1.
20	.25 - " "	2.	1.6
21	.35	1.	1.
22	.35 - Amt. consumed	1.	1.5
23	.35 - " "	1.	.8
24	.35 - " "	1.	2.5
25	.35 - " "	1.	1.

FLIGHT #3 - n-Heptane at cabin temperature

Test #	Oxygen Concentration (mol %)	Pressure - Atm.	Drop Diameter - mm
1	.21	1.	1.
2	.21 - Amt. consumed	1.	1.5
3	.21 - " "	1.	.8
4	.21 - " "	1.	2.5
5	.21 - " "	1.	1.6
6	.21 - " "	1.	1.
7	.21	.5	1.
8	.21 - Amt. consumed	.5	1.5
9	.21 - " "	.5	.8
10	.21 - " "	.5	2.5
11	.5	.5	1.
12	.5 - Amt. consumed	.5	1.5
13	.5 - " "	.5	.8
14	.5 - " "	.5	2.5
15	.5 - " "	.5	1.6
16	.5 - " "	.5	1.
17	.18	1.	1.
18	.18 - Amt. consumed	1.	1.5
19	.18 - " "	1.	.8
20	.18 - " "	1.	1.
21	.35	2.	1.
22	.35 - Amt. consumed	2.	1.5
23	.35 - " "	2.	.8
24	.35 - " "	2.	2.5
25	.35 - " "	2.	1.

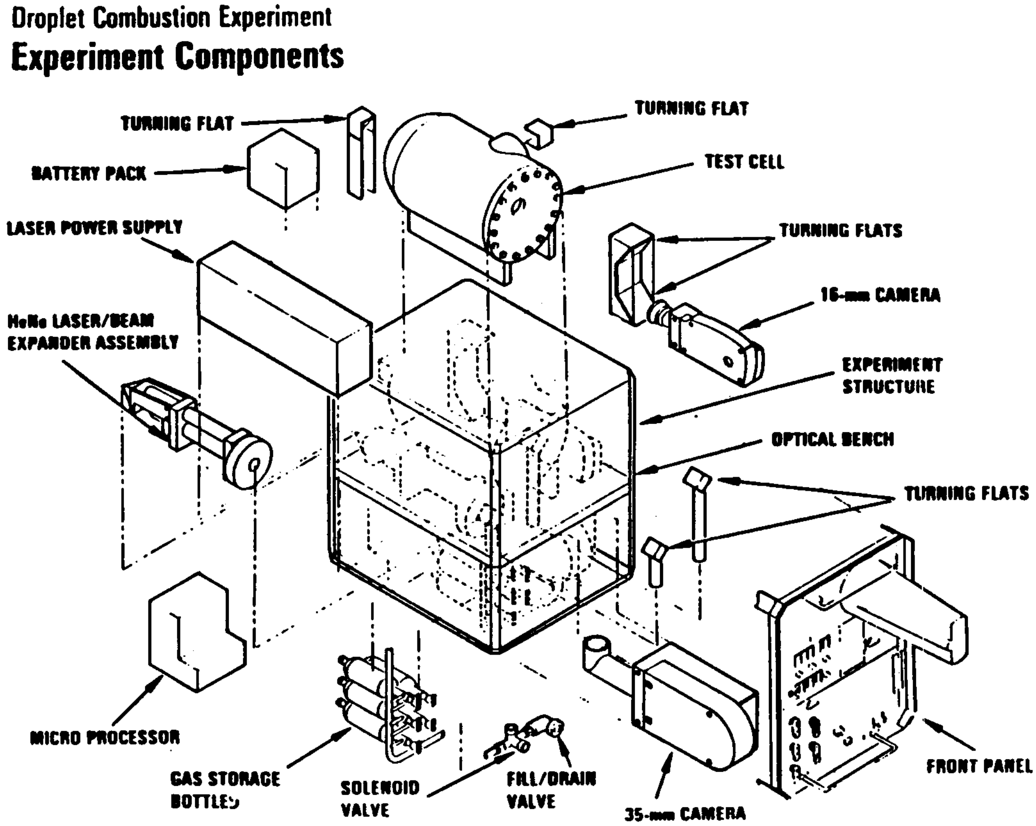

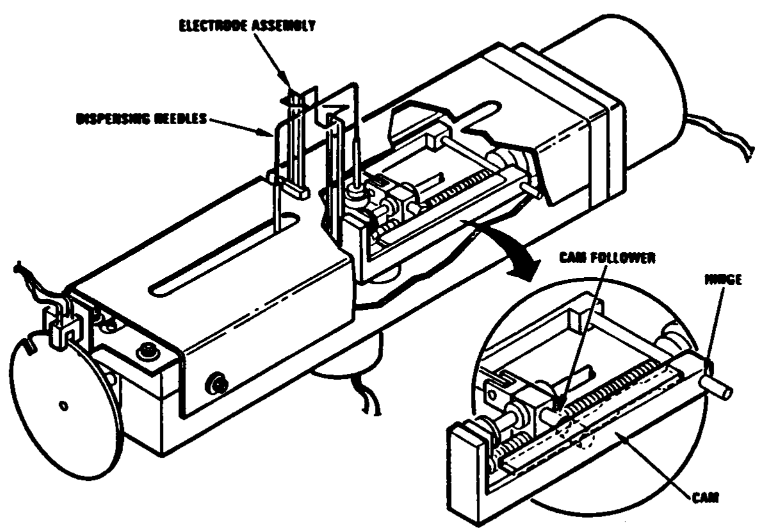

FIGURE 2. Diagram of components of the flight experiment.

electronics. The component shown at the bottom of the figure is the dispensing, positioning and ignition assembly that is located inside the test cell. In this design, the test fuel is stored in two fuel systems at the base of the dispensing needles. An engineering model of the system at the bottom of the figure is to be employed in the drop towers to test its performance and to acquire data for the test-matrix points accessible to drop-tower experiments.

An earlier, development version of the apparatus shown at the bottom of Fig. 2 has been employed in experiments performed in the 2.2 s drop tower. Unanticipated results were obtained on droplet-combustion processes.

Recent Results and Future Directions

Recent results from drop-tower testing of decane droplet combustion exhibit unexpected instances of disruptive burning [41]. Theoretically, disruption does not occur for pure fuels. Earlier drop-tower tests encountered only two such events [39,42], both with small and unresolved satellite droplets burning in atmospheres having an oxygen mole fraction of 0.50. The recent tests demonstrate disruptions of larger, resolved droplets burning in air and suggest that disruption may be the rule rather than the exception under the experimental conditions. One hypothesis attributes the new results to improved achievement of spherical symmetry (droplet velocities sometimes below 2 mm/s), allowing increased absorption of gas-phase fuel pyrolysis products into the liquid to form a multicomponent mixture susceptible to disruption. These pyrolysis products could be soot precursors or soot itself. Future work includes evaluation of this hypothesis, further developments of theory for disruption, and exploration of ranges of conditions over which this mode of combustion occurs.

Other results have been described in recent publications [41,43,44]. Theoretical studies have identified transient evolution of temperature profiles within droplets during combustion by use of asymptotic analysis. Impulses delivered to droplets by sparks and by g-jitter have been calculated theoretically. Further theoretical investigations are planned on thermophoretic motion of soot particles formed around burning droplets, e.g. in relationship to disruptive burning.

Laboratory experiments have characterized spark transients and measured impulses delivered to droplets by sparks [44]. Clarification of aspects of droplet formation on opposing needles also has been achieved in the laboratory [41]. Future laboratory work will extend information on individual droplet ignition by sparks with attention paid to influences of fuel type, oxygen content of the atmosphere, and pressure. Analyses of soots collected under different laboratory combustion conditions also are planned. Further consideration will be given to nonphotographic methods of data acquisition such as laser scattering for soot measurements. Future studies will devote special consideration to transients, extinction, soot and disruption.

References

1. Godsave, G.A.E., "Studies of the Combustion of Drops in a Fuel Spray -- The Burning of Single Drops of Fuel", Fourth Symposium (International) on Combustion, Williams and Wilkins Co., Baltimore, 1953, pp. 818-830.

2. Hall, A.R. and Diederichsen, J.D., "Experimental Study of the Burning of Single Drops of Fuel in Air at Pressures up to Twenty Atmospheres", Fourth Symposium (International) on Combustion, Williams and Wilkins, Co., Baltimore, 1953, pp. 837-846.

3. Spalding, D.B., "The Combustion of Liquid Fuels", Fourth Symposium (International) on Combustion, Williams and Wilkins Co., Baltimore, 1953, pp. 847-864.

4. Williams, A., "Fundamentals of Oil Combustion", Progress in Energy and Combustion Science 2, 1976, pp. 167-179.

5. Faeth, G.M., "Current Status of Droplet and Liquid Combustion", Progress in Energy and Combustion Science 3, 1977, pp. 191-224.

6. Law. C.K., "Mechanisms of Droplet Combustion", Proceedings of the Second International Colloquium on Drops and Bubbles, edited by le Croisette, D.H., JPL Publication 82-7, Jet Propulsion Laboratory, Pasadena, 1982, pp. 39-53.

7. Law, C.K., "Recent Advances in Droplet Vaporization and Combustion", Progress in Energy and Combustion Science 8, 1982, pp. 171-201.

8. Williams, F.A., "Diffusion Flames and Droplet Burning", Chapter 3 of Combustion Theory, Second Edition, Benjamin/Cummings Publ. Co., Menlo Park, CA, 1985, pp. 52-91.

9. Law, C.K. and Williams, F.A., "Kinetics and Convection in the Combustion of Alkane Droplets", Combustion and Flame, 1972, pp. 393-405.

10. Williams, F.A., "On the Assumptions Underlying Droplet Vaporization and Combustion Theories", Journal of Chemical Physics 33, 1960, pp. 133-144.

11. Law, C.K., "Unsteady Droplet Combustion with Droplet Heating", Combustion and Flame 26, 1976, pp. 17-22.

12. Law, C.K. and Sirignano, W.A., "Unsteady Droplet Combustion with Droplet Heating II. Conduction Limit", Combustion and Flame 28, 1977, pp. 175-186.

13. Williams, F.A., "Studies of Experiments on Droplet Burning at Reduced Gravity", Proceedings of the 4th European Symposium on Materials Sciences Under Microgravity, Madrid, ESA SP-191, 1983, pp. 191-196.

14. Antaki, P. and Williams, F.A., "Transient Processes in a Non-Rigid Slurry Droplet During Liquid Vaporization and Combustion", Combustion Science and Technology 49, 1986, pp. 289-296

15. Antaki, P. and Williams, F.A., "Observations on the Combustion of Boron Slurry Droplets in Air", Combustion and Flame 67, 1987, pp. 1-8.

16. Waldman, C.H., "Theory of Non-Steady State Droplet Combustion", Fifteenth Symposium (International) on Combustion, The Combustion Institute, Pittsburgh, 1975, pp. 429-442.

17. Crespo, A. and Liñán, A., "Unsteady Effects in Droplet Evaporation and Combustion", Combustion Science and Technology 11, 1975, pp. 9-18.

18. Law, C.K., Chung, S.H. and Srinivasan, N., "Gas-Phase Quasi-Steadiness and Fuel Vapor Accumulation Effects in Droplet Burning", Combustion and Flame 38, 1980, pp. 173-198.

19. Matalon, M. and Law, C.K., "Gas-Phase Transient Diffusion in Droplet Vaporization and Combustion", Combustion and Flame 50, 1983, pp. 219-229; 59, 1985, pp. 213-215.

20. Kumagai, S. and Isoda, H., "Combustion of Fuel Droplets in a Falling Chamber", Sixth Symposium (International) on Combustion, Reinhold Publishing Corp., New York, 1957, pp. 726-731.

21. Kumagai, S., Sakai, T. and Okajima, S., "Combustion of Free Fuel Droplets in a Freely Falling Chamber", Thirteenth Symposium (International) on Combustion, The Combustion Institute, Pittsburgh, 1971, pp. 779-785.

22. Okajima, S. and Kumagai, S., "Further Investigations of Combustion of Free Droplets in a Freely Falling Chamber Including Moving Droplets", Fifteenth Symposium (International) on Combustion, The Combustion Institute, Pittsburgh, 1975, pp. 401-407.

23. Tarifa, C.S., "On the Influence of Chemical Kinetics on the Combustion of Fuel Droplets", Congres Internacional des Machines a Combustion, Paper B9, A. Busk, Copenhagen, 1962.

24. Tarifa, C.S., del Notario, P.P. and Garcia Moreno, F., "Combustion of Liquid Monopropellants and Bipropellants in Droplets", Eighth Symposium (International) on Combustion, Williams and Wilkins Co., Baltimore, 1962, pp. 1035-1056.

25. Law, C.K., "Asymptotic Theory for Ignition and Extinction in Droplet Burning", Combustion and Flame 24, 1975, pp. 89-98.

26. Liñán, A., "The Asymptotic Structure of Counterflow Diffusion Flames for Large Activation Energy", Acta Astronautica 1, 1974, pp. 1007-1039.

27. Williams, F.A., "A Review of Flame Extinction", Fire Safety Journal 3, 1981, pp. 163-175.

28. Kent, J.H. and Williams, F.A., "Extinction of Laminar Diffusion Flames for Liquid Fuels", Fifteenth Symposium (International) on Combustion, The Combustion Institute, Pittsburgh, 1975, pp. 315-325.

29. Seshadri, K. and Williams, F.A., "Structure and Extinction of Counterflow Diffusion Flames above Condensed Fuels: Comparison between Poly(methyl Methacrylate) and Its Liquid Monomer, Both Burning in Nitrogen-Air Mixtures", Journal of Polymer Science: Polymer Chemistry Edition 16, 1978, pp. 1755-1778.

30. Yap. L., "Some Fundamental Studies of Disruptive Burning Phenomena of Isolated Droplets", Ph.D. Thesis, Department of Mechanical and Aerospace Engineering, Princeton University, Princeton, NJ 1986.

31. Peters, N. and Seshadri, K., "Asymptotic Analysis of the Structure of a Methane-Air Diffusion Flame Using a Three-Step Chemical-Kinetic Mechanism", in preparation, 1987.

32. Treviño, C. and Williams, F.A., "An Asymptotic Analysis of the Structure and Extinction of Methane-Air Diffusion Flames", in preparation, 1987.

33. Lasheras, J.C., Fernandez-Pello, A.C. and Dryer, F.L., "Initial Observations on the Free Droplet Combustion Characteristics of Water-in-Fuel Emulsions", Combustion Science and Technology 21, 1979, pp. 1-14.

34. Lasheras, J.C., Fernandez-Pello, A.C. and Dryer, F.L., "Experimental Observations on the Disruptive Combustion of Free Droplets of Multicomponent Fuels", Combustion Science and Technology 22, 1980, pp. 195-209.

35. Lasheras, J.C., Fernandez-Pello, A.C. and Dryer, F.L., "On the Disruptive Burning of Free Droplets of Alcohol/n-Paraffin Solutions and Emulsions", Eighteenth Symposium (International) on Combustion, The Combustion Institute, Pittsburgh, 1981, pp. 293-305.

36. Avedision, C.T. and Sullivan, J.R., "A Generalized Corresponding States Method for Predicting the Limits of Superheat of Mixtures", Chemical Engineering Science 39, 1984, pp. 1033-1041.

37. Saito, K., Williams, F.A. and Gordon, A.S., "Effects of Oxygen on Soot Formation in Methane Diffusion Flames", Combustion Science and Technology 47, 1986, pp. 117-138.

38. Berlad, A.L., Huggett, C., Kaufman, F., Markstein, G.H., Palmer, H.B. and Yang, C.H., "Study of Combustion Experiments in Space", NASA CR-134744, 1974.

39. Williams, F.A., "Droplet Burning at Zero G", NASA CR-159531, NASA Lewis Research Center, Cleveland, February, 1979.

40. Williams, F.A., "Droplet Burning", Chapter 11 of Combustion Experiments in a Zero-Gravity Laboratory, edited by Cochran, T.H., Vol. 73 of Progress in Astronautics and Aeronautics, American Institute of Aeronautics and Astronautics, New York, 1981, pp. 31-60.

41. Haggard, J.B. and Kropp, J.L., "Development of a Droplet Combustion Experiment for Low Gravity Operation", AIAA Paper No. 87-0576, January 1987.

42. Knight, B. and Williams, F.A., "Observations on the Burning of Droplets in the Absence of Buoyancy", Combustion and Flame 38, 1980, pp. 111-119.

43. Williams, F.A., "Ignition and Burning of Single Liquid Droplets", Acta Astronautica 12, 1985, pp. 547-553.

44. Shaw, B.D., Dryer, F.L., Williams, F.A. and Gat, N., "Interactions between Gaseous Electrical Discharges and Single Liquid Droplets", in Chemical and Physical Processes in Combustion, Fall Meeting, Eastern Section of the Combustion Institute, San Juan, Puerto Rico, December 15-17, 1986, pp. 54-1 - 54-4.

FLUIDS AND TRANSPORT PHENOMENA

PRECEDING PAGE BLANK NOT FILMED

N89-20314

SURFACE TENSION DRIVEN CONVECTION EXPERIMENT

Simon Ostrach and Yasuhiro Kamotani
Department of Mechanical and Aerospace Engineering
Case Western Reserve University
Cleveland, Ohio 44106

I. INTRODUCTION

Thermocapillary flow is driven by a thermally induced surface tension variation along a liquid free surface. In the earth-gravity environment such flows are usually overshadowed by buoyancy driven flows, but at reduced gravity conditions their influence could be significant ([1]). Among various types of flows that can occur at low-gravity thermocapillary flows are perhaps the most interesting not only scientifically but also because of their importance to such technological applications as the containerless processing of materials. Therefore with the advent of the microgravity sciences and applications program considerable attention began to be given to thermocapillary flows.

We at Case Western Reserve University started a comprehensive theoretical and experimental research program on the subject as early as 12 years ago and it is still being continued. Our past work as well as the work done by others is summarized in Chapter II. From those studies it became apparent that thermocapillary flows are very complex and that there are several serious limitations to the ground-based work. Therefore, experiments at low-gravity are needed in order to understand better such complex flows. The justification for low-gravity experiments is presented in Chapter III.

Our original design of a space experiment, which started about 10 years ago, was intended to demonstrate thermocapillary flow in a reduced-gravity environment. Since then the scope of the experiment has been expanded so that quantitative

PRECEDING PAGE BLANK NOT FILMED

scientific tests will be performed in space. The Science Requirements Document (SRD) for the expanded experiment was issued in 1985 and was reviewed by the PACE science review board. To clarify aspects raised by the board the SRD was revised and accepted in June 1985 by the board. The Conceptual Design Review of the experiment was held in November, 1985 and because of the Challenger accident the board asked us to expand further the scope of the experiment to reflect decreased reflight possibilities. The current science requirements are based on this further expansion and are discussed in Chapter IV.

To obtain as much information as possible from the proposed experiments it is necessary to continue our ground-based research work especially on oscillaory thermocapillary flow. The support work is described in Chapter V.

II. PAST WORK ON THERMOCAPILLARY FLOW

Since several papers (e. g. [1-3]) discuss in detail the past work on thermocapillary flow and its importance in crystal growth, only the work pertinent to the proposed experiment is discussed herein.

Ostrach [2] derived by a formal procedure the important dimensionless parameters for thermocapillary flow including the effect of buoyancy. The work shows that in liquids other than liquid metals thermocapillarity is dominated by buoyancy in a normal gravity environment unless the system is made very small. Flat and rigid free surfaces were assumed in the work. The important parameters in reduced gravity with flat free surfaces are:

Marangoni number, $Ma = \partial\sigma/\partial T \;\; \Delta TH/\mu\alpha$

Prandtl number, $Pr = \nu/\alpha$

aspect ratio, $Ar = H/L$

where $\partial \alpha / \partial T$ is the variation of surface tension with temperature, ΔT the overall temperature variation along the free surface, μ the viscosity of the fluid, ν the kinematic viscosity, α the thermal diffusivity, and H and L are the depth and length of the fluid domain.

Because of difficulties in investigating thermocapillary flows experimentally over wide ranges of parameters in one-g the effects of the above parameters on the flows were studied mainly by numerical analyses. Clark and Wilcox [4] investigated thermocapillary flow in floating zone. They imposed fixed surface temperature distributions, thereby missing an important feature of the flow, namely, the coupling between the surface temperature distribution, which is directly related to the driving force of the flow, and the velocity field. Fu and Ostrach [5] were the first to study the coupling phenomenon over wide ranges of Ma, Pr, and Ar. It is shown in that work that with increasing Ma the surface temperature distribution tends to be relatively flat over a large part of the free surface and sharp temperature drops occur in small regions adjacent to the hot and cold ends, so the flow is mainly driven in those corner regions. Recent numerical analyses [6, 7] improved the numerical accuracy of Fu and Ostrach but their accuracy is still poor beyond about $Ma = 5 \times 10^4$ due to the existence of very thin corner regions.

Experimentally Ostrach and Pradhan [8] demonstrated the existence of thermocapillary flow in reduced gravity in drop tower tests. Chun and Wuest [9] and Schwabe et al. [10] studied thermocapillary flows in small floating zones. Those two groups also found a transition from steady to oscillatory convection ([11, 12]), which they claimed occurred beyond a critical Ma. Kamotani et al. [13] conducted an extensive experimental study on the effects of various parameters on the onset of oscillation and concluded that Ma is not the only parameter to determine the onset. They suggested that flexibility of the free surface could play an important role and thus the capillary number (Ca) should be an important dimensionless parameter for oscillation. The idea was supported by the experimental data, which indicated that the oscillations are a result of coupling among the free-surface temperature distribution, the velocity field, and the free-surface shape (return flow). Subsequently Lai et al. [14] confirmed the idea mainly by a physical and scaling argument. They showed that the oscillation originates in the corner regions and the surface flexibility is represented by the parameter $S = (1/Pr)\ (|\partial\sigma/\partial T|\Delta T/\sigma)$, which can be called a modified capillary number. The parameter is the ratio of the surface deformation time scale to the thermal-diffusion time scale in the corner regions. Based on the data taken in float-zones the oscillation occurs when Ma is above 10^4 and S is larger than about 1.4×10^{-3}. Napolitano et al. [15, 16] conducted experiments in space with large float-zones ($\sim$ 10 cm, Ma $\sim 5 \times 10^5$) but did not observe oscillations, probably because S was too small. Not much is known about oscillations in other configurations. Lee and Kamotani [17] used a small rectangular container (< 1 cm) and heated the fluid by a thin wire spun across the container in the middle. They observed oscillations but they were of a different type caused by a Kelvin-Helmhotz instability along the interface between the surface flow and the relatively quiescent bulk fluid, in other words, the fluid was thermally stratified.

Theoretically the effect of free surface deformation on thermocapillary flow has been investigated in the past. Sen and Davis [18] solved steady thin liquid-layer problems in a two dimensional slot including surface deformation under zero-gravity by asymtotic expansion and matching techniques. Strani et al. [19] also treated a similar problem both by asymptotic theory and numerical solution, in which the surface deformation was shown to have a negligible influence on the steady flow field structure in the ranges of parameters encountered in practice. Pimputkar and Ostrach [20] were the first to discuss the transient phenomena of thermocapillary flows in thin-liquid layers. A formal non-dimensionalization was made which indicated an explicit ordering of the equations so that ad hoc assumptions were unnecessary. The flows and surface shapes were determined numerically for a family of different imposed surface temperature distributions.

As for theoretical analysis of the oscillation phenomenon Smith and Davis [21, 22] studied the stability problems of two-dimensional thin liquid layers by using linear stability analysis. They considered separately two types of instabilities called surface modes and thermal modes but did not obtain a proper criterion for the prediction of oscillations as obtained in experiments. It should be noted that their analyses were for very thin liquid layers and the aforementioned coupling was not considered, so the instabilities studied by them are not really related to the oscillation phenomenon observed experimentally in the past.

III. RATIONALE FOR SPACE EXPERIMENT

Despite the past work reviewed above, there are some important unanswered questions about thermocapillary flow:

1. oscillation phenomenon - effects of configuration, surface thermal signature and heating mode
2. flow at large Ma ($> 10^5$) - thin corner regions, contact line behavior, subregions
3. flow in a low-gravity environment - effects of curved free surface at large Ma, g-jitter and free-surface deformability

The main reason why these subjects have not been investigated is that it is extremely difficult to study them in ground-based work due to the following problems.

Experimentally because of the effect of gravity on the free surface and that of buoyancy on the flow predominantly thermocapillary flow can be realized in one-g only in very small configurations (less than a few mm usually). As mentioned above, with liquid metals it is possible to generate thermocapillary flow in a relatively large configuration (~ 10 cm) but the dominant thermocapillarity is limited to the surface flow region only and also the static Bond number is large. Limited regions of thermocapillary flows can be obtained with other fluids when the free surfaces are heated from above to minimize natural convection. Considering the fact that the number of test fluids is limited because of the problem of surface contamination, a small configuration means a small Ma. It is possible to obtain only up to $Ma = 10^4$ in one-g but in actual crystal growth systems Ma can be up to 10^5 or above. Also with a small configuration it is difficult to investigate the flow in detail by quantitative measurements especially in the important corner regions. With increasing Ma the corner regions become thinner (their length scale relative to the geometric length scale is on the order of 1/Ma as discussed in ([23]), so normally small effects in the corners could become important. For example, the contact line behavior (dynamic wetting characteristics, wetting transition, wall corner shape and condition) could influence the flow. It is also possible that with the driving force concentrated in such small regions the flow develops subregions (cells) especially with a curved free surface. In one-g a curved free surface is possible only in a small configuration. The driving force for thermocapillary flow acts in the direction tangent to local free surface, so with a curved surface the driving force direction changes along the surface. This is quite different from the behavior with a flat surface in one-g.

As for numerical analysis of steady thermocapillary flow at large Ma, there are a few serious problems at present. First, to resolve the important corner regions we need a large computational power and an accurate numerical scheme especially with a highly curved free surface. Secondly not all the boundary conditions are well known. It is difficult to specify the contact line conditions accurately. The degree of surface contamination is also difficult to be specified. There is also a possibility that $\partial\sigma/\partial T$ is not the only parameter to describe the surface condition even when the surface is clean [24]. Therefore, as was done in the field of natural convection in the past, numerical work needs to be carefully guided by experiments before they yield meaningful and useful results. A numerical analysis helped design the proposed experiment and it will also complement the experimental data but it cannot replace the experiments.

So far observations of oscillatory thermocapillary flow have been limited to a simulated floating zone configuration in which a small liquid column is suspended vertically between differentially heated cylindrical metal rods. In that situation the free surface is vertical so that a strong surface flow can oppose directly the effect of buoyancy, which makes it easier to avoid thermal stratification. That configuration also makes it easier for the flow to oscillate by allowing azimuthal traveling of disturbances [11]. If we inhibit the traveling, the critical temperature difference increases substantially [13]. In other configurations with horizontal free surfaces the fluid layer tends to be thermally stratified unless the configurations are very small. The stratification gives rise to a Kelvin-Helmholtz type instability before the onset of oscillations associated with thermocapillary flow [17]. It thus seems that the effect of various configurations on the oscillation phenomenon can only be studied in reduced gravity conditions. In the floating zone configuration the heating mode is fixed (imposed temperature difference) and the thermal signatures are more or less independent of other parameters. The effects of heating mode and surface thermal signature can be studied in that configuration (as we are currently doing) but they need to be studied also in other configurations. Numerical analysis of the phenomenon is extremely difficult because, in addition to the problems associated with steady flow analysis discussed above, the flow is unsteady and it is necessary to incorporate the coupling among the free surface shape, the surface thermal signature, and the velocity field. We need to do more work on the subject and, at the same time, considerably more experimental information must be obtained in reduced gravity to guide the numerical work.

In a reduced gravity environment the dynamic behavior of a large free surface is different from that in one-g in that instead of gravity, surface tension controls the behavior. Thus, how the free surface deforms during oscillation cannot be studied accurately in one-g. Besides, the deformation is too small to be measured accurately in one-g. According to our previous study [25] the effect of g-jitter on the free surface motion is negligible as long as its level is kept less than 10^{-4}g. However, at large Ma even a small free surface motion near the contact lines could induce a large change in the flow structure for the reasons discussed above.

IV. DESCRIPTION OF SPACE EXPERIMENTS

Experiments on thermocapillary flow in reduced gravity have been proposed to study the following aspects:

1. the extent and nature of thermocapillary flows at large Ma ($> 10^4$)
2. temperature distributions along the free surface and in the bulk fluid, and their effect on the flow fields
3. the effect of heating mode on the flows
4. the effect of the liquid free surface shape on the flows
5. the onset conditions and nature of oscillatory flows

The study of the oscillation phenomenon is expected to be a difficult one, so the experimental system to study it in detail requires preliminary information from space experiments and continued ground-based work. For this reason two experimental series are proposed to accomplish the above objectives: the first one in which the first four items in the above list will be studied and the second one in which the oscillations will be the main subject. Attempts will be made in the first experiment to make the flow oscillatory. Only the design and procedure of the first experiment are described herein. A more complete description is given in [26].

4.1 Experimental Design

In the proposed experiment a circular dish of 10 cm in diameter and 5 cm in depth will be used to hold the test fluid (Fig. 1). A circular geometry is chosen to make the flow axisymmetric to simplify the analysis and to maintain the axisymmetry even when the free surface is highly curved. A floating zone configuration is also an important one especially because the oscillation phenomenon has been studied in that geometry on the ground. However, the latter configuration is being studied in space by Napolitano et al. [15, 16] and it is not a convenient configuration to impose various surface heat fluxes. The dimension of the container is chosen for the convenience of flow observation. The test fluid will be 10 centistokes silicone oil ($Pr \approx 100$). It is safe and transparent, and it has been found to be reasonably insensitive to surface contamination. Its viscosity value gives the desired Ma range. The fluid will be heated in two ways as illustrated in Fig. 1. In one case the fluid will be heated by an outside heating source to impose fixed heat flux distributions along the free surface (called CF (constant heat flux) tests herein). In the other case a cylindrical heater (1 cm dia.) will be placed at the center of the container to impose fixed overall temperature differences along the free surface (CT (constant temperature) tests). In the CF tests both the heating zone diameter and the total heat flux will be varied while in the CT tests only the imposed temperature difference (ΔT) will be varied. At the present a CO_2 laser seems to be a good heating source in the CF tests because the heating area can be easily adjusted by a lens and it has been found to be absorbed readily by silicone oil (within about 0.2 cm depth). The side wall of the container will be cooled by forced liquid flow around it in order to maintain a uniform temperature over the side wall and to minimize the time to reach steady conditions. In most of the tests the free surfaces will be kept flat to simplify the analysis and measurement. In the tests with curved free surfaces the amounts of the fluid in the container will be adjusted to obtain the surface shapes shown in Fig. 2. The situation with 0 deg. apparent contact angle is avoided to maintain a well defined contact line position.

The flow field will be studied by flow visualization. Particles of order several microns will be mixed with the test fluid. A cross-section of the container will be illuminated by a laser sheet and the particle motions in the plane will be recorded by a sufficiently high resolution recording system (video system or movie camera). (Fig. 3). The temperature field will be studied by thermocouples (a thermistors) which will be placed at specified locations in the fluid. The surface temperature distribution will be measured by a scanning radiometer which will create an infrared image of the surface from which the surface temperature distribution will be determined. A numerical analysis of the flow will complement the measurements.

4.2 Experimental Procedure

Two heating modes (CF and CT experiments) will be studied. In the CF experiment a total of seven tests will be conducted with various total heat inputs and heating zone diameters. The conditions for those tests are summarized in Table 1. In one test the flow will be observed from the initial quiescent state to the final steady state to study the complete time history of the flow development, which is expected to take about one hour according to our numerical calculation. Other tests will be conducted successively with each test lasting 10 minutes, which is about the time for the velocity field to become nearly steady. The free surface will be curved in two tests. Because of the surface curvature the flow visualization and the surface temperature measurement are inaccurate in some regions especially near the control line, so we will investigate ways to correct the errors as much as possible.

A total of five tests will be conducted in the CT experiment with various values of ΔT and two free surface shapes as summarized in Table 2. Again one run is for complete flow development study.

In both CF and CT experiments the values of Ma and S are selected so that in some cases their values far exceed those critical values for the onset of oscillation in floating zones.

V. SUPPORTING GROUND-BASED WORK

To obtain as much useful information as possible from the space experiments three main subjects are being studied: the experimental techniques, the thermocapillary flow and oscillation phenomenon, and the numerical analysis.

5.1 Experimental Techniques

Some experimental techniques employed for the proposed experiments are being evaluated and calibrated.

In the thermography technique used to measure the free surface temperature it is important to relate what is measured to the surface temperature. The radiation detected by the instrument comes from a finite thickness layer below the surface, so if there is a large temperature variation within that layer, the measured temperature could be much different from the surface temperature. With the laser heating the temperature gradient tends to be very large near the surface, so the problem needs to be carefully assessed. The system is being calibrated using an arrangement identical to the proposed setup in conjunction with the numerical analysis.

The quality of information we can extract from the flow visualization technique depends on several factors. At present we are working on the resolution of the recording system. A movie camera is preferred over a video system because of its high image quality but the recording time of the former presents a problem and a real time transmission of the experimental data to the ground (if available) requires the latter.

When we study the oscillation phenomenon in the second space experiment, the free surface motion will be analyzed in detail. Since it is expected to be small, an accurate optical system to measure a small deflection needs to be developed.

5.2 Study of Thermocapillary Flow

At present it is very important that we learn more about the oscillation phenomenon under various conditions. Experimentally we are testing configurations, heating modes and fluids including a miniature model of the space experiment to see whether and when the flows become oscillatory by thermocapillarity. Theoretically we are trying to incorporate the flexibility of the free surface into a relatively simple thermocapillary flow model to see if it is possible thereby to obtain oscillatory flows.

The effect of the corner region on thermocapillary flow at high Ma is another important subject. In the analysis of the flow the contact line is mathematically singular and, moreover, a wetting transition could occur in the region, so if the flow becomes driven mainly in that region at high Ma, the analysis could be difficult. On the other hand, a very minute amount of contamination could nullify the corner region especially the cold corner region toward which the flow (and the surface contaminants, if present) is driven. The subject is being studied experimentally and numerically.

5.3 Numerical Analysis

The existing finite difference program used in our past studies of thermocapillary flows is being modified to analyze large Ma ($> 5 \times 10^4$) flow accurately. Smaller grid sizes and increased number of grids are required. The CRAY X-MP24 system at NASA Lewis will be used to speed up the computations.

As mentioned above, we are also developing numerical programs to study the oscillations and the effect of the corner regions. The former includes the flexibility of the free surface. In the latter program the effect of curved free surfaces is included because the corner region is expected to be very much influenced by the free surface shape.

REFERENCES

1. Ostrach, S., Annual Review of Fluid Mechanics, Vol. 14, 1982, 313-345.

2. Ostrach, S., Proc. Int. Conf. Physico Chemical Hydrodynamics (Levich Conference 1977) Advanced Publications, 1977.

3. Schwabe, D., PCH Physico Chemical Hydrodynamics, Vol. 2, No. 4, 1981, 263-280.

4. Clark, P. A. and Wilcox, W. R., J. Crystal Growth, Vol. 50, 1980, 461-469.

5. Fu, B-I. and Ostrach, S., Proc. 4th European Symposium on Materials Sciences under Microgravity, 1983, 239-245.

6. Zebib, A., Homsy, G. M. and Meiburg, E., Physics of Fluids, Vol. 28, 1985, 3467-3476.

7. Bergman, T. L. and Ramadhyani, S., Numerical Heat Transfer, Vol. 19, 1986, 441-451.

8. Ostrach, S. and Pradhan, A., AIAA J., Vol. 16, No. 5, 1978, 419-424.

9. Chun, Ch.-H. and Wuest, W., Acta Astronautica, Vol. 5, 1978, 681-606.

10. Schwabe, D., Scharmann, A., Preisser, F. and Oeder, R., J. Crystal Growth, Vol. 43, 1978, 305-312.

11. Chun, Ch.-H. and Wuest, W., Acta Astronautica, Vol. 6, 1979, 1073-1082.

12. Schwabe, D. and Scharmann, A., J. Crystal Growth, Vol. 46, 1979, 125-131.

13. Kamotani, Y., Ostrach, S. and Vargas, M., J. Crystal Growth, Vol. 66, 1984, 83-90.

14. Lai, C. L., Ostrach, S. and Kamotani, Y., Proc. 1985 U. S.-Japan Heat Trjansfer Joint Seminar, San Diego, 1985.

15. Napolitano, L. G., Monti, R. and Russo, G., Proc. 5th European Symposium on Material Sciences and Microgravity, 1984.

16. Napolitano, L. G., Monti, R. and Russo, G., Naturwissenschaften, 1986, 352-355.

17. Lee, K-J., M. S. Thesis, Case Western Reserve University, 1986.

18. Sen, A. K. and Davis, S. H., J. Fluid Mech., Vol 121, 1982, 163-186.

19. Strani, M., Riva, R. and Graziani, G., J. Fluid Mech., Vol. 130, 1983, 347-376.

20. Pimputkar, S. and Ostrach, S., Phys. Fluids, Vol. 23, 1980, 1281-1285.

21. Smith, M. K. and Davis, S. H., J. Fluid Mech., Vol. 132, 1983, 119-144.

22. Smith, M. K. and Davis, S. H., J. Fluid Mech., Vol. 132, 1983, 145-162.

23. Lai, C. L., Ph.D. Thesis, Case Western Reserve University, 1984.

24. Neuhaus, D., Naturwissenschaften, 1986, 348-349.

25. Ostrach, S. and Kamotani, Y., Science Requirements Document, 1985.

26. Kamotani, Y. and Ostrach, S., J. Thermophysics and Heat Transfer, Vol. 1, No. 1, 1987, 83-89.

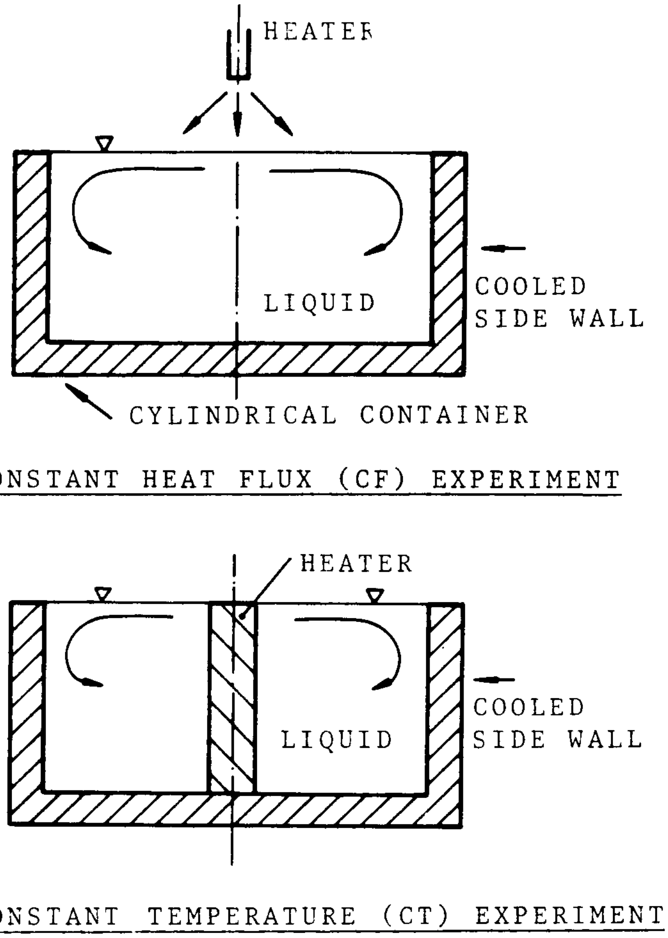

Fig. 1 Surface tension driven convection experiment

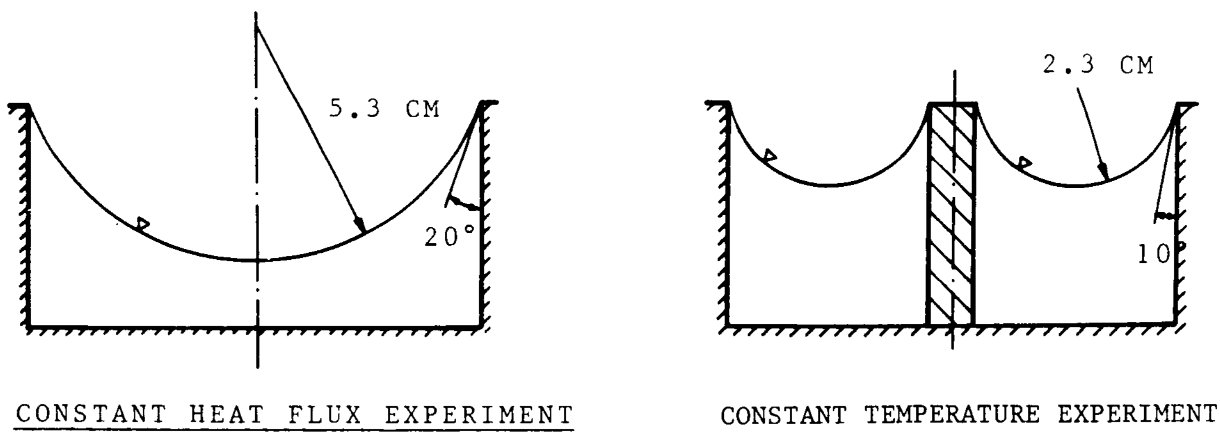

Fig. 2 Experiments with curved free surfaces

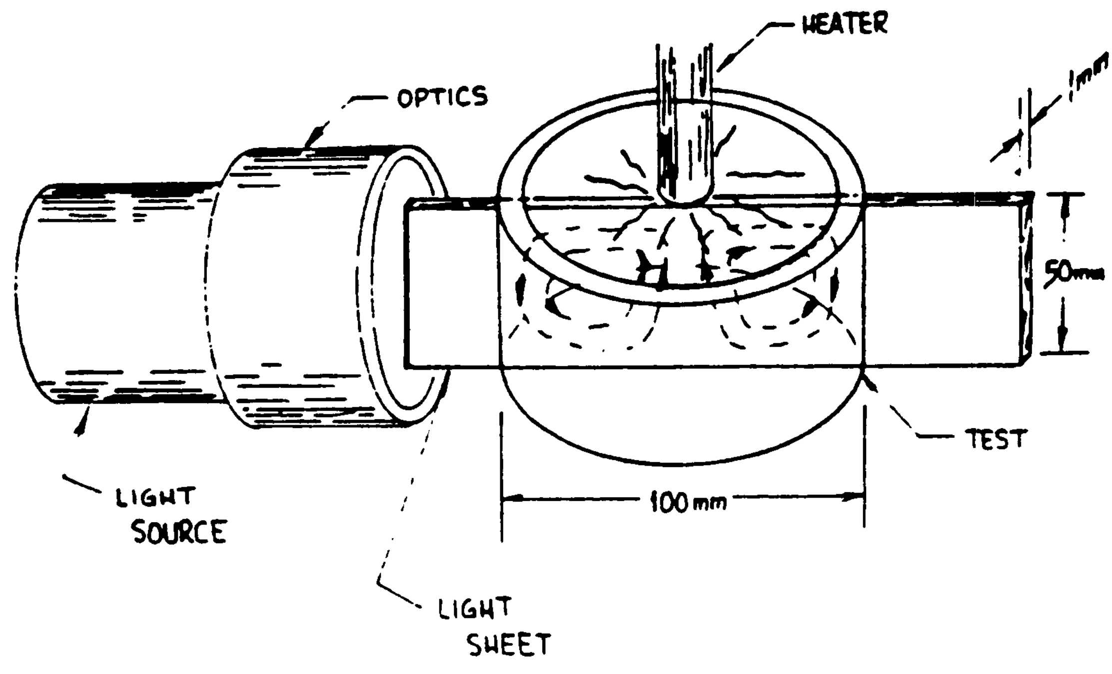

Fig. 3 Flow visualization system

Test No.	Heating Zone Dia. (mm)	Total Power (W)	ΔT (°C)	Ma	Free Surface Shape	Duration (min)
1	10	.5	10.4	4.2×10^4	flat	60
2	10	3.0	36.8	1.5×10^5	"	10
3	30	3.0	12.4	5.0×10^4	"	10
4	5	0.2	10.2	4.1×10^4	"	10
5	5	3.0	64.7	4.4×10^5	"	10
6	5	3.0	-	-	curved	10
7	30	3.0	-	-	"	10

The values of ΔT and Ma are computed by numerical analysis.

Table 1 Constant heat flux (CF) tests

Test No.	ΔT (°C)	Ma	Heater Power (W)	Free Surface Shape	Duration (min)
8	10	3.9×10^4	1.5	flat	60
9	25	1.2×10^5	6.8	"	10
10	60	4.1×10^5	32.8	"	10
11	≈ 10	3.2×10^4	1.5	curved	10
12	≈ 60	3.3×10^5	32.8	"	10

The values of heater power are computed by numerical analysis.

The values of ΔT for curved surface are estimates and Ma are based on average liquid depth.

Table 2 Constant temperatute (CT) tests

N89-20315

ELECTROMAGNETIC, HEAT AND FLUID FLOW PHENOMENA IN LEVITATED METAL DROPLETS BOTH UNDER EARTHBOUND AND MICROGRAVITY CONDITIONS

Julian Szekely
Room 4-117, MIT
Cambridge, MA 02139
Principal Investigator

INTRODUCTION

The purpose of this investigation is to develop an improved understanding of the electromagnetic, heat and fluid flow phenomena in electromagnetically levitated metal droplets, both under earthbound and microgravity conditions. In the following, we shall discuss the main motivation for doing this work, together with the past accomplishments and the plans for future research.

MOTIVATION

The main motivation for this work lies in the following:

(1) The electromagnetic, heat transfer and mass transfer problems in levitated metal droplets pose important fundamental scientific issues; here we are concerned with both laminar

and turbulent recirculating flows in a spherical (or distorted spherical) system driven by an electromagnetic force field. Due to the curvilinear nature of the system, significant damping of the turbulence will occur in the vicinity of the free surface; furthermore, there are important issues of velocity transients and the laminar/turbulent transition which are little explored. Finally, in levitation melting there are important problems of surface stablity and surface wave formation. A fundamental understanding of these phenomena could well provide the key to electromagnetic near net shape casting--a topic of very great current interest.

(2) Electromagnetically driven flows are of great technical importance in materials processing, including induction furnaces, electromagnetic stirring, welding, plasmas, electromagnetic casting, and confinement. An improved fundamental understanding of these phenomena could greatly improve the efficiency and effectiveness of these operations.

(3) The Electromagnetic Levitator is a key item in materials processing in space, because it allows containerless processing and ready heating and quenching of specimens. The numerous research projects using the EML for undercooling and alloy development studies would greatly benefit from a precise, quantitative description of the transient velocity, tempera-

ture and composition fields in these systems. Indeed, the availability of this information could be an important component of these studies.

THE NEED FOR MICROGRAVITY

In studying levitation melting under earthbound conditions, quite high currents have to be employed in order to levitate the specimens; this will necessarily lead to turbulent flow conditions and frequently to flow instabilities. Furthermore, when performing levitation melting studies on earth, significant deformation of the specimen will occur due to the force of gravity. In fact, levitation-melted specimens are never spherical on earth, but have an "inverted teardrop" shape. On performing levitation under microgravity, much lower currents will suffice to position the specimen, once it has been melted, so that one can study the laminar flow regime and the turbulent-laminar transition as well as turbulent conditions. Furthermore, the specimen will retain its spherical shape, which will make the analysis of both flow and instability phenomena much more straightforward.

ACCOMPLISHMENTS TO DATE

The purpose of the research has been to perform mathematical model development and to carry out ground-based experiments in order to allow rational planning of the in-flight studies.

The principal accomplishments to date may be summarized as follows:

(1) Through the statement and numerical solution of Maxwell's equations and the laminar/turbulent Navier-Stokes equations for a system with spherical symmetry, we were able to represent the temperature, velocity and concentration fields in levitated metal droplets under both earthbound and microgravity conditions (1,2,3,6,8). The theoretical predictions for the lift force and for mass transfer were in excellent agreement with the experimental measurements.

Here Fig. 1 shows the computed lift as a function of position; also shown is the weight of the droplet used in the experiment. The conditions depicted represented the threshold of the onset of levitation--in agreement with the measurements.

Fig. 2 shows the computed velocity fields in levitation melted specimens for earthbound conditions, while Fig. 3

shows a comparison between experimentally measured carburization rates and those predicted on the basis of the model.

Finally, Fig. 4 shows the computed circulation field for μg conditions. It is seen that under these conditions, the nature of the circulation is quite different, because of the symmetry; i.e. the droplet does not "sag" due to gravity.

(2) As part of this work, we have developed a general technique for calculating the electromagnetic force field and the corresponding velocity fields in inductively stirred vessels. The theoretical predictions were found to be in very good agreement with measurements (7,9,10,11,12,13).

Of the many possible examples, Figs. 5, 6, and 7 show a comparison between the experimentally measured and the theoretically predicted velocity fields in inductively stirred vessels. The excellent agreement is readily apparent.

(3) Work has also been done to represent the damping of convection that is attainable using an externally imposed magnetic field, and it was shown that convection cannot be readily damped under these conditions (5).

(4) Work has also been done to develop the technique of velocity measurement in molten Woods metal using hot film anemometry (4).

CURRENTLY ONGOING RESEARCH

Research is currently proceeding in the following areas:

(1) We are developing the computational algorithm to represent the electromagnetic force field produced by induction coils in the presence of a metallic body hav ing unbounded (free) surfaces. This will allow us to represent accurately the deformation and the onset of surface instabilities, important not only in the accurate analysis of the levitation measurements, but also in the electromagnetic deformation processing of metals in general.

(2) We are developing techniques for the measurements of surface velocities by means of tracers and time-lapse photography for levitation-melted specimens. Here, the streaklines will give us both the magnitude and the direction of the velocities. This work is a crucial component of the planned in-flight experiments.

Here, Fig. 8 shows a photograph of an inductively heated specimen in an induction coil; the picture was taken by Dr. H. Edgerton. Figs. 9 and 10 show the streaklines obtained on the surface of a silver specimen at two different current levels.

Analysis of the streaklines has shown that at the lower current, velocities were of the order of 1-2 cm/s, while at the higher current, velocities were of the order of 6-7 cm/s.

(3) We are continuing with our work to study electromagnetically driven flows in molten Woods metal, as produced by a diverging current path between two electrodes, to compare theoretical predictions with measurements. This research is helpful for the independent testing of the model predictions.

THE PROPOSED FLIGHT EXPERIMENTS

The proposed in-flight experiments would involve levitation melting of a silver or gold alloy specimen about 1 cm in diameter, and tracking the path of tracer particles by using time-lapse photography. A major attraction of this technique is that the tracers would not have to be deposited on the surface, but would be contained in the sample prior to the flight. This has been proven in the laboratory. As per the results of the ground-based laboratory experiments, exposure times of the order of 1/10-1/30 of a second would give good streaklines.

Experiments would be carried out under conditions when the flow is quite turbulent, and upon reducing the current we would trace the trajectory of the system through the turbulent-laminar transition. Furthermore, the photographs taken will also provide information on the presence of surface waves and on the time-dependent shape of the metallic specimens.

The mathematical models predicting the steady state electromagnetic, temperature and velocity fields for an idealized spherical metal droplet are in place and may be run routinely, providing a first-level interpretation of the measurements. More refined models, allowing for deformation and transient behavior, are currently under development, and will be ready well before the time of the proposed in-flight experiments.

SUMMATION

The proposed in-flight experiments have both fundamental significance and important applications, earthbound and within the context of materials processing in space. Significant preparatory work has been carried out which in its own right has made major contributions to the understanding of electromagnetically driven flows. The preparatory ground-based work has been completed or is shortly to be finished; thus, the project has an excellent chance of success. Furthermore, the proposed work relies critically on the unique attributes of the microgravity environment. More specifically:

-- The proposed research addresses the fundamental issues of electromagnetically driven flow in spherical or near-spherical droplets, and the associated deformation and surface stability.

-- This work is important within the space processing context, because electromagnetic levitation is a standard tool of materials preparation in microgravity. Our research will allow precise definition of the flow and temperature conditions under which these experiments are carried out.

-- The work done to date, and the future work planned, have had, and will have, significant "fallout," helping the earthbound materials and metals processing industry through an improved understanding of electromagnetically driven flows and electromagnetic containment.

-- Microgravity is essential for this work, as laminar flow or turbulent/laminar transitions could not be achieved under earthbound conditions; furthermore, the nature of free surface behavior and free surface stability would be very different in the presence and the absence of gravity.

Significant, well-documented accomplishments have been made as part of this research to date, including computational methodology for handling the electromagnetically driven flow of molten metals. These calculations, together with ground-based experiments, provide an excellent basis for planning the in-flight research.

BIBLIOGRAPHY

1. El-Kaddah, N., and Szekely, J., "Heat Transfer and Fluid Flow in Levitation Melted Droplets," Materials Research Society Symposium on Materials Processing in Reduced Gravity Environment (Rindone, G., ed.), 1982, p. 191.
2. El-Kaddah, N. and Szekely, J., "The Turbulent Recirculating Flow Field in a Coreless Induction Furnace: A Comparison of Theoretical Predictions with Measurements," J. Fluid Mechanics, 133, 37 (1983).
3. El-Kaddah, N. and Szekely, J., "The Electromagnetic Force Field Fluid Flow Field and Temperature Field in Levitation Melted Droplets," Met. Trans. 14B, 401 (1983).
4. Murthy, A. and Szekely, J., "Hot Film Anemometry in Molten Woods Metal," Met. Trans. B, 14B, 499 (1983).
5. Oreper, G. and Szekely, J., "The Effect of a Magnetic Field on Transport Phenomena in a Bridgman-Stockbarger Crystal Growing System," J. Crystal Growth 67, 405-419 (1984).
6. El-Kaddah, N. and Szekely, J., "Heat and Fluid Flow in Levitation Melted Sphere Under Zero Gravity Conditions," Met. Trans. 15B, 183 (1984).

7. El-Kaddah, N., Szekely, J. and Carlsson, G., "Fluid Flow and Mass Transfer in a 4-Ton Inductively Stirred Melt," Met. Trans. 15B, 633 (1984).

8. Frost, R.T., Flemings, M.C., Szekely, J., El-Kaddah, N., and Shiohara, Y., "Electromagnetic Containerless Undercooling Facility and the Space Shuttle," Adv. Space Research 4(5) (1984).

9. El-Kaddah, N., Szekely, J., Taberlet, E. and Fautrelle, Y., "Turbulent Recirculating Flow in Induction Furnaces: A Comparison of Measurements with Predictions over a Range of Operating Conditions," Met. Trans. B (1987), in press.

10. Meyer, J.-L., Szekely, J., and El-Kaddah, N., "Calculation of the Electromagnetic Force Field for Induction Stirring in Continuous Casting," Trans. Iron and Steel Institute of Japan (1987), in press.

11. Meyer, J.-L., N. El-Kaddah, and Szekely, J., "A New Method for Computing Electromagnetic Force Fields in Induction Furnaces," IEEE Transactions on Magnetics, in press (1987).

12. Meyer, J.-L., El-Kaddah, N., Szekely, J., Vives, C., and Ricou, R., "A Comprehensive Study of the Induced Current, the Electromagnetic Force Field and the Velocity Field in a Complex Electromagnetically Driven Flow System," Met. Trans. B, in press (1987).

13. Meyer, J.-L., Szekely, J., El-Kaddah, N., Vives, C., and Ricou, R., "Electromagnetic and Fluid Flow in the Electromagnetic Casting of Aluminum," Met. Trans. B, in press (1987).

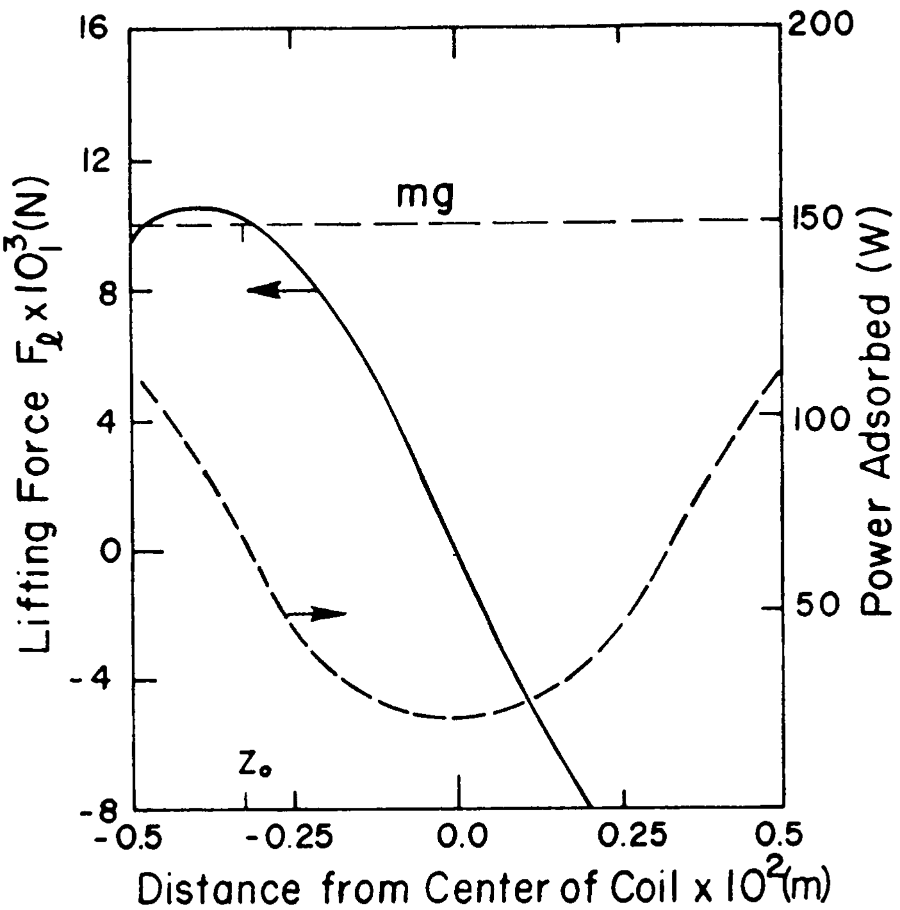

Fig. 1—Computed lifting force and power adsorption for a molten iron droplet along the axis of the coil. Coil current 250 Amp.

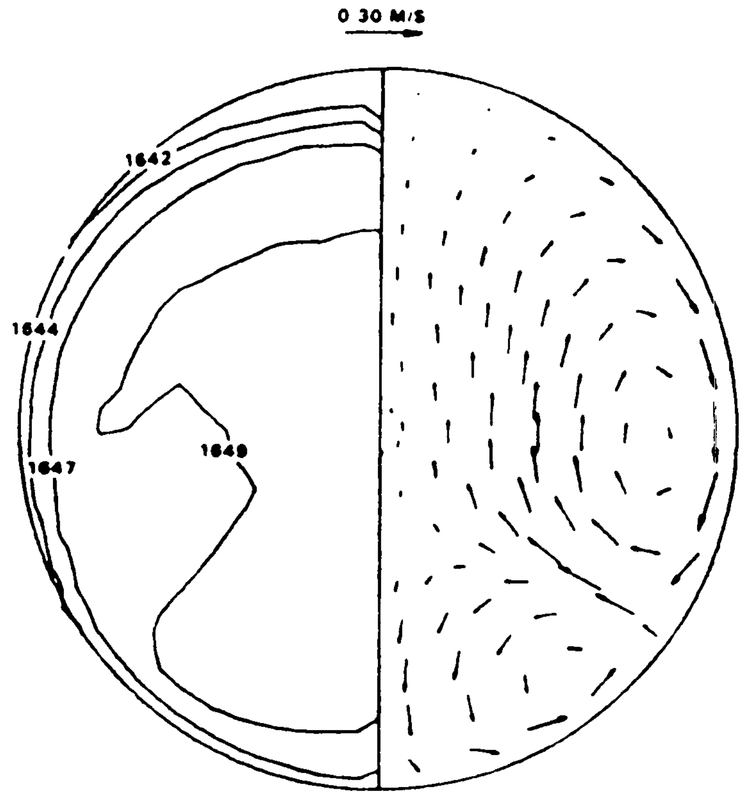

Fig. 2 Computed velocity field and temperature for a 6 mm iron droplet in earthbound gravity force (coil current = 250 A).

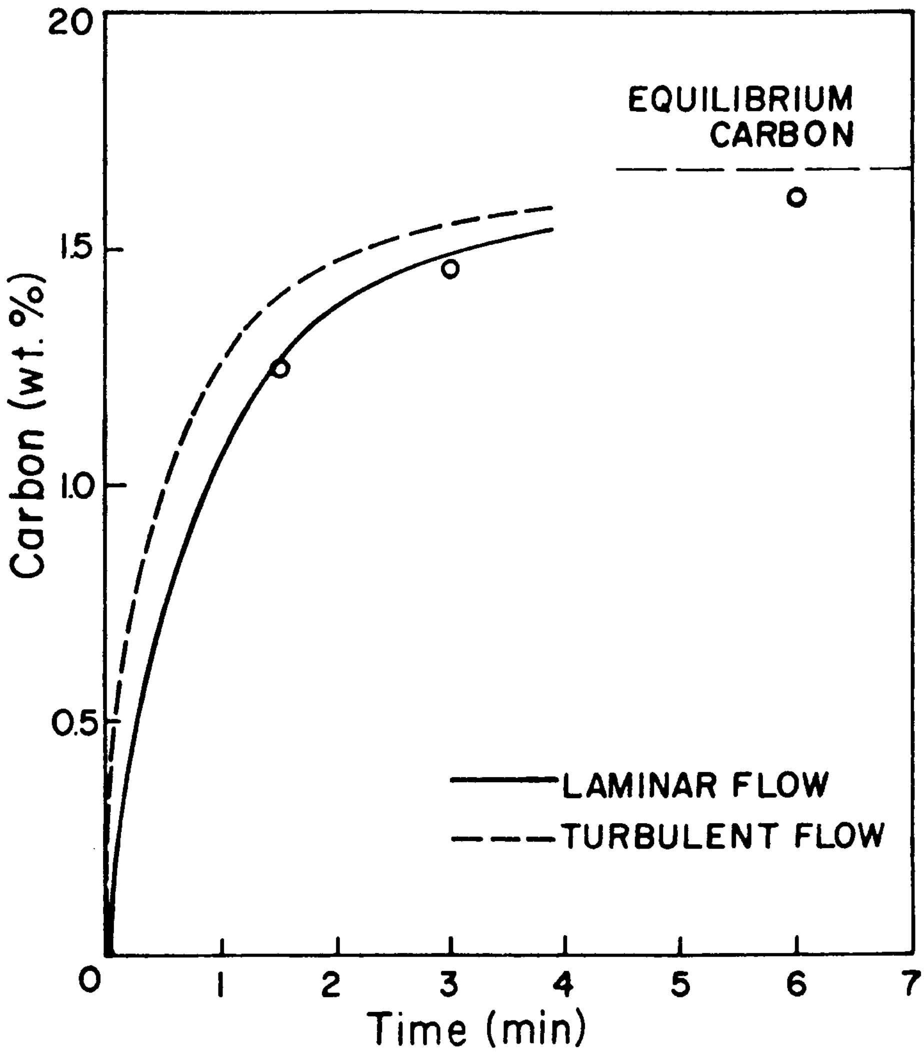

Fig. 3 —Experimental carburization results (CO 2.15/CO_2 at 38.9 atm and 1650 °C)[■,■] compared with the theoretical predictions for turbulent and laminar flow in the levitated drop.

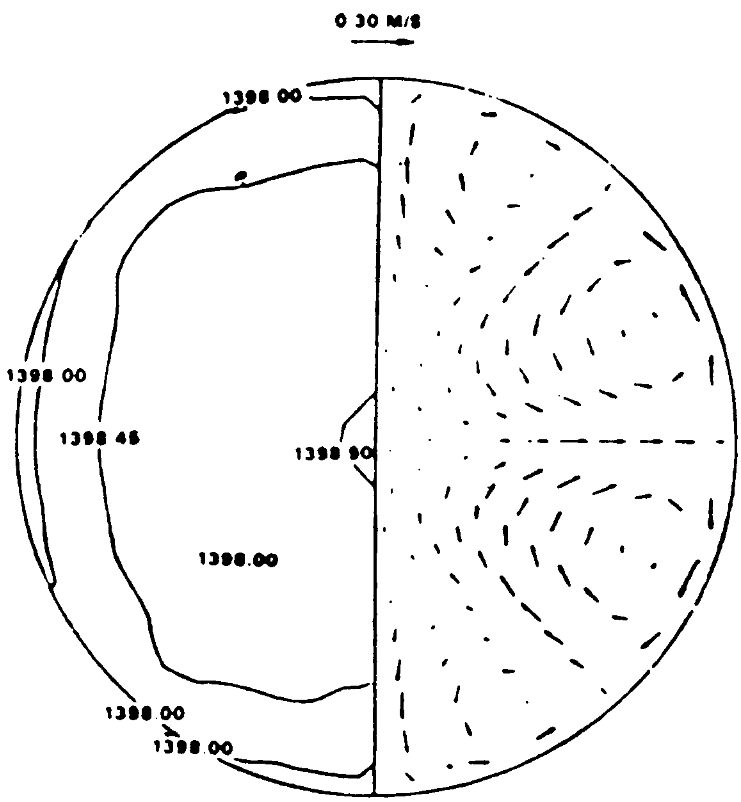

Fig. 4 Computed velocity field and temperature distribution for a 9 mm beryllium drop at zero-g.

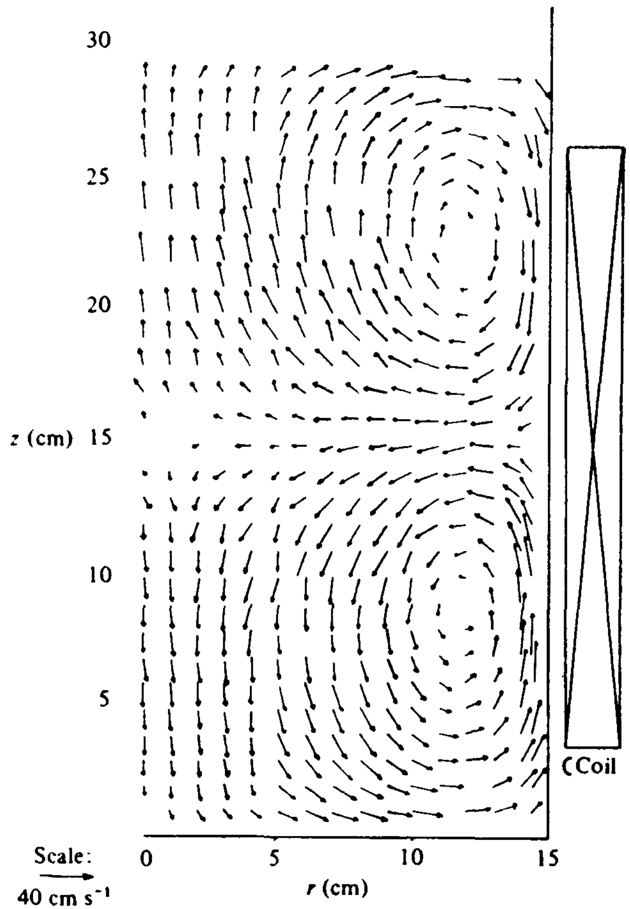

FIG 5a Experimentally measured velocity field for 1900 A coil current.

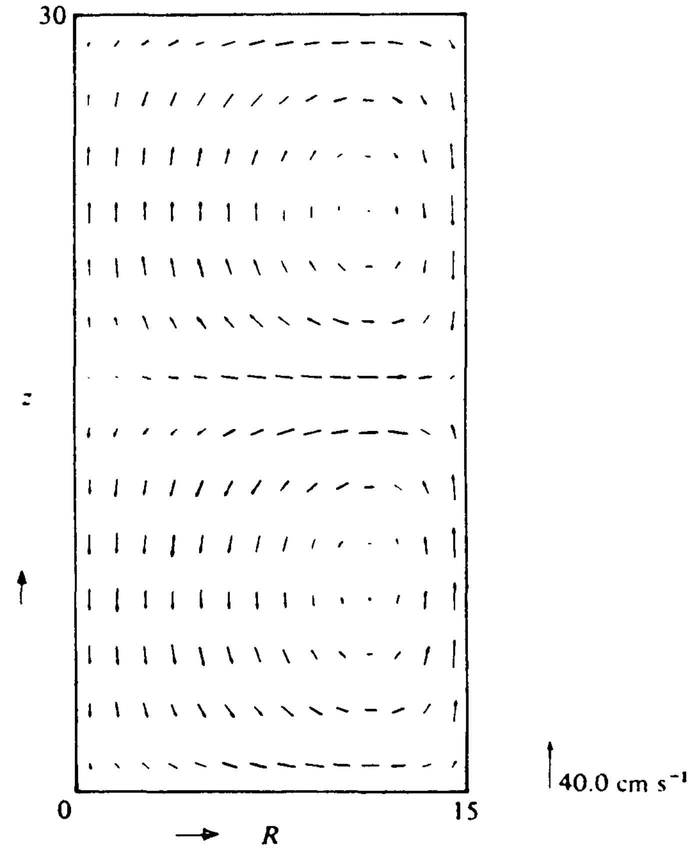

FIG 5b Computed velocity field for 1900 A coil current.

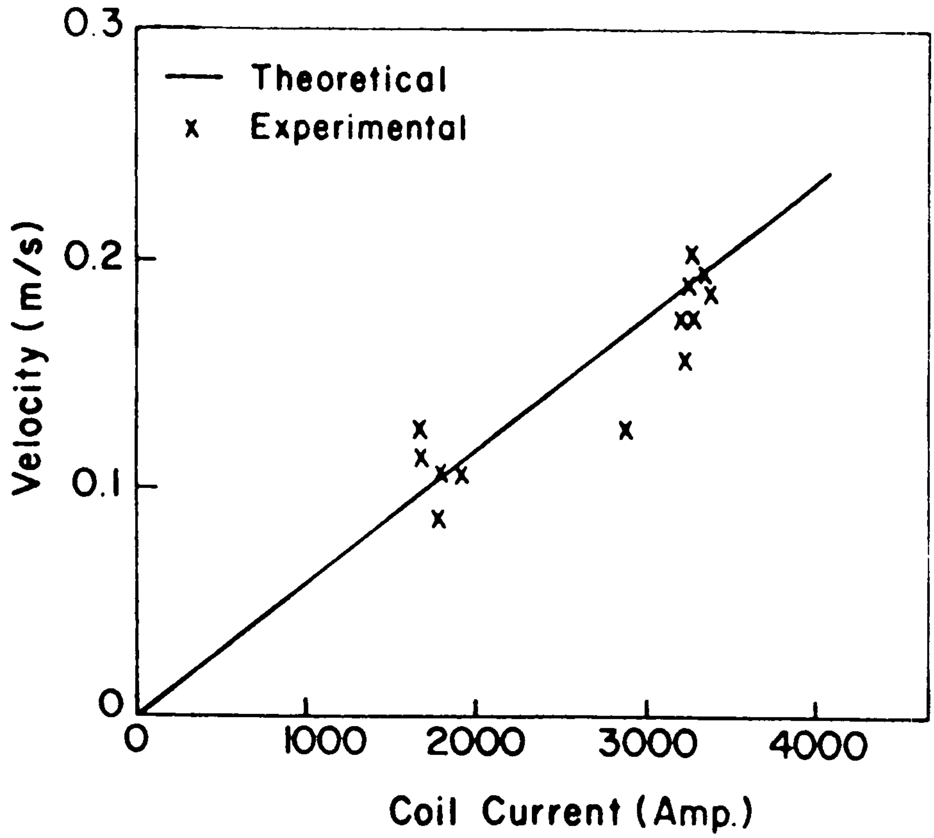

Fig. 6 Comparison between the measured and the computed near surface velocity for a four ton melt of steel as a function of the coil current .

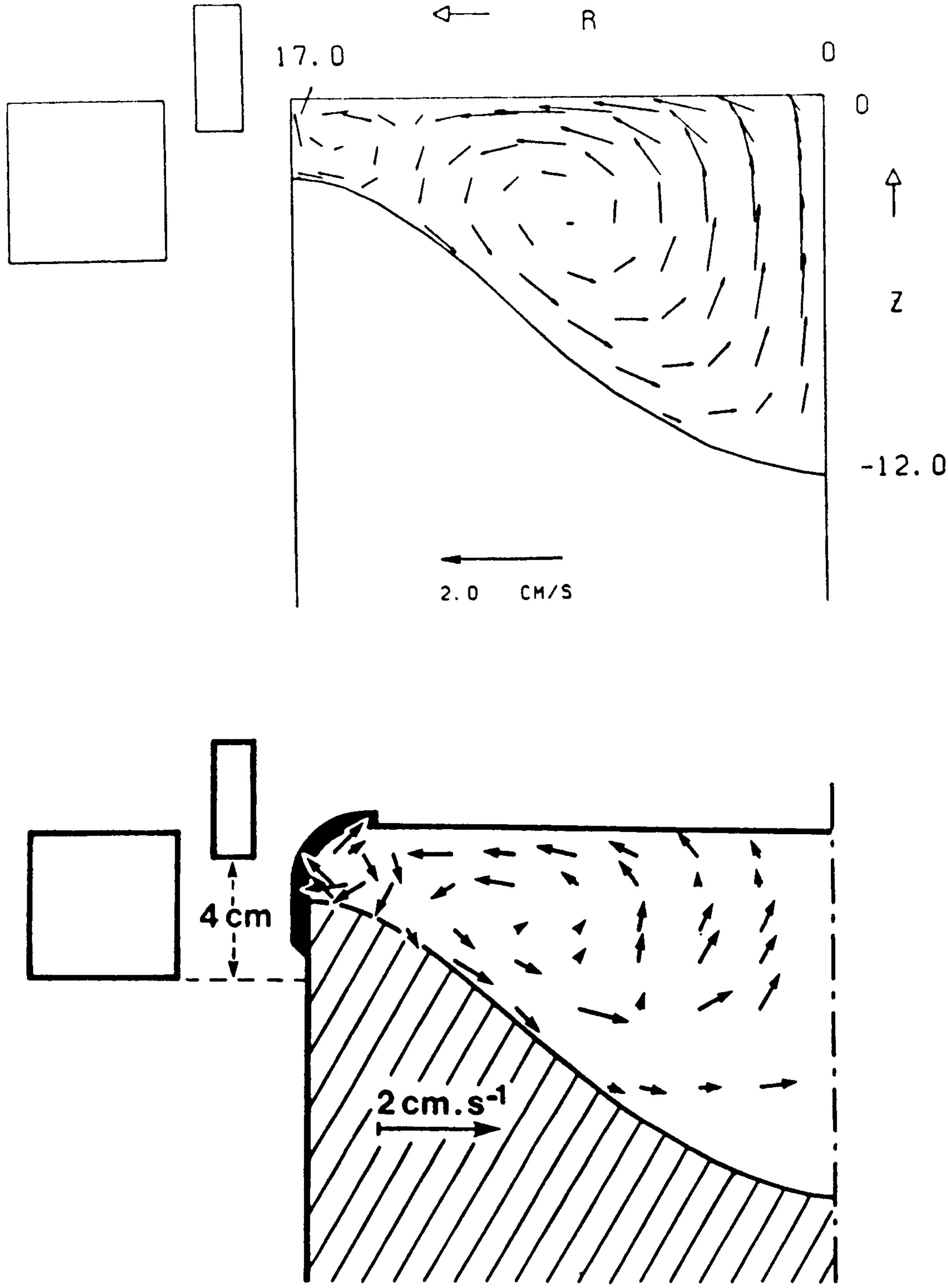

Fig. 7 Comparison between the computed (a) and the measured (b) fluid flow fields for the EM casting of Aluminum .

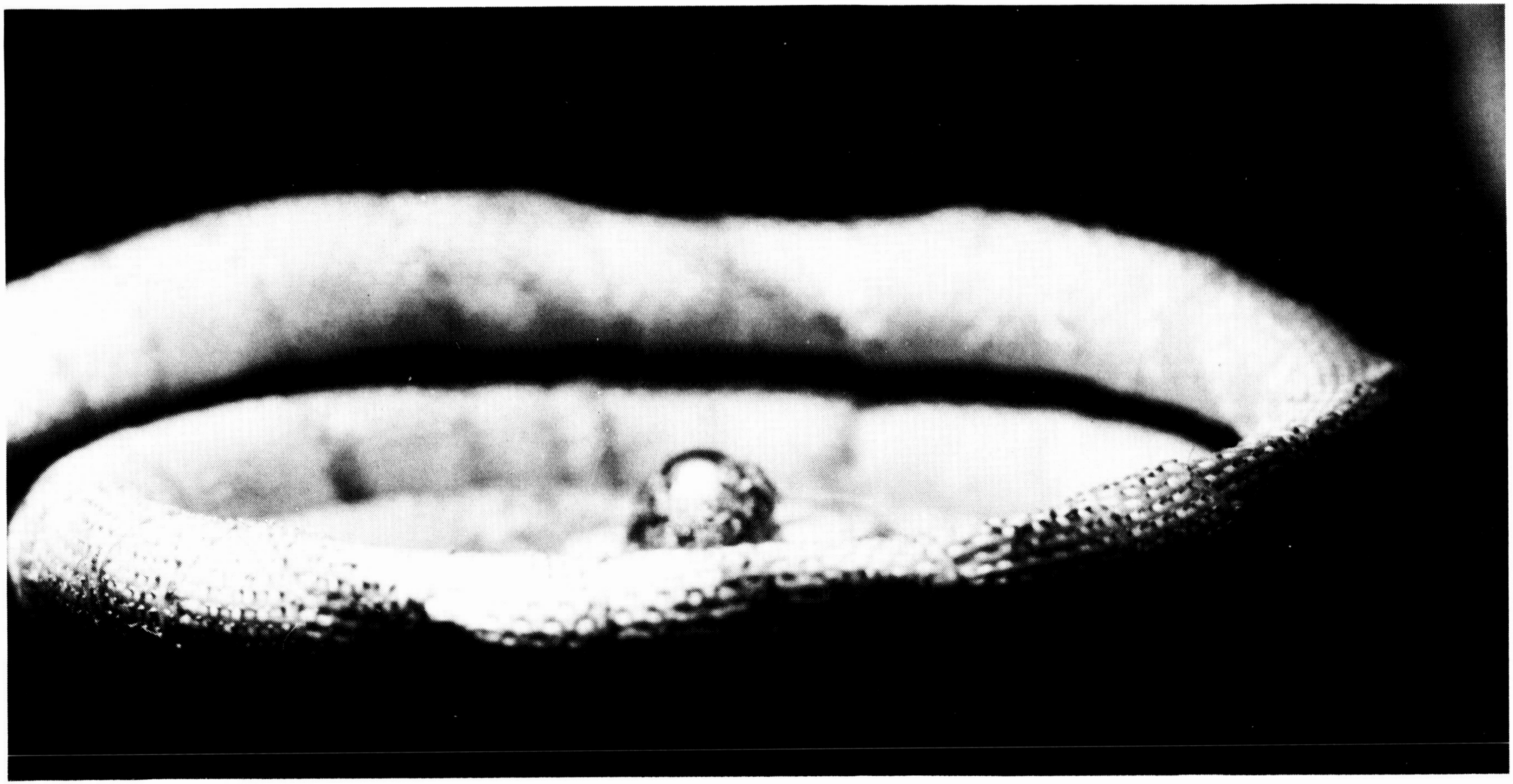

Fig. 8. The experimental set-up showing the coil, the sample and the quartz rod used to support the sample (photo by H. Edgerton).

Fig. 9. Silver droplet showing tracer particle paths. The current in the coil is about 600 A.

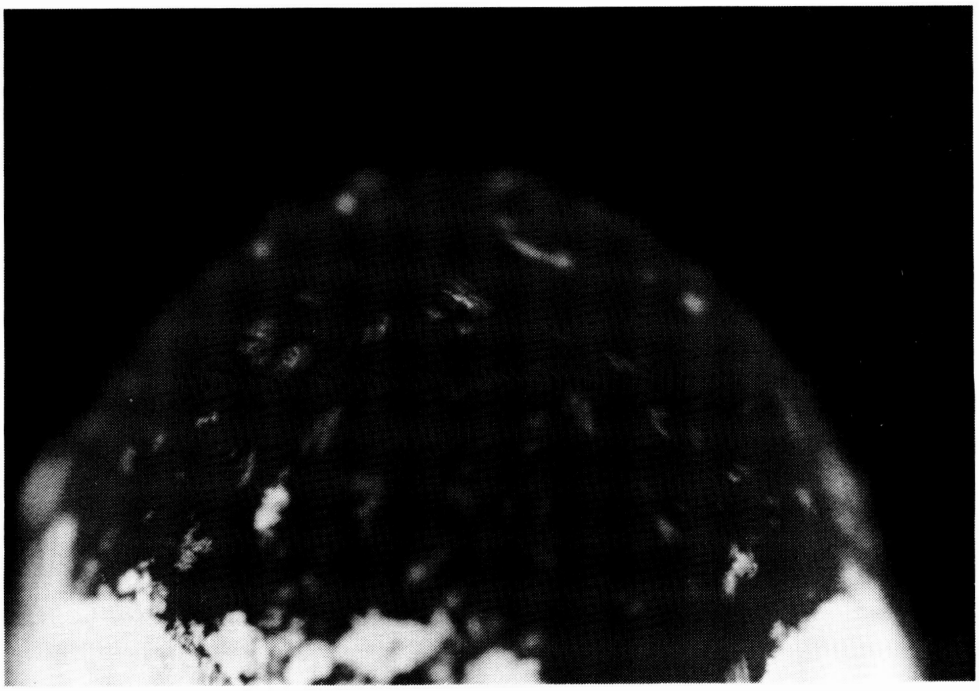

Fig. 10. Silver droplet showing tracer particle paths. The current in the coil is about 400 A.

Microgravity Experiments on Granular Materials, N.C. Costes, V.C. Janoo, and S. Sture

(Reprint, to be sent under separate cover)

PRECEDING PAGE BLANK NOT FILMED

N89-20316

THE DYNAMICS OF FREE LIQUID DROPS

T. G. Wang, E. H. Trinh, A. P. Croonquist, and D. D. Elleman

Jet Propulsion Laboratory
California Institute of Technology

ABSTRACT

The behavior of rotating and oscillating free liquid drops has been studied by many investigators theoretically for many years. More recent numerical treatments have yielded predictions which are yet to be verified experimentally. The purpose of this paper is to report the results of laboratory work as well as of experiments carried out in space during the flight of Spacelab 3, and to compare with the existing theoretical studies. Ground-based experiments have been attempted as a first approximation to the ideal boundary conditions used by the theoretical treatments by neutralizing the overwhelming effects of the earth's gravitational field with an outside supporting liquid and with the use of levitation technology. The viscous and inertial loading of such a suspending fluid has been found to profoundly affect the results, but the information thus gathered has emphasized the uniqueness of the experimental data obtained in the low-gravity environment of space.

INTRODUCTION

The specific problems under consideration include experimental studies of the equilibrium shapes of drops in solid-body rotation, the shape oscillation spectrum of freely suspended liquids, and the interaction between rotation and vibration. The obvious difficulty in studying these phenomena dominated by the weak capillary forces is the presence of the earth's gravitational field. An experiment to be performed in the microgravitational environment of space was thus proposed and it has recently been carried out. This paper will describe the outcome of the operation of the Drop Dynamics Module[1] during the flight of Spacelab 3.[2] In order to obtain a more complete overview of the subject matter and to emphasize the need for a space experiment, the results of extensive ground-based studies will also be reported.

I. THE EQUILIBRIUM SHAPE OF ROTATING DROPS: THE PLATEAU EXPERIMENT REVISITED

A. Theoretical Background

Swiatecki[3] fits the problem of the liquid drop held together by surface tension into a broader scheme in which fluid masses may, in addition to having a surface tension, be self-gravitating and/or possess a uniform density of electric charge. The astrophysical problem of the stability of rotating stellar masses and the problem of the fissionability of rotating uniformly-charged nuclei are thus unified with the problem of equilibrium shapes and stability of ordinary liquid drops.

Confining discussion to the case of surface tension forces only, and assuming that the drop is actually confined within another fluid (e.g., a gaseous atmosphere) which rotates with the drop at the same angular velocity, the equilibrium shape must satisfy the Young-Laplace equation[4,5]

$$\Delta P_o + \frac{1}{2}\Delta\rho\Omega^2 r_\perp^2 = \sigma\,\nabla . n \tag{1}$$

The drop has density ρ_D and rotates with angular velocity Ω. The outer fluid has density ρ_F. The drop has a fixed volume. $\Delta P_O \equiv P_{D_0} - P_{F_0}$ is the difference in pressures on the axis of rotation inside and outside the drop, $\Delta\rho = \rho_D - \rho_F$ is the density difference, $r_\perp$ is the radius perpendicular to the axis of rotation and extending to the drop's surface, σ is the interfacial tension, and n is the surface normal ($-\frac{1}{2}\nabla . n$ is the local mean curvature).

Brown[6] rewrites equation (1) in the dimensionless form

$$Ha_o = K + 2\Sigma\left(\frac{r_\perp}{a_o}\right)^2 \tag{2}$$

where $H \equiv \frac{1}{2}\nabla . n$ is the local mean curvature, a_0 is the radius of the sphere of same volume as the drop, and the parameters Σ and K are rotational Bond number and dimensionless reference pressure defined as

$$\Sigma \equiv \frac{\Omega^2\Delta\rho a_o^3}{8\sigma} \tag{3}$$

$$K \equiv \frac{\Delta P_o a_o}{2\sigma} \tag{4}$$

Figure 1 shows cross-sectional profiles of axisymmetric shapes for values of the reduced rotation rate squared, derived from reference 4. These cross sections lie in the meridional plane. The figures showing a dip at the axis are not lobed shapes, but are biconcave discs similar in form to red blood cells. The biconcave discs pinch off at $\Sigma = \frac{1}{2}$ and become tori ("tori" is used loosely to describe shapes which no longer intersect the axis of rotation).

A substantial extension to the theory to include the shapes and stabilities of nonaxisymmetric figures of equilibrium has been provided by Brown and Scriven[6]. Along the simply-connected sequence, the axisymmetric drop shape was shown to be stable to two-lobed perturbation for $\Sigma < 0.313$. At this point the drop is neutrally stable to these perturbations; above it, the axisymmetric shape becomes unstable. Similarly, as shown in Figure 2, Brown calculated bifurcation points to three- and four-lobed families from the simply-connected sequence at $\Sigma = 0.500$ and $\Sigma = 0.567$.

B. The Plateau Experiment Revisited

This experiment was first performed by Plateau[7] in the last century, and has been repeated at JPL using advanced photographic and electronic systems to achieve a better control of the various relevant parameters.[8]

A large (15 cc) viscous liquid drop is formed around a disc and shaft in a tank containing a much less viscous mixture having the same density. This supporting liquid and that of the drop are immiscible. If the shaft and disc were not present, the drop would float freely in the surrounding medium, and have the shape of a sphere. The gravitational forces are greatly reduced, and become small compared to the surface forces. With the drop attached and initially centered about the disc, the shaft and disc are set into rotation almost impulsively, reaching a final steady angular velocity within 1/2 to 2 revolutions. The drop deforms under rotation, and develops into a variety of shapes depending upon the shaft velocity. The process of spin-up, development, and decay (or fracture) to some final shape is recorded on motion picture film.

In this system, gravity is diminished at the expense of introducing a supporting liquid which is viscous, and which may be entrained by the motion of the drop, thereby allowing momentum to be transferred from the drop.[9] Rotation is achieved only by introducing the shaft and disc; adhesion to these surfaces distorts the drop shape. Nevertheless, comparison of this experiment's results to the theory of free rotating liquid drops is prompted by the fact that several novel families of drop shapes have been observed. It is important to recognize, though, that existing theories deal mainly with equilibrium shapes and their stability, while the drop in this experiment is undergoing a far more complicated process; the shape of a liquid drop spun from a shaft is a dynamical problem.

Plateau originally observed axisymmetric equilibrium shapes as well as tori when the rotation velocity was high enough. He found that the motion of the ring was that of a rigid body for several seconds. Most of Plateau's attention was devoted to the study of the rings which he thought were similar to the rings of Saturn.

The shapes observed in the JPL experiment were those of flattened, slowly rotating drops, as well as toroidal, two-, three-, and four-lobed shapes. Neutrally buoyant tracer particles allowed the study of the dynamics of the behavior, the secondary flow generated by the rotation, the interaction between the drop and the host liquid, and the coupling between the shaft/disc and the drop.

In the case of slowly rotating axisymmetric drops, comparison with the theory was possible and the resulting near-agreement was nevertheless remarkable: the qualitative shape of the equatorial area versus the reduced rotation rate were similar, only differing from theory by 30%. When generating $n>2$ lobed drops in a controlled manner, primarily two- and three-lobed shapes were obtained. The latter had not been observed before. The behavior of the lobed shapes was not easily compared with theory, however. The study of the angular velocities and momenta demonstrated that the development of the various lobed shapes takes similar paths, but no evidence was found for the location of the branch points between axisymmetric and triaxial behavior. Figure 3 reproduces photographs of some of the drop shapes obtained.

C. Ground-Based Studies of Rotating Charged Drops

The investigation of the behavior of rotating charged drops under the full effect of the earth's gravitational field has been made possible by electrostatic and acoustic levitation technologies. A small (3-4 mm in diameter) charged liquid drop could be electrostatically levitated and acoustically rotated.[10] The first bifurcation point marking the transition from axisymmetric to two-lobed shape was accurately observed. The detailed analysis revealed the action of gravity in the geometry of the drop. The theory is not applicable to a nonuniform charged drop, and the stability of the equilibrium shape must be greatly modified by the electrostatic stresses at the drop boundary.

II. THE DYNAMICS OF SHAPE OSCILLATIONS OF FREE DROPS: LABORATORY EXPERIMENTS

A. Theoretical Background

Extensive theoretical work exists on the subject of drop shape oscillations.[11-19] Miller and Scriven[17] have produced a comprehensive theoretical analysis of the natural, small amplitude, shape oscillations of a drop by using the normal-mode approach. Marston[18] has offered a derivation for the case of a liquid drop immersed in another liquid of similar properties. Prosperetti[16] has obtained a solution to the initial value problem and has provided theoretical predictions concerning the behavior of a freely oscillating drop in the early transient period.

An expression for the L_{th} resonant mode frequency of a <u>driven</u> oscillating drop is given by

$$\omega_L = \omega_L^{\bullet} - \frac{1}{2}\alpha\,\omega_L^{\bullet} + \frac{1}{2}\alpha^2, \tag{5}$$

where ω_L is the angular response frequency, and ω_L^{*} is Lamb's natural resonance frequency.[11]

$$\left(\omega_L^{\bullet}\right)^2 = \frac{L(L+1)(L-1)(L+2)}{R^3[L\rho_o + (L+1)\rho_i]}\sigma \tag{6}$$

R is the radius of the undisturbed spherical drop, σ is the interfacial tension, and ρ_i and ρ_o are the density of the inner and outer fluid respectively.

α is given by

$$\alpha = \frac{(2L+1)^2(\mu_i\mu_o\rho_i\rho_o)^{\frac{1}{2}}}{\sqrt{2}\,R[L\rho_o + (L+1)\rho_i][(\mu_i\rho_i)^{\frac{1}{2}} + (\mu_o\rho_o)^{\frac{1}{2}}]} \tag{7}$$

μ_o and μ_i being the dynamic viscosity of the two liquids.

The free decay of an oscillating drop is given by the damping constant τ_L^{-1}

$$\tau_L^{-1} = \frac{1}{2}\alpha\,\omega_L^{*\frac{1}{2}} + \frac{1}{2}\Gamma - \frac{1}{2}\alpha^2 \tag{8}$$

where

$$\Gamma = \frac{(2L+1)\left\{2(L^2-1)\mu_i^2\rho_i + 2L(L+1)\mu_o^2\rho_o + \mu_i\mu_o[(L+2)\rho_i - (L-1)\rho_o]\right\}}{R^2[(\mu_i\rho_i)^{\frac{1}{2}} + (\mu_o\rho_o)^{\frac{1}{2}}]^2[L\rho_o + (L+1)\rho_i]} \tag{9}$$

The first term in the expression for the damping constant [equation (8)] expresses the damping in the oscillating boundary layer of the drop, while the second term reflects the dissipation mechanism due to viscous effects within the drop itself and is equivalent to the damping normally associated with the well-known harmonic oscillator.

These results are valid under the assumptions of small-amplitude oscillations, vanishing tangential stresses at the drop boundary, and the absence of internal circulation. No dependence of the resonance frequencies on the oscillation amplitude can be derived, and the various modes are assumed to be decoupled. One may notice that each normal mode denoted by the integer L is actually degenerate in the axisymmetric case. For example, for the $L = 2$ mode, there exist five degenerate modes corresponding to the integer values $m = \pm 2,\ \pm 1,\ 0$, all having the same frequency, but differing by the geometry of their oscillations.

Foote[15] has carried out computer calculations without the restriction of small-amplitude oscillations and has determined that the frequency of each normal mode decreases with increading oscillation amplitude. In addition, his results indicate that for the $L = 2$ mode, the drop spends more time in the prolate configuration than in the oblate one. Tsamopoulos and Brown[19] have obtained similar results for the oscillation frequency.

Busse[20] has carried out an asymptotic expansion analysis of the problem of the oscillation dynamics of a rotating drop in the small oscillation amplitude region.

B. Ground-Based Experiments

Novel acoustic levitation techniques have allowed the study of the oscillatory behavior of freely suspended drops both in an immiscible liquid system as well as with liquid suspended in a gaseous atmosphere.[21-26] The detailed experimental investigation of the small-amplitude shape oscillation of liquid drops suspended in an immiscible liquid host has allowed the verification of theoretical results.[21] Figure 4 presents a series of photographs of the first three pure resonant modes of shape oscillation of an acoustically levitated and excited drop. Heretofore undetermined experimentally, the resonance frequencies of these modes were accurately measured and closely correlated with the calculated values. Table I reproduces the results of the comparison between experimental and theoretical values. In the same manner, the decay rate of the fundamental mode has been accurately measured and compared with the theory. The results are summarized in Table II.

Nonlinear effects were also experimentally studied as drops could be driven into high-amplitude oscillation with modulated acoustic radiation forces. A markedly soft nonlinearity was observed for freely decaying drops as the data reported in Figure 5 illustrate. Tsamopoulos[19] compared these data with his computer calculations, and found good agreement. The case for driven drops is more complicated, however, because of the subtle effect of the static shape on the oscillatory modes: the resonant modes of a slightly oblate drop have been found to increase as the level of deviation from sphericity was increased, an effect until now unreported.[21-23] Flow visualization studies of the internal fluid particle motion within an oscillating drop have revealed a qualitative change in the flow pattern as the oscillation amplitude grows: vorticity not present in the small-amplitude region exists in each of the quadrants of a drop under quadrupolar vibration. Figure 6 reproduces some of the photographs obtained from tracer particles illuminated with sheet lighting. The streak pattern is obtained through a time exposure lasting several oscillation cycles.

Experiments using smaller (4 mm diameter) drops levitated in air have also yielded similar soft nonlinearity for driven large-amplitude oscillation. Similarly, the resonant modes of oscillations have been experimentally investigated for a drop in solid-body rotation, freely suspended in an immiscible host liquid and restrained by an ultrasonic field. Sample results are reproduced in Figure 7. The relative shift in the resonance frequency has been plotted as a function of the ratio of the rotation velocity to the angular resonant frequency of the nonrotating drop. Very good agreement with the theory[24] has been discovered for the fundamental mode. An intriguing experimental observation was provided by the multiplicity of resonant modes as the rotation rate was increased: it appeared that the rotation removed the degeneracy of the fundamental mode. Such evidence correlates with observations of frequency shift of the oscillation modes of the sun due to its rotation. The physical processes in that particular case are more complicated due to the differential rotation.

III. SPACELAB 3 DROP DYNAMICS EXPERIMENTS

A. Introduction

The video downlink from the Space Shuttle Challenger on May 3, 1985, displayed a liquid drop being held and manipulated within a seemingly invisible container. This was the first live demonstration in the microgravitational environment of space of the capabilities of acoustic radiation forces: a resonant cavity confining three-dimensional standing waves was used to create a stable potential well to position, rotate, and oscillate a liquid sphere. Promising future applications of such techniques may be found in space where the reduction of the effects of gravity allows the effective use of relatively small forces to manipulate materials samples without interfering with their behavior and thereby introducing extraneous artifacts.

The purpose of this first set of experiments in Spacelab was the investigation of the rotational and oscillatory dynamics of free liquid drops under the subtle influences of surface tension and acoustic radiation pressure forces. The specific goals were to test the capabilities of acoustic manipulation techniques, to gather the first experimental data on the equilibrium shapes of rotating free liquid drops, and to demonstrate the capability of drop oscillation techniques for the measurement of the surface tension and viscosity of liquids. All experiments were carried out at ambient temperature and in the Spacelab atmosphere. Data were primarily obtained in the form of 16 mm cinefilms. Each frame of the film was divided into four subframes, three of these contained views of the drops along three orthogonal axes, and the fourth quadrant was devoted to the display of data relating to the operation of the instrument. The bulk of the engineering data was recorded on magnetic tapes.

B. Acoustic Positioning and Torque Applied to Liquid Drops in Microgravity

Available experimental evidence appears to indicate that the steady-state acceleration levels in the Spacelab 3 module during a gravity gradient attitude is on the order of 0.001 g (where g is the gravitational level at sea level on earth) with occasional deviations reaching amplitudes up to 0.1 g. Our observations reveal that the acoustic positioning forces generated in the experiment chamber (DDM chamber) were capable of containing a 7 cc liquid drop having a density of 1.18 g/cc when subjected to the steady-state level of residual acceleration, but were unable to restrain liquid drops during spacecraft maneuvers characterized by peak acceleration levels of 0.1 g. Figure 8 is a plot of the maximum acoustic force generated at four different sound pressure levels (140, 143, 146, and 149 dB re. 0.0002 microbar) as a function of the drop volume. The 7cc drop mentioned above would thus require an SPL of about 143 dB for trapping within the acoustic potential well. The drop was observed, however, to remain near the center of the chamber for long periods of time during which the sound level was significantly lower than 143 dB, thus suggesting that the steady-state acceleration level might be lower than 0.001 g for those periods of time.

The acoustic restoring force in a one dimensional standing wave may be expressed as[27]

$$F = \frac{5\pi}{6}\left(\frac{P_i^2}{\rho c^2}\right) k R^3 \sin 2kx , \tag{10}$$

where ρ_i is the pressure amplitude, ρ and c are the density and sound velocity characteristic of air, k is the wave vector, and R is the radius of a spherical sample. Theoretically, the restoring force is reduced to zero at the center of the chamber, and increases sinusoidally as the sample deviates from that position. In practice, the force profile is not sinusoidal, and is fairly distorted due to scattering effects from the sample.

During the operation of the experiment, the acoustic pressure levels were maintained between 135 and 145 dB and little static distortion of the drop was observed during normal operating sequences. This absence of static, acoustically induced distortion is crucial to the viability of acoustical manipulation techniques as experimental tools for materials science and fluid dynamics investigations.

Should a freely suspended drop receive an impulse from a transient acceleration spike, it will undergo translatory oscillations within the potential well controlled by the acoustic restoring force. The frequency of this oscillatory motion may be used to estimate the magnitude of this restraining force if the drop mass is known.

When two sides of the acoustic resonant cavity have equal length, it is possible to generate a steady-state torque by means of appropriate phasing of the associated acoustic waves. When the two waves along the x and y axes are related by $+90°$ (or $-90°$), a torque with direction vector in the $+z$ (or $-z$) direction is induced and drives a clockwise (counterclockwise) rotation of a sample suspended in the center of the chamber. The theoretical expression for this torque is given by[28]

$$T = \frac{3}{2} L_\eta \frac{P_x P_y}{2\rho c^2} \mathrm{A} \sin \phi_o , \tag{11}$$

where T is the torque, L_η the acoustic boundary layer (or viscous length) defined as $(2\nu/\omega)^{\frac{1}{2}}$, P_x and P_y the pressure amplitudes of the waves in the x and y direction respectively, A the total surface area of the sample, ν the kinematic viscosity of the air, ω the angular frequency of the sound wave, and ϕ_o the phase angle between the waves along the x and y axes.

By knowing the torque acting on the liquid drop, the deformation of the drop as it rotates, and the drag of coefficient of the air, it is possible to plot the rotation rate of a given sample as a function of time. The results of such a calculation are reported in Figure 9 for a 3 cc drop of water/glycerin mixture with a kinematic viscosity of 100 centiStokes. The theoretical curve has been obtained by fitting the experimental data with the air drag coefficient as an adjustable parameter. The data included in Figure 9 pertains to a drop having a shape axisymmetric with respect to the axis of rotation.

C. Equilibrium Shapes of Acoustically Rotated Drops

As an initially spherical liquid drop is rotated around a fixed axis, its equilibrium shape has been predicted[3] to first remain axisymmetric with respect to the rotation axis. However, as the rotation rate is further increased, a sudden transition to a two-lobed shape will take place at a well-defined rotation speed. This transition point, commonly referred to as a bifurcation point, marks the limit of stability of the axisymmetric shape in favor of the two-lobed configuration. Numerical computations[4] have also predicted the existence of three- and four-lobed shapes appearing at higher rotational velocities. These higher order lobed shapes, however, are not stable configurations. For an isolated drop, the two-lobed configuration is the only stable equilibrium shape as the first bifurcation point is passed.

Figure 10 reproduces the experimentally measured rotation velocity of a 3 cc water/glycerin drop as the acoustic torque is applied and removed. The horizontal axis displays time. As the drop is spun up, it flattens at the pole and bulges at the equator, remaining axisymmetric and gaining in rotation speed. At the bifurcation point, the two-lobed shape becomes the stable equilibrium geometry and the drop slows down because the moment of inertia increases as well as the surface area. Although the speed decreases, the largest dimension of the drop cross section continues to increase, leading to an eventual fission of the liquid into two separate drops. In this particular case, however, the data of Figure 10 show that the acoustic torque is turned off before fission is allowed to occur, and the rotation speed increases again as the drop-stretch is reversed. The axisymmetric equilibrium shape is recovered when the same rotation speed as that measured at bifurcation during the spin-up phase is reached. No "hysteresis" has been detected within the present experimental uncertainty.

Due to imperfect conditions in the lighting system, the quality of the images recorded on the 16 mm films were slightly degraded, affecting the precision with which the drop shape and speed could be measured. As a result, measurements of the relative change in the drop cross section and profile could be accomplished with an uncertainty of about $\pm 8\%$. The rotation velocity of the drop was measurable to within $\pm 5\%$.

A plot of the axial ratio of the spheroidal drop in the axisymmetric regime is reproduced in Figure 11. The drop profile has been measured with images recorded on views along axes perpendicular to the rotation axis. The drop deformation is plotted as a function of the rotation velocity.

Figure 12 presents the experimental data together with available theoretical predictions. In this case, the largest dimension in the rotating drop equatorial cross section (measured perpendicularly to the rotation axis) divided by the radius of the nonrotating drop, is plotted as a function of the rotation rate divided by the frequency of the fundamental mode of shape oscillation. This frequency is given by

$$F = \frac{1}{2\pi}\left(\frac{8\sigma}{\rho^{*}R^{3}}\right)^{\frac{1}{2}} \tag{12}$$

where σ is the surface tension of the liquid and ρ^{*} its density. The liquids used in these experiments were water, a series of water and glycerin mixtures of increasing viscosity (from 10 to 500 cSt), and finally silicone oil. The density was between 1.0 and 1.18 g/cc, and the surface tension had values between 20 and 70 dynes/cm.

The results in Figure 12 have been obtained with a 100 cSt liquid drop 3 cc in volume, and using rotational acceleration of about 0.01 revolution/sec. Under these particular circumstances, solid-body rotation is easily attained, and the effects of differential rotation are minimized. The behavior of the drop should then approach that of a fluid mass rotating at constant velocity since the rotation rate changes very little during the characteristic time required for reaching solid-body rotation. This assumption would not be valid if the viscosity were significantly lower.

The data reveal very good agreement with the theoretical predictions corresponding to the axisymmetric regime. On the other hand, a quantitative confirmation of the theoretical prediction was not obtained for the specific value of the reduced rotation rate at the bifurcation point. Experimental evidence suggests that the onset of secular instability for the axisymmetric shape is located at a lower rotational velocity than that predicted theoretically.

Figure 13 reproduces both experimental and theoretical results for an experimental sequence including a drop fission. Once again qualitative agreement is obtained, but the experimental data reveal a much faster increase in deformation with the decrease in rotation velocity. Fission generally produces two main drops of equal volume and a satellite droplet arising from the breakup of the liquid bridge forming the central region of the stretched rotating single drop. Assessment of the volumes of the drops resulting from fission is difficult to obtain, but their volumes were probably equal to within 10%. No evidence for two-lobed configurations with greatly differing volume for the lobes has been obtained.

D. Shape Oscillations and Measurement of Surface Tension and Viscosity

The portion of the experiment dealing with shape oscillation studies has been curtailed due to a subnominal performance of phase control which resulted in the inability to completely null out the acoustic torque. It was nevertheless possible to obtain free decay measurement of the frequency and damping of shape oscillations as a means for determining the surface tension and viscosity.

Figure 14 reproduces the experimental results obtained for a freely decaying 4.5 cc drop of water/glycerin mixture having a viscosity of 10 cSt. A fit of the experimental data using an exponentially decaying sine wave yielded a surface tension of 60 dynes/cm and a viscosity of 12 cSt. The experimental uncertainty is primarily due to the relatively low frame rate used for the 16 mm camera.

Nonlinear effects arising during large amplitude oscillations of the drops were among the unfulfilled experimental goals due to lack of operation time as well as subnominal control over the nulling of the acoustic torque. Ground-based experiments[5] using immiscible liquid systems have suggested a soft nonlinearity in the resonance frequencies for shape oscillations as the amplitude grows large. The scant data available from this flight do not appear to confirm this finding, but suggest the existence of a hard nonlinearity. The results are very inconclusive, however, and these experiments must be repeated in possible subsequent flights. Additional phenomena to be studied in the future include the oscillatory dynamics of a rotating drop, the behavior of a compound drop, and the detailed behavior of particles inside a rotating and oscillating drop.

Preliminary observations concerning the last item mentioned above have demonstrated the ability to separate different phases present inside a liquid drop by simple rotation. Immiscible liquid droplets initially uniformly distributed within the main drop were quickly gathered at the center during rotation. The droplet density was 15% lower than the main drop density, and the centering process took approximately 2 minutes with rotation rate increasing from zero to about 2 revolutions/sec. An air bubble having diameter on the order of a millimeter and injected within the main drop only took 30 seconds to migrate to the center when the drop was accelerated from zero to 0.24 revolution/sec.

CONCLUDING REMARKS

Although certain ones of the planned experiments dealing with the oscillatory behavior of free drops could not be fully completed, and some of the precision of the measurement capability of the instrument was compromised by hardware malfuction, a very needed and successful test of the capabilities of acoustic positioning and manipulation techniques was carried out, an experimental confirmation of the theory of acoustic torque has been obtained with deformable liquid samples, the first set of data on the equilibrium shapes of rotation drops has been gathered to partially confirm available theories, and finally a successful demonstration of the contactless method of measuring surface tension and viscosity has been obtained. As is usually the case in experimental science, however, additional data must be obtained in order to confirm the results of this first flight.

It must be reiterated that the availability of a greatly reduced gravitational acceleration condition is essential to the rigorous performance of this experiment. This seemingly simple problem involves boundary conditions which are theoretically simple, but which are an earthbound experimentalist's nightmare. A neutral buoyancy system may be used to remove the effects of the gravitational field, but the host liquid alters the boundary conditions through viscous and inertial stresses. Levitation of free drops in a gaseous atmosphere on earth introduces non-negligible drop distortion as well as artifacts due to the levitating acoustic or electrical fields.

ACKNOWLEDGMENTS

The research described in this paper was carried out at the Jet Propulsion Laboratory, California Institute of Technology, under contract with the National Aeronautics and Space Administration.

REFERENCES

1. T. G. Wang, M. M. Saffren, and D. D. Elleman, "Acoustic Chamber for Weightless Positioning," AIAA paper, 74-155 (1974).
2. T. G. Wang, E. H. Trinh, A. P. Croonquist, and D. D. Elleman, "The Shapes of Rotating Free Drops: Spacelab 3 Experimental Results," Phys. Rev. Lett. (1986).
3. W. J. Swiatecki, "The Rotating, Charged, and Gravitating Liquid Drop and Problems in Nuclear Physics and Astronomy," Int'l. Colloquium on Drops & Bubbles, Proceedings, M. M. Saffren, D. Collins, Eds., Pg. 52, (1974).
4. S. Chandrasekhar, Proc. Roy. Soc. London, 286, 1, (1965).
5. D. K. Ross, Aust. J. Phys. 21, 823, (1968).
6. R. A. brown and L. E. Scriven, Proc. Roy. Soc. London, 371, 331, (1980).
7. J. Plateau, "Experimental and Theoretical Researches on the Figures of Equilibrium of a Liquid Mass Withdrawn From the Action of Gravity," Annual Report of the Board of Regents of the Smithsonian Institution, p.207, (Government Printing Office, Washington, DC, 1963).
8. R. Tagg, L. Cammack, A. Croonquist, and T. G. Wang, "Rotating Liquid Drops: Plateau's Experiment Revisited," JPL Publication 80-66 (1980).
9. E. H. Trinh, T. G. Wang, and M. C. Lee, "A Technique for the Study of Drop Dynamics in Liquid-Liquid Systems," J. Acoust. Soc. Am., 67 (1980).
10. W. K. Rhim, S. K. Chung, E. H. Trinh, and D. D. Elleman, "Charged Drop Dynamics Experiments Using an Electrostatic-Acoustic Hybrid System," Proc. Mat'ls. Research Soc. Symp. on Microgravity (Boston) (1986).
11. H. Lamb, Hydrodynamics, 6th Edition, Cambridge Univ. Press, 473, (1932).
12. Lord Rayleigh, The Theory of Sound, Dover, NY, 371, (1945).
13. W. H. Reid, Quart. Appl. Math., 18, 86, (1960).
14. S. Chandrasekhar, Hydrodynamic and Hydromagnetic Stability, Oxford Univ. Press (1961).
15. G. B. Foote, "A Theoretical Investigation of the Dynamics of Liquid Drops," PhD Thesis, Univ. of Arizona, (1971).
16. A. Prosperetti, J. Fluid Mech., 100, 333, (1980), and J.Mechanique, 19, (1980).
17. C. Miller and L. Scriven, J. Fluid Mech., 32, 417, (1968).
18. P. Marston, J. Acoust. Soc. Am., 67, 15, (1980).

19. J. Tsamopoulos and R. Brown, J. Fluid Mech., 127, 519, (1983).
20. F. Busse, J. Fluid Mech., 142, 1, (1984).
21. E. H. Trinh, A. Zwern, and T. G. Wang, "An Experimental Study of Small Amplitude Drop Oscillations in Immiscible Liquid Systems," J. Fluid Mech., 115, 453, (1982).
22. E. H. Trinh and T. G. Wang, "Large Amplitude Drop Shape Oscillations: An Experimental Approach," J. Fluid Mech., 122, 315, (1982).
23. E. H. Trinh, IEEE Proceedings in Ultrasonics, vol. 2, 1143, (1983).
24. E. H. Trinh and T. G. Wang, Proceedings of the Second Int'l. Colloquium on Drops and Bubbles, D. H. LeCroissette, Ed., JPL Publications 827, 143, (1981).
25. P. Annamalai, E. H. Trinh, and T. G. Wang, "Experimental Study of the Oscillations of a Rotating Drop," J. Fluid Mech, 158, 317 (1985).
26. E. H. Trinh and T. G. Wang, "A Quantitative Study of Some Nonlinear Aspects of Drop Shape Oscillations," J. Acoust. Soc. Am. 68, (1980).
27. E. Leung, N. Jacobi, and T. G. Wang, "Acoustic Radiation Force on a Rigid Sphere in a Resonance Chamber," J. Acoust. Soc. Am. 70, 6, (1981).
28. F. G. Busse and T. G. Wang, "Torque Generated by Orthogonal Acoustic Waves - Theory," J. Acoust. Soc. Am. 69, (1981).

TABLE CAPTIONS:

Table I Comparison of experimental results with theoretical calculations for the first four resonant modes of shape oscillations.

Table II Comparison of experimental results with theoretical calculations for the damping constant of the fundamental resonant mode of shape oscillations.

FIGURE CAPTIONS:

Figure 1: Axisymmetric equilibrium shape according to Chandrasekhar's results.

Figure 2: Predicted bifurcation points from axisymmetric to multi-lobed shapes according to the results of Brown.

Figure 3: Equilibrium shapes of rotating drops obtained in the JPL Plateau experiment.

Figure 4: Photographs of silicone oil drops oscillating in water. The first three resonant modes are shown (from ref. 21).

Figure 5: Experimental results for the frequency shift at high amplitude oscillation for the fundamental mode (from ref. 22).

Figure 6: Streak patterns photographs of suspended tracer particles in silicone oil drops levitated in water and oscillating in the fundamental mode at increasingly larger amplitude (from ref. 22).

Figure 7: Relative frequency shift of the second resonant mode of shape oscillation for a rotating drop levitated in water as a function of the square of the reduced rotation rate. (from ref. 25).

Figure 8: Maximum acoustic force at 1kHz and for four different sound prssure levels (SPL in dB re. 0.0002 microbar).

Figure 9: Rotation rate of axisymmetric drops. Theoretical fit for drop spin-up.

Figure 10: Axisymmetric and two-lobed regions of rotating drop.

Figure 11: Axial ratio of axisymmetric rotating drop.

Figure 12: Comparison of experimental with theoretical results for a 100 cSt. liquid drop.

Figure 13: Experimental data for drop fission due to rotation.

Figure 14: Free decay of shape oscillation.

	f_2 (Hz)	f_3	f_4	f_5	$\frac{f_3}{f_2}$	$\frac{f_4}{f_2}$	$\frac{f_5}{f_2}$	
Silicone/CCl_4 water ,3.2 cst. 1.9 cm^3	3.56 (±0.07)	6.49 (±0.13)	9.37 (±0.19)	13.1 (±0.25)	1.82 (±0.07)	2.63 (±0.1)	3.67 (±0.15)	Experimental
					1.89	2.89	3.99	Lamb's formula
					1.82	2.64	3.69	Theory (Marston)
Silicone/CCl_4 in water,3.2 cst. 1.7cm^3	3.66	6.81	10.21	13.65	1.86	2.79	3.73	Experimental
					1.86	2.79	3.74	Theory
Silicone/CCl_4 in water, 3.2 cst. 1.5 cm^3	3.87	7.21	10.45		1.86	2.70		Experimental
					1.86	2.81		Theory
Phenetole in water/Methanol 1.2 cst. 1.5 cm^3	2.97	5.54	7.85	10.47	1.87	2.65	3.52	Experimental
					1.85	2.90	3.65	Theory

TABLE I

Inside Viscosity	Outside Viscosity	Damping Constant (sec^{-1})	
1.05 cst.	10 cst.	1.52 (±0.1)	Experiment
		1.16	Marston Theory
1.05 cst.	20 cst.	2.93 (±0.15)	Experiment
		3.66	Theory
16.5 cst.	1.1 cst.	1.58 (±0.1)	Experiment
		1.82	Theory
36.8 cst.	1.1 cst.	2.63 (±0.15)	Experiment
		3.1	Theory

TABLE II

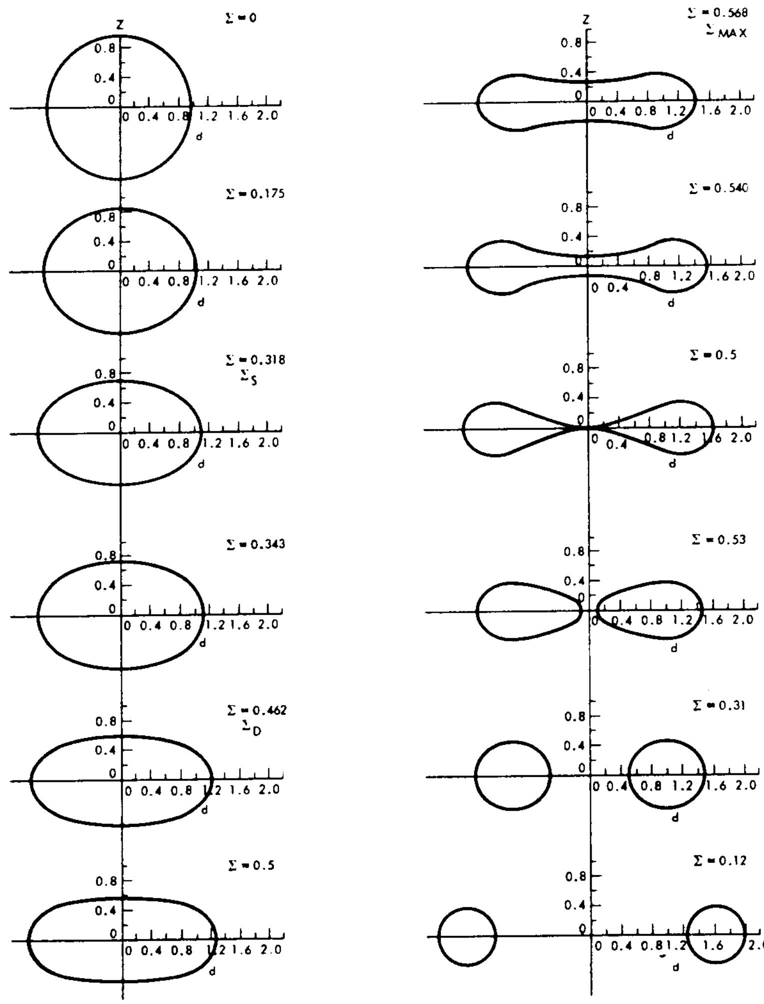
Σ = 0
Σ = 0.175
Σ = 0.318
Σ_S
Σ = 0.343
Σ = 0.462
Σ_D
Σ = 0.5
Σ = 0.568
Σ_MAX
Σ = 0.540
Σ = 0.5
Σ = 0.53
Σ = 0.31
Σ = 0.12
z
d

Figure 1

ORIGINAL PAGE IS OF POOR QUALITY

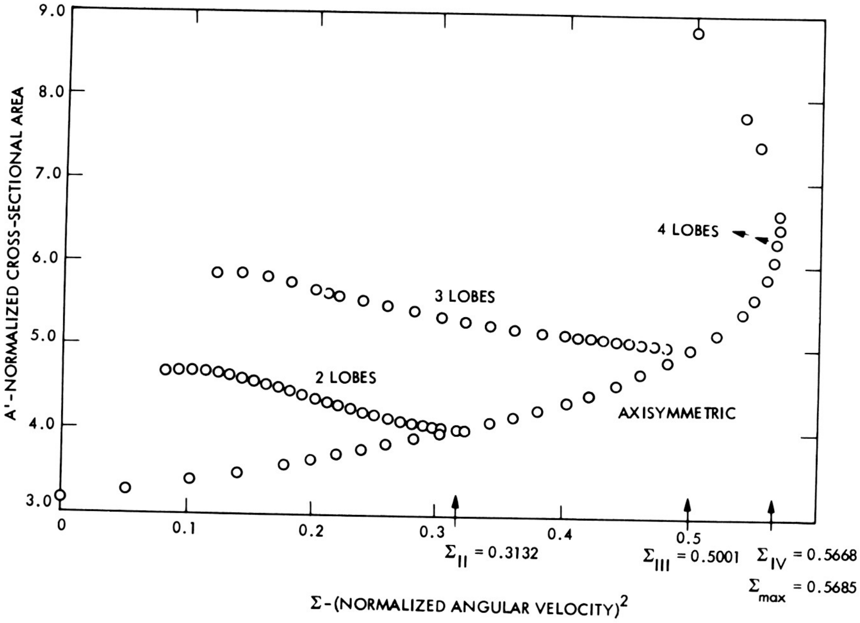

Figure 2

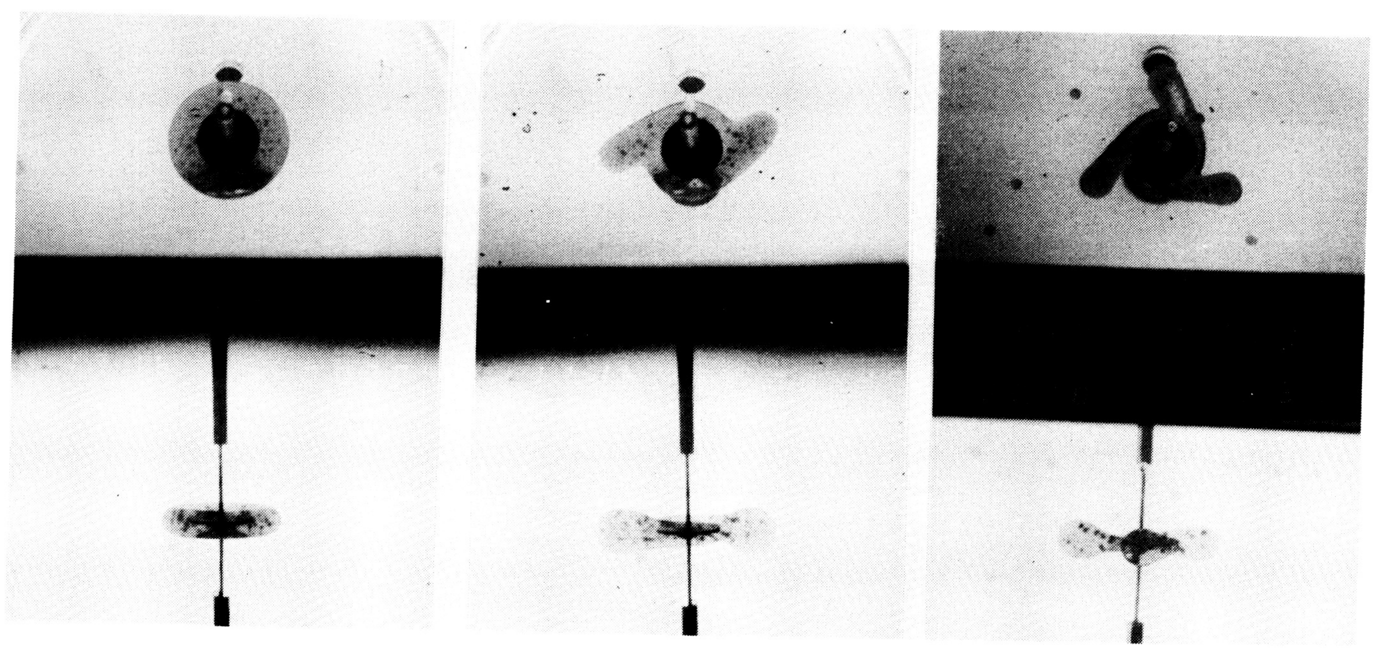

Figure 3

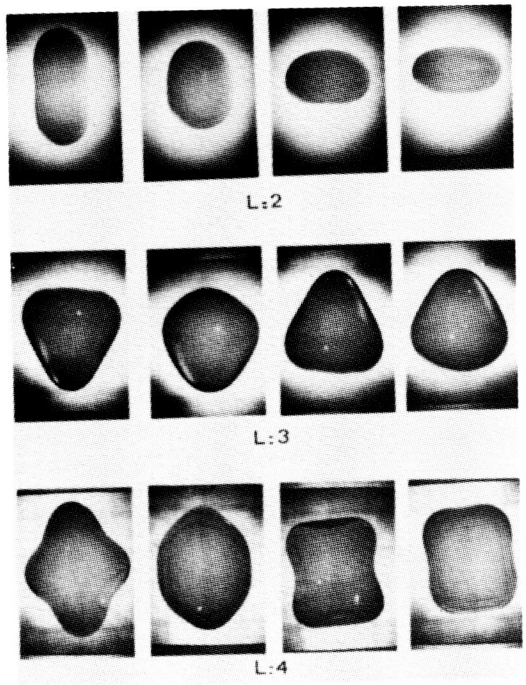

Figure 4

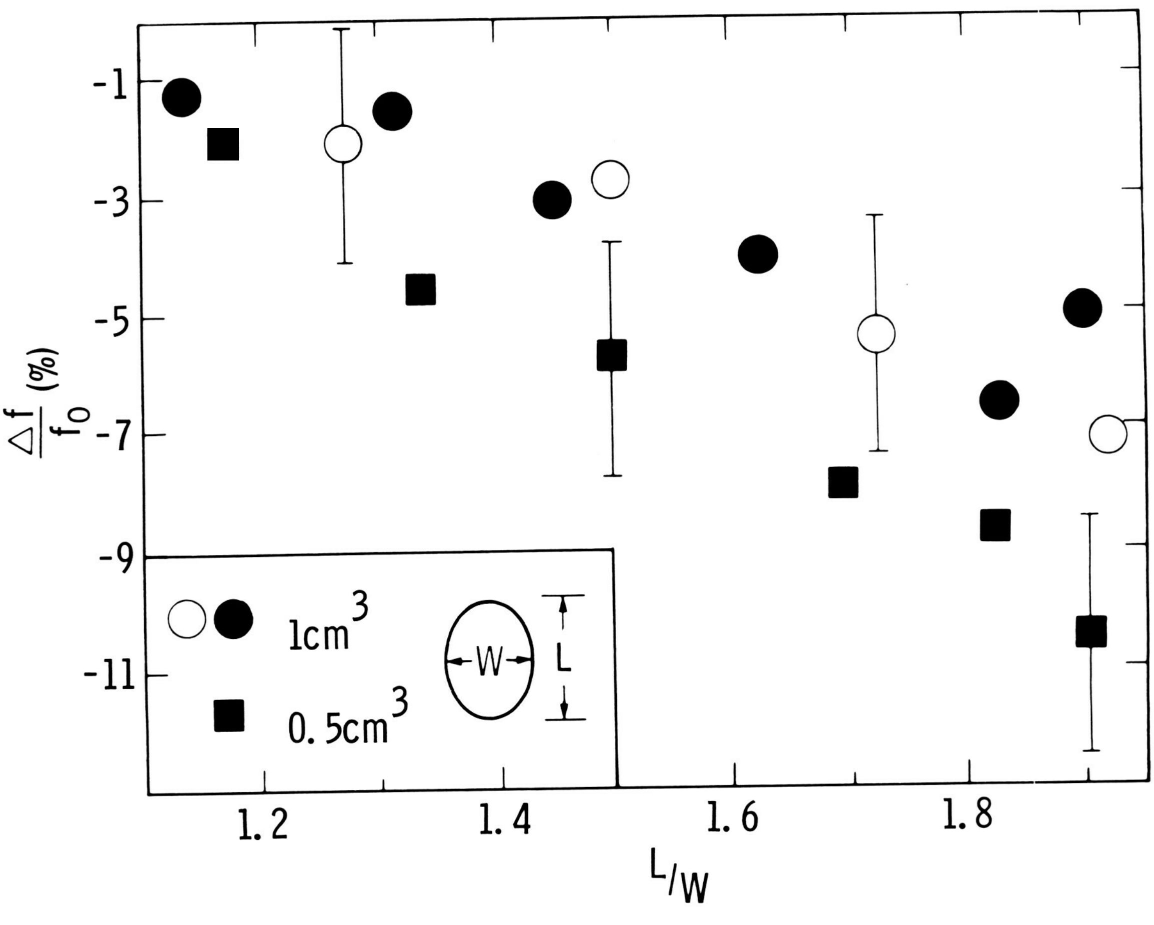

Figure 5

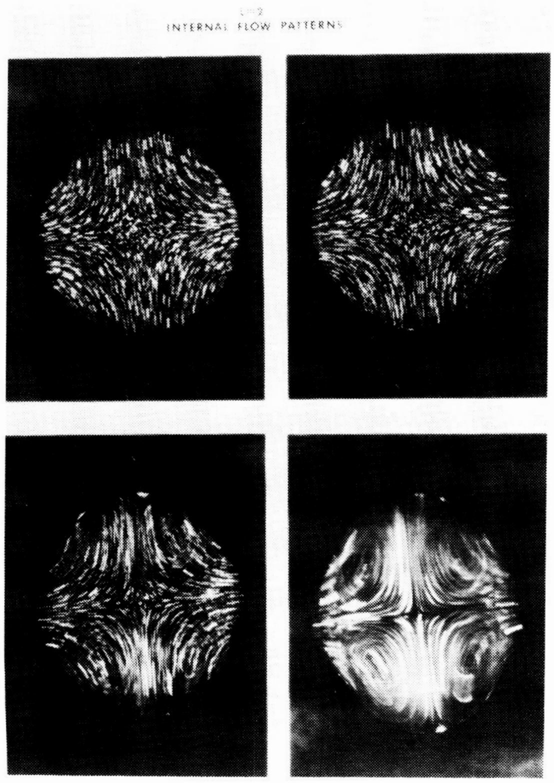

Figure 6

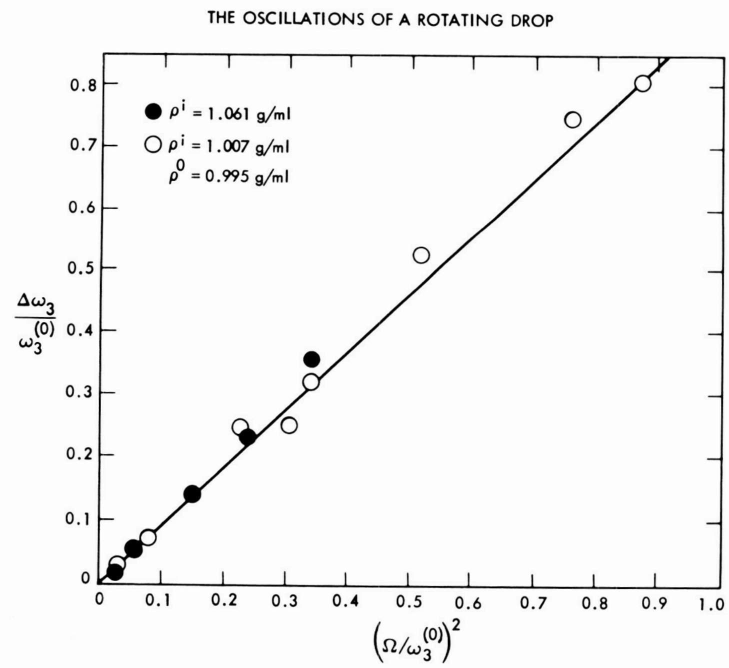

Figure 7

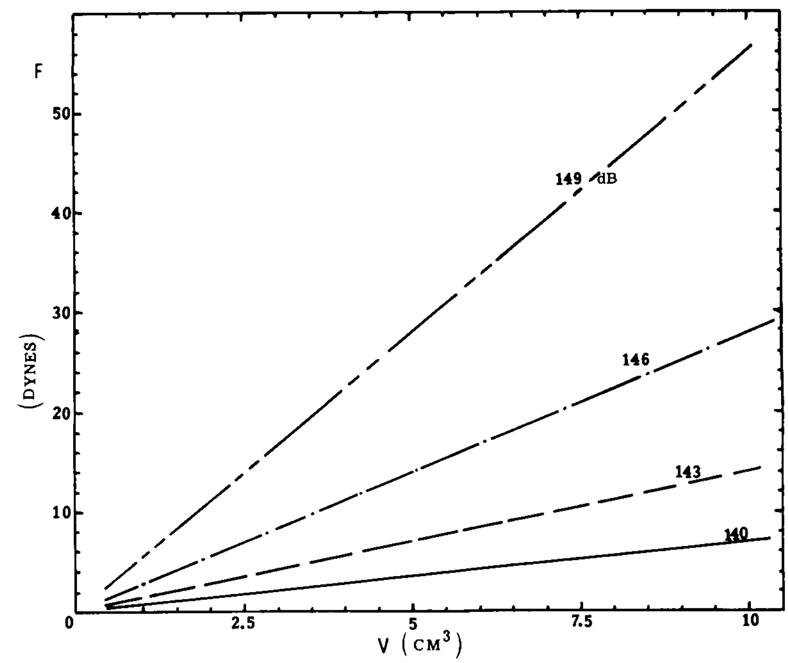

Figure 8

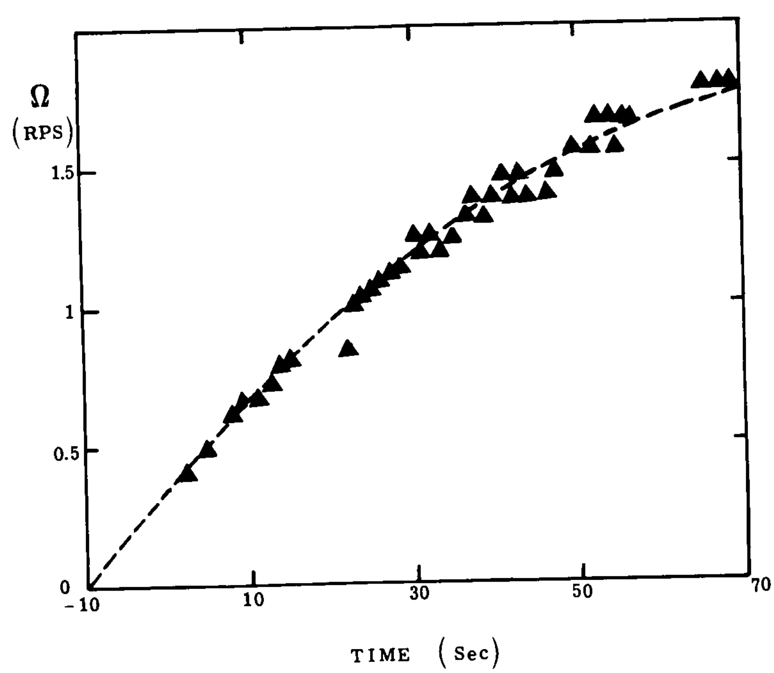

Figure 9

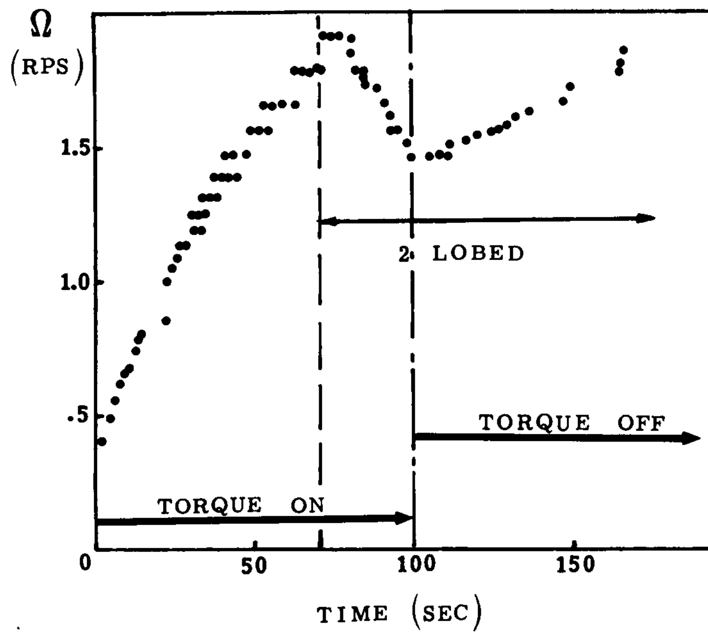

Figure 10

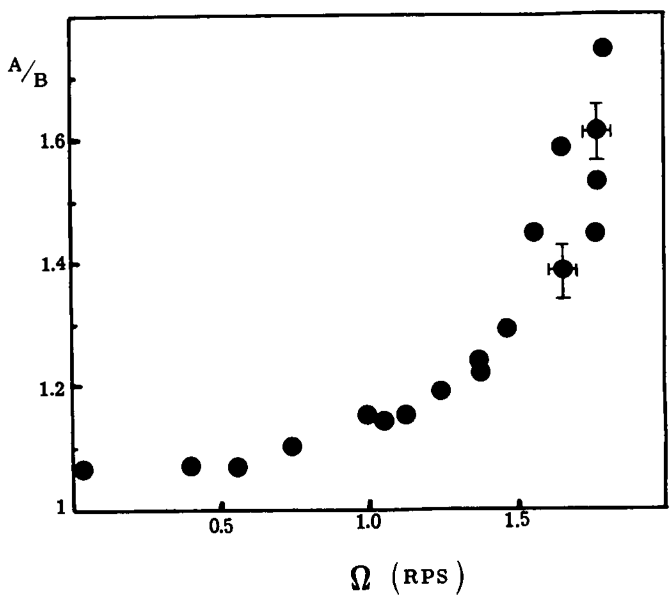

Figure 11

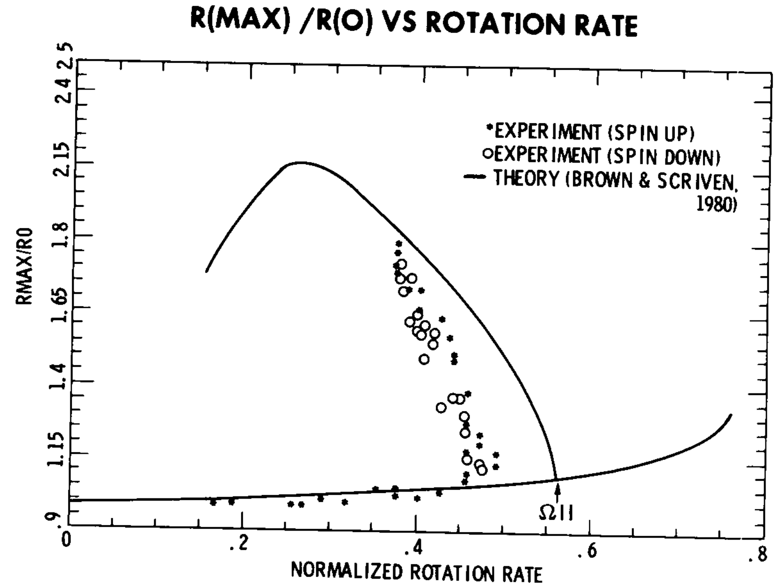

Figure 12

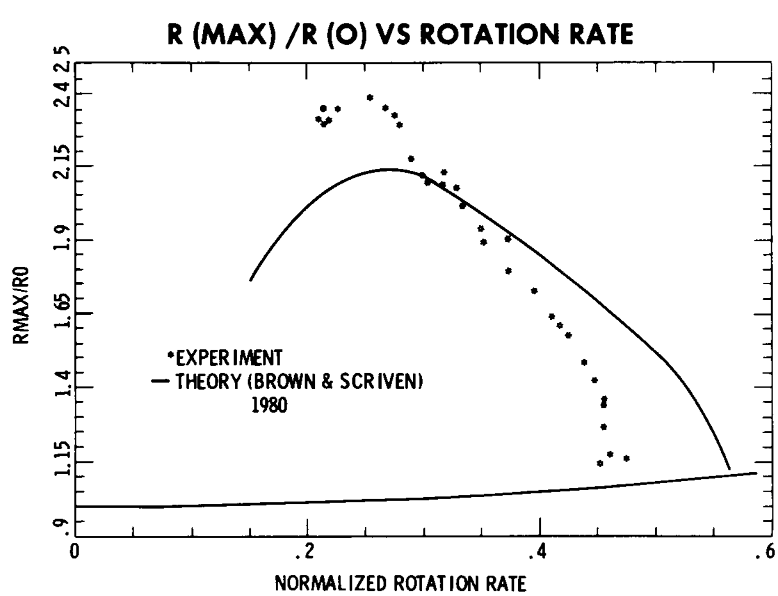

Figure 13

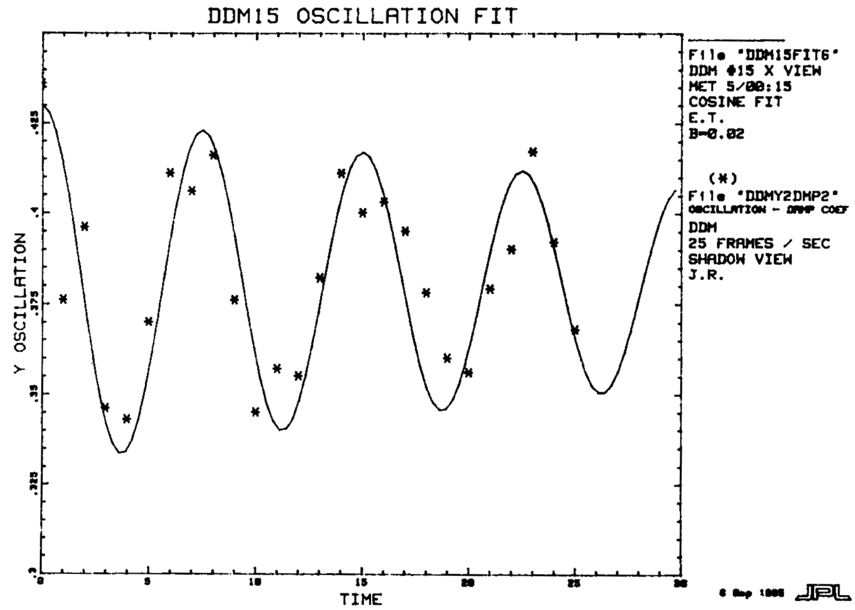

Figure 14

ORIGINAL PAGE IS
OF POOR QUALITY

DYNAMIC THERMOPHYSICAL MEASUREMENTS IN SPACE

Ared Cezairliyan and Archie P. Miiller

Thermophysics Division
National Bureau of Standards
Gaithersburg, Maryland 20899

Text of Presentation at the Microgravity Science Review
February 10-12, 1987
Marshall Space Flight Center
Alabama

ABSTRACT

The objective of this research is to develop an accurate dynamic technique which, in a microgravity environment, would enable performance of thermophysical measurements on high-melting-point electrically conducting substances in their liquid state. In spite of the critical need in high temperature technologies related to spacecraft, nuclear reactors, effects of powerful laser radiation, etc., and in validating theoretical models in related areas, no accurate data on thermophysical properties exist. This is primarily due to the limitation of the reliable steady-state techniques to temperatures below about 2000 K, and the accurate millisecond-resolution pulse heating techniques to the solid state of the specimen. The limitation of the millisecond-resolution techniques to temperatures below the melting point stems from the fact that the specimen collapses due to the gravitational force once it starts to melt. The rationale for the use of the microgravity is that by performing the dynamic experiments in a microgravity environment the specimen will retain its geometry, and thus it will be possible to extend the accurate thermophysical measurements to temperatures above the melting point of high-melting-point substances.

The research includes: (1) establishment of the geometrical stability criteria for specimens when heated rapidly, in a microgravity environment, to temperatures above their melting point, (2) development of techniques and instruments for the accurate measurement of quantities, such as current, voltage, temperature, under conditions required for dynamic experiments in a microgravity environment, (3) demonstration of the applicability of the millisecond-resolution pulse heating technique by performing, in a microgravity-environment, definitive measurements of the heat of fusion of a refractory metal such as niobium and tests for heat capacity and electrical resistivity measurements in the liquid phase, (4) exploratory work on the feasibility of measuring thermal conductivity of high temperature conducting and semiconducting liquids, and (5) design and construction of a system for accurate dynamic measurements of thermophysical properties in the Space Shuttle.

1. INTRODUCTION

1.1. Objective

The objective of the research is to develop an accurate dynamic technique which, in microgravity environment, would enable thermophysical measurements to be performed on high-melting-point electrically-conducting substances in their liquid state at temperatures above 2000 K.

1.2. Rationale

Reliable thermophysical properties data on high-melting-point substances in their liquid phase are almost nonexistent due to the serious and often unsurmountable difficulties involved in performing experiments at very high temperatures. Yet, such data are critically needed in various areas of high-temperature technologies related to spacecraft and rocketry (protective heat shield, etc.), understanding the behavior of substances exposed to powerful laser radiation, studies related to the operation of nuclear reactors, as well as in validating the theoretical models and predictions of the behavior of substances under extreme conditions.

Steady-state techniques for the reliable measurements of properties are generally limited to temperatures below about 2000 K. Dynamic techniques involving rapid pulse heating of the specimen have the potential of extending this limit to higher temperatures. Millisecond-resolution techniques have been developed which can provide accurate data up to about 4000 K. Such techniques, however, are limited to the solid phase of the specimen, since the specimen disintegrates and collapses under the gravitational force once it reaches its melting point. It seems logical, therefore, that by performing the experiments in a microgravity environment, it will be possible to extend the limits of the accurate dynamic techniques to temperatures above the melting point of the specimen.

1.3. Summary of Research

The first phase of the work is to establish the geometrical stability of a specimen when heated rapidly to temperatures above its melting point in a microgravity environment. A system has been designed and constructed which permits rapid heating of the specimen to temperatures above its melting point and checking of the geometrical stability of the liquid specimen. This system has been flown three times on board of KC-135 aircraft. The results suggested several refinements and modifications in the system, which are presently being made. Some additional work is needed in this direction to understand the complete behavior (geometrical stability) of the liquid specimen heated rapidly by the passage of a high current pulse through it, and as a result, optimize the specimen geometry and the operating conditions of the overall system.

The second phase of the work is to add new measurement capabilities to the system and to demonstrate the applicability of the technique by performing definitive measurements of the heat of fusion of a refractory metal, such as niobium, in a microgravity environment. In addition, measurements of heat capacity and electrical resistivity in the liquid phase will also be performed. Exploratory research will be conducted to determine the feasibility of measuring another important property, thermal conductivity, of high temperature conducting or semiconducting liquids utilizing the dynamic heating technique in a microgravity environment.

As much as possible, some of the initial tests will be conducted on board of KC-135 aircraft. However, the ultimate goal is the performance of the measurements in the Space Shuttle for reasons that it provides a better, a more reliable, and a longer microgravity environment essential for the success of all the experiments. For this purpose, a miniaturized and highly automated millisecond-resolution system will be designed and constructed.

2. BACKGROUND

2.1. Measurements on Solids by a Dynamic Technique

The increasingly critical need for thermophysical properties data above the limit of accurate steady-state experiments has motivated the establishment of the Dynamic Measurements Laboratory at the National Bureau of Standards. As the result of the pioneering research conducted in this laboratory, a novel dynamic technique has been developed for accurate thermophysical measurements at high temperatures. During the past decade or so, this laboratory has provided reliable data on selected thermal, electrical, and optical properties of a number of electrically-conducting solids at high temperatures (1500 - 3700 K), up to their melting points. The measured properties include: heat capacity, electrical resistivity, thermal expansion, hemispherical total emissivity, normal spectral emissivity, temperature and energy of solid-solid phase transformations, and melting temperature.

The technique involves heating the specimen resistively from room temperature to temperatures of interest in short times (typically about 1 s) by passing an electrical current pulse through it; and simultaneously measuring the pertinent experimental quantities with millisecond resolution. Because of the short heating time, this dynamic technique circumvents, to a very large extent, the problems (such as, chemical reactions, evaporation, specimen containment, large heat transfers, etc.) which seriously affect the reliable operation of conventional steady-state techniques at temperatures above about 2000 K. The dynamic technique is limited, however, to measurements on solids up to their melting temperatures, at which point the specimens become geometrically unstable and collapse due (in large measure) to the influence of gravity.

2.2. Measurements on Liquids by Dynamic Techniques

There are two possible options in extending the measurements to temperatures above the melting point of the specimen. These options are: (1) submillisecond heating of the specimen and performance of the measurements with microsecond resolution, and (2) performance of the experiments in a microgravity environment with millisecond resolution.

In the first case, heating of the specimen is very fast in comparison to its movement under the gravitational force; thus, all the pertinent measurements may be performed on the liquid specimen before the specimen collapses. This technique has been used by a few investigators to obtain data on liquid metals. However, there are two major objections to this technique: (1) because of the very high speeds (microsecond resolution) measurements of the experimental quantities are considerably less accurate than those made at slower speeds (millisecond resolution), and (2) because of the very high heating rates, the validity of the assumption that the specimen is under thermodynamic equilibrium at any given instant becomes doubtful and, as a result, the significance of determined properties becomes questionable.

The second case, namely performing the measurements in a microgravity environment, is very attractive because it is a natural extension of the highly accurate millisecond-resolution technique.

3. Measurements in a Microgravity Environment

3.1. Accomplishments and Present State

A research project, supported in part by NASA, was initiated in our laboratory to investigate the feasibility of performing thermophysical measurements in a microgravity environment utilizing the millisecond-resolution dynamic heating technique. The first step was the design, construction and testing of an equipment package, and performance of preliminary experiments to determine stability of the liquid specimens at high temperatures. For this initial phase, we selected the KC-135 flight program from among several NASA facilities for microgravity research (drop tubes, drop towers, other research aircraft, etc.) on the basis of compatibility with our measurement system requirements: (1) near-zero gravity time of 2 to 5 s duration, (2) short time interval (few minutes) between successive experiments, (3) "hands-on" access to the experiment package by test personnel, (4) flexibility of performing experiments in a "free-float" or "tied-down" mode, and (5) large experiment package (volume $\approx$ 40 ft^3, weight $\approx$ 700 lbs).

3.1.1. Test Equipment package

The test equipment package for experiments on board of KC-135 aircraft was constructed as two separate units: (1) the pulse-heating system (nominally 2′ wide x 4.5′ long x 3.5′ high; weight $\approx$ 450 lbs) which includes the specimen cartridge cell and all measuring and recording instruments; and (2) the main battery pack (nominally 2′ wide x 4′ long x 1′ high; weight $\approx$ 250 lbs) which supplies the electrical power for pulse heating the specimen.

The instrumentation in the pulse-heating system includes: a single-wavelength pyrometer, a high-speed framing camera, a two-channel digital storage oscilloscope for recording the specimen temperature and the current through the specimen, and a four-channel time delay generator for controlling the timing of various events such as, triggering the recording system, turning the framing camera on and off, closing and opening two fast-acting relay-driven switches which are connected in series in the power-pulsing circuit, etc. The second switch is closed 100 ms before and opened 100 ms after the first switch and thus serves as a backup in the (unlikely) event the first one fails to open at the end of the heating period. An "oscillo-streak" attachment on the framing camera enables a streak-image of an analog oscilloscope display of the pyrometer signal and the image of the rapidly heating specimen to be simultaneously recorded on the film; this feature greatly simplifies the analysis of the high-speed photographs. The framing camera is powered by a separate pack of gel cells in order to minimize the need for electrical power from sources external to the test equipment package. However, approximately 0.5 kilowatts of 110 V (60 Hz) a.c. power is required to operate certain instruments such as oscilloscopes and timers.

Each specimen is mounted inside its own cartridge cell containing argon gas at a pressure of 1 atm (gauge). The cells are designed so that they can be quickly inserted into and removed from the power-pulsing circuit before and after each experiment. A total of ten identical cartridge cells were fabricated thereby permitting up to ten specimens to be studied during a single KC-135 flight.

3.1.2. Preliminary Experiments on Board of KC-135

Three series of dynamic experiments under microgravity conditions were performed on board of KC-135 aircraft. The objectives were: (1) to test the integrity and operation of the equipment package, and (2) to investigate the behavior of the specimen during melting and postmelting periods. As the result of the experiments, after each flight, additions and changes were made in the equipment and specimen assembly to improve the operation of the system and specimen stability in the liquid phase.

The specimens (niobium) were fabricated in the form of cylindrical rods, 3 mm in diameter and 18 mm in length (distance between clamps). The center portion of each rod was reduced in diameter or "necked-down" in order to define the length of the zone which undergoes melting. The nominal dimensions of the melting zone, that is, the "effective" specimen, were as follows: a diameter of about 2.5 mm, and an aspect ratio (length:diamter) in the range of 1:1 to 3:1. The portions of the rods near the clamps were tapered to a diameter of 2 mm in order to reduce axial heat conduction from the "effective" specimen. The duration of the current pulse varied, depending on the experiment, between approximately 1.8 and 4.5 s. The corresponding heating rates were in the range 700 to 1700 $K \cdot s^{-1}$. During pulse heating, the behavior of the specimen was photographed by a high-speed framing camera operating at 500 fps while other pertinent experimental quantities such as the signals from the optical temperature sensor and from the accelerometers were recorded every 5 ms by digital storage oscilloscopes. Analyses of the (surface) radiance temperature-time data revealed that "effective" specimens with aspect ratios of 1.5:1 or less tended to yield the largest excursions (about 50 K) into the liquid phase before becoming unstable.

3.2. Planned Work

Research is in progress to establish optimum configuration of the specimen geometry and optimum operational conditions of the measurement system in order to maximize the temperature excursion of the specimen in the liquid phase. A new design, triaxial configuration for the specimen and current return paths, for the experiment chamber is being investigated. With this new design, it will be possible to balance electromagnetic forces on the specimen, and account for the surface tension of the specimen.

As a step toward thermophysical measurements, research has been initiated to design and construct novel high-speed pyrometers (multiwavelength and spatial scanning) for temperature measurements and instrumentation for pulse electrical measurements. As a part of the verification scheme, measurement of the heat of fusion of niobium has been performed in our laboratory utilizing a recently developed microsecond-resolution technique. This result will be compared with the data on heat of fusion that will be obtained in the first phase of the thermophysical measurements in the microgravity environment. The next step will be measurements of heat capacity and electrical resistivity of liquid niobium. Exploratory work has begun to determine the feasibility of measuring another important property, thermal conductivity, of high temperature conducting or semiconducting liquids utilizing the dynamic heating technique in a microgravity environment. These measurements are likely to require experiment durations greater than 20 s. Studies of the requirements for the experiments in the Space Shuttle have begun. Upon completion of these studies and the preliminary experiments on board of KC-135 aircraft, design and construction of a highly-automated apparatus for thermophysical measurements in the Space Shuttle will be started.

4. PUBLICATIONS

1. A. Cezairliyan, Dynamic Technique for Measurements of Thermophysical Properties at High Temperatures, International Journal of Thermophysics, 5, 177 (1984).
   (This publication is a summary of research performed in the Dynamic Measurements Laboratory at NBS and contains 50 references to publications describing the results of various aspects of our work until 1984).
2. A. Cezairliyan and A.P. Miiller, Heat Capacity and Electrical Resistivity of POCO AXM-5Q1 Graphite in the Range 1500-3000 K by a Pulse Heating Technique, International Journal of Thermophysics, 6, 285 (1985).
3. A.P. Miiller and A. Cezairliyan, Thermal Expansion of Molybdenum in the Range 1300-2800 K by a Transient Interferometric Technique, International Journal of Thermophysics, 6, 695 (1985).
4. A. Cezairliyan and J.L. McClure, A Microsecond-Resolution Transient Technique for Measuring Heat of Fusion of Metals: Niobium, International Journal of Thermophysics, in press.

N89-20318

THE FIRST PRODUCTS MADE IN SPACE: MONODISPERSE LATEX PARTICLES

J. W. Vanderhoff, M. S. El-Aasser, F. J. Micale,
E. D. Sudol, C.-M. Tseng, and H.-R. Sheu
Emulsion Polymers Institute and Departments
of Chemistry and Chemical Engineering
Lehigh University
Bethlehem, Pennsylvania 18015

and

D. M. Kornfeld
George C. Marshall Space Flight Center
Marshall Space Flight Center, Alabama 35812

ABSTRACT

The monodisperse polystyrene latexes widely used for calibration and other scientific uses are made by seeded emulsion polymerization, i.e., by polymerizing styrene in a previously prepared monodisperse latex, to grow the particles to larger size while maintaining their uniformity. The emulsifier concentration is critical: too little results in coagulation of the latex; too much, in the nucleation of a new crop of particles. Monodisperse latexes of 0.1-2.0 µm particle size have been available for some years. Larger sizes are difficult to prepare: the extent of coagulation increases with increasing particle size above 2 µm to complete coagulation at 10 µm. Brownian motion ceases for particles larger than 2 µm, and the large sticky monomer-swollen particles cream and the polymerized particles settle; this creaming or settling is offset by stirring the emulsion polymerization, but the monomer-swollen particles are sensitive to coagulation by mechanical shear, so that the amount of coagulum increases with increasing particle size. Polymerization in space eliminates the settling or creaming, so that the latex need be stirred only enough to give good heat transfer and mixing, thus alleviating or eliminating the coagulation by mechanical shear. Thus twenty monodisperse polystrene latexes were prepared in the MLR flight hardware on the STS-3, STS-4, STS-6, STS-7, and STS-11 flights of the Shuttle. Two polymerizations were small-particle-size controls. Of eighteen large-particle-size latex polymerizations, four on STS-4 failed owing to malfunction of the flight hardware, one on STS-6 owing to a broken heating wire, and one on STS-11 owing to a broken stirrer shearpin. The remaining twelve monodisperse latexes of 4-30 µm size had narrower particle size distributions (coefficients of variation 0.9-1.4%) than the ground-based control latexes (coefficients of variation 2-5%) and contained fewer offsize larger particles. The flight polymerizations produced only negligible amounts of coagulum; the ground-based control polymerizations produced increasing amounts with increasing particle size, and so were discontinued for latexes larger than 18 µm. The polymerization rates in space were the same as on earth within experimental error. The 10 µm STS-6 (coefficient of variation 0.9%) and the two 30 µm STS-11 (coefficients of variation 1.3%) latexes were accepted by the National Bureau of Standards as Standard Reference Materials, the first products made in space for sale on earth. Moreover, these particles were more perfect spheres than the ground-based control particles. Thus the original rationale of the experiments was confirmed unequivolcally by: 1. the negligible amounts of coagulum formed in the flight polymerizations; 2. the smaller number of offsize larger particles in the flight latexes; 3. the broadening of the particle size distribution and the formation of more larger offsize particles during the completion on earth of the polymerization of the partially-converted STS-4 flight latexes. The unanticipated advantages were: 1. the better uniformity of all flight latexes 4 µm or larger in size; 2. the more perfect sphericity of the 10 and 30 µm flight particles. More recent ground-based polymerizations gave monodisperse particles as large as 100 µm with tolerable levels of coagulum; however, their coefficient of variation (2.5%) was greater than those of the flight latexes. Monodisperse nonspherical particles (symmetric and asymmetric doublets, ellipsoids; egg-shaped, pear-shaped, ice cream cone-shaped, popcorn-shaped particles) were prepared by careful control of the polymerization recipe.

INTRODUCTION

Since 1947 monodisperse polystyrene latexes have found wide application as calibration standards and other scientific uses [1]. Series of monodisperse latexes were prepared by seeded emulsion polymerization, i.e., by polymerizing monomer in a previously-prepared monodisperse latex [2,3]; the particle size distribution was self-sharpening at small particle sizes [4-6]. The emulsifier concentration was critical: too little resulted in flocculation of the latex, too much, in nucleation of a new crop of particles [6].

The first series of monodisperse latexes ranged in average diameter from 88 nm (standard deviation σ 8.0 nm) to 340 nm (σ 5.2 nm) to 1171 nm (σ 13.3 nm) [3]. These standard deviations included not only the width of the particle size distributions, but also the errors involved in measuring the individual particle images of the electron micrographs and the difference in magnification from one exposure to another [3]. A later series showed improved monodispersity: the average particle diameters ranged from 91 nm (σ 5.8 nm) to 176 nm (σ 2.3 nm) to 1100 nm (σ 3.5 nm) to 2020 nm (σ 13.5 nm) [7].

Even larger sizes were prepared in the laboratory, i.e., up to 5.6 µm in 100-gm quantities and 10-12 µm in much smaller quantities [8]. The quantities were small because the polymerizations produced increasing amounts of coagulum, giving complete coagulation of the 10-12 µm sizes. The range of emulsifier concentrations which gave neither coagulum nor a new crop of particles was relatively broad at submicroscopic particle sizes [6], but narrowed with increasing size, so that duplicate polymerizations yielding 2 µm particles gave either stable latexes contaminated with a new crop of smaller particles or relatively unstable monodisperse latexes [8].

Particles larger than 2 µm in size show little or no Brownian motion; polystyrene (1.050 gm/cc) seed latex particles swollen with styrene monomer (0.905 gm/cc) cream and the polymerized particles settle. Of course, creaming or settling of the particles can be offset by stirring, which is always used in emulsion polymerizations; however, the large, soft, sticky monomer-swollen particles are sensitive to mechanical shear and thus are easily coagulated by too-vigorous stirring. The result is that the larger the particle size, the faster must be the stirring to avoid creaming and settling; however, too-fast stirring gives mechanical coagulation, so that it is difficult to prepare large-particle-size latexes without excessive coagulum.

In space, the particles show no tendency to cream or settle; therefore, the polymerization need be stirred only well enough to ensure good heat transfer and mixing (for the latex to be monodisperse, each particle must have the same temperature-time history, as the rate of polymerization increases with increasing temperature). Thus seeded emulsion polymerization in space would allow growth of the particles to larger sizes without excessive coagulum [9]; moreover, such a system would comprise an ideal model of a heterogeneous chemical reaction in space. This paper describes such polymerizations carried out on the STS-3 and STS-4 flights of the Columbia, and the STS-6, STS-7, and STS-11 flights of the Challenger.

EXPERIMENTAL DETAILS AND PROCEDURES

The flight hardware comprised the Monodisperse Latex Reactor (MLR; General Electric Space Sciences Laboratory) and the Support Electronics Package (SEP; Rockwell International). The MLR comprised four stirred 100-cc stainless-steel piston-cylinder dilatometers [10] (see Figure 1) in a sealed cylindrical container; the polymerization conversion-time curves were measured from the decrease in volume using a linear-variable-differential-transformer (LVDT); the temperatures in each dilatometer were measured by four three-pellet diodes in: 1. a probe in the center of the dilatometer; 2. the top of the reactor (piston face); 3. the wall midway between the top and bottom; 4. the bottom near the stirrer shaft. The SEP comprised the requisite DC voltage converters, electronic equipment, and data tape cassette in a sealed rectangular container. Both containers, connected with cables, were mounted on the forward bulkhead of the mid-flight deck of the Shuttle in place of three locker-drawers. The dilatometers were loaded with the monomer-swollen seed latexes and mounted on the circular base. Both containers were sealed, flushed with helium to detect leaks, and then with nitrogen to give an inert atmosphere. The sealed containers were mounted in the Shuttle 24-48 hours before launch.

The dilatometers were operated in preprocessing and processing modes. The preprocessing mode comprised intermittent stirring for 90 sec every 30 min (STS-3, STS-4, STS-6) or continuous stirring (STS-7, STS-11). The processing mode comprised continuous stirring while the contents were heated to 70° for 10.5 or 17.0 hrs, according to the flight, and then to 90° for 0.75 hrs, to complete the polymerization. The intermittent preprocessing stirring was used from the time of loading until the astronauts switched to processing at the predetermined time in orbit, and between the end of the processing and the recovery of the flight hardware on earth; the continuous preprocessing stirring was used from the time of loading until the Shuttle was in orbit, after which it was discontinued. After recovery from the Shuttle, the MLR was either stirred in the preprocessing mode until it was unloaded, or it was left unstirred and inverted periodically to redisperse the settled particles.

The polymerization recipes comprised seed latex, styrene monomer, azo initiator, inhibitor, and emulsifier. These recipes were developed after extensive ground-based research on the kinetics of seeded emulsion polymerization using oil-soluble azo and water-soluble persulfate ion initiators [11,12] and development of a three-component (sulfonated monomer or sulfonate emulsifier-carboxylated oligomer-water-soluble polymer) emulsifier mixture (instead of the single sulfonate emulsifier used earlier) to give better stability during polymerization [13]. The small-particle-size control polymerizations comprised 0.19 µm seed latex, styrene monomer, potassium persulfate initiator, and sodium bicarbonate buffer. The styrene monomer was distilled twice just before use to remove inhibitor; the desired amount containing initiator and inhibitor was added to the seed latex, and the mixture was agitated gently for 20 hrs; the monomer not absorbed by the latex was separated, and the monomer-swollen latexes were degassed and loaded into the dilatometers.

After the flight, the dilatometers were unloaded and cleaned, and ground-based control polymerizations were carried out using the same seed latex, monomer, and temperature-time schedule, except for STS-3 in which another seed latex of the same size was used for the control polymerizations and for STS-11 in which the control polymerizations were not run because of excessive coagulum. The data tape cassettes were processed by computer, to give the conversion-time curve and the four temperature-time variations for each dilatometer. The latexes were examined by optical microscopy immediately after unloading to gain an impression of their monodispersity, and later by transmission electron microscopy (Philips Model 400) or scanning electron microscopy (ETEC Autoscan) to determine the particle size distributions. The distributions were measured using the Zeiss MOP-3 Modular System for Quantitative Digital Analysis, and the offsize larger particles were counted.

EXPERIMENTAL RESULTS AND DISCUSSION

Several preliminary descriptions of the flight experiments were given earlier [14-17]. Four polymerization experiments were carried out on STS-3; three used a 2.52 µm monodisperse seed latex with nominal 2:1, 4:1, and 10:1 monomer-polymer ratios; the fourth control polymerization used a 0.19 µm monodisperse seed latex with a 2:1 monomer-polymer ratio. The polymerization time at 70° was 10.5 hrs. For 24-48 hrs before opening, the MLR was inverted periodically to redisperse the settled latex particles and then the stirrers were turned on. The rotation of the stirrer of flight latex 2 dilatometer was restricted, so it was turned off.

Figure 2 shows electron micrographs of the seed latexes and the large-particle-size flight latexes prepared on STS-3, STS-6, STS-7, and STS-11, and Table I gives the nominal monomer-polymer (M-P) ratio, preprocessing/processing agitation rates, initiator concentration [I], number-average diameter D_n, standard deviation σ, number of particles measured n, coefficient of variation σ/D_n in percent, and the number of offsize larger particles relative to the number in the main distribution. Except where noted, all latexes were completely polymerized when removed from the dilatometers, as determined by the absence of styrene odor. The flight latex 2 dilatometer contained a small lump of hard coagulum adhering to the wall, which

TABLE I

Particle Size Distributions

Latex	Flight	Nominal M-P Ratio	rpm	[I] mM	D_n µm	σ µm	n	σ/D_n	Offsize Larger Part*
seed	STS-3	---	---	---	2.52	0.046	1024	1.84	-----
flight 1	STS-3	2:1	13/13	3.9	3.44	0.064	2777	1.87	1/264
ground 1	STS-3	2:1	13/13	3.9	3.72	0.057	1363	1.54	1/339
flight 2	STS-3	4:1	13/13	6.6	4.08	0.069	2256	1.69	1/207
ground 2	STS-3	4:1	13/13	6.6	3.93	0.077	913	1.96	1/172
flight 3	STS-3	10:1	13/13	12.6	4.98	0.082	2095	1.64	1/99
ground 3	STS-3	10:1	13/13	12.6	4.74	0.167	1232	3.51	1/65
seed	STS-6	---	---	---	5.63	0.073	328	1.30	1/168
flight 9	STS-6	2:1	13/13	2.5	7.94	0.122	829	1.53	1/267
ground 9	STS-6	2:1	13/13	2.5	7.86	0.137	675	1.74	1/220
flight 11	STS-6	6:1	13/13	5.3	9.96	0.115	1102	1.15	1/106
ground 11	STS-6	6:1	13/13	5.3	10.04	0.281	1059	2.80	1/93
seed**	STS-7	---	---	---	7.94	0.046	1024	1.53	1/267
flight 13	STS-7	6:1	13/13	5.3	13.12	0.149	327	1.13	1/360
ground 13	STS-7	6:1	13/13	5.3	13.89	0.371	308	2.67	1/120
seed	STS-7	---	---	---	10.30	0.135	300	1.31	1/130
flight 14	STS-7	4:1	13/13	4.1	16.64	0.201	322	1.21	1/90
ground 14	STS-7	4:1	13/13	4.1	17.17	0.394	326	2.29	1/50
flight 15	STS-7	6:1	13/6	5.3	17.81	0.210	321	1.18	1/70
ground 15	STS-7	6:1	13/6	5.3	17.68	0.949	275	5.37	>1/50
flight 16	STS-7	6:1	6/3	5.3	18.18	0.200	321	1.10	1/110
ground 16	STS-7	6:1	6/3	5.3	16.97	0.778	361	4.58	-----
seed***	STS-11	---	---	---	17.81	0.210	321	1.18	1/70
flight 17	STS-11	5:1	13/6	5.5	30.42	0.41	310	1.35	1/30
flight 18	STS-11	5:1	6/3	5.5	30.92	0.44	320	1.42	1/25
seed	STS-11	---	---	---	10.30	0.135	300	1.31	1/130
flight 19	STS-11	6:1	13/6	5.5	18.4	-----	---	----	----
flight 20	STS-11	6:1	6/3	5.5	19.44	0.24	256	1.22	1/66

* relative to the main distribution
** flight latex 9 from STS-6
*** flight latex 15 from STS-7

restricted the motion of the stirrer; the other flight latexes contained negligible amounts of coagulum.

Figure 2a shows the three monodisperse flight latexes. Table I shows that there were subtle differences in particle size distribution between the three flight latexes and the corresponding ground-based control latexes. The coefficients of variation were about the same for all latexes except for ground-based control latex 3, which was broader in particle size distribution. The standard deviations increased only slightly with increasing particle size; however, they express not only the breadth of the particle size distribution, but also the errors in measuring the particle images of the electron micrographs and the variation in magnification from one exposure to another. For the 2.52 µm seed latex, measurement of the same particle image twenty times gave a standard deviation of 0.015-0.018 µm (coefficient of variation 0.6-0.7%). Earlier, it was shown that the standard deviation of the averages of 24 exposures of 1.17 µm-size particles was 0.0092µm (coefficient of variation 0.8%) [3]. The contributions of these two sources of error to the standard deviations are significant.

These latexes contained a small number of particles which were 30-80% larger than those of the main distribution. Table I shows that the relative numbers of the larger offsize particles increased with increasing monomer-polymer ratio. Moreover, the number was slightly smaller for ground-based latex 1 and slightly larger for ground-based latexes 2 and 3, as compared with those of the corresponding flight latexes. Polymerizations of latexes of these sizes on earth gave relative numbers of 1/60 at best, greater that those of flight latexes 1 and 2 and slightly greater than that of the flight latex 3.

These larger offsize particles were attributed to the coalescence of two or more monomer-swollen seed particles or the presence of a few larger offsize particles in the seed latex which grew proportionately during the polymerization. The coalescence of two particles of the main distribution would give a particle of 26% larger diameter, three a 44% larger diameter, four a 59% larger diameter, five a 71% larger diameter, and six an 82% larger diameter. These larger offsize particles are difficult to remove because their sizes are only slightly larger than those of the main distribution.

The smaller offsize particles can be removed completely by repeated sedimentation-decantation or serum replacement [18]. The number of these smaller particles was not determined accurately; however, their relative number was small and increased with increasing monomer-polymer ratio. Some were about the same size as the original seed latex particles, which suggests that the latexes became contaminated by unpolymerized seed latex particles which were lodged in the entry ports of the dilatometers.

Figure 3 shows the conversion-time curves of the large-particle-size latexes. The data points were 1-min averages of the tape data, which formed a continuous line on this scale. For all three monomer-polymer ratios (Figure 3a), the conversion-time curves of the flight and ground-based control polymerizations were parallel; however, these curves virtually coincided when shifted slightly along the ordinate. The initial dips in these curves were attributed to the errors in the calibration of the dilatometers. The lab prototype dilatometer, which had been calibrated more rigorously, showed no such dips in the conversion-time curves. The leveling-off of the conversion-time curves was attributed to the formation of a gas bubble or sticking of the dilatometer; the nitrogen formed by decomposition of the azo initiator may have exceeded its solubility in the latex and thus formed a bubble; since gas bubbles are compressible, the dilatometer reading beyond this point would not change. Sticking of the dilatometer would also give such a leveling-off.

Despite these discrepancies, the conversion-time curves of the flight polymerizations were essentially the same as those of the corresponding ground-based control polymerizations: the 2:1 ratio gave a significant upward deviation from linearity indicative of autoacceleration, the 4:1 ratio only a slight upward deviation from linearity, and the 10:1 ratio a near-linear variation. Since the critical particle size for the transition from emulsion polymerization kinetics to bulk polymerization kinetics is ca. 1.3 μm for the styrene-polystyrene system at 70° [19], the polymerization rate should be proportional to the monomer concentration and the square root of the initiator concentration in the absence of autoacceleration. The upward deviation from linearity began earlier, the lower the monomer-polymer ratio, as expected from the higher viscosity of the particles.

Four polymerizations were carried out on STS-4; all used a 5.5 μm ground-based monodisperse polystyrene seed latex with nominal 2:1, 4:1, 6:1, and 8:1 monomer-polymer ratios in flight polymerizations 5, 6, 7, and 8, respectively, and preprocessing/processing stirring rates of 13/13 rpm. The polymerization of all four latexes was incomplete as evidenced by the odor of styrene; moreover, the data tape cassette yielded only meaningless numbers for the dilatometer volume and temperature readings. A DC voltage converter in the SEP had failed, with the consequent failure of other electrical components, so that the temperature-time variation of the monomer-swollen latexes was not known and the voltage signals to the data tape cassette were inconsistent and nonrepresentative. The conversions were 48-67% by gravimetric measurement and 54-73% by ultraviolet absorbance of isooctane extracts. Optical microscopy showed that the latex particles were monodisperse with only a few offsize larger particles; moreover, their size was that expected from the stoichiometry of the seeded polymerizations, i.e., 7.2, 8.6, 9.5, and 10.4 um, respectively, for the 2:1, 4:1, 6:1, and 8:1 monomer-polymer ratios. The residual monomer in these latex particles made them useless as calibration standards. Moreover, completion of the polymerizations on earth gave a broader particle size distribution and an increased number of larger offsize particles, the result of further coalescence of the monomer-swollen particles during polymerization.

Four polymerizations were carried out on STS-6; three used a 5.63 μm ground-based monodisperse polystyrene seed latex with nominal 2:1, 4:1, and 6:1 monomer-polymer ratios, and the fourth control polymerization used the 0.19 μm seed latex with a 2:1 monomer-polymer ratio. Flight latex 10 displayed a strong odor of styrene; this sample had not polymerized owing to a broken wire in the heating circuit. It is not known whether the wire broke before or during the launch; however, the reactor functioned satisfactorily in the test polymerizations carried out two weeks before the flight.

Figure 2b shows electron micrographs of the two flight latexes. Table I shows that the coefficients of variation for the flight latexes were slightly smaller than for the ground-based control latexes. The values of the standard deviations were similar for the two flight latexes and slightly greater than that of the seed latex; these values were slightly smaller than those of the ground-based latexes, especially for flight latex 11.

All of the STS-6 latexes contained a small number of offsize larger particles. Their numbers were slightly smaller for flight and ground-based latexes 9, and slightly greater for flight and ground-based latexes 11, as compared with the number for the seed latex; moreover, the numbers for the flight latexes were slightly smaller than for the ground-based latexes.

In summary, both flight latexes 9 and 11 were clearly superior in uniformity to the ground-based control latexes. Flight latex 11 (D_n 9.96 µm; σ 0.115; σ/D_n 1.15%) was accepted by the National Bureau of Standards as a Standard Reference Material and placed on sale in July 1985, to make it the first product made in space for sale on earth. These particles were also found to be more perfect spheres than the ground-based particles [20]. The Bureau gave average diameters of 9.886±0.029 µm (σ 0.09 µm; σ/D_n 0.91%) by metrology electron microscopy, 9.89±0.04 µm by optical-microscopic center-distance-finding, and 9.90 µm by resonance light scattering. The Lehigh 9.96 µm value was in excellent agreement with these values.

Figure 3b shows that the conversion-time curves were similar for the flight and ground-based latexes. The leveling-off of the conversion-time curves of the flight latexes was attributed to the formation of a nitrogen bubble or sticking of the dilatometer. The curves for the flight and ground-based latexes 9 showed a significant upward deviation from linearity, indicative of autoacceleration; those for latexes 11 showed near-linear variations. The conversion-time curves of the flight polymerizations leveled-off at a relatively early stage, which was more likely due to sticking of the dilatometer than to the formation of a nitrogen bubble. The curves for the flight and ground-based polymerizations were similar up to this point, with the flight polymerizations showing slightly faster polymerization rates. The disparity was attributed to the poorer mixing of the ground-based latexes, which would give a greater temperature gradient and thus a greater variation in polymerization rates. The upward deviation from linearity began earlier, the lower the monomer-polymer ratio, as expected from the higher viscosity of the monomer-swollen particles. The failure of the curves for latexes 11 to show upward deviations from linearity was attributed to sticking of the dilatometers or formation of nitrogen bubbles before the polymerizations reached the autoacceleration stage.

Four polymerizations were carried out on STS-7; three used a 10.30 µm ground-based monodisperse polystyrene seed latex with nominal 4:1, and 6:1 monomer-polymer ratios; the fourth used the 7.94 µm flight latex 9 as seed with a 6:1 monomer-polymer ratio. Figure 2c shows electron micrographs of the four monodisperse flight latexes. Table I shows that the coefficients of variation of the flight latexes were slightly smaller than those of the seed latexes, 1.13% for flight latex 13 as compared to 1.53% for the flight latex 9 seed, and 1.21, 1.18, and 1.10% for flight latexes 14, 15, and 16, respectively, as compared to 1.31% for the 10.30 µm seed latex; the values for the ground-based control latexes were 2.67%, and 2.29, 5.37, and 4.58%, respectively, significantly greater than for the flight latexes. All latexes contained a small number of larger and smaller offsize particles. The numbers of offsize larger particles were slightly smaller for the flight latexes than for the ground-based control latexes and increased with increasing particle size and monomer-polymer ratio.

Figure 3c shows that the conversion-time curves of flight latexes 13 and 16 virtually coincided with those for the ground-based control polymerizations; the curves for the flight latexes 14 and 15 fell slightly above those for the control latexes. The leveling-off of the conversion-time curves was attributed to the formation of a nitrogen bubble or sticking of the dilatometer. The temperature gradients between the wall and center of the dilatometer increased with increasing latex particle size and monomer-polymer ratio. The differences in temperature gradient between the flight and ground-based control polymerizations ranged from 0.46^o for latexes 13 to 2.85^o for latexes 15.

Four polymerizations were carried out on STS-11; two used the 10.30 µm ground-based seed latex used on STS-7; two used the 17.81 um flight seed latex 15 prepared on STS-7 flight with a nominal 5:1 monomer-polymer ratio. For several hours before unloading, the MLR was inverted periodically to redisperse the settled latex particles. When the stirrers were turned on, the movement of the flight latex 19 stirrer was restricted; therefore, it was turned off immediately; the dilatometer had a broken stirrer-shaft shear-pin, and it contained a mass of coagulum between one side of the stirrer blade and the wall. It is not known whether the formation of coagulum stalled the stirrer and broke the shear pin or the failure of the shear pin caused the formation of coagulum: flight latex 20, which was identical except for the stirring rates, contained no coagulum, yet failure analysis of the broken shear pin showed no evidence of fatigue failure. Ground-based control polymerizations were not carried out for this series because the STS-6 and STS-7 control polymerizations showed that the coagulum increased so strongly with increasing particle size that the valuable seed latex would have been wasted.

Figure 2d shows electron micrographs of the two seed latexes and three flight latexes, and Table I shows that the coefficients of variation of the flight latexes were about the same or slightly greater than those of the seed latexes. The standard deviations were slightly greater than those of the seed latexes.

All of the STS-11 latexes contained smaller and larger offsize particles. The smaller offsize particles were removed by repeated sedimentation-decantation. The numbers of offsize larger particles determined by particle counts in the optical microscope were about twice those of the seed latexes. Flight latexes 17 and 18 (30 µm) were accepted by the National Bureau of Standards as a Standard Reference Material, to make them the second product made in space for sale on earth. These particles were also found to be more perfect spheres than the ground-based particles [20].

Figure 3d shows that initially the conversion-time curves of the flight latexes virtually coincided, but that flight latexes 17 and 18 showed a slightly greater upward deviation from linearity than flight latexes 19 and 20, which was attributed to the higher monomer-polymer ratio and hence lower viscosity delaying the onset of autoacceleration.

The monomer-swollen seed latexes used in the STS-11 experiments creamed at the preprocessing stirring rates used (their stability during polymerization was satisfactory, however), and it was feared that flight polymerization of larger particles would fail because of this creaming. Therefore, an extensive investigation was carried out to develop recipes that would give better stability before and during polymerization. This investigation included: 1. the use of denser monomers, e.g., chlorostyrene, to make the monomer-swollen particles neutrally buoyant; 2. the use of divinylbenzene crosslinking monomer to make the particle-particle collisions more elastic; 3. the use of higher-molecular-weight water-soluble polymer to enhance its adsorption on the particles; 4. the optimization of the buffer electrolyte system to keep the pH at a value where the carboxylated oligomer was near-completely ionized. The result was a series of polymerizations [21] in which 0.2-µm particles were grown in eighteen steps to 100 µm particles (Figure 4) with tolerable levels of coagulum. Their coefficient of variation was 2.5%, typical of ground-based latexes and significantly greater than that of flight latexes. Thus these new recipes enhance the probability of success in making monodisperse 100-µm latexes in future flights.

These experiments also showed that spherical lightly-crosslinked particles swollen with styrene containing small concentrations of divinylbenzene sometimes became nonspherical during polymerization. The second crosslinked network polymerized in the first crosslinked network became incompatible and separated [22]. The tendency to separate was determined by the balance between: 1. the osmotic swelling force; 2. the elastic retractile force of the network; 3. the interfacial tension between the particles and the medium. By careful control of the divinylbenzene concentration and the other parameters of the system, uniform nonspherical particles of various shapes were made. Figure 5 shows scanning electron micrographs of uniform: (a) egg-shaped particles; b. ellipsoids; c. asymmetrical doublets; d. symmetrical doublets; e. ice cream cone-shaped particles; f. popcorn-shaped particles. These particles will find application in fundamental studies of rheology, sedimentation, electrophoresis, and other hdyrodynamic phenomena.

CONCLUSIONS

The preparation of large-particle-size 3-30 µm monodisperse latexes in space confirmed the original rationale unequivocally: 1. the flight polymerizations formed negligible amounts of coagulum as compared to increasing amounts for the ground-based polymerizations; 2. the number of offsize larger particles in the flight latexes was smaller than in the ground-based latexes; 3. the particle size distribution broadened and more larger offsize particles were formed when the polymerizations of the partially converted STS-4 latexes were completed on earth. Polymerization in space also showed other unanticipated advantages: 1. the flight latexes had narrower particle size distributions than the ground-based latexes; 2. the particles of the flight latexes were more perfect spheres than those of the ground-based latexes. The superior uniformity of the flight latexes was confirmed by the National Bureau of Standards acceptance of the 10 µm STS-6 latex and the 30 µm STS-11 latexes as Standard Reference Materials, the first products made in space for sale on earth. The polymerization rates in space were the same as those on earth within experimental error. Further development of the ground-based polymerization recipes gave monodisperse particles as large as 100 µm with tolerable levels of coagulum, but their uniformity was significantly poorer than that of the flight latexes. Careful control of the polymerization parameters gave uniform nonspherical particles: symmetrical and asymmetrical doublets, ellipsoids, egg-shaped, ice cream cone-shaped, and popcorn-shaped particles.

ACKNOWLEDGMENTS

The authors acknowledge gratefully the support of the National Aeronautics and Space Administration Contract NAS8-32951, as well as the technical support and assistance of the George C. Marshall Space Flight Center, the ground support of the Kennedy Space Center, and the performance of the experiments in space by astronauts and mission specialists of the Johnson Space Center.

REFERENCES

1. J. W. Vanderhoff, Org. Coatings Plastics Chem. 24(2), 223 (1964).
2. T. Alfrey, Jr., E. B. Bradford, J. W. Vanderhoff, and G. Oster, J. Opt. Soc. Am. 44, 603 (1954).
3. E. B. Bradford and J. W. Vanderhoff, J. Appl. Phys. 26, 864 (1955).
4. E. A. Willson, J. R. Miller, and E. H. Rowe, J. Phys. Colloid Chem. 53, 357 (1949).
5. J. W. Vanderhoff, J. F. Vitkuske, E. B. Bradford, and T. Alfrey, Jr., J. Polym. Sci. 20, 225 (1956).
6. E. B. Bradford, J. W. Vanderhoff, and T. Alfrey, Jr., J. Colloid Sci. 11, 135 (1956).
7. J. W. Vanderhoff, M. S. El-Aasser, and F. J. Micale, Abstracts, 175th Meeting, ACS, Anaheim, March 13-17, 1978, COLL-110.
8. J. W. Vanderhoff, unpublished research, Dow Chemical Co., 1958-1962.
9. J. W. Vanderhoff, M. S. El-Aasser, F. J. Micale, and D. M. Kornfeld (to NASA), U. S. Patent 4,247,434, January 27, 1981.
10. E. D. Sudol, F. J. Micale, M. S. El-Aasser, and J. W. Vanderhoff, Rev. Sci. Instruments 57 2332 (1986).
11. E. D. Sudol, M. S. El-Aasser, and J. W. Vanderhoff, J. Polym. Sci., Part A: Polym. Chem. 24 3499 (1986).
12. E. D. Sudol, M. S. El-Aasser, and J. W. Vanderhoff, J. Polym. Sci., Part A: Polym. Chem. 24 3515 (1986).
13. J. W. Vanderhoff, C.-M. Tseng, and M. S. El-Aasser, U.S. Patent Application Ser. No. 682,181, filed December 17, 1984.
14. J. W. Vanderhoff, M. S. El-Aasser, F. J. Micale, E. D. Sudol, C.-M. Tseng, A. Silwanowicz, D. M. Kornfeld, and F. A Vicente, J. Dispersion Sci. Technol. 5 231 (1984).
15. J. W. Vanderhoff, M. S. El-Aasser, F. J. Micale, E. D. Sudol, C.-M. Tseng, A. Silwanowicz, and D. M. Kornfeld, Polym. Materials Sci. Eng. 54 587 (1986).
16. J. W. Vanderhoff, M. S. El-Aasser, F. J. Micale, E. D. Sudol, C.-M. Tseng, H.-R. Sheu, and D. M. Kornfeld, Preprint 04.4, Fall Meeting, Materials Research Society, December 1-6, 1986, Boston; to be published in J. Materials Res.
17. J. W. Vanderhoff, M. S. El-Aasser, F. J. Micale, E. D. Sudol, C.-M. Tseng, H.-R. Sheu, and D. M. Kornfeld, Preprint AIAA-87-0389, AIAA 25th Aerospace Sciences Meeting, January 12-15,

1987, Reno; submitted to J. Spacecraft Rockets.
18. V. Lowry, M. S. El-Aasser, and J. W. Vanderhoff, Graduate Research Progress Reports, Emulsion Polymers Institute, Lehigh University 14 13 (1980); ibid. 15 13 (1981); ibid. 16 23 (1981).
19. J. W. Vanderhoff and E. B. Bradford, Tappi 39, 650 (1956).
20. T. E. Lettieri, National Bureau of Standards, private communication, 1986.
21. H.-R. Sheu, M. S. El-Aasser, and J. W. Vanderhoff, Graduate Research Progress Reports, Emulsion Polymers Institute, Lehigh University 26 6 (1986).
22. H.-R. Sheu, M. S. El-Aasser, and J. W. Vanderhoff, Graduate Research Progress Reports, Emulsion Polymers Institute, Lehigh University 26 11 (1986).

ORIGINAL PAGE IS
OF POOR QUALITY

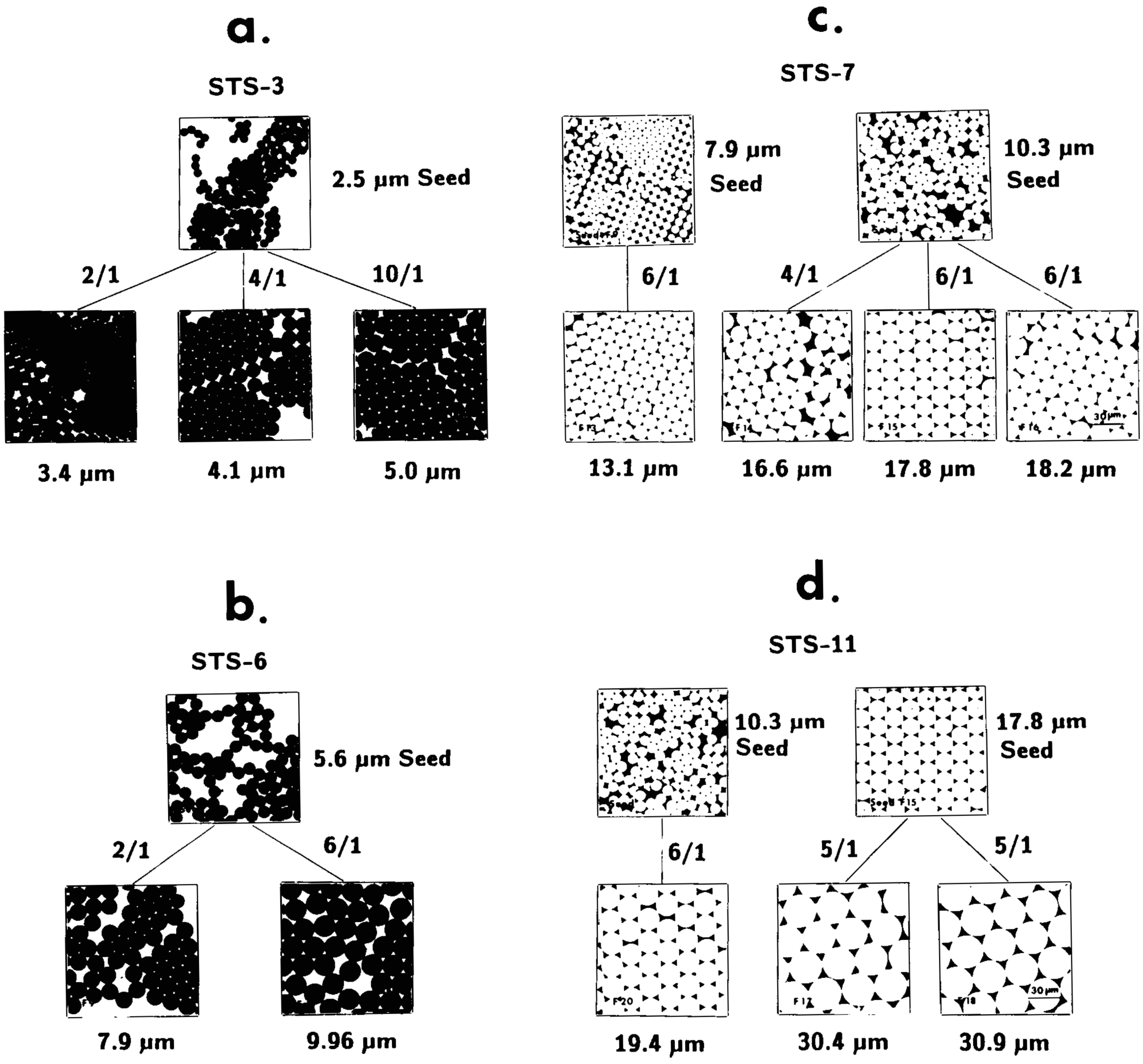

Figure 2. Electron micrographs of the seed and flight latexes.

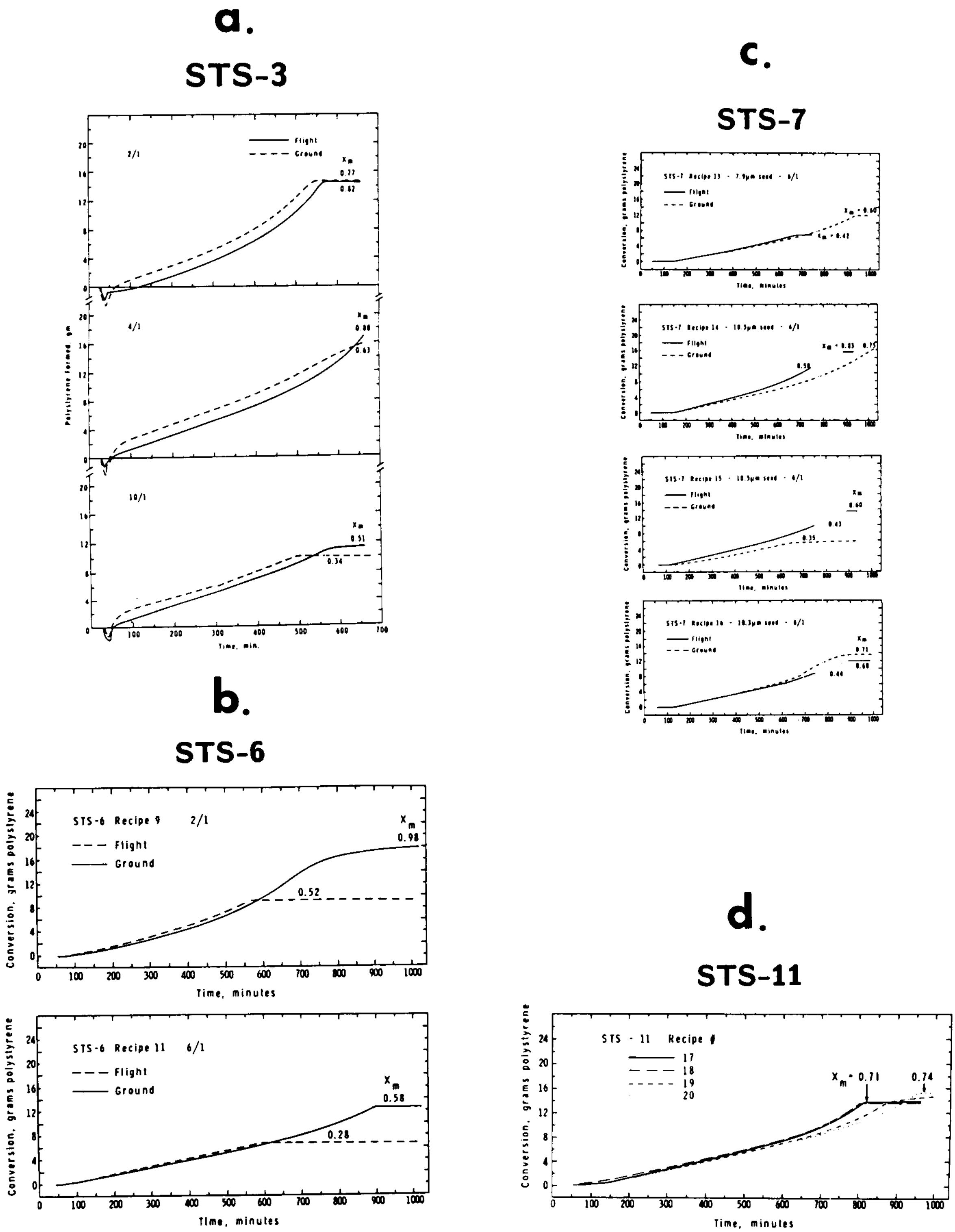

Figure 3. Variation of conversion with time for the flight and ground-based control latexes.

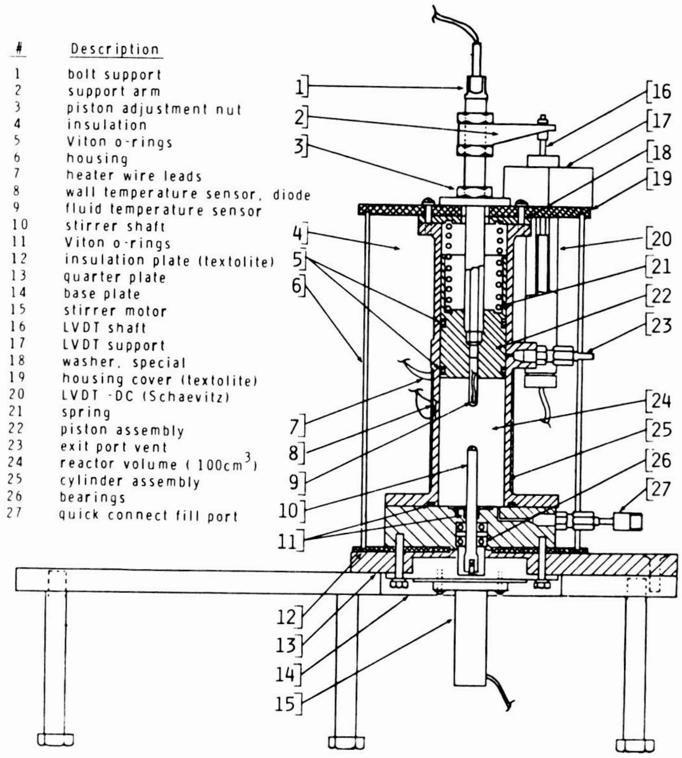

Figure 1. Schematic diagram of the flight dilatometer.

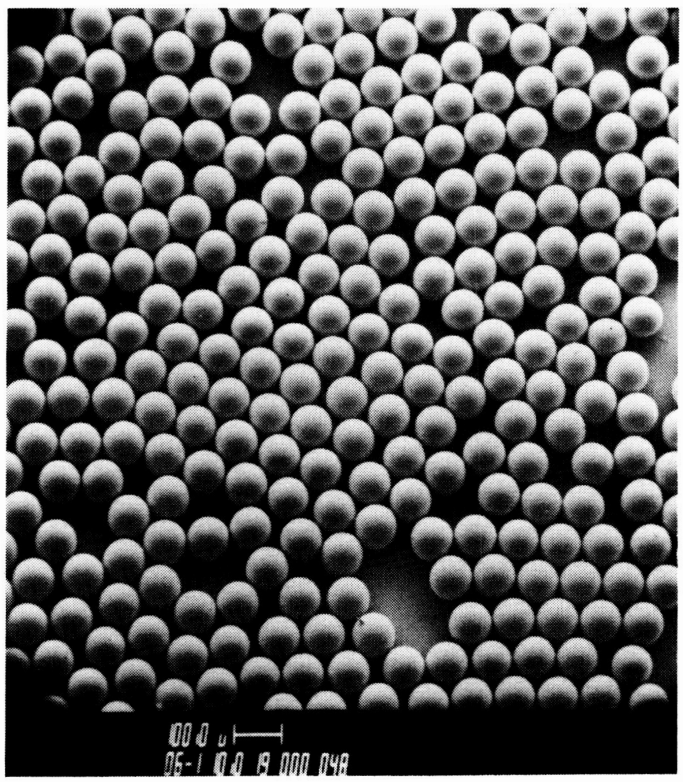

Figure 4. Scanning electron micrograph of 100-μm particles

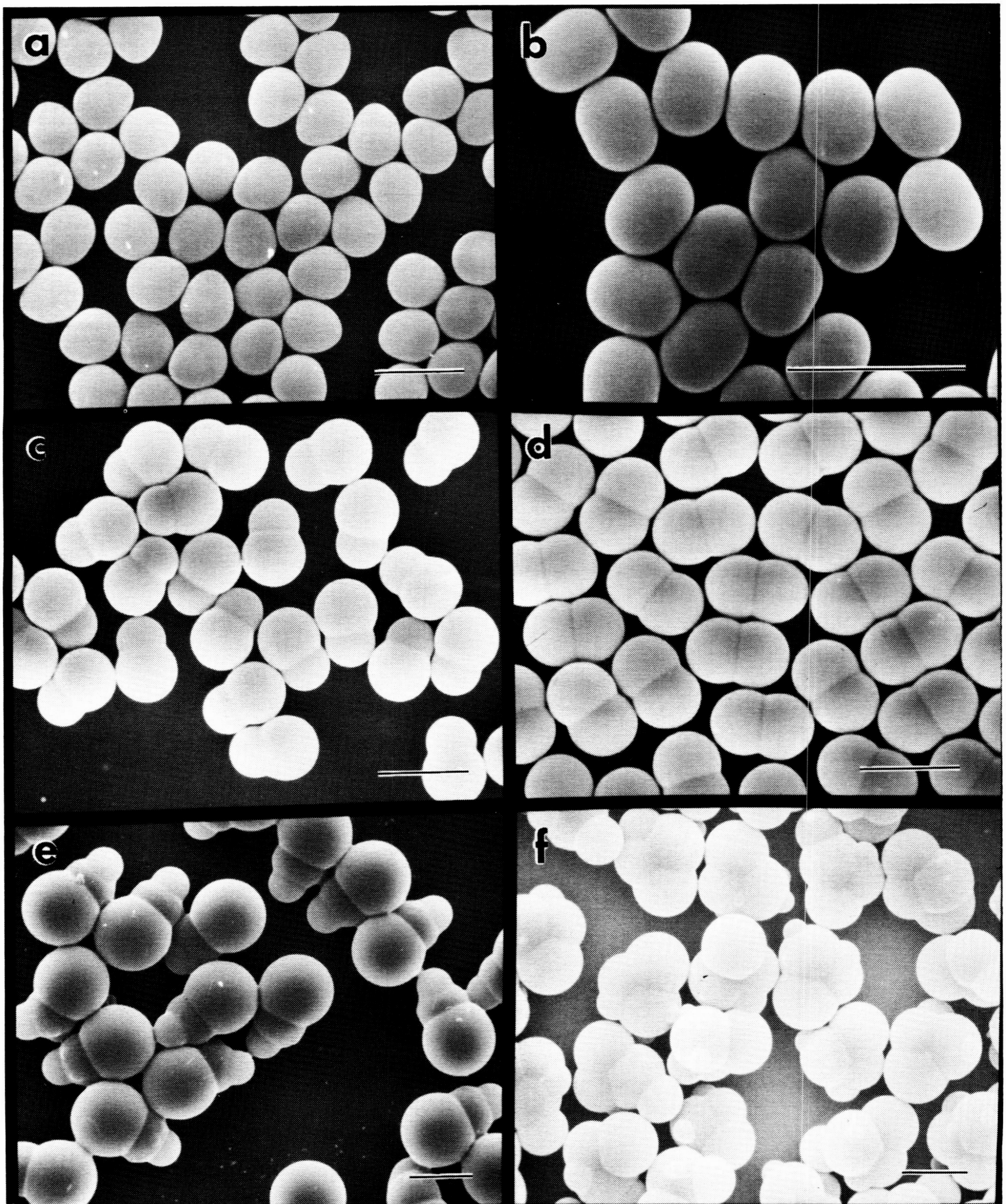

Figure 5. Scanning electron micrographs of uniform nonspherical particles (bar = 10 μm).

CRITICAL PHENOMENA

THE LAMBDA POINT EXPERIMENT IN MICROGRAVITY

J. A. Lipa

Physics Department, Stanford University
Stanford, California 94305

INTRODUCTION

The remarkable phenomena which occur when a system undergoes a cooperative phase transition have claimed the attention of scientists for many years. It was recognised that the unusual behavior was a result of the interactions between the constituents of the system, but a realistic treatment of the problem, either microscopic or phenomenological, appeared prohibitively difficult. In the early 70's Wilson[1] developed a new model of these transitions based on the application of the Renormalization Group (RG) technique. In general, the predictions of this theory were found to be in reasonable agreement with experiment, but in at least some of the highest resolution experiments discrepancies have been reported.[2,3] This situation has led us to develop new, advanced experimental tests which can be performed deep in the asymptotic region, close to a transition, where the theoretical predictions are most firmly established. Careful evaluation of candidate systems exhibiting cooperative transitions has led us to choose the lambda point of helium as the system with the most potential for improved measurements. In this paper we briefly outline the factors that limit the resolution of the lambda transition in space, and describe the status of a flight program to perform heat capacity measurements to the limit of resolution possible on the Shuttle.

All experimental tests of theoretical predictions for cooperative phenomena to date have encountered severe difficulties due to the need to avoid both intrinsic broadening close to the transition and non-asymptotic behavior far from the transition. These effects limit the dynamic range of the measurements and hence the accuracy of the parameters to be compared with theory. To obtain significantly better tests of the RG theory it is not enough to simply increase the accuracy of the measurements. The existence of the non-asymptotic corrections makes this approach unattractive by dictating further reductions of the range of the measurements. Only by obtaining data extending deeper into the asymptotic region near the transition is there hope of a significant gain. Fortunately in this region the cooperative effects are strong and the limitations are primarily of a technical nature.

Two major classes of systems exhibiting cooperative transitions can be studied expeimentally: solids and fluids. In the former case, impurity gradients and crystal imperfections generally cause uncontrolled distortion of the idealised singularity at a resolution $t \sim 10^{-4}$ or 10^{-5} at best. Here $t = |1-T/T_c|$ is a dimensionless temperature parameter, where T_c is the transition temperature. These difficulties are avoided in fluid systems, but instead gravitational compression causes distortion. For example at the critical point of a single component fluid the compressibility diverges, causing unacceptably large density gradients in samples with vertical heights as small as a few microns. In practice this limits the experimental resolution to $t \sim 10^{-5}$. In the case of the lambda transition of helium this problem is minimised, since the compressibility is only weakly divergent. Here the major effect of gravity is due to the pressure dependence of the transition temperature, T_λ . On earth a resolution of about 5×10^{-8} is possible, making this transition the primary testing ground for the RG theory. Unfortunately it is here that the strongest case can be made for potential departures from the predictions.[3] In the case of solid systems with sample defects the main source of rounding, improved materials processing is dictated. However, major improvements in the quality of these materials are needed before they will become competitive with fluid systems. In this case the effect of gravity can relatively easily be reduced by performing the experiments in space. Here, the lambda transition again provides the maximum potential resolution, perhaps to $t \sim 10^{-12}$ in ideal circumstances. For reasons discussed elsewhere, a measurement of the heat capacity singularity at the transition currently appears to be the most useful for advancing our knowledge of cooperative phenomena.

TRANSITION BROADENING

In a spacecraft with no external forces and far from all sources of gravitational fields, the broadening of the heat capacity singularity at the lambda point is governed by two effects. First, a finite size effect occurs due to the divergence of the correlation length at the transition, dictating a large sample size for small rounding. It is easy to show that for a spherical sample a nominal 1% correction to the heat capacity occurs when

$$t = 4.6 \times 10^{-10} r_s^{-3/2} \tag{1}$$

where r_s is the radius of the sample in cm. In addition, the transition will be completely smeared out when r_s equals the correlation length, giving a second relation

$$t = 2.8 \times 10^{-12} r_s^{-3/2} \tag{2}$$

Competing with the finite size effect is the self-gravitation of the helium, generally negligible, but nevertheless setting an ultimate limit on the sharpness of the transition. For a self-gravitating sphere of helium in hydrostatic equilibrium it is easy to show that the pressure difference ΔP between the surface and the center is given by

$$\Delta P = \frac{2}{3} \pi \rho^2 G r_s^2 \tag{3}$$

where G is the gravitational constant and ρ is the density of the fluid. Since the transition broadening due to any source of pressure gradient is just

$$\Delta t = \frac{\Delta P}{T_\lambda}\left(\frac{dP}{dT}\right)_\lambda \qquad (4)$$

where $(dP/dT)_\lambda$ is the slope of the lambda line separating the normal and superfluid sections of the phase diagram, we obtain the result

$$\Delta t = 2.6 \times 10^{-16}\ r_s^2 \qquad (5)$$

In figure 1 we show the various resolution limits set by (1), (2) and (5). It can be seen that the maximum possible resolution is t ~10^{-12} with the application of minor corrections to the data, and t ~ 10^{-13} if extensive corrections are used, with corresponding optimum sample sizes in the 10-100 cm range. These levels of resolution represent the best that can be achieved in any presently envisaged situation, extending four to five orders of magnitude beyond that possible on earth.

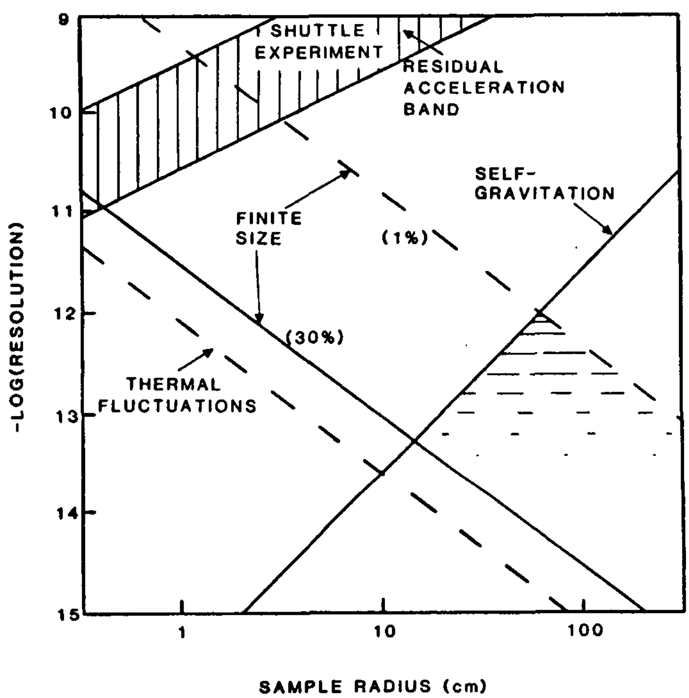

Figure 1 Comparison of the factors limiting the ultimate resolution of the lambda transition in space

In more practical situations, effects other than self-gravitation often compete with finite size rounding to limit the resolution attainable. On board the Shuttle, residual acceleration in the range 10^{-3} to 10^{-4} g is the dominant factor competing with the finite size effect. In this case transition broadening is given by substituting $\Delta P = a\rho r_s$ in (4), where a is the acceleration. We obtain

$$\Delta t = 1.8 \times 10^{-9} a\rho r_s \tag{6}$$

Between the lambda point and the temperature given by (6) the helium is in a two-phase region with co-existing superfluid and normal fluid, and the heat capacity curve is highly distorted. It can be seen from (6) that the width of the perturbed region is proportional to both the size of the sample and the acceleration level. In figure 1 we have plotted (6) as a band covering the range of acceleration between 10^{-3} and 10^{-4} g expected on the Shuttle. This pressure broadening again competes with the finite size effect described by (1) or (2) to give an optimum resolution in the range 5×10^{-10} to 10^{-11}, depending on the details of the situation.

TABLE 1

g/g_o	Δt	r_0 (cm)
1	5.0×10^{-8}	.088
10^{-1}	1.3×10^{-8}	.22
10^{-2}	3.2×10^{-9}	.56
10^{-3}	7.9×10^{-10}	1.40
10^{-4}	2.0×10^{-10}	3.5
10^{-5}	5.0×10^{-11}	8.8
10^{-6}	1.3×10^{-11}	22.2
10^{-9}	2.0×10^{-13}	351.

Table 1: Optimum sample size, r_0, and corresponding temperature resolution, Δt, as a function of residual acceleration, g/g_o.

Starting from a slightly different perspective, we can ask how the maximum resolution varies as a function of acceleration if the sample size is always optimised. The results of approximate calculations for this case are summarized in table 1. For a Shuttle environment of 10^{-4} g we obtain a resolution of about 2×10^{-10}, two orders of magnitude better than on earth. For comparison, at the critical point of a typical fluid, the maximum resolution on the Shuttle is expected[4] to be of the order 10^{-8}, comparable to the lambda-point resolution on the ground. If we optimise the lambda transition experiment for the Space Station or a free-flying spacecraft in low earth orbit, we must also consider tidal forces due to the earth's field, the self-gravitation of the vehicle, and other effects. If the environment is carefully stabilized to the nano-g acceleration level, it appears possible to approach the self-gravitation limit, at a resolution of about 10^{-12}.

THERMAL FLUCTUATIONS

Goldstein[5] has pointed out that temperature fluctuations ultimately will wash out any cooperative transition. For the lambda transition this effect occurs at

$$t = 8.7 \times 10^{-13} r_s^{-3/2} \qquad (7)$$

which is somewhat less than the limit set by (2). More important, thermal fluctuations have the practical effect of directly limiting the resolution of the thermometers used in an experiment. It can be shown that the mean squared noise due to thermal fluctuations in a thermometer is given by

$$<\Delta T^2> = 2kT^2 \tau_0 / c_e\tau \qquad (8)$$

where k is Boltzmann's constant, c_e is the heat capacity of the sensing element, τ_0 is the thermometer relaxation time and τ is the integration time. With the best available devices, this limit at present corresponds to a resolution $\delta t_{rms} = <\Delta T^2>^{1/2}/T_\lambda$ of about 8×10^{-11}. In principle significantly higher resolution can be obtained by increasing the heat capacity of the thermometer until it is comparable to that of the helium sample, and by reducing the detector bandwidth significantly below 1Hz.

FLIGHT EXPERIMENT

For some years we have been developing the technology to perform a high resolution heat capacity experiment near the lambda point on the Shuttle. Since the low frequency acceleration environment of the Shuttle is quite variable, the experiment was conservatively optimised for a level of 3×10^{-4} g, and a corresponding resolution of 4×10^{-10}. This will allow about two orders of magnitude higher resolution than is possible on earth, resulting in a much improved estimate of the asymptotic exponent describing the heat capacity singularity. This measurement will lead to a much stronger confrontation between theory and experiment than previously has been possible, and perhaps as severe a test as is presently feasible with current technology. Also, the data will allow exponent estimates deep in the asymptotic region which are of comparable accuracy to existing results further from the transition. These estimates will be extremely useful in testing the validity of the asymptotic representation assumed in all theoretical models to date. The ground-based results obtained so far indicate some possibility of a breakdown of this assumption.[3]

In figure 2 we show the historical development of the resolution of cooperative transitions. The data shown in this figure are not intended to be all-inclusive, but are representative of the progress in a given era. The points connected by the solid line represent the resolution at which data was available to allow some type of theoretical test; the resolution quoted by some authors is a little higher. It is clear that there is a large unexplored region, at least on a logarithmic scale, beyond the gravity cut-off on earth, where measurements near the lambda point could add substantially to our knowledge of cooperative transitions.

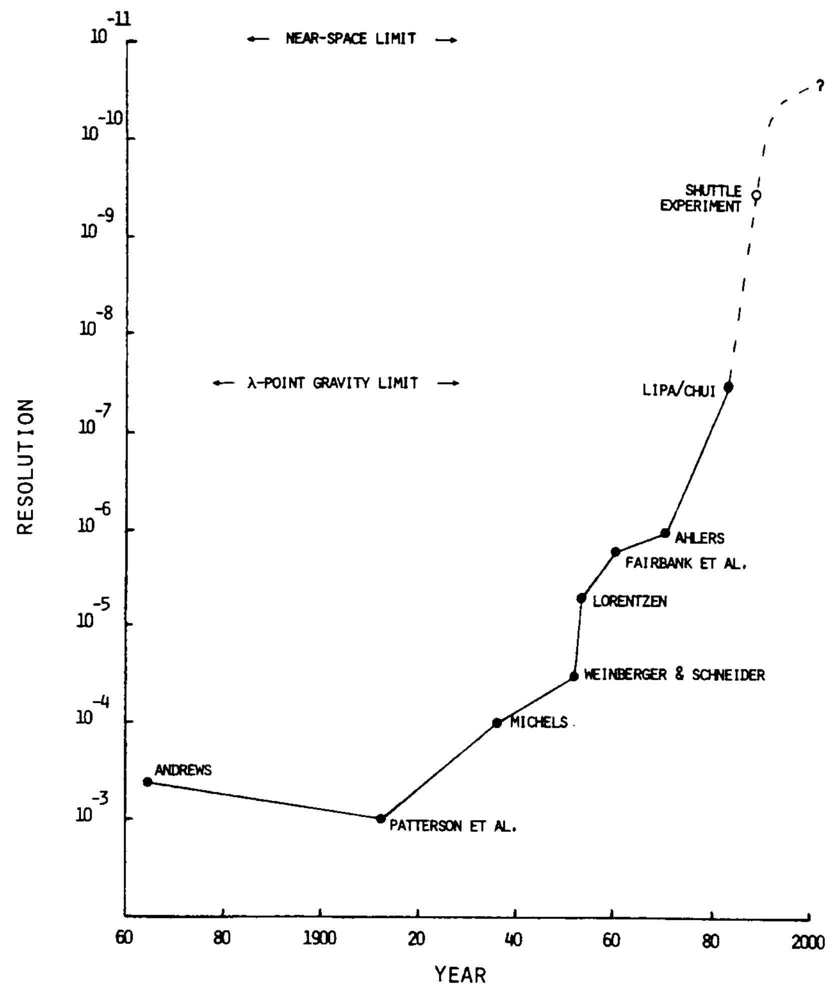

Figure 2: Historical development of resolution of cooperative transitions.

TECHNOLOGY DEVELOPMENT

The lambda point flight experiment requires a number of technology developments that go significantly beyond the level usually encountered in the laboratory. To make use of the potential resolution available in space, significant advances in thermometry and thermal control are required. Also a zero-g superfliud helium facility is needed, and the experiment must be designed to function correctly after being subjected to launch loads. The status of our work in these areas is described briefly below.

High Resolution Thermometers

Of utmost importance in any high resolution experiment near a phase transition is the temperature sensor. For the flight experiment it is necessary to resolve to t $\sim 10^{-11}$ in an integration time of a few minutes in order to make individual heat capacity measurements of sufficient accuracy. In addition, extremely low dissipation is needed, since the uncertainty in the power input to the sample must be held below $\sim 10^{-11}$ W. These requirements ruled out conventional low temperature thermometers and forced us to construct a special sensor optimized for the present application.

The new thermometer we developed is based on measuring the temperature dependent magnetization of a paramagnetic salt in a constant applied magnetic field. The device has an exceptionally low intrinsic dissipation level ($<10^{-17}$ W), and a very high sensitivity due to the use of a superconducting SQUID magnetometer as the detector. Similar devices have been built[6] for use below 1°K, but their noise characteristics were not reported. We constructed a device[7] optimized for use near the lambda point and provided it with a high degree of shielding to minimize the effect of external magnetic fields. A schematic view of the thermometer is shown in figure 3. Table 2 lists some of its operating characteristics obtained with two different salt materials. To date we have achieved a resolution of about 5×10^{-11} in a 1Hz bandwidth, which is adequate for the Shuttle experiment. This resolution compares well with the intrinsic thermodynamic limit for such a device given by (8).

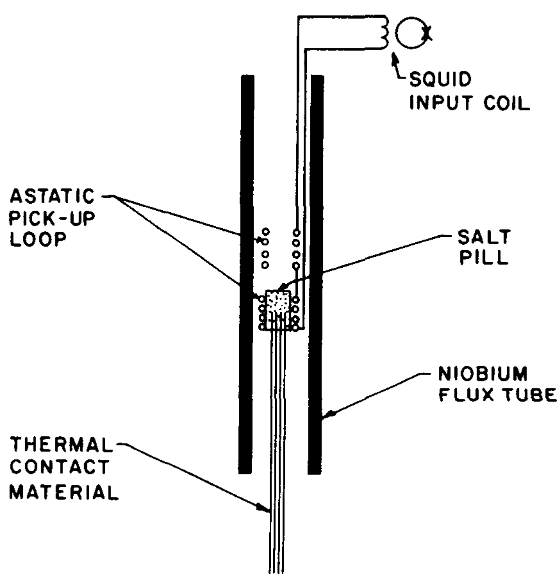

Figure 3: Schematic view of paramagnetic salt thermometer.

TABLE 2

SALT MATERIAL:	$Cu(NH_4)_2Br_4 \cdot 2\ H_2O$	$Mn(NH_4)_2(SO_4)_2 \cdot 6\ H_2O$
Curie Temperature; ^oK	1.8	0.150
Sensitivity at 2.17 K; $\Phi_o/\mu K$	3.86	1.08
RMS Noise Level at 1 Hz, ΔT_{RMS}; ^oK	1.04×10^{-10}	6.48×10^{-10}
Resolution at 1 Hz; $\Delta T_{RMS}/T_\lambda$	4.8×10^{-11}	3.0×10^{-10}
Thermodynamic Resolution Limit	8.7×10^{-11}	2.1×10^{-10}
Heat Capacity; 10^{-3} J/K	1.82	0.31
Response Time; sec.	2	0.7
Drift; K/sec.	$\sim 10^{-14}$	5×10^{-14}

Table 2: Operating parameters for paramagnetic salt thermometers

Thermal Control System

A second factor limiting the accuracy of high resolution heat capacity measurements is stray heat leak control. An advanced thermal control system designed to minimise this problem is shown in figure 4. It contains three stages of thermal isolation controlled with conventional germanium resistance thermometers. Within this system is located a thermal shield which can be controlled to level of a few nano-kelvins using a paramagnetic salt thermometer of the type described above. This shield isolates the experiment module from ambient and stray room temperature radiation, and from gas transfer effects associated with temperature changes elsewhere in the apparatus. The experiment module consists of a sample container and a pair of high resolution thermometers, and is attached to the inside of the thermal shield using low conductivity supports. A prototype version of this system has been operated in the laboratory for a number of months and shown to provide adequate control for the Shuttle experiment. It has also passed launch level shake qualification tests.

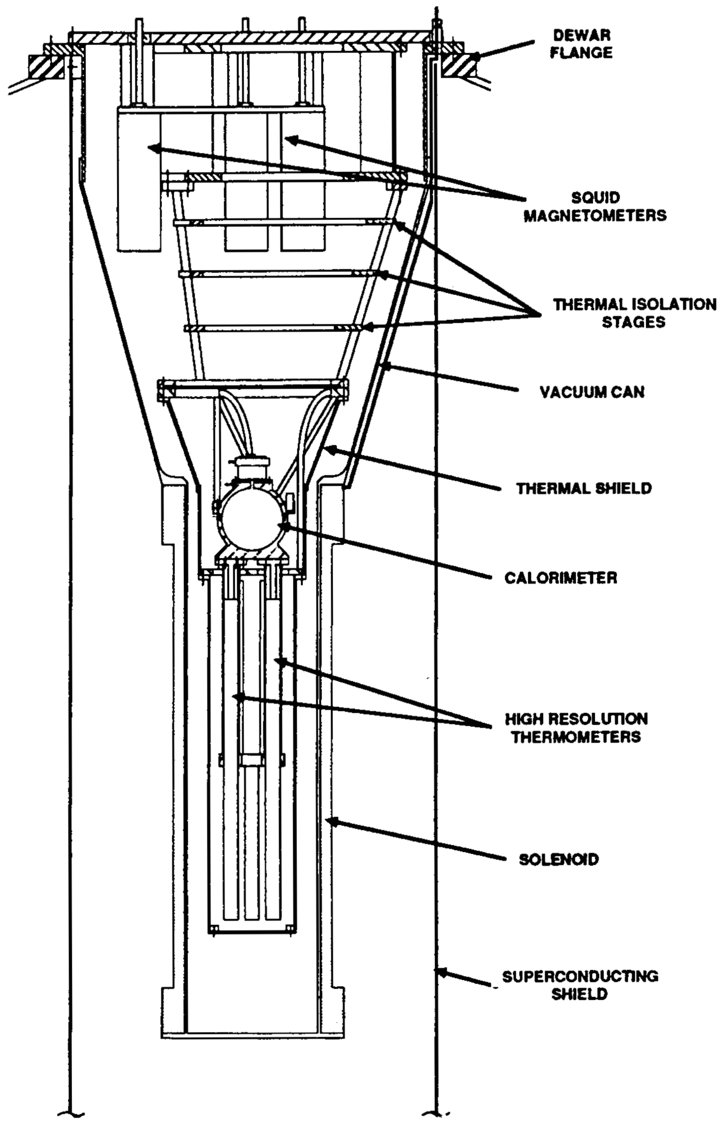

Figure 4: Thermal control system for flight experiment

Helium Facility

In order to reduce the cost and effort of cryogenic experiments in space the Jet Propulsion Laboratory has constructed a re-usable, flight qualified superfluid helium dewar. This facility was flown with the first set of experiments in July 1985 as part of the Spacelab-2 program, when it was located on a pallet in the Shuttle bay. A schematic view of the system is shown in figure 5. Experiments can be attached to the cover plate sealing the helium tank, and can interface with external electronics via an evacuated feedthrough area. Liquid helium is placed in the dewar several days before launch, and is maintained in the superfluid state with a small vacuum pump. On orbit, the system is vented to space through a throttling orifice designed to maintain the operating temperature in a range from 1.5 to 2.1 Kelvins. After equilibrium is established, the dewar temperature is stable to within 100 millikelvins for an 8-day flight.

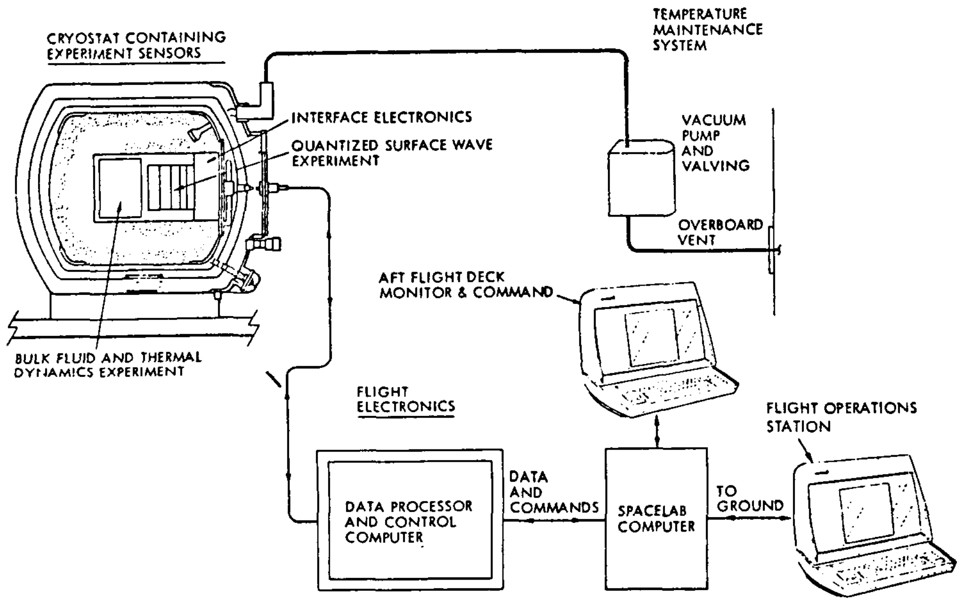

Figure 5: Schematic view of JPL superfluid helium facility as configured for the SL-2 flight

PROGRAMMATICS

The possibility of measuring the heat capacity singularity at the lambda point in space was first considered seriously at the Quantum Fluids in Space Conference held in 1975. It was determined that the major obstacle preventing improved experiments in space was temperature resolution since at that time no devices existed to resolve below $t \sim 10^{-7}$. Over the following seven years the paramagnetic salt thermometer described above was developed at Stanford using funds from the NASA PACE program. By 1982 the capability of resolving to $t \sim 5 \times 10^{-11}$ was demonstrated, which is of the order of the fundamental limit set by thermodynamic fluctuations. This technological development set the stage for proceeding with the flight experiment. In Jan. 1984 a Science Review was held and the project was recommended to proceed with planning for a flight. Work was intensified after

CoDR in Sept. 1984 and, shortly after PRR in Oct. 1985, approval was obtained to proceed with flight hardware development.

A prototype of the instrument shown in figure 4 has been fabricated by Ball Aerospace and has passed shake qualification tests. Thermal and functional tests are now in progress at Stanford. So far no major difficulties have been encountered and development is proceeding on schedule. Almost all operating modes of the prototype have been demonstrated to the level of performance needed for the flight. Detailed design of the flight electronics is now underway, with completion of the whole system scheduled for Nov. 1988. After testing at Stanford, the instrument will be integrated with the dewar system at JPL for final functional and environmental check-out. The experiment is expected to be available for flight by the second half of 1990. The major programmatic milestones of the experiment are shown in table 3.

1975:	Proposed at Quantum Fluids in Space Conference
1977:	Proposed to PACE
1979:	Phase I Study Completed
Jan. '84:	Science Review, Phase III
Sept. '84:	Conceptual Design Review, recommended for transfer from PACE to Microgravity
May '85:	Subcontractor for Hardware Development selected
Oct. '85:	Preliminary Requirements Review
Mar. '87:	Preliminary Design Review
Oct. '87:	Critical Design Review
Aug. '90:	Experiment available for Launch

Table 3: Lambda point experiment milestones

CONCLUSION

We have briefly discussed the motivation and potential for performing very high resolution measurements of the heat capacity singularity at the lambda point of helium in micro-gravity conditions. It is clear that tests extending deep into the asymptotic region can be performed, where the theoretical predictions take on their simplest form. This advantageous situation should lead to a major improvement in our understanding of the range of applicability of current theoretical ideas in this field. The lambda transition holds out the prospect of giving the maximum advance of any system, and with the application of cryogenic techniques, the potential of this system can be realised. The technology for the initial experiments is already well developed, and results could be obtained in 1990.

TABLE 4

Static scaling at the lambda point:

1) Temperature dependence of the order parameter
2) Test of universality along the lambda lines

Dynamic scaling at the lambda point:

1) Thermal conductivity of ^4He and ^3He-^4He mixtures above T_λ
2) Second sound damping coefficient below T_λ

Critical point measurements:

1) Heat capacity of ^3He and ^4He
2) Order parameter measurements below T_c
3) Thermal conductivity and viscosity of ^3He and ^4He above T_c

Tri-critical point measurements:

1) Heat capacity singularity
2) Concentration susceptibility

Observation of new phenomena:

1) Cross-over to 2-dimensional behavior
2) Finite size effects in controlled geometries
3) Proximity effect near the He-I/He-II interface
4) Josephson effects in helium

Table 4: Possible follow-on experiments which could take advantage of the technology developed for the heat capacity experiment described here

It is easy to imagine a number of follow-on experiments which could be performed near the lambda point, significantly extending the range of existing ground-based measurements. Some of these are listed in Table 4. Also listed are some other experiments on helium that can take advantage of the technology advances being developed for the lambda point work. In the ^3He-^4He system there are two pure fluid critical points, two phase separation lines and a tri-critical point. All these systems involve cooperative transitions and can benefit from being studied in space. Both static and dynamic properties can be studied, allowing a wide range of potential tests for the continually developing RG theory. Some of the experiments are already under development, and ultimately additional work may be conducted on the Space Station. The advantages of this environment will be extended observation times and the availability of sub-microgravity conditions. Hopefully the possibilities described in this paper will also stimulate additional theoretical effort in this exciting area of physics.

ACKNOWLEDGEMENT

This work was supported by NASA contract # JPL 957448.

REFERENCES

1. K. G. Wilson, Phys. Rev. B 4, 3174 (1971).

2. F. M. Gasparini and A. A. Gaeta, Phys. Rev. B 17, 1466 (1978).

3. J. A. Lipa, Proceedings of Near Zero Conference, Stanford University, 1982 (in press).

4. M. R. Moldover, J. V. Sengers, R. W. Gammon, and R. J. Hocken, Rev. Mod. Phys. 51, 79 (1979).

5. L. Goldstein, Phys. Rev. 135, A1417 (1964).

6. R. P. Giffard, R. A. Webb and J. C. Wheatley, J. Low Temp. Phys. 6, 533 (1972).

7. J. A. Lipa, B. C. Leslie and T. C. Wallstrom, Physica (Utrecht) 107B, 331 (1981).

N89-20320

Critical Fluid Light Scattering

Robert W. Gammon
Institute for Physical Science and Technology
University of Maryland

Abstract

The objective is to measure the decay rates of critical density fluctuations in a simple fluid (xenon) very near its liquid-vapor critical point using laser light scattering and photon correlation spectroscopy. Such experiments have been severely limited on earth by the presence of gravity which causes large density gradients in the sample when the compressibility diverges approaching the critical point. The goal is to measure fluctuation decay rates at least two decades closer to the critical point than is possible on earth, with a resolution of 3 μK. This will require loading the sample to 0.1% of the critical density and taking data as close as 100 μK to the critical temperature (T_c = 289.72 K). The minimum mission time of 100 hours will allow a complete range of temperature points to be covered, limited by the thermal response of the sample. Other technical problems have to be addressed such as multiple scattering and the effect of wetting layers.

We have demonstrated the ability to avoid multiple scattering by using a thin sample (100 microns), and a temperature history which can avoid wetting layers, a fast optical thermostat with satisfactory microcomputer temperature control and measurement, and accurate sample loading. With the questions of experimental art solved, there remain the important engineering tasks of mounting the experiment to maintain alignment during flight and using vibration isolation to prevent Shuttle motions from distorting the sample.

The experiment entails measurement of the scattering intensity fluctuation decay rate at two angles for each temperature and simultaneously recording the scattering intensities and sample turbidity (from the transmission). The analyzed intensity and turbidity data gives the correlation length at each temperature and locates the critical temperature.

The fluctuation decay rate data set from these measurements will provide a severe test of the generalized hydrodynamics theories of transport coefficients in the critical region. When compared to equivalent data from binary liquid critical mixtures they will test the universality of critical dynamics.

1 Introduction

Near a critical point it is possible to approach a macroscopic instability continuously through equilibrium states. This instability is the source of a continuous symmetry breaking or *ordering*. The key to understanding the anomalous phenomena observed in the critical region is the thermodynamic fluctuations. Approaching the critical point the fluctuations in the order parameter become extremely large in amplitude, show long range correlations, and decay exceedingly slowly. The large amplitude and extent of the fluctuations means that they can not longer be neglected and are truly dominating the properties of the system. This dominance of the order parameter fluctuations leads to a universality of the behavior, an independence from the details of the molecular interactions, so that descriptions of the anomalies only depends on the dimensionality of the system and the number of components of the order parameter. The prediction of asymptotic static properties near critical points is now more precise than experiments.

We now know that there are many examples of critical transitions: liquid-vapor critical points, magnetic transitions such as Curie ferromagnetic points or Neel anti-ferromagnetic points, superconductivity, the helium lambda transition, binary mixture miscibility critical points, ferroelectric Curie points, etc. All these continuous transitions share in having divergent thermodynamic fluctuations. It is the study theoretically and experimentally of these fluctuations that marks this current era of critical phenomena research.

Thermodynamic fluctuations are the variations in space and time of a thermodynamic variable from its equilibrium value. The fluctuations reflect the underlying heat modes (thermally excited microscopic material modes) of the material. From condensed matter physics point of view the divergence of fluctuations is the result of the instability of a heat mode. The eigenfrequency goes to zero at the critical point and its thermal population diverges. The energy stored in this mode diverges and this is seen in the divergence of the heat capacity. In a liquid-vapor critical point the relevant modes can be described by generalized hydrodynamics. For each wavevector $\vec{q}$ there are five modes, two sound modes, two shear modes, and a thermal diffusion mode. At the liquid-vapor critical point the diffusive density fluctuation is unstable and through couplings to the other modes from the non-linearities of hydrodynamics, the other modes are affected leading to anomalies in sound propagation and shear viscosity. These modes can be used as a basis for describing the static and dynamic properties of a material and are the fundamental excitations of the material.

Experimentally it is often possible to look directly at the microscopic excitations. Most commonly this is done with a scattering measurement where one can measure either the static or dynamic structure factors of the modes. Such measurements probe modes having wavevector magnitude q, with

$$q = 2k\sin(\theta/2) \quad ,$$

where k is the wavevector magnitude of the incident radiation and θ is the scattering angle. Measurements of the intensity versus angle gives the correlation length ξ of the fluctuations and spectroscopy of the scattered light gives the spectrum or time correlation of the modes. For liquid-vapor transitions light scattering has furnished the best method. The techniques are now highly developed and by using photon correlation measurements of the scattered laser light intensity it is possible to have accurate measurements of the space and time correlations of the critical fluid density fluctuations.

In what follows we describe the context for the proposed experiment on critical fluid light scattering named Zeno, give the Zeno Science Requirements which will produce a significant data set during a Shuttle flight, and describe the Zeno apparatus conceptual design to meet the Science Requirements.

2 The Context for Zeno

2.1 Critical Exponents and Universality

The theory of critical phenomena is overseen by an experimental fact: thermodynamic response functions are singular at a critical point; and a conjecture: the principle of universality. The theoretical approach to critical phenomena has matured in the past decade to the point where its predictive success is rivaled only by quantum electrodynamics.

The singularity of response functions suggests that they be described simply near a critical point. Measuring the distance from the critical point by the reduced temperature $t \equiv (T - T_c)/T_c$, where T_c is the critical temperature, one expects the response function $f(t)$ to satisfy a power law $f(t) \sim t^{\varsigma}$ as $t \to 0$. The value of the critical exponent ς depends on the particular function $f(t)$. Examples for a liquid-vapor critical point are:

$$\begin{array}{rccc}
\text{specific heat,} & C_v & \sim & t^{-\alpha}\,, \quad \alpha = 0.110; \\
\text{correlation length,} & \xi & \sim & t^{-\nu}\,, \quad \nu = 0.630; \\
\text{isothermal compressibility,} & \kappa_T & \sim & t^{-\gamma}\,, \quad \gamma = 1.241.
\end{array}$$

The universality principle makes critical exponents more than just a mathematical curiosity. Separate all critical points into universality classes, where each universality class has two unique properties: the spatial dimension of the system in question (3 for a fluid), and the degree of the order parameter for the critical point (1 for a liquid-gas critical point since the order parameter, the difference between liquid and gas densities $\rho_L - \rho_G$, is a scalar). Then, within a universality class, the critical exponents of all static properties should be universal, unvarying from system to system.

Critical exponents are a powerful way to characterize critical phenomena, but they provide a challenge for experiment. Since they are defined from the limiting, or asymptotic, behavior of the thermodynamic functions, the exponent of a particular function will not be clearly revealed unless an experiment reaches the so-called asymptotic region. The challenge is that critical behavior is often not manifestly evident before reduced temperatures less than 10^{-6} are reached. Thus, experiments in critical phenomena are usually very concerned with penetrating ever closer to the critical point.

2.2 Critical Dynamics in Fluids

The critical fluctuations in a liquid-vapor system correspond to density fluctuations which decay isobarically by thermal diffusion. The mean square fluctuation in density is proportional to the isothermal compressibility and hence diverges with exponent $\gamma = 1.241$. From the thermal conduction equation it follows that the density fluctuation with wavevector $\vec{q}$ (its qth Fourier component) decays with a rate given by

$$\Gamma = Dq^2 \quad ,$$

with D the thermal diffusivity, which in the hydrodynamic limit $q \rightarrow 0$, is given by

$$D_0 = \frac{\Lambda}{\rho C_p} \quad ,$$

with Λ the thermal conductivity, ρ the density, and C_p the heat capacity at constant pressure. The thermal conductivity diverges approximately like ξ and C_p diverges with exponent γ. The result is that as the critical point is approached, D_0 goes to zero about like ξ^{-1}. For finite q, Γ and D approach finite limits with a strong q dependence. One of the principle results of dynamic scaling is the prediction that

$$\lim_{t \rightarrow 0} D = q^{(1+x_\eta)} \quad ,$$

where x_η is the correlation range exponent of the viscosity divergence.

2.3 The Need for Low Gravity

The techniques of temperature control in the laboratory are sufficiently advanced that it is possible to begin penetrating deeply into the critical region. However, once there it is impossible to obtain the desired result of measuring critical anomalies. The problem is gravity.

The compressibility of a fluid system diverges at the critical point: $\kappa_T \sim t^{-\gamma}$. The compressibility expresses the response of the fluid's density to pressure on the fluid. Across any fluid container, there is of course a pressure differential caused by the weight of the fluid itself: $\Delta P = \rho g h$. In normal circumstances, when a fluid is nearly incompressible, this is barely noticeable; near the critical point, the effects of the pressure differential are greatly magnified by diverging compressibility.

Under the influence of its weight, the fluid develops a density gradient; that is, fluid at the bottom of a container is more dense than fluid at the top. As the critical point is approached, the density gradient increases. What happens is that the fluid density at the extremes of the container deviates more from the critical density, and the regions of deviation grow toward each other. The net result is that only a thin layer of fluid near the center of the container is close enough to the critical density to show critical behavior; as t is reduced, the thickness of the layer decreases. This is a severe limitation for measurements on macroscopic samples.

In a light scattering experiment the laser beam used to probe the sample can only be usefully focused to a diameter of about 100 μm. When the thickness of the layer of critical fluid drops approaches this size, the light is no longer sampling a homogeneous critical system. In effect, the density gradients limit the useful range of t which can be explored. This is shown in figure 1, which gives the acceleration dependence of the limiting temperature at which the density of xenon varies by more than 1% over a 100 μm distance. At 1 g the critical point may be approached to within 14.5 mK, while at 10^{-3} g the limit is 145 μK.

This result is disappointing. At $t = 5 \times 10^{-5}$, the asymptotic region for these fluctuation wavelengths is just being reached. The decay rate for any finite wavevector will saturate at a finite, lowest value as the critical point is approached. This is shown in figure 2 for the wavevectors corresponding to the 12° and 168° scattering angles planned for Zeno. At the 1 g limit, the small angle decay rates have not yet really begun to saturate. By going to at least the 10^{-3} g limit the asymptotic behavior at both angles will be reached. This then sets the minimal requirement for reduced gravity for critical fluid light scattering. The Zeno instrument flown on the Shuttle provides a solution to this problem.

2.4 Previous Work

Progress in understanding critical phenomena has been substantial in the past decade since the methods of the renormalization group theory, first developed to solve problems in high-energy physics, have been applied to calculating the critical exponents of static divergent quantities. This theoretical work has given a computational base to the ideas of universality classes and two-scale universality, as well as accurate estimates of many critical exponents (Sengers, 1982).

In contrast, the theory of critical fluctuation dynamics and transport phenomena, although actively pursued, leaves many questions unanswered. The questions are both theoretical, because the calculations have proved difficult to perform; and experimental, because of limitations imposed by gravity as well as experimental problems with multiple scattering in light scattering experiments.

C-4

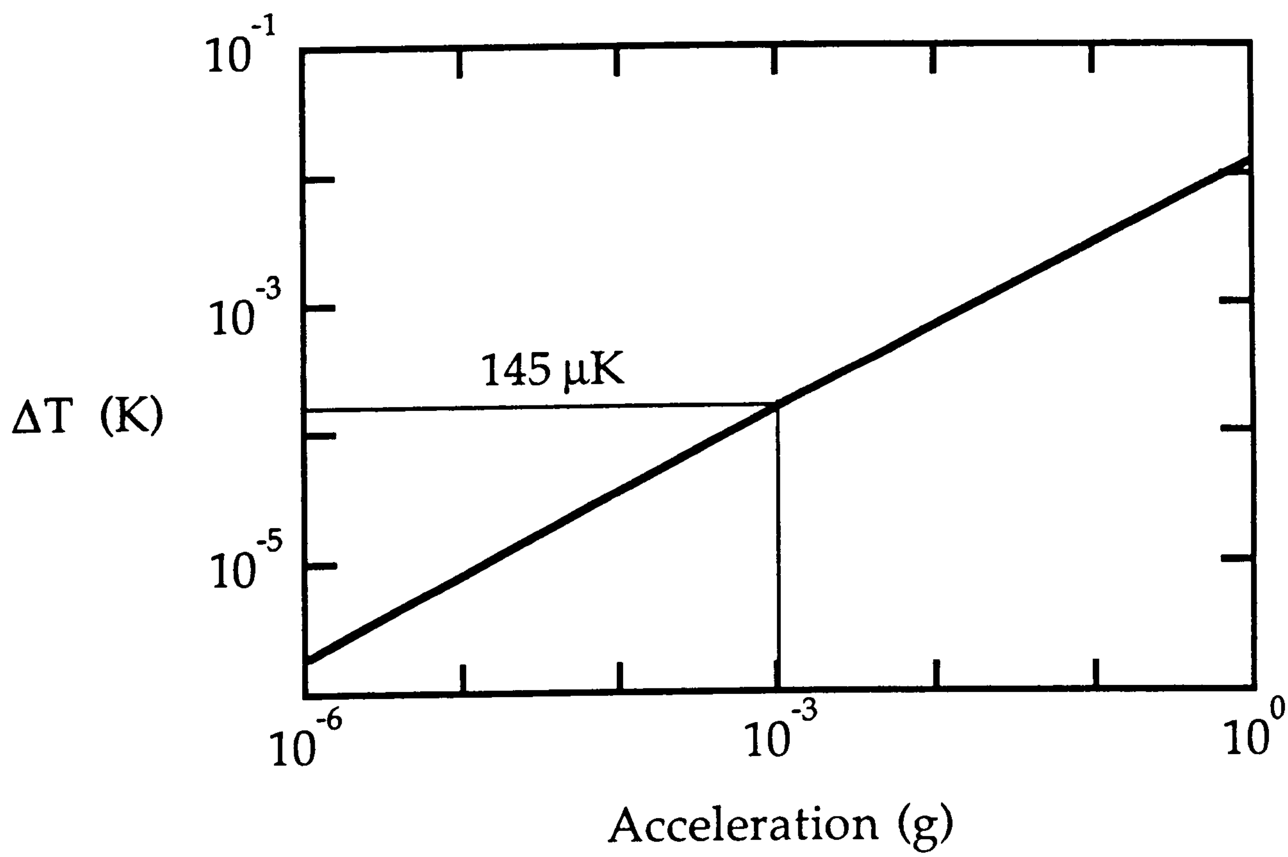

Figure 1. ΔT limit set by acceleration for 100 μm height and 1% precision.

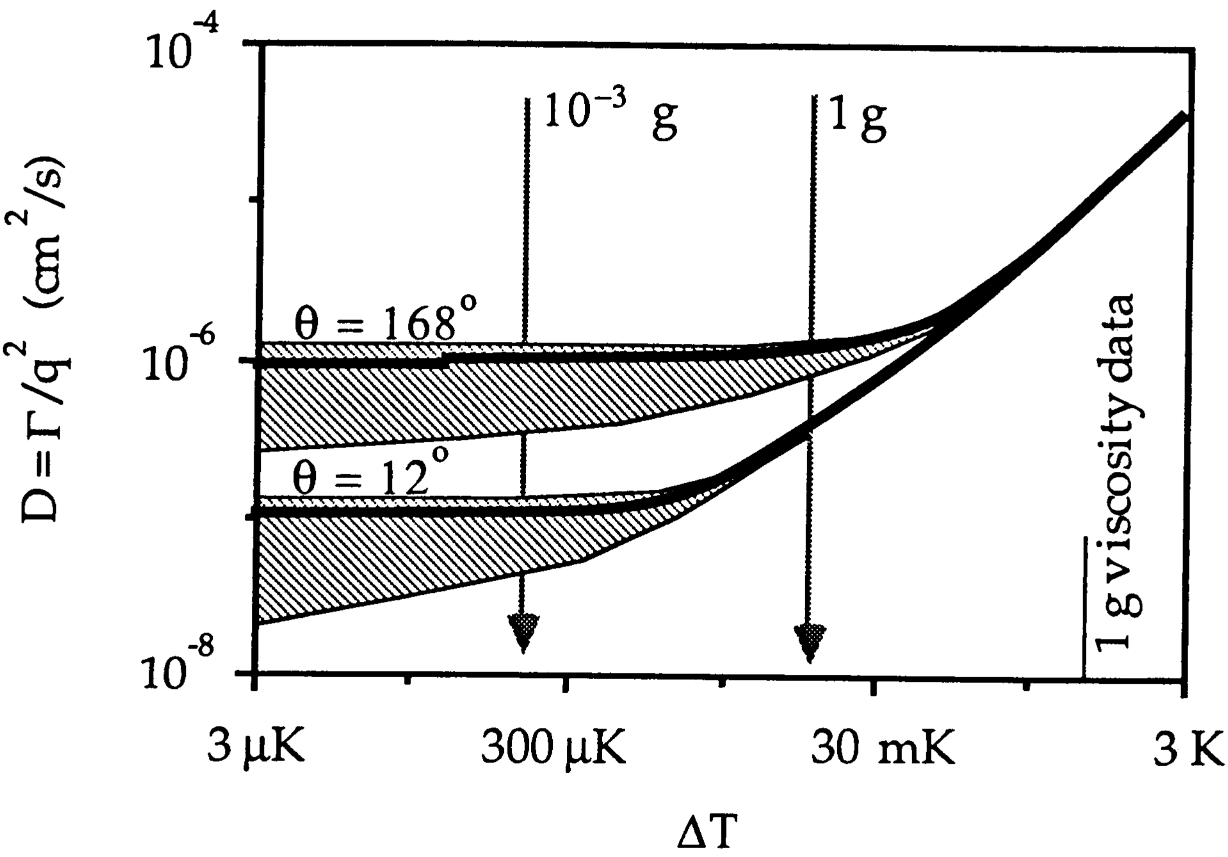

Figure 2. Calculated Xenon Diffusivity

The general state of experiment and comparison with current theory has been left at about the state of the experiments by Swinney and Henry (Swinney and Henry, 1973). Figure 3 is taken from their paper and shows the level of agreement. The quantity Γ^* is a scaled decay rate from which viscosity and angular dependence has been divided out, plotted as a function of scattering wavevectors scaled by the correlation length: $x = q\xi$. The range in x of 0.01 to 8.0 corresponds to a temperature range of 5.8 K to 3 mK from the critical temperature. The most recent and only other work on xenon was by Güttinger and Cannell (Güttinger and Cannell, 1980). They covered the same range in x with fitting errors of $\pm 5\%$ using more accurate values for ξ.

Other efforts have included work to account for multiple scattering (Bray and Chang, 1975; Reith and Swinney, 1975; Sorenson *et al.*, 1977; Beysens and Zalczer, 1977), or to avoid it altogether (Chang, Burstyn and Sengers, 1979). Particularly notable is the work by Burstyn and Sengers (1982) on the index-matched, weakly scattering binary liquid mixture 3-methylpentane-nitroethane. Excellent, precise results to 0.3 mK from its critical temperature were obtained. No significantly improved light scattering studies of the fluctuation decay rates for single component fluids have been possible.

2.5 Xenon: A Simple Fluid

Theory presumes that the liquid-gas critical point of simple fluids and the component-separation critical point of binary liquid mixtures belong to the same universality class; more specifically, that they belong to the same *static* universality class. Hence, they should exhibit the same critical behavior, at least for the static properties.

As an example of a simple fluid, xenon is without competition. The molecule is monatomic, spherically symmetric, and has no dipole moment; one expects the inter-atomic forces to be as simple as possible. While this would be the case for any of the noble gases, xenon wins as a choice for experimental use because it has a convenient critical temperature (16 °C), and many of its properties have been studied extensively. Nevertheless, if density-matched binary fluids, with their greater insensitivity to gravity, could apparently provide the same results on earth as a space experiment on xenon, why use xenon?

Studying critical point dynamics at a simple fluid, liquid-vapor critical point can yield better critical point measurements than in any mixture. We present the following reasons.

1. A simple fluid can be more accurately loaded to its critical density than can a mixture to its critical concentration.

2. A simple fluid reaches equilibrium more quickly after crossing the phase boundary since no time is taken for molecular diffusion to readjust the concentration profile.

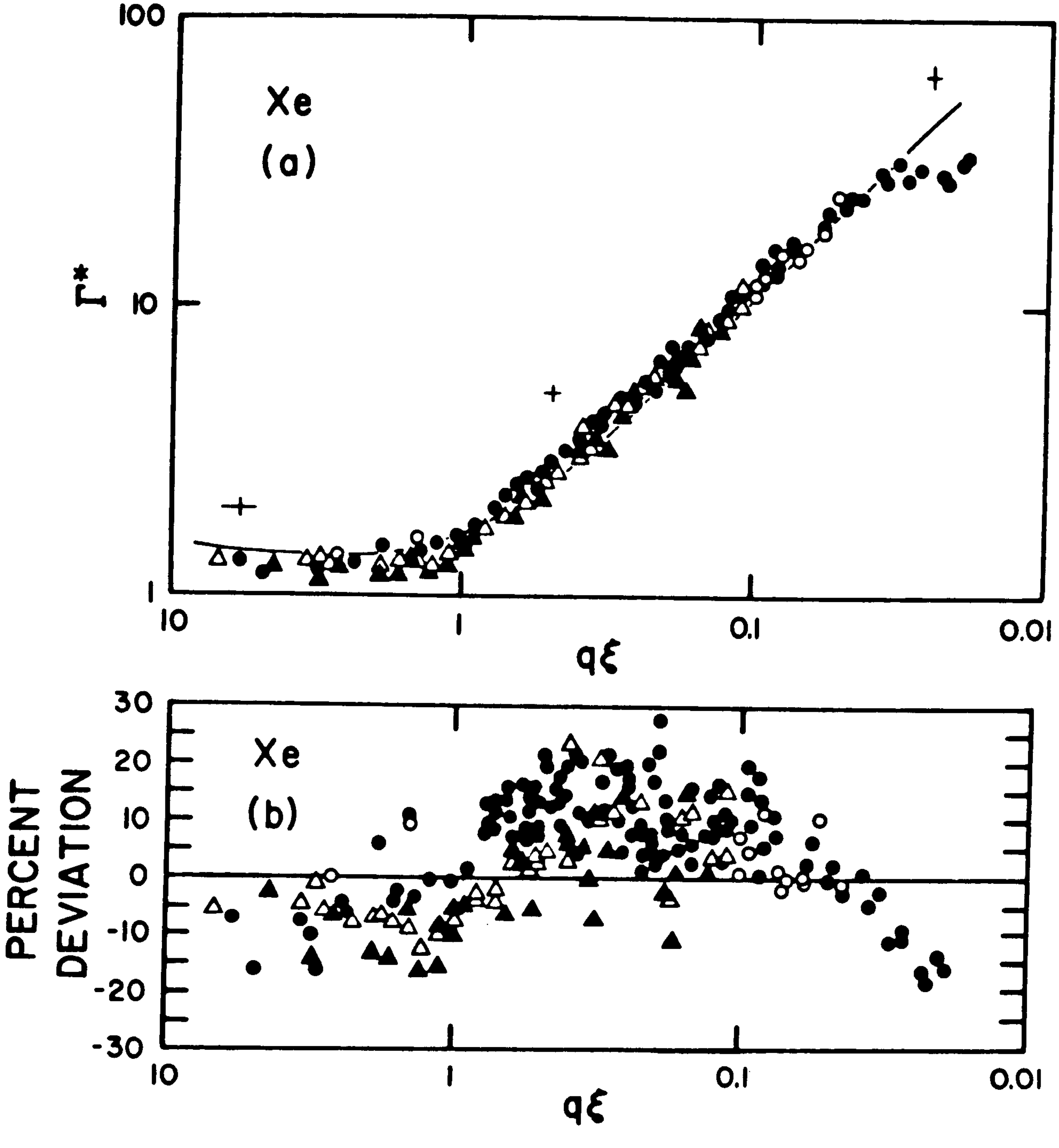

Figure 3. Reduced decay rate vs. scaled wavevector (from Swinney and Henry, 1973).

3. Simple fluid systems have smaller viscosity and correlation ranges so that the order parameter relaxation time, ξ^2 / D (D is the thermal diffusivity), is 100 times shorter than for the most favorable density-matched mixtures. This allows the measuring of viscosity one decade close to the critical temperature than for any mixture.

4. The viscosity background is smaller in the pure fluid while the amplitude of the critical part of the viscosity is about the same, making it easier to analyze the critical part.

5. A simple fluid is less susceptible to a drifting critical temperature.

6. A simple fluid has no diffusion controlled, surface wetting, sample segregation processes.

7. The order parameter in a simple fluid is identified with greater ease and certainty.

8. Additional thermodynamic measurements necessary for analyzing the dynamics into background and critical contributions exist in sufficient detail only for pure fluids.

9. Only by studying both systems can one experimentally answer the question: Do both of these fluid systems belong to the same *dynamical* universality class?

As mentioned previously, for static properties, universality classes of critical points are characterized completely by the spatial dimension of the system under study and the symmetry of its order parameter; all other properties of the system are assumed to be irrelevant. However, for dynamical properties, the static universality classes must be subdivided according to whether the order parameter is conserved in the system's dynamics. Conservation laws for other hydrodynamic variables may further subdivide universality classes (Hohenberg, 1977; Bhattacharjee and Ferrell, 1983). In contrast to pure fluids, binary liquid mixtures contain an extra hydrodynamic variable which is conserved. This is thought to be irrelevant asymptotically close to the critical temperature, although it can be relevant in the temperature range experimentally accessible on earth.

The complications that can occur when an extra degree of freedom is introduced are illustrated by the recent measurements of transport properties by Meyer and co-workers (Cohen, 1982; Cohen, 1983) near the critical point of mixtures of ^{3}He and ^{4}He. Meyer did not observe distinct composition and density fluctuations. He did observe the thermal conductivity and thermo-diffusion ratio diverging as ξ and ξ^2 respectively. To interpret Meyer's data, it was necessary to introduce the concept of the "degree of azeotropy" and to argue that the asymptotic behavior of transport properties would only become evident at reduced temperatures smaller than 10^{-5}.

Since the very careful work by Swinney and Henry and the refinement by Güttinger and Cannell on xenon, it has been clear that to apply the theories which attempt to calculate the modification of dynamic properties due to divergent fluctuations in a critical system, one needs to know the "bare" properties (without the effects of critical fluctuations) in particular of the thermal conductivity, heat capacity at constant volume, and pressure coefficient on the isochore. Then, accurate measurements of the correlation range, viscosity, and fluctuation decay rates for several wavevectors can be used to explore solutions of the coupled equations for the critical enhancements of the fluctuation lifetimes and the viscosity. Most systems do not have a large enough data base of critically evaluated properties to allow crucial comparisons. As Swinney discussed, for those systems with enough of the properties known (CO_2, SF_6, and Xe), the crucial uncertainties entering the comparison with theoretical forms are from the correlation range and the viscosity. Except for the correlation range, we still depend on the properties gathered and evaluated by Swinney and Henry in 1973.

Meanwhile, the theoretical developments of the renormalization group calculations and universality have established the static critical exponents reliably. This requires that the old data be refitted to modern forms and exponents. But, when one is finished, the fact remains that we are still extrapolating old measurements well beyond their range to provide a "test" of the new and accurate decay rate measurements. New measurements taken closer to the critical point are needed for anyone who wishes to evaluate current theoretical ideas.

2.6 Experiment and Theory at their Limit

The current theoretical treatments of dynamic critical fluctuations can be reduced to the form from generalized hydrodynamics which shows that the wavevector dependent, fluctuation corrections to the viscosity and fluctuation decay rate are coupled in a pair of integral equations over particular functions of the static structure factor (Kawasaki, 1976). Various iterative approximations to these equations have lead to several estimates for the viscosity anomaly and decay rates which differ depending on where the iteration is stopped. Bhattacharjee and Ferrell (1983) have clarified the calculation of the critical viscosity exponent, Bhattacharjee, Ferrell, Basu and Sengers (1981) showed how to treat the cross-over region of viscosity data, and Burstyn, Sengers, Bhattacharjee and Ferrell (1983) applied the calculations of the dynamic scaling function to classical fluids. Of particular interest is the prediction (Bhattacharjee and Ferrell, 1983) for the dynamic scaling exponent, i.e. the exponent, as ξ diverges, for the wavevector dependence of the decay rate, which has only been tested on binary liquid mixtures. The results for the decay rates differ from earlier estimates when the scaled wavevector becomes greater than 10. The experiment described in this document should reach scaled wavevectors of

1000.

The form suggested by Ferrell (Burstyn, 1983) for the critical part of the diffusivity is

$$D_c = \frac{\Gamma_c}{q^2} = \mathrm{R}\,\frac{kT}{6\pi\eta\xi}\,\Omega(x)\,(1+b^2x^2)^{x_\eta/2} \quad ,$$

where R is the amplitude factor, η the shear viscosity, ξ the correlation range, $x = q\xi$ the scaled wavevector, $\Omega(x) = \mathrm{K}(x)/x^2$ with $\mathrm{K}(x)$ the Kawasaki function, b the amplitude of the dynamical correction, and x_η the exponent of the correlation range in the viscosity.

The real tension between theory and experiment at present is over the viscosity exponent x_η. Siggia *et al.* (1976) suggested that $x_\eta = 0.065$ and that the amplitude, R, of the Stokes-Einstein-Kawasaki form of the decay rate was 1.20 rather than 1.00. Experiments have been rather convincing that the amplitude is 1.00, but they are not independent of the method used to estimate the correct extrapolation of the viscosity into the temperature range of the light scattering measurements. Measurements of the viscosity seem to show that the binary mixtures are best described by $x_\eta = 0.065$ (Burstyn *et al.*, 1983), but recent fitting of the available data for liquid-vapor critical systems favors the value $x_\eta = 0.054$. This is in agreement with the suggestion of Ferrell that the Siggia calculation had missed a cancellation of corrections and that the exponent is nearer the original estimate (Bhatacharjee and Ferrell, 1983).

Because the viscosity exponent is not established, the predicted values of the decay rates close to the critical temperature are very uncertain. Figure 4 shows the scaled decay rate calculated with two fits to the Strumpf xenon viscosity data (using the exponents 0.065 and 0.054) extrapolated into the temperature range of the space experiment which we are discussing. The difference grows to 10% and illustrates why we must measure the decay rates in this region. They simply cannot be calculated with the limited viscosity data available: even with improvements to viscosity data from a low-gravity experiment, they would still need to be extrapolated into the temperatures reached in this scattering experiment. We do not know whether the equations used for binary mixtures (Burstyn and Sengers, 1982; Kopelman, 1983) will work for a liquid-vapor system. The only way to determine this is to have measurements close to the critical point *without the distortions in the density of the sample induced by gravity.*

We see this experiment as a means to probe the fundamental dynamics of a critical system, specifically that of a simple fluid, by accurately measuring the critical fluctuation decay rates closer to the critical point than is possible in any earth-bound experiment. We expect to measure the actual limiting decay rates at finite wavevector and determine their wavevector dependence. In addition, we will measure the correlation length of the fluctuations. As discussed above, it is not possible at present to calculate the decay rates to the accuracy with which they can be measured in this experiment. Thus, it is a worthy goal to make such a set of measurements on a carefully chosen, simple fluid system like

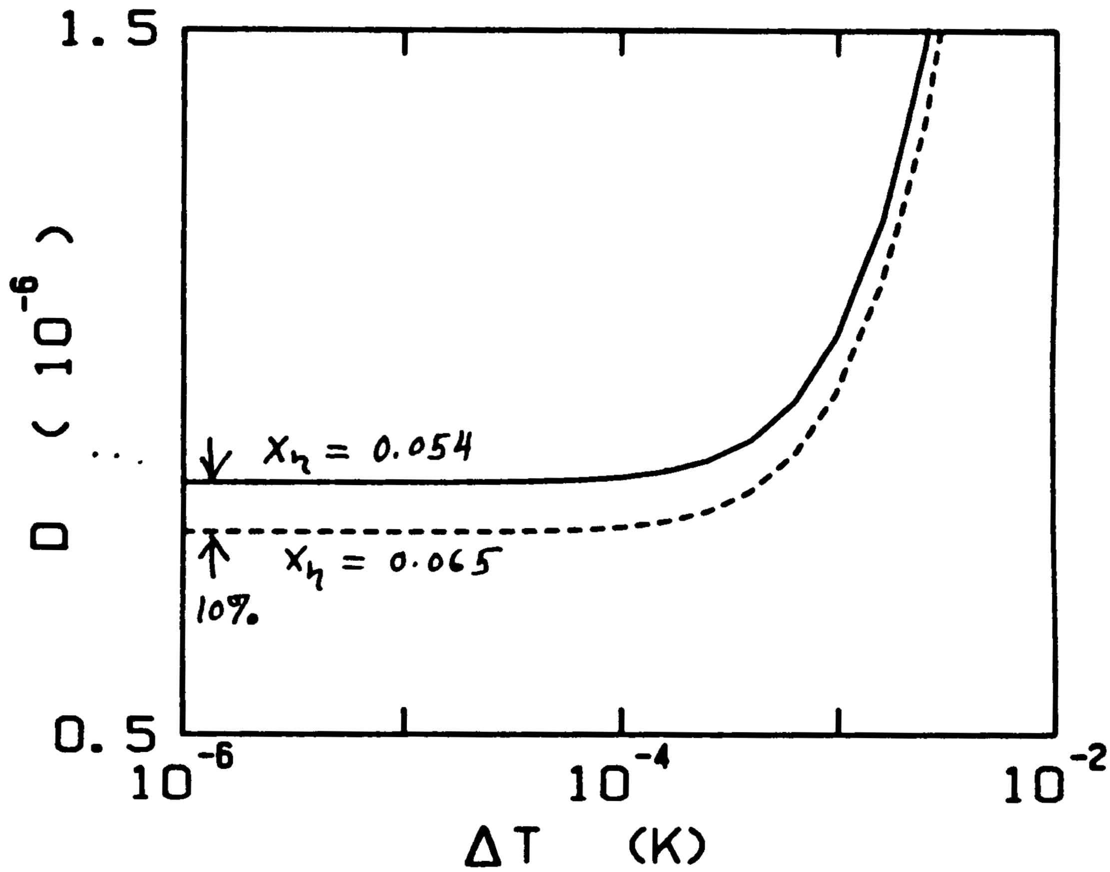

Figure 4. Calculated diffusivity of xenon at a scattering angle of 12°.

xenon. This *data set* will have a lasting value as a testing ground for any ideas about transport properties and dynamics in thermodynamic systems with large fluctuations.

3 Zeno Science Requirements

The list of science requirements distills the experiment into its barest essentials, to provide a foundation on which to build engineering requirements. The list derives from two principle considerations.

First, there are two major measurement goals of the experiment, namely decay rates and correlations lengths of critical fluctuations. Further, the decay rate measurements are to be performed at two angles to fix their dependence on the scattering wavevector. The associated science requirements specify the conditions that must be met to accomplish the precision and range of the measurements that will lead to a satisfactory data set.

1. Determine the decay rates of critical fluctuations in xenon.

   1.1. Measure to $\pm 1\%$ from correlation functions.

   1.2. Measure at two angles, θ and $\pi - \theta$ ($\theta \cong 12°$), with angles known to $\pm 0.03°$.

   1.3. Maintain the multiple scattering below 1% of the scattered intensity.

   1.4. Measure over a temperature range of 1 K to 100 μK from the critical point, with at least two values per decade.

2. Determine the correlation length of critical fluctuations in xenon.

   2.1. Measure to $\pm 3\%$ from transmission and intensity data.

   2.2. Measure time-averaged transmission continuously, to $\pm 0.1\%$.

   2.3. Measure the scattered intensity continuously, to $\pm 0.1\%$.

   2.4. Measure over a temperature range of 1 K to 100 μK from the critical point, with at least two values per decade.

3. Establish the thermodynamic trajectory towards the critical point of xenon.

   3.1. Measure and control the temperature of the sample to ± 3 μK for periods of at least 3 hours.

   3.2. Locate the critical temperature of the sample to ± 20 μK.

   3.3. Establish the absolute temperature of the critical point to ± 10 mK.

   3.4. Load the sample cell to within $\pm 0.1\%$ of the critical density of pure xenon.

3.5. Allow no temperature gradients across the sample larger than 1 μK/cm.

3.6. Limit residual and vibrational accelerations to $\leq 10^{-3}$ g.

3.7. Limit radiation heating of the sample to < 1 μW.

4 The Zeno Experiment

The instrument which performs the experiment divides easily into two subsystems. The optics subsystem includes the xenon sample under study, the means to maintain its thermodynamic state, the light source to probe its fluctuations, and the optical, thermal, and mechanical transducers which monitor its environment and collect the results of the interaction between light and critical fluid. The electronics subsystem oversees the control of the sample's environment, collects information from the transducers, and processes, reports, and stores the information. The operating of the subsystems are coordinated by the control software which manipulates the components of the optics subsystem, supervises the components of the electronics subsystem, and directs the experiment so that it can meet its science goals within the mission timeline.

4.1 Optics

4.1.1 Sample Cell

The xenon sample cell, shown schematically in figure 5, contains the sample at its critical temperature of 289 K and critical pressure of 58 atmospheres, while providing optical access for the light scattering measurements. The primary design constraint, to meet the science requirement of less than 1% multiple scattering, is that the laser beam have a 100 μm path length through the fluid, accomplished simply by having the windows of the sample cell separated by this amount. However, this would create such a small total volume of sample that meeting the science requirement that the cell be loaded to within 0.1% of the critical density would be difficult. Thus, the 100 μm sample space is surrounded by a reservoir of xenon sample, but the reservoir must be designed carefully. If its volume is too large, the heat capacity of the xenon would begin to slow the response of the thermostat. If its surface to volume ratio is too small, the divergent thermal conductivity of xenon at its critical point would lead to unacceptably long thermal relaxation times.

4.1.2 Thermostat

The only parameter controlling the thermodynamic state of the xenon sample is temperature; this is the responsibility of the thermostat. To achieve the goals of the experiment,

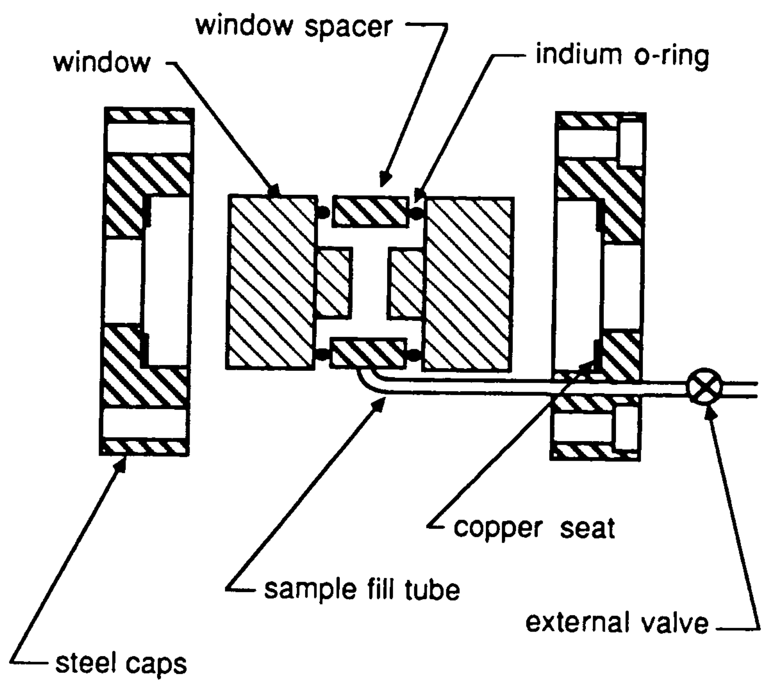

Figure 5. Xenon sample cell with 100 μm optical path length.

the requirements that it must satisfy are severe: controlling and measuring the temperature of the sample to $\pm$ 3 μK (near a temperature of 298 K), and preventing temperature gradients across the sample larger than 1 μK/cm. Furthermore, for its trip into space, the thermostat must be small, lightweight, and able to change temperature quickly to meet accommodation and mission time restrictions.

The thermostat shown schematically in cross section in figure 6 satisfies these goals, assuming an ambient environment stable only to $\pm$ 1 K. It is constructed of four co-axial cylindrical shells (numbered 1 through 4, innermost to outermost), with the sample cell contained within shell 1. The thermal coupling between shells is radiant, with 15 minute time constants. Optical access to the interior is provided by windows mounted on the ends of each shell. The overall size is 16 cm by 7 cm diameter, and the mass is less than 1.5 kg.

Mounted on shell 1 is a platinum resistance thermometer, used for absolute temperature calibrations; in operation, temperature sensing is done with thermistors. Each shell has at least one thermistor mounted on its surface to monitor temperature. On each of the outer three shells, the thermistor is part of a feedback circuit, which includes surface-mounted heaters on the shell, to control the temperature of the shell. Proceeding inward, each shell reduces temperature gradients by a factor of 100.

4.1.3 Optical Paths

A schematic layout of the optical configuration is shown in figure 7. The layout satisfies the science requirements for measuring fluctuation decay rates at two scattering angles and the correlation length of the fluctuations.

The beam from the low-power (5 mW) Helium-Neon laser can take one of two paths through the xenon sample; the path is chosen by the shutters, only one of which is open at a time. In the forward scattering configuration (top of figure 7), part of the beam is deflected into a photodiode to provide a reference for turbidity measurement. The remainder, focused by a lens, passes through the thermostated sample. The light which is scattered by fluctuations in the sample into a small solid angle (defined by the pinholes) at angle θ is collected for decay rate analysis by the photomultiplier tube. That light which survives its trip through the sample unscattered is directed to a second photodiode.

In the backscattering configuration (bottom of figure 7), the beam follows in reverse the path of the forward scattering beam. Again, part of the beam is deflected into a photodiode for turbidity reference. The remainder is focused and passes through the sample. That which makes it through unscattered is collected by another photodiode. The light scattered by the fluctuations in the sample is still collected by the photomultiplier tube, but the scattering angle is now $\pi - \theta$, the supplement of the forward scattering angle.

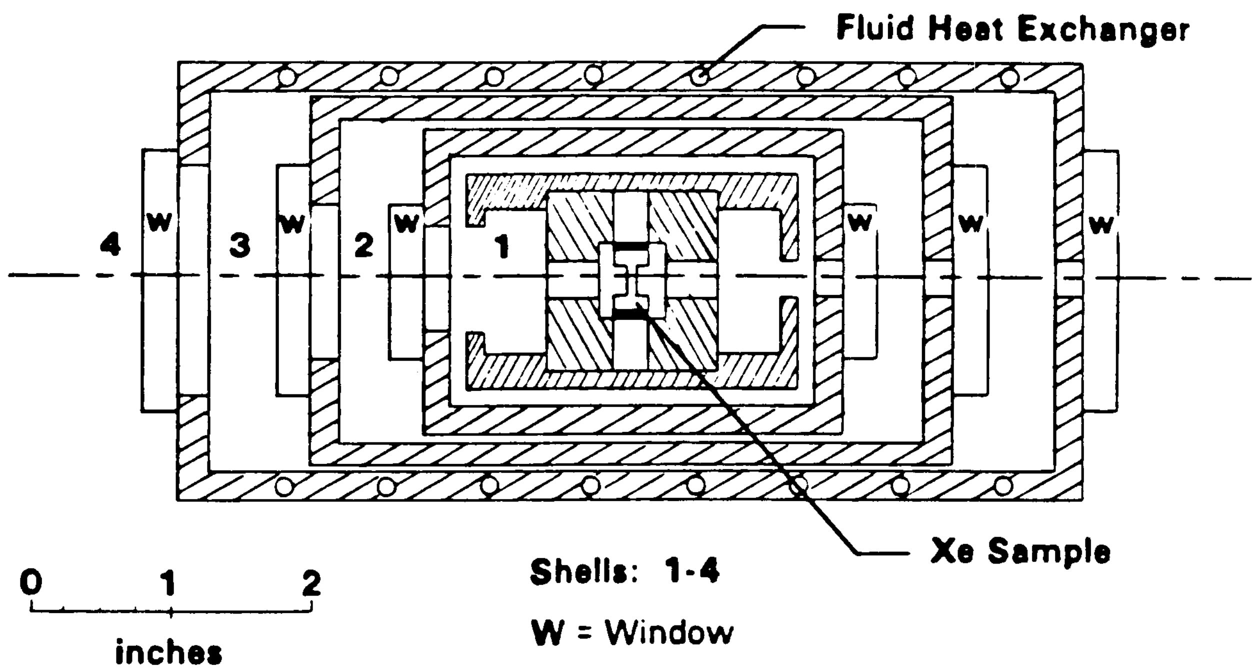

Figure 6. Thermostat

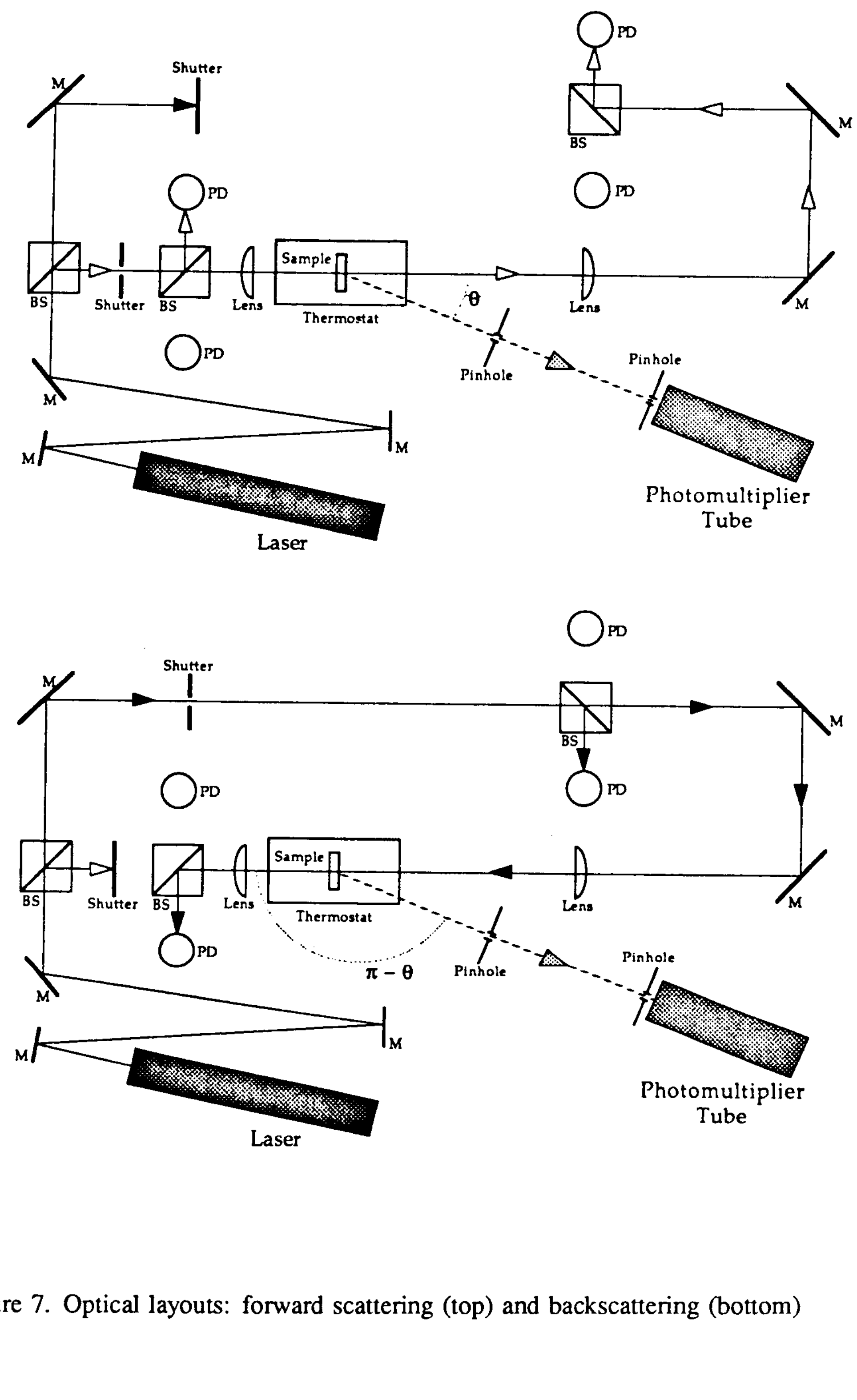

Figure 7. Optical layouts: forward scattering (top) and backscattering (bottom)

4.1.4 Mechanical Environment

The degree to which the experiment achieves its scientific goals increases in proportion to the degree to which it is isolated from vibrations on the STS. Thus the table on which the optics are mounted, beyond providing a stable surface to prevent distortion of the optical paths, is a component of a vibration isolation system to protect the optics subsystem.

Adjunct to the isolation system is the means for real-time monitoring of disturbances passes to the table from the STS. A high dynamic-range triaxial accelerometer is mounted on the surface of the optical table to inform the operating software of vibrational disturbances, also providing information on the size and duration of the disturbance.

4.2 Electronics

The electronics which support the experiment provide five basic functions: thermometry and temperature control, processing of the light scattering signal, processing of the turbidity signal, processing of the accelerometer signal, and opening and closing the shutters which set the scattering configuration. These operations are under the control of a microcomputer which coordinates them and effectively runs the experiment. The system is shown in figure 8.

4.2.1 Temperature Measurement and Control

Thermometry is done using AC bridge circuitry, where one of the bridge is formed by a thermistor and reference resistor (located on each of the thermostat shells), and the other arm is provided by a ratio transformer. The bridge is nulled (i.e. temperature is measured) by changing the tap position in the ratio transformer; null detection is accomplished with a phase sensitive, lock-in amplifier. Using AC signals to excite the bridge with lock-in signal recovery is necessary to achieve the temperature resolution required by the experiment. The output of the lock-in amplifier is a DC voltage representing the amount by which the bridge is out of balance. In the case of the shell 1 thermometer, this error signal represents the temperature of the sample. in the case of the outer shells (2, 3, and 4) the error signal is processed by the temperature controller, which drives heaters mounted on the shells to maintain their temperature, which is set by the ratio transformers. The ratio transformers are in turn set by the microcomputer, in this way determining the temperature profile across the thermostat and monitoring the temperature of the sample via the shell 1 thermometer.

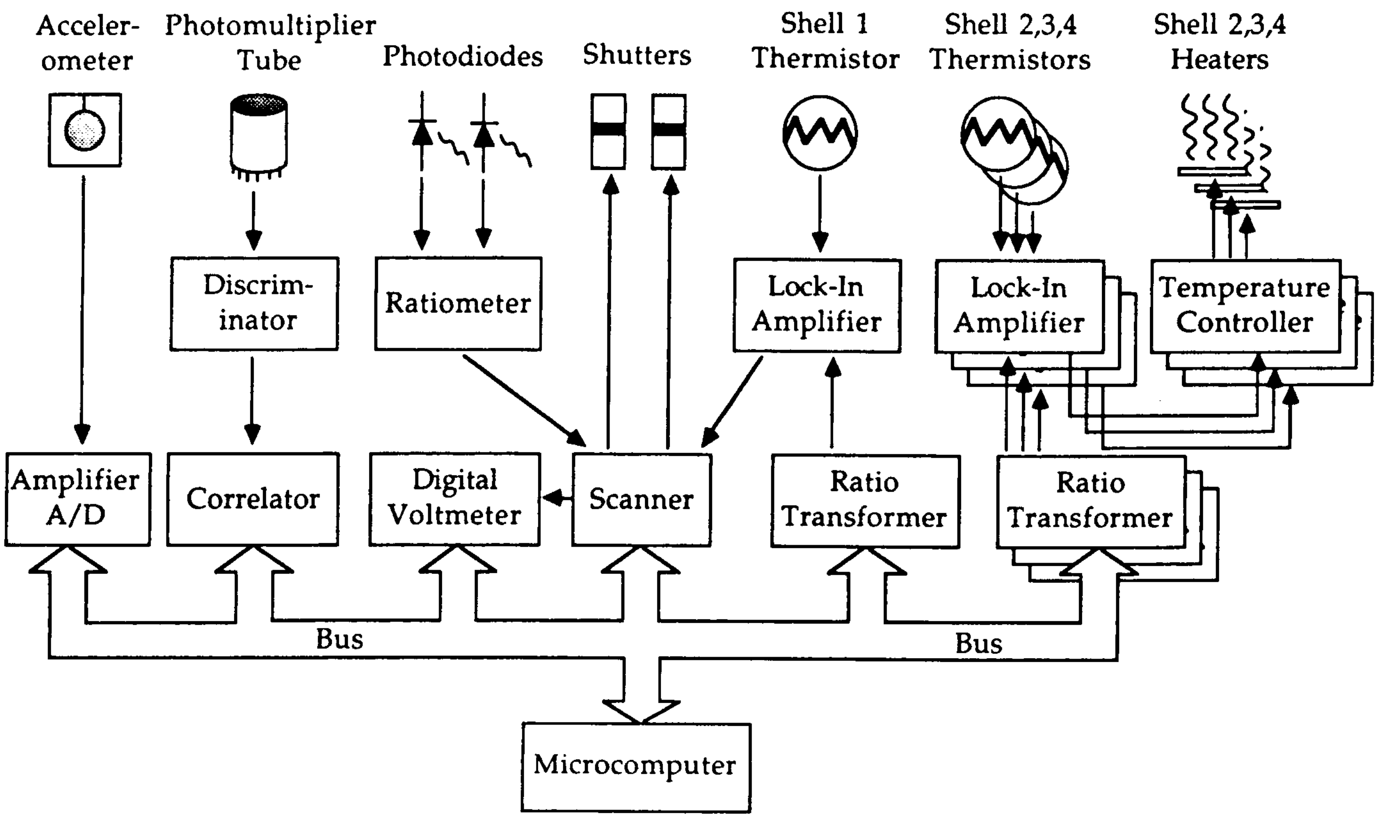

Figure 8. Control and Data Acquisition System

4.2.2 Transducer Signals

The light scattering signal is collected on the optical table by a high-gain, high quantum efficiency photomultiplier tube. The output of the tube is converted by the preamplifier/discriminator into a high-frequency (order MHz) stream of TTL pulses, with the pulse count rate proportional to the intensity of the scattered light. The programmable correlator calculates in real-time the autocorrelation function of the pulse stream as well as the average intensity, then makes the results available to the microcomputer after a pre-determined time. From these data the microcomputer calculates decay rates of the fluctuations, and some of the correlation length information.

In each of the two light path configurations, there is a pair of photodiodes which produce the raw signals for the turbidity measurements. In each case, one photodiode produces a current proportional to the intensity of the test beam to use as an amplitude reference, and a second photodiode produces a current proportional to the intensity of the light transmitted by the sample. The output of the ratiometer circuit is the logarithm of the ratio of transmitted to reference current, which is proportional to the turbidity of the sample. This signal is averaged by a digital voltmeter and passed to the microcomputer.

The signal from the accelerometer mounted on the optical table is processed by its amplifier, and the results passed to the microcomputer when safe levels of acceleration, determined by the current operating temperature of the experiment, are exceeded. With information about the level and duration of the detected disturbances, the control software can choose the proper strategy for accumulating data during the disturbance that takes best advantage of the limited mission time.

4.3 Timeline and Control Software

The software which controls the experiment is responsible for the operation of the electronics, and for coordinating them in the most efficient way to accomplish the science goals. Figure 9 shows a hierarchy of functions to be performed by the control software. Coordination of experimental activity is the primary responsibility of the experiment scheduling program, which decides the optimal approach to data taking, subject to programmmed information from the planned mission schedule and real-time information from the accelerometers located on the optics table. This schedule is passed to the synchronous device controller which is responsible for overseeing the actual operation of the electronics, as well as handling data storage. Some results of the lower lever operations are made known to the scheduling program to inform it of progress. With this feedback the scheduler is able to report both its decisions and the progress of the experiment based on those decisions to a ground-based monitor which can override its decision process.

The time line for the experiment breaks down into four parts:

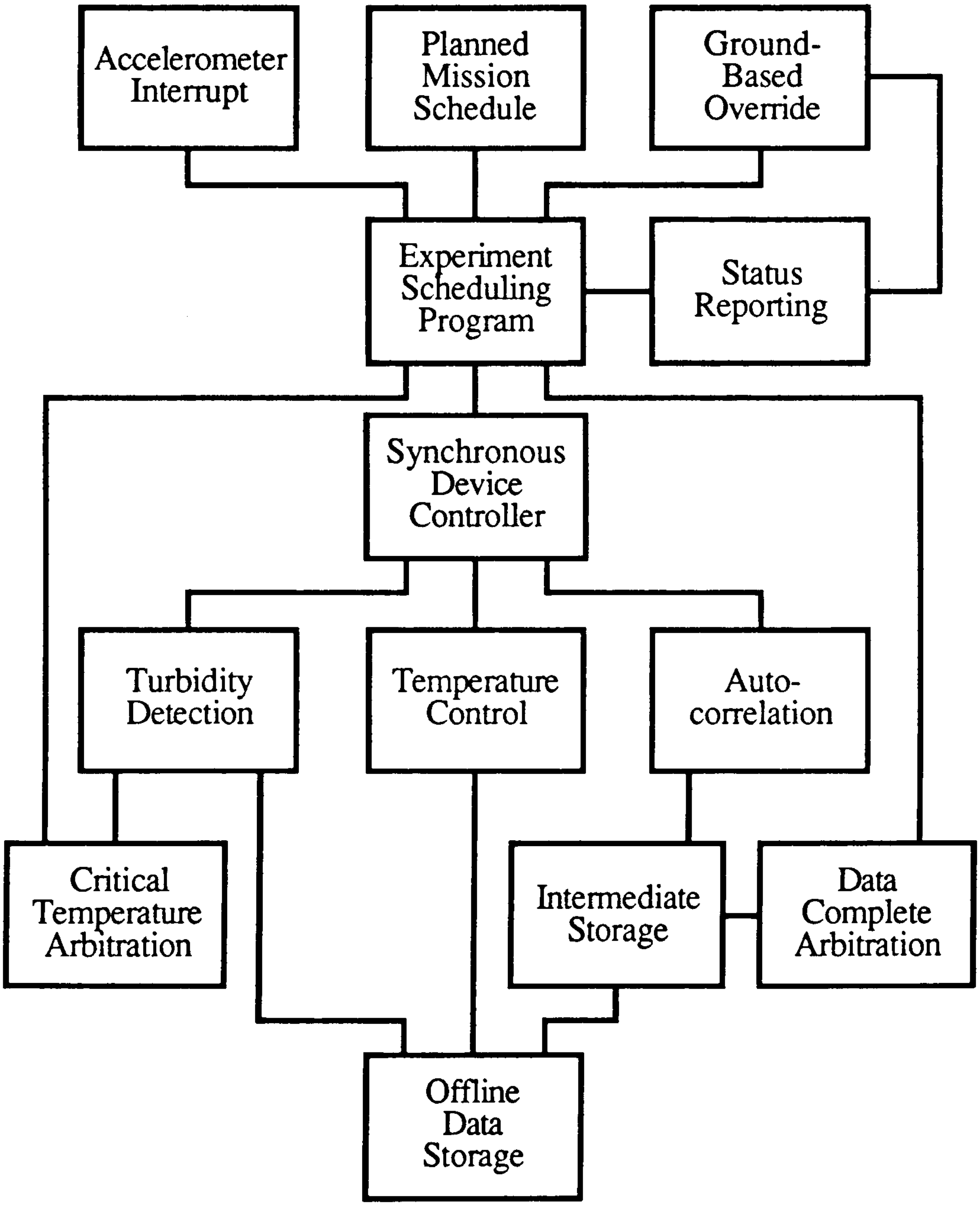

Figure 9. Experiment Control Hierarchy

1. Turn-on, initialize, and establish stating conditions.

2. Locate the critical temperature of the sample.

3. Measure decay rates and turbidity at temperature sequence.

4. Verify the critical temperature of the sample.

The turn-on of the instrument proceeds automatically after being actuated by the STS crew. The xenon sample must be put at a known, equilibrium state at a determined temperature, in order that it be homogeneously mixed and ready for operations. Given intershell time constants in the thermostat of 15 minutes, and an overall time constant of 45 minutes, reaching the initial temperature would take several hours. To allow the sample to equilibrate thoroughly, we allow 6 hours for the initialization procedure.

Locating the critical temperature of the sample is done by first cooling the sample quickly to a temperature near the critical temperature (typically within 100 μK); distance from the critical temperature can be inferred from the turbidity of the xenon sample. Once near the critical point, the thermostat alternately cools and warms the sample, looking for hysterisis in the turbidity signal which marks the beginning of the irreversible spinodal decomposition of the fluid which marks the critical point. The final steps in the cooling and warming are made at the temperature resolution of the thermostat, establishing the critical temperature of the sample to 100 μK. At present, the most length searches performed in the laboratory take from 4 to 6 hours; for the mission, we allow 8 hours as an upper bound and expect the actual time needed to be shorter.

The turbidity and fluctuation decay rates of the xenon sample are to be measured throughout the temperature range of 1 K to 100 μK from its critical point. Depending on the severity of the vibration environment encountered by the experiment, this range could be extended from 1 K to 3 μK. We plan to take measurements at a sequence of temperatures of two per decade, at temperature differences of 1 K, 0.3 K, 0.1 K,$\ldots, 3 \times 10^{-5}$K$, 10^{-6}$K$, 3 \times 10^{-6}$K. The last points will be more difficult than the first and may require extra attention. Thus, the sequence will have about 12 temperature points as a minimum set. At each temperature a sequence of forward ($\theta = 12°$) and backward ($\theta = 168°$) scattering fluctuation decay rates will be taken automatically by the correlator and analyzed, alternating between forward and backscattering configurations. Fitted correlation functions give the experimentally determined decay rate. These are compared as they accumulate; when the prescribed statistical accuracy is achieved, that determination is considered complete and the microcomputer moves the experiment on to the remaining temperatures.

Each correlation takes about 15 minutes for reasonable statistics and 10 points at each angle should reduce the statistical uncertainty of the decay rates to the required accuracy

6 References

Beysens, D. and G. Zalczer (1977), Phys. Rev. **A15**, 765.

Bhattacharjee, J. K., R. A. Ferrell, R. S. Basu, and J. V. Sengers (1981), Phys. Rev. **A24**, 1469.

Bhattacharjee, J. K., and R. A. Ferrell (1983), Phys. Rev. **A28**, 2363.

Bray, A. J. and R. F. Chang (1975), Phys. Rev. **A12**, 2594.

Burstyn, H. C., J. V. Sengers, J. K. Bhattacharjee, and R. A. Ferrell (1983), Phys. Rev. **A28**, 1567.

Burstyn, H. C. and J. V. Sengers (1982), Phys. Rev. **A25**, 448.

Chang, R. F., H. Burstyn and J. V. Sengers (1979), Phys. Rev. **A19**, 866.

Cohen, L. H., M. L. Dingus and H. Meyer (1982), J. Low Temp. Phys. **A49**, 545.

Cohen, L. H., M. L. Dingus and H. Meyer (1983), Phys. Rev. Lett. **50**, 1058.

Güttinger, H. and D. S. Cannell (1980), Phys. Rev. **A22**, 285.

Kawasaki, K. (1976), in *Phase Transitions and Critical Phenomena* ed. C. Domb and M. S. Green (Academic, New York, 1976), Vol. 5A, p. 165.

Kopelman, R. B. (1983), Ph. D. thesis, University of Maryland, "Light Scattering Measurements of Critical Fluctuations in an Optically Thin Binary Liquid Sample".

Reith, L. A. and H. L. Swinney (1975), Phys. Rev. **A12**, 1094.

Sengers, J. V. (1982), from *Phase Transitions: Cargese 1980*, ed. Maurice Levy, Jean-Claude Le Guillou, and Jean Zinn-Justin (New York: Plenum Publishing Corporation).

Siggia, E. D., B. I. Halperin and P. C. Hohenberg (1976), Phys. Rev. **B13**, 2110.

Sorenson, C. M., R. C. Mockler and W. J. O'Sullivan (1977), Phys. Rev. **A16**, 365.

Swinney, H. L. and D. L. Henry (1973), Phys. Rev. **A8**, 2586.

of 1%. The switch between forward and backscattering configurations is accomplished by the shutters on the optical table in less than 1 second. During the time that correlation functions are accumulating (in either configuration), the turbidity of the sample is logged continuously at the rate of approximately 1 sample/second. Thus the time for accumulating the correlation functions sets the time scale of the experiment at 6 hours per temperature point or a total of 78 hours.

If more time is available to the experiment during this phase, then the control program would concentrate on obtaining additional information in the temperature range from 3 mK to 3 μK from the critical point, the range in which earthbound measurements are impossible. Note that, for the self-consistency and integrity of the data set for post-flight analysis, we do take time to measure the turbidity and decay rates rather far from the critical temperature.

Finally, to check for possible (but unexpected) drifts in the thermometry, the experiment will verify its earlier determination of the critical temperature. We expect again that this will take no longer than 8 hours.

Thus, the total time line is made up of 6 hours to establish initial operating conditions, 8 hours for locating the critical temperature of the xenon sample, 78 hours for completing the turbidity and decay rate data set, and a final 6 hours for verifying the critical temperature, for a total mission time of 100 hours. We expect that some of the start-up time and time for locating the critical temperature can be eliminated. If more time is available for data taking, the measurements can be made in a smaller temperature sequence concentrating on the smaller temperature differences.

5 Acknowledgements

This project is currently funded under NASA grant NAG3-727 through NASA/Lewis Research Center. The Lewis project manager is Dr. R. Lauver. The project has been named Zeno after the Greek philosopher famous for his paradoxes about limits.

The principal investigator wishes to acknowledge his many collaborators in this project. The principal scientist for the project is Dr. J. Shaumeyer, who has made major contributions to all phases of the work and particularly to the automation of the present laboratory prototype of the experiment. University of Maryland graduate students M. Briggs and H. Boukari have each taken on portions of the lab work. Many of the design ideas have been developed and refined with the help of our design subcontractor Ball Aerospace Systems Division, with the team under project manager Dr. R. Reinker.

LIST OF AUTHORS

Dr. Robert A. Altenkirch
Department of Mechanical Engineering
University of Kentucky
Lexington, KY 40506

Dr. A. Z. Atassi
Baylor University of Medical School
Department of Biochemistry
Houston, TX 77030

Dr. Martin Barmatz
Mail Code 183-401
Jet Propulsion Laboratory
Pasadena, CA 91109

Dr. Abe L. Berlad
AMES Dept., B-010
University of California, San Diego
La Jolla, CA 92093

Dr. Milan Bier
Center for Separation Science
Electrical Engineering Bldg. 20, Room 157
University of Arizona
Tucson, AZ 85721

Dr. Donald E. Brooks
Department of Pathology
University of British Columbia
Vancouver, BC 6VT 1W5
CANADA

Dr. Charles Bugg
University of Alabama
Room 246 LHR
SDB 13 University Station
Birmingham, AL 35294

Dr. Ared Cezairliyan
National Bureau of Standards
Building 236
Washington, DC 20234

Dr. R. S. Cherry
Chemical Engineering Department
Rice University
Houston, TX 77251

Dr. Delbert E. Day
Department of Ceramic Engineering
107 Fulton Hall
University of Missouri, Rolla
Rolla, MO 65401

Professor Robert H. Doremus
Materials Engineering Department
Rensselaer Polytechnic Institute
Troy, NY 12181

Dr. Daniel D. Elleman
Mail Code 183-401
Jet Propulsion Laboratory
Pasadena, CA 91109

Professor Merton C. Flemings
Materials Processing Center
MIT
Cambridge, MA 02139

Dr. A. L. Fripp
Mail Stop 473
NASA Langley Research Center
Hampton, VA 23665

Dr. Robert W. Gammon
Institute for Physical Science and Technology
University of Maryland
College Park, MD 20742

Dr. Harry C. Gatos
Department of Materials Sciences & Engineering
MIT
Cambridge, MA 02139

Dr. Stanley H. Gelles
S. H. Gelles Associates
2836 Fisher Road
Columbus, OH 43204

Dr. Martin E. Glicksman
Materials Engineering Department
Rensselaer Polytechnic Institute
Troy, NY 12181

Dr. C. F. Goochee
Department of Chemical Engineering
University of Houston
Houston, TX 77004

Professor Wesley C. Hymer
Department of Microbiology
Pennsylvania State University
University Park, PA 16802

Dr. J. A. Kafalas
GTE Laboratories, Inc.
40 Sylvan Road
Waltham, MA 02254

Professor R. B. Lal
Department of Physics & Mathematics
Alabama A&M University
Normal, AL 35762

Dr. David J. Larson, Jr.
Materials & Structural Mechanics Research
Grumman Corporation
Bethpage, NY 11714

Dr. V. Laxmanan
Mail Stop 49-3
NASA Lewis Research Center
Cleveland, OH 44135

Dr. Sandor L. Lehoczky
Mail Code ES72
Marshall Space Flight Center
MSFC, AL 35812

Dr. John Lipa
Department of Physics
Stanford University
Stanford, CA 94350

Dr. M. H. McCay
University of Tennessee Space Institute
Tullahoma, TN 37388

Dr. L. V. McIntire
Biomedical Engineering Laboratory
Department of Chemical Engineering
Rice University
Houston, TX 77251

Dr. Dennis R. Morrison
Mail Code SD3
NASA/Johnson Space Center
Houston, TX 77058

Dr. Simon Ostrach
Department of Mechanical & Aerospace Engineering
Case Western Reserve University
Cleveland, OH 44106

Professor Robert B. Pond
Materials Science & Engineering Dept.
Johns Hopkins University
107 Maryland Hall
Baltimore, MD 21218

Dr. K-Y. San
Chemical Engineering Department
Rice University
Houston, TX 77251

Dr. Robert S. Snyder
Mail Code ES73
Marshall Space Flight Center
MSFC, AL 35812

Dr. Stein Sture
Department of Civil, Environmental & Architectural Engineering
Campus Box 428
University of Colorado
Boulder, CO 80309

Professor R. S. Subramanian
Department of Chemical Engineering
Clarkson College
Potsdam, NY 13676

Dr. D. M. Surgenor
Center for Blood Research
800 Huntington Avenue
Boston, MA 02115

Professor Julian Szekely
Department of Materials Engineering
MIT
Cambridge, MA 02138

Professor Paul W. Todd
Center for Chemical Engineering
Mail Stop 773.010
National Bureau of Standards
325 Broadway
Boulder, CO 80303

Dr. John W. Vanderhoff
Center for Surface Coatings & Research
Sinclair Laboratory
Lehigh University
Bethlehem, PA 18015

Dr. L. van den Berg
EG&G, Inc.
130 Robin Hill Road
Goleta, CA 93017

Dr. Taylor G. Wang
Mail Code 183-401
Jet Propulsion Laboratory
Pasadena, CA 91109

Dr. Michael C. Weinberg
Department of Mat. Sci. & Engr.
University of Arizona
Tucson, AZ 85721

Dr. Heribert Wiedemeier
Department of Chemistry
Rensselaer Polytechnic Institute
Troy, NY 12181

Dr. Forman A. Williams
Department of Mechanical & Aerospace Engineering
Princeton University
Princeton, NJ 08544

NASA
National Aeronautics and Space Administration

Report Documentation Page

1. Report No. NASA TM-4069 Vol. 2	2. Government Accession No.	3. Recipient's Catalog No.
4. Title and Subtitle Microgravity Science and Applications Flight Programs, January-March 1987, Selected Papers		5. Report Date October 1988
		6. Performing Organization Code EN
7. Author(s)		8. Performing Organization Report No.
		10. Work Unit No.
9. Performing Organization Name and Address NASA Office of Space Science and Applications Microgravity Science and Applications Division		11. Contract or Grant No.
		13. Type of Report and Period Covered Technical Memorandum
12. Sponsoring Agency Name and Address National Aeronautics and Space Administration Washington, DC 20546		14. Sponsoring Agency Code

15. Supplementary Notes

16. Abstract

This report is a compilation of selected papers written by the flight program principal investigators. The Microgravity Science and Applications Flight Program was reviewed by a panel of eight chaired by Professor J. Robert Schrieffer in 1987. Dr. Schrieffer and his committee reviewed the flight program and made recommendations to the Director of the Microgravity Science and Applications Division as to the quality of the science contained in the program and improvements that could be made in some of the research efforts.

17. Key Words (Suggested by Author(s)) electronic materials, combustion science, microgravity science and applications	18. Distribution Statement Unclassified - Unlimited. Subject Category 29

19. Security Classif. (of this report)	20. Security Classif. (of this page)	21. No. of pages	22. Price
Unclassified	Unclassified	324	A14

NASA FORM 1626 OCT 86 Available from the National Technical Information Service, Springfield, VA 22161